2-1-2013

Particle image velocimetry studies of an oscillating flow in a thermoacoustic device

Michael Rezk Saad

Recommended Citation

APA Citation

Saad, M. (2013).*Particle image velocimetry studies of an oscillating flow in a thermoacoustic device* [Master's Thesis, the American University in Cairo]. AUC Knowledge Fountain.
https://fount.aucegypt.edu/etds/1273

MLA Citation

Saad, Michael Rezk. *Particle image velocimetry studies of an oscillating flow in a thermoacoustic device*. 2013. American University in Cairo, Master's Thesis. *AUC Knowledge Fountain*.
https://fount.aucegypt.edu/etds/1273

The American University in Cairo
School of Sciences and Engineering

PARTICLE IMAGE VELOCIMETRY STUDIES OF AN OSCILLATING FLOW IN A THERMOACOUSTIC DEVICE

A Thesis Submitted to
The Mechanical Engineering Department

In partial fulfillment of the requirements for the degree of
Master of Science

by

Michael Rezk Saad

Under the Supervision of

Dr.Ehab Abdel-Rahman
Associate Professor, Physics Department
Associate Dean for Graduate Studies, School of Sciences and Engineering
The American University in Cairo

Dr.Mustafa Arafa
Associate Professor, Mechanical Engineering Department
The American University in Cairo

Dr.Abdelmaged H. Ibrahim Essawy
Assistant Professor, School of Sciences and Engineering
The American University in Cairo

January 2013

To all those who follow, believe in a solution to find it.

Acknowledgements

First of all, I would like to express my deepest gratitude to Dr. Ehab Abdel-Rahman for his continuous support, encouragement and guidance. Dr. Ehab taught me to believe that any task is possible only when enough effort is wisely made. Dr. Ehab helped me through the hard and dark times to pick myself up and move forward. To him I owe the enriched time I spent at AUC.

I would like to thank Dr.Abdelmaged Ibrahim, for being my teacher and companion throughout all the hardships and the achievements in this work. Starting from nowhere and ending where everything starts to make sense, he was always there watching every detail and seeking perfection.

I would like to thank Dr. Mustafa Arafa for his continuous support that started the minute I stepped into AUC. Regardless of what problems I had, he was always there to listen and provide advice. He taught me a great deal on both the professional and personal level.

I would like to thank Professor Steven Garrett, one of the pioneers of thermoacoustics in the world. Without the knowledge that Professor Garrett had passed to our research group, this work wouldn’t have been completed.

I would like thank Dr. Hosny Omar, Dr. Ahmed Ibrahim and Dr. Karim Addas and for their support and contribution to complete this work.

I would like to thank Dr. Mohie Mansour whom without his advice this work wouldn’t have been validated.

I would like to thank Eng. Hani Mostafa and Eng. Sherif Selim for their support and technical assistance.

I would like to thank all the staff of the Physics workshop, the Mechanical Engineering workshop and the Yousef Jamil Science and Technology research center for their continuous support and technical assistance.

Also, I would like to thank Dr. Maher Younan for his time, his patience, his advice and above all his inspiration. Dr. Maher is a role model for several generations of engineers and researchers.

I would like to thank the staff of the Dean's office, the office of the Associate Dean for Graduate Studies, the Physics Department and the Mechanical Engineering Department for facilitating all requirements at need.

I would like to thank my fellow colleagues at AUC; Nadim Arafa, Ahmed Eladawy, Mohamed Beshr, Mazen Eldeeb, Diaaeldin Mohamed, Kahled Elbeltagy, Ahmed Elbeltagy, Mahmoud Emam, Hassan Adel, Tarek Nigim, Moamenbellah Abdou, Mohamed Adam and Marwa Tewfik for sharing their efforts and knowledge and above all for being there whenever needed.

I would like to express my special gratitude to Dr. Tamer Elnady and Dr. Adel Elsabbagh; my mentors from the Mechanical Design and Production Department at Ain Shams University, for they have introduced me to the field of scientific research. To them I owe my career.

I would also like to express my special gratitude to Dr. Ahmed Hussein who always inspires me to search for more, learn more and by all means work even more.

As for my family, all the words can never describe how lucky I am to have each and every one of you by my side. All the words can never show how much you sacrifice to make me happy. To each and every one of you, I owe my life.

In conclusion, this work would never have been possible without the financial support of King Abdullah University for Science and Technology (KAUST) as part of the Integrated Desert Building Technology (IDBT) project.

Abstract

Flow visualization is a necessity in thermoacoustic devices to study the behavior of the devices and relate visualization outcomes to other experimental and computational results to help obtaining a complete understanding of physics of flow in thermoacoustics. In this work particle image velocimetry (PIV) was used to investigate the effects of changing the porosity and length of meshed ceramic stacks on the acoustic behavior of thermoacoustic oscillations in a thermoacoustic refrigerator with no heat exchangers and operated at atmospheric pressure. PIV was also used to study the vortex generation morphology at the premises of parallel plate stacks as vortices are one important source of efficiency loss in thermoacoustic devices. A glass-quartz acoustic resonator was built with a loudspeaker attached to induce a standing acoustic wave inside the resonator. Meshed ceramic stacks with different porosities and lengths were utilized to study the acoustic behavior. In addition, sets of parallel plates of aluminum and acrylic were used to study the flow morphology. The acoustic behavior measurements showed that as the meshed stack porosity increases the value of the acoustic power decreases unlike expected. This concludes that the viscous friction effects are dominant over the change in porosity as far as the gas parcel velocity and acoustic pressure amplitude are concerned. The morphology study aimed at visualizing the change in vortex generation behavior at different amplitudes and different configurations of the parallel plate sets. The results showed that as the amplitude of the dynamic pressure increases the size and displacement of a vortex increases. Also, as the plate spacing decreases the amount of disturbance increases due to the interaction of vortex structures together. Additionally, the combined effect of increasing amplitude and decreasing plate spacing would lead to higher disturbance. Vortex shedding was not observed, but visual inspection of the results showed that the existence of vortex shedding is affected by both the frequency and the dynamic pressure. Vortex shedding would occur if the acoustic cycle period is less than the time required by a vortex to completely develop. The time of vortex development is a function of its size and thus of the dynamic pressure amplitude. The results also showed that the flow in between the parallel plates is disturbed only when a vortex re-enters into the parallel plate channels. The amount of disturbance that the re-entering vortex causes is directly proportional to the size of the vortex.

TABLE OF CONTENTS

.

NOMENCLATURE

PIV	Particle Image Velocimetry
c	Speed of sound
λ	Wave length
f	frequency
Q_h	Input heat energy
Q_c	Rejected waste energy
W	Produced work
T_h	Heat source temperature
T_c	Heat sink temperature
δ_k	Thermal penetration depth
K	Gas thermal conductivity
ω	Angular frequency
ρ	Density
c_p	Specific heat at constant pressure
δ_v	Viscous penetration depth
ν	Kinematic viscosity
R	Ratio between the seeding particle velocity and the flow velocity, or the ratio between the flow wave period and the seeding particle response time
$v_{particle}$	Velocity of seeding particle
v_{flow}	Flow velocity
t_{flow}	Flow wave period
$t_{particle}$	Seeding particle response time
γ	Ratio between the seeding particle density and the fluid density
d	Diameter of seeding (tracer) particle
e	Supply voltage of a loudspeaker
R_e	DC resistance of a loudspeaker
L_e	Imaginary part of the voice coil inductance of a loudspeaker
R_{evc}	Real part of the voice coil inductance of a loudspeaker
M_m	Moving mass of a loudspeaker
C_m	Compliance of the moving mass of a loudspeaker
R_{me}	Suspension system of a loudspeaker
M_A	Air mass of a loudspeaker
r_A	Radiation impedance of a loudspeaker

A_{eff}	Effective cone area of a loudspeaker
R_{DC}	DC resistance of a loudspeaker
f_o	Resonance frequency of a loudspeaker in free field
k	Lumped stiffness of a loudspeaker
m_o	Lumped mass of a loudspeaker
τ	Time constant
R_m	Mechanical impedance of a loudspeaker
Z_e	Electric impedance at resonance of a loudspeaker
Bl	Electro-dynamic force factor
Z	Electric impedance
D	Diameter of loudspeaker's diaphragm
ω_o	Resonance angular frequency
m	Total mass of a loudspeaker
T	Period of the acoustic wave
m_i	Added mass
U	A symbolic equivalent of $\frac{T^2}{4\pi^2}$
$f_{free\ decay}$	Resonance frequency measured using the free decay method
V	Voltage
t	Time
V_o	Mean voltage
Q_{factor}	Quality factor of a resonator
L	Voice coil inductance of a loudspeaker
V_c	Voltage across loudspeaker's coil
V_Ω	Voltage across resistance
I	Electric current
R_{high}	High value resistance
U_∞	Settling velocity of seeding (tracer) particles
g	Gravity constant
d_p	Seeding particle diameter
ρ_p	Seeding particle density
ρ_f	Fluid density
μ_f	Fluid viscosity
$Power_{max}$	Maximum power of a loudspeaker
V_{max}	Maximum voltage across the coil of a loudspeaker

cos Ø	Power facotr
V_{p-p}	Peak to peak voltage
V_{rms}	Root mean square voltage
L_r	Length of the resonator from loudspeaker’s surface to the hard end
$P_{electret}$	Pressure measured using the electret microphone
Re	Reynolds’ number
V_{Dim}	Velocity measured to compute the values of different dimensionless numbers
D_p	Plate spacing
St	Strouhal number
Wo	Womersley number
KC	Keulegan-Carpenter number
L_s	Plate length

LIST OF FIGURES

LIST OF TABLES

Chapter 1. Introduction

Thermoacoustics relates to the rich and complex interactions between thermodynamics and acoustics. Thermoacoustic engines convert thermal energy into acoustic energy, which is one form of mechanical work. Thermoacoustic refrigerators convert acoustic energy into refrigeration effect. Research in the thermoacoustics field has gained great interest throughout the past decade as thermoacoustic devices can be driven by solar energy or waste heat, operate with inert gases – thus are environmentally friendly – and without moving parts. Additionally, a thermoacoustic refrigerator can be driven with a thermoacoustic engine, which in turn is driven with solar energy, thus making a solar-energy-driven refrigerator.

Although simple in concept, rather complex phenomena are present in thermoacoustics. This multidisciplinary field involves the integration of acoustic systems, thermal components, electro-dynamic drivers, fluid-mechanics, heat transfer under oscillating flow conditions, and mechanical issues related to sealing. The process of generating electricity or refrigeration effect through thermoacoustic devices has interesting results especially when the linear theory is not applicable anymore.

Thus the need to study the phenomenon of thermoacoustics with all its aspects arose. It became necessary to go deeper into studying the flow morphology and the thermal interactions.

The objectives of this work are to perform two main tasks; the first is to study the acoustic behavior of a thermoacoustic refrigerator with no heat exchangers experimentally and numerically in order to determine how changing the stack configuration affects the two main acoustic parameters: the acoustic pressure and the gas particle velocity. As the device is operated at atmospheric pressure, the refrigeration effect is rather very low and can be neglected. The presence of heat exchangers would sustain any thermal effect, but this is beyond the scope of this work, as the aim in this work is to study the acoustic and viscous effects only. Inherent in this task is to quantify the parameters of the electro-dynamic speaker used to drive the thermoacoustic refrigerator. The second task is to visualize the flow of air particles inside and outside the channels of a set of parallel plates, aiming at defining the effect of changing plate configurations (thickness and separation between plates) on the flow physics and particularly the vortex generation behavior as vortices are one major source of efficiency losses in thermoacoustic devices.

For both tasks pressure and velocity measurements are necessary: A differential microphone setup to measure the end pressure in the thermoacoustic resonator and an electret microphone setup to measure the spatial pressure distribution along the length of the resonator were used. As for velocity, particle image velocimetry (PIV) was used to determine the spatial and temporal gas parcel velocity behavior.

Chapter 1 is an introduction to the thesis. Chapter 2 is a review of the previous work. Chapter 3 introduces the experimental technique used to characterize loudspeakers for the sake of use in thermoacoustics modeling. Chapter 4 illustrates the PIV and pressure measurement setups used for studying acoustic behavior and flow visualization. Chapter 5 describes the measurements performed to quantify the acoustic behavior of the thermoacoustic refrigerator under different meshed stack configurations. Chapter 6 is composed of two parts; the first part is the flow visualization experiments done outside a parallel plate stack and the second part is the flow visualization inside the parallel plate stack channels. Conclusions are illustrated in Chapter 7 and recommendations and future work in Chapter 8.

Chapter 2. Review of previous work

2.1. Literature review

The use of particle image Velocimetry (PIV) in studying the non-linear effects occurring in thermoacoustic devices such as vortex structures has gained much interest in the past decade. The study of the flow physics and specially vortex structures analysis has become of great importance aiming to quantify the non-linear parameters affecting efficiency of thermoacoustic devices.

The use of PIV in thermoacoustics was strongly advised after successful PIV measurements were performed on measuring acoustic velocity of particle in normal acoustic field that are unrelated to thermoacoustics. Hann and Greated used PIV to measure acoustic particle velocity and streaming velocity in a standing wave tube [1]. Navaei and Sharp also used PIV to image standing acoustic waves in an air column [2]. Fischer *et al* used a synchronized PIV measurement technique to measure velocity fields in non-standing wave acoustic fields using an algorithm to differentiate between acoustic particle velocity and flow field velocity [3]. Nabavi *et al.* also used synchronized PIV measurement technique to measure spatial and temporal velocity distributions to study non-linear effects in acoustic flow and compare those to numerical solutions of the wave equation [4]. Siddiqui and Nabavi used out of phase PIV to measure the acoustic field of a standing wave proving that the acoustic field can be measures at separate location and then constructed again to give the complete wave form [5]. Rafat and Mongeau used PIV to measure the acoustic particle velocity and the streaming velocities in a standing wave environment [6].

One of the early works of using PIV in thermoacoustics was the work of Benon *et al.* where PIV was used to study the formation of vortex structures experimentally and a numerical model was developed for the same purpose and both experimental and numerical results were compared [7]. Berson *et al.* used PIV to study the formation of vortex structures at the edge of stacks at different configurations and also study the physics of the oscillatory boundary layer occurring at the inner surfaces of the thermoacoustic device [8]. Mao *et al.* were able to develop an experimental setup to visualize the flow inside a parallel plate stack's channels defining distributions of turbulence intensities and calculating vorticity fields within stack premises [9]. Debesse *et al.* also measured acoustic particle velocity and velocity streaming but in a nitrogen filled standing wave resonator and at the free stream zone away from the stack region [10]. Aben *et al.* used dimensionless numbers that are used in describing fluid mechanics to quantify the resulted vortex generation mechanisms visualized by PIV [11]. They also measured acoustic streaming and studied the influence of different stack parameters and stack edge shapes on the generated vortex structures. Jaworski *et al.* used PIV to study the flow morphology at the stack edges at the stage of entry into the stack [12]. They also studied the oscillatory boundary layer occurring during entry and built a numerical model to validate experimental results. Mao *et al.* used PIV results imaging flow physics at parallel plate stacks to build reference 3D maps to describe the flow in reference to the Reynolds' number and the Keulegan-Carpenter number [13]. Shi *et al.* categorized several vortex wake patterns occurring at the end of a parallel plate stack into eight typical wake patterns and described them in the form of "combined symbolic codes of letter" [14]. Shi *et al.* also used PIV measurements of wake patterns to describe different vortex shedding patterns phase by phase during the ejection stage of the flow outside of the stack and discussed the impact of changing Reynolds number and the stack plate thickness on the vortex shedding patterns [15]. Babaei and Siddiqui measured acoustic streaming using PIV at both ends of a thermoacoustic stack at different drive ratios [16]. Mao and Jaworski used an analysis algorithm based on Fast Fourier Transform special filtering techniques to categorize vorticity fields imaged using PIV according to their intensities as large and small scale fluctuations and study their effect on the heat transfer process [17]. Shi *et al.* combined the use of PIV and PLIF (Particle Laser Induces Fluorescense) to measure velocity fields using PIV and thermal fields using PLIF [18]. Shi *et al.* continued the work of Mao *et al.* to include a wider range of parameters to quantify the relationship between vortex wake patterns and experimental parameters [19].

The aim of this work is to use PIV to study the acoustic behavior of a thermoacoustic refrigerator with no heat exchangers operated at atmospheric pressure with meshed ceramic stacks and to study the flow morphology at the premises of sets of parallel plate in the same device without considering the thermal effects.

2.2. Theoretical overview

2.2.1. Thermoaoustics

2.2.1.1. Basic acoustics principles

Sound defined as the vibration of air parcels can be generated as result of several interactions; the vibration of bodies, the change in air flow, rapid heating of air particles and supersonic flow [20]. The most important acoustic term used in thermoacoustics is the drive ratio. The drive ratio is the maximum dynamic pressure in the resonator divided by the mean gas pressure as shown in Eq. 2.1 .

$$\text{Drive ratio} = {}^{P_{acousitc\ maximum}}\!/_{P_{mean}} \qquad \textbf{Eq. 2.1}$$

It is more practical to use the drive ratio to define the dynamic pressure amplitude in a thermoacoustic device to accommodate for different operating gases.

Figure 2.1 shows a schematic describing the motion of air particles due to a sound wave. Air particles don't move a great distance away from their initial equilibrium position, but rather oscillate around the equilibrium position moving very small distances to the right and left of the equilibrium position [21]. The sound energy is thus transferred from one particle to another and moved from the source to the target without changing the original location of air particles.

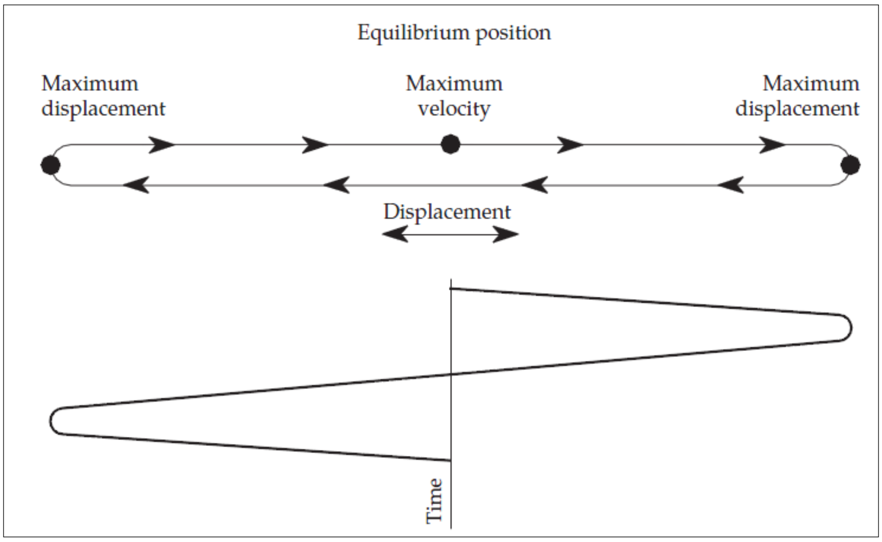

Figure 2.1 Air particle motion around equilibrium position due to a sound wave. (Courtesy of Everest, Pohlmann, "Master handbook of acoustics" [21]).

The speed of energy transfer between particles is called the speed of sound while the speed of particle oscillation around the equilibrium position is called the acoustic particle velocity. The displacement of the acoustic particle away from its equilibrium position is a function in the dynamic pressure. The dynamic pressure and the acoustic particle velocity are the most important acoustic variables. Their dot product is called the acoustic power. Sound wave is a longitudinal wave where particles motion is parallel to the direction of wave propagation.

Eq. 2.2 shows the definition of the speed of sound;

$$c = \lambda f$$ **Eq. 2.2**

where (c) is the speed of sound in [m/sec], (λ) is the wave length in [m] and (f) is the frequency of the sound wave in [Hz].

Similar to any wave a sound wave reflects, refracts and is damped. An important feature in sound wave reflection is the occurrence of a standing wave. A standing wave is the constructive interference of two sound waves having the same frequency with a phase shift of 180^o between each other. A standing wave occurs when sound is driven in a tube or cavity and certain conditions are fulfilled. The two most common cases of standing waves in thermoacoustics are the half wave and quarter wave resonators. Both cases have different pressure and velocity boundary conditions. The half wave resonator has the wave length of the sound wave as twice as much as the length of the tube and both ends of the tube are closed, while the quarter wave resonator has the wave length of the sound wave as four times as much as the tube length while one end is open and the other is closed. For a standing wave to occur in both cases the length of the tube and the end conditions lust be fulfilled together for each case alone, both cases are not interchangeable. In other words even if the length of the tube is correctly related to the wave length of the sound wave but the end conditions are not matched the standing wave will not occur. The interesting factor in standing waves is the amplification of dynamic pressure and acoustic particle velocity under natural conditions without the need of external energy, thus increasing the total acoustic power inside the tube which is translated in thermoacoustics to higher acoustic power.

2.2.1.2. Basic thermoacoustic principles

Thermoacoustics is the science concerned with the study of the combination of acoustic pressure oscillation, particle velocity oscillations, particle temperature oscillations and the thermal interaction between particles and solid boundaries occurring due to the presence of a sound wave in a cavity [22]. This combination of effect is small to notice in normal daily conditions but the harnessing of these effects in well sealed cavities increases their output to produce powerful thermoacoustic devices. For example, during ordinary speech the sound intensity is 65 dB. The pressure variations are about 0.05 Pa, the displacements are about 0.2

μm, and the temperature variations are about 40 μK and thus the thermal effects of sound are not observed in daily life. However, at sound levels of 180 dB, which are normal in thermoacoustic systems, the pressure variations are 30 kPa, the displacements are more than 10 cm, and the temperature variations are about 24 K [23] .

Thermoacoustic devices are of two types; thermoacoustic engines and refrigerators. A thermoacoustic engine employs heat energy originally generated from a heat source (hot heat exchanger) to produce acoustic energy and reject waste heat. Figure 2.2 shows a schematic of a thermoacoustic engine applying the first law of thermodynamics where (Q_h) is the input heat energy, (Q_c) is the rejected waste energy, (W) is the produced acoustic energy, (T_h) is heat source (hot heat exchanger) temperature and (T_c) is heat sink (cold heat exchanger) temperature. The engine efficiency is then the ratio between the output acoustic power and the input heat energy (W/Q_h). Such efficiency is bound by Carnot's efficiency according to the second law of thermodynamics. The main components as shown for the thermoacoustic heat engine are the resonator, the stack, the hot heat exchanger, the cold heat exchanger and the linear alternator. The linear alternator is the component that converts the output acoustic energy into useful electric energy.

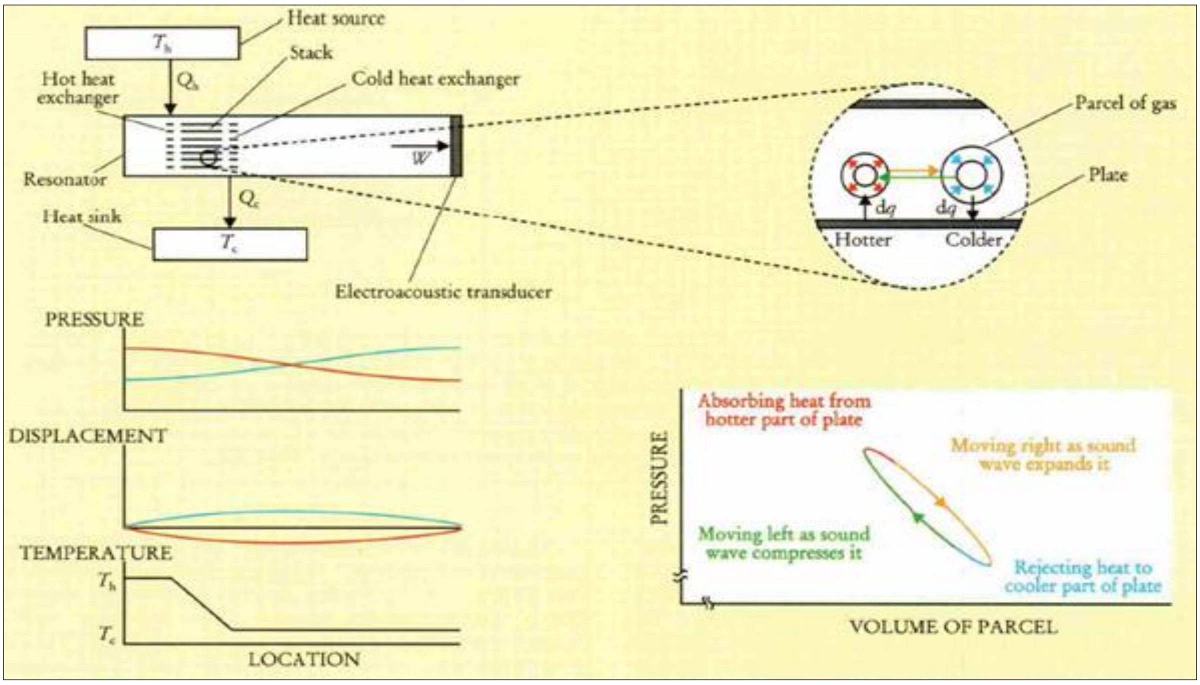

Figure 2.2 A schematic of a thermoacoustic heat engine with all its components, the spatial distributions of dynamic pressure, displacement and temperature along the length of a resonator and the gas parcel thermal cycle in a thermoacoustic heat engine device. The recommended distance between the plates is defined as four times the thermal penetration depth. (Courtesy of Swift, "Thermoacoustic engines and refrigerators – Physics Today July 1995 [24])

As illustrated before in (Section 2.2.1.1) the length of the resonator, the boundary conditions and the speed of sound are what determine the value of the operating frequency. It is also shown in Figure 2.2 in the lower left part of the figure the distribution of dynamic pressure and acoustic particle velocity (displacement) as imposed by the conditions of the standing wave. The spatial temperature distribution mainly changing in the stack zone due to thermal energy exchange between the stack and the surrounding gas medium is also shown. The stack must be of material that has high heat capacity so as not to oscillate thermally as the gas and low thermal conductivity to reduce the conduction losses between the hot and cold sides of the stack and must be placed in a zone where the resultant acoustic power is not zero. Thus stacks and heat exchangers are typically placed in the first or last quarters of a resonator.

The total acoustic energy produced in the thermoacoustic engine is the integration of the energy produced from each of the gas parcels alone due to parcel interaction with surroundings (stack and other parcels with different temperatures). The gas parcel energy is delivered every acoustic cycle through the produced acoustic wave to operate the electro-acoustic transducer. As shown in Figure 2.2 on the right side of the image the gas parcel activity starts by absorbing an amount of heat energy from hot location on the stack length and then moving towards a cooler location to deliver the heat energy where it delivers the energy, the net work done by the gas parcel motion is thus the resultant of the difference in temperature due to the imposed external heat at one side of the stack, the produced acoustic standing wave and the adiabatic heat exchange between the parcels and the stack. The gas parcels act as a bucket brigade causing a total amount of heat energy absorption (Q_h) for the whole engine at the hot heat exchanger with temperature (T_h) and an overall heat rejection of (Q_c) at the cold heat exchanger with temperature (T_c).

Two important length scales in thermoacoustic devices are the thermal penetration depth (Eq. 2.3) and the viscous penetration depth (Eq. 2.5) [22]. The thermal penetration depth is the distance in which heat can diffuse through the in a time of ($1/\pi f$), where (f) is the operating frequency of the thermoacoustic device. To keep the pressure and temperature oscillation running and the energy transfer process going on, imperfect thermal contact is required. Studies have shown that the convenient plate spacing value for such imperfect contact runs around four times the thermal penetration depth [22].

$$\delta_k = \sqrt{\frac{2K}{\omega\rho c_p}} \qquad \textbf{Eq. 2.3}$$

where (δ_k) is the thermal penetration depth in [m], (K) is the thermal conductivity of the gas in [W/m.K], (ω) is the rotational frequency in [rad/sec], (ρ) is the density of the gas in [kg/m^3] and (c_p) is the specific heat at constant pressure of the gas in [J/Kg.K].

The viscous penetration depth the distance in which momentum can diffuse through the in a time of ($1/\pi f$), where (f) is the operating frequency of the thermoacoustic device

$$\delta_\mathrm{v} = \sqrt{\frac{2\nu}{\omega}} \qquad \textbf{Eq. 2.4}$$

where (δ_ν) is the viscous penetration depth in [m] and (ν) is the kinematic viscosity of the gas in [m^2/sec].

A thermoacoustic refrigerator on the other hand Figure 2.3 is where acoustic energy (W) is supplied through an electro-acoustic transducer and similar to a thermodynamic heat pump the thermoacoustic refrigerator withdraws heat from a the cold heat exchanger (Q_c) producing a refrigeration effect and rejecting waste heat (Q_h) into the hot heat exchanger. The temperature gradient of the thermoacoustic refrigerator is less steep than that of the thermoacoustic engine.

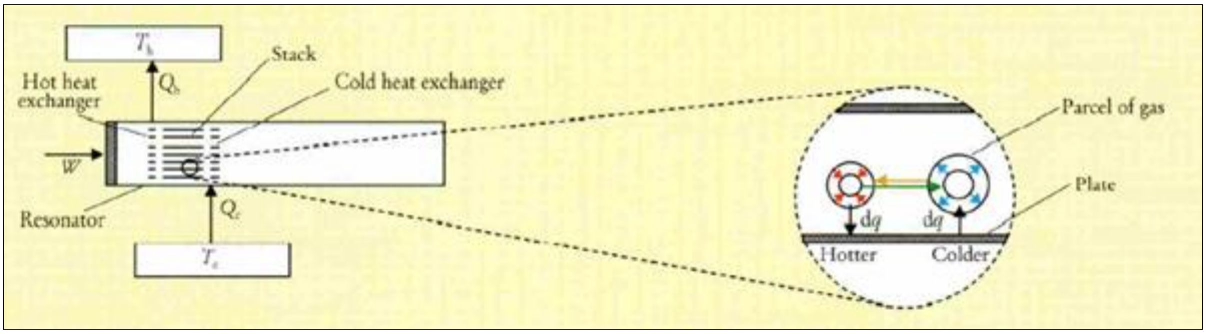

Figure 2.3 A schematic of a thermoacoustic refrigerator with all its components. The recommended distance between the plates is defined as four times the thermal penetration depth. (Courtesy of Swift, "Thermoacoustic engines and refrigerators – Physics Today July 1995 [24])

2.2.2. Particle Image Velocimetry (PIV)

2.2.2.1. Main components and basic theory

PIV is a non-intrusive, whole field and direct technique of measuring flow velocity. A PIV system is a body of smaller subsystems where tracer particles are added to the flow measured and illuminated using a laser light plane exposing a plane portion of the flow [25]. The illumination has to occur at least twice in very close time periods to capture the locations of the illuminated tracer particles at each illumination, measure the displacement and calculate the direction and amplitude of the particle displacement. The seed particle is to be selected carefully to reasonably follow the flow being measured exactly without slip. As shown in Figure 2.4 two short laser pulses with very small time delay (in the order of micro or milli-seconds according to the measured velocity) are used to illuminate the tracer particles in a plane of the measured flow. A high speed, high resolution camera is used to record the scattered light by the tracer particles at the two different frames. The recorded graphical photos of the measurement are then digitized for further analysis. The cameras used commonly nowadays for PIV recording are charged couple device camera (CCD) having a large number of array sensor elements and very high rate of image capturing. The analysis of PIV recordings is done by dividing the photographed area into smaller sub-areas called interrogation areas. The motion of all seed particles within one interrogation area is assumed to be the same and the tracer particles are expected to follow the flow measured without any deviations. The velocity value is calculated by measuring the displacement of the particles and taking into consideration the time delay between the two illuminations frames.

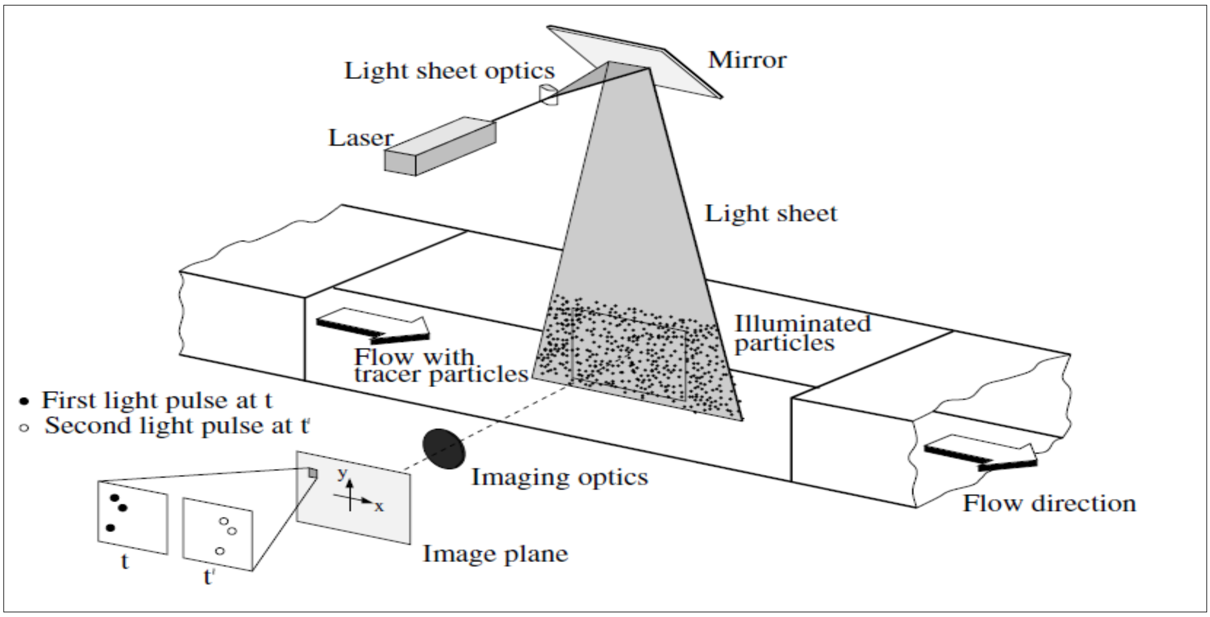

Figure 2.4 Experimental arrangement of PIV in a wind tunnel (Courtesy of Raffel *et al.*, "Particle image velocimetry 2007" [25])

2.2.2.2. Seeding selection

In general seed particles must be small enough to follow the flow yet large enough to reflect enough light, must be neutrally buoyant to allow enough time for imaging before the particles settle. The first key factor for selecting the type of seeding particles is the ability of the tracer particles to follow the flow correctly without slipping effects occurring. The second key factor is the light scattering properties of the tracer particles which is governed by the size of the tracer particles and the material type [5] [25] [26]. The ratio of the tracer particle velocity to the flow velocity is computed according to Eq. 2.5 [5]. Convenient values for this ratio start from a minimum of 1000.

$$R = {}^{\mathrm{v_{particle}}}/_{\mathrm{v_{flow}}} = {}^{\mathrm{t_{flow}}}/_{\mathrm{t_{particle}}} \qquad \textbf{Eq. 2.5}$$

where (R) is the ratio of the characteristic particle velocity ($\mathrm{v_{particle}}$) in [m/sec] to the flow velocity ($\mathrm{v_{flow}}$) in [m/sec]. Or; the flow wave period ($\mathrm{t_{flow}}$) in [sec] to the response time of the tracer particles ($\mathrm{t_{particle}}$) also in [sec].

$$\mathrm{t_{particle}} = \frac{(\gamma - 1)(\mathrm{d}^2)}{18\nu} \quad [\mathrm{sec}] \qquad \textbf{Eq. 2.6}$$

where (γ) is the ratio of the particle density to the fluid density, (d) is the diameter of the tracer particles in [m], (ν) is the kinematic viscosity of the fluid in [$\mathrm{m^2/sec}$].

$$\mathrm{t_{flow}} = \frac{1}{\mathrm{f}} \qquad \textbf{Eq. 2.7}$$

where (f) is the flow oscillation frequency.

2.2.2.3. Light scattering and particle density distribution

For most PIV setups the value of the tracer particle diameter is larger than the wavelength of the incident laser light. Thus, Mie scattering theory applies [25]. Figure 2.5 shows a typical Mie scattering by a 1 μm oil particle in air.

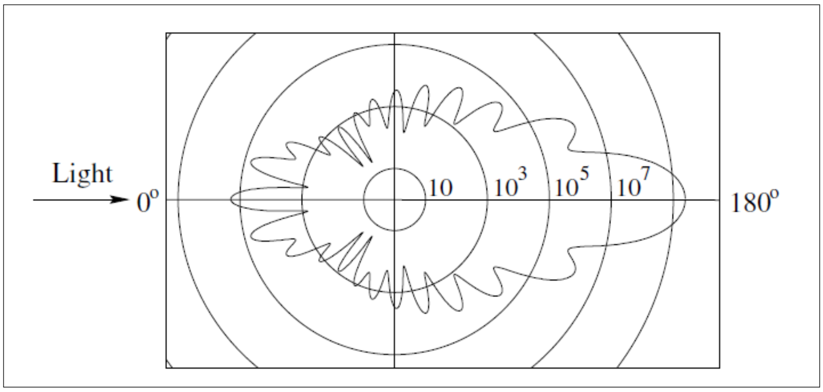

Figure 2.5 A typical Mie scattering by a 1 μm oil particle in air (Courtesy of Raffel *et al.*, “Particle image Velocimetry” [25]).

As for particle density distribution, medium density of images is the convenient one for PIV. As shown in Figure 2. the middle photo shows the relative medium density image. The low and high density images cannot be correctly analyzed by PIV. If the seed particles are too low, then the number of seeds inside an interrogation area is too low to produce a significant correlation. If the seed particles are too much, then it becomes difficult for the PIV to identify individual seed particles for analysis.

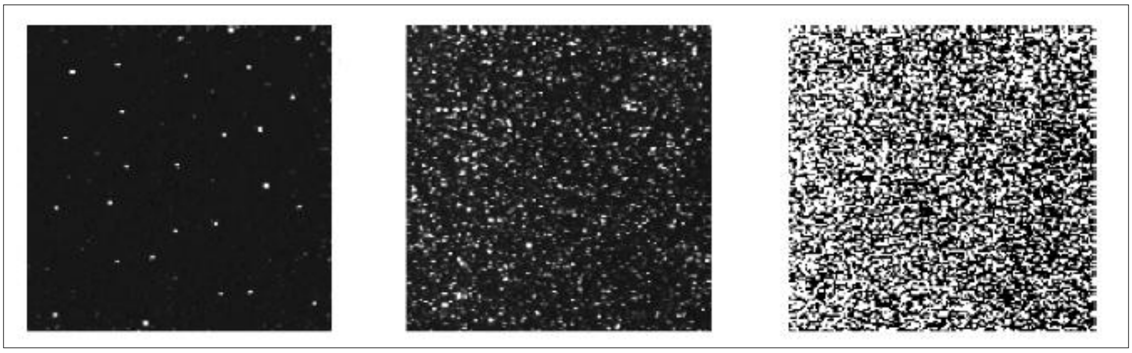

Figure 2.6 Low, medium and high image densities according to the amount if particles per image. The middle image with medium density is the one that should be attained in PIV (Courtesy of Raffel *et al.*, "Particle image velocimetry" [25])

2.2.2.4. Double frame/single exposure recording technique

Several techniques are used in PIV from which is double frame-single exposure, multi frame-multi exposure, single frame-single exposure and single frame-double exposure. The use of a double or mutli-frame technique is only possible at the presence of high speed cameras. However the most commonly used technique is the double frame-single exposure taking two single images at two distinct frames that have a very short duration in between. Figure 2.7 shows different types of single frame exposures and Figure 2.8 shows other types of double and multi-frame exposure.

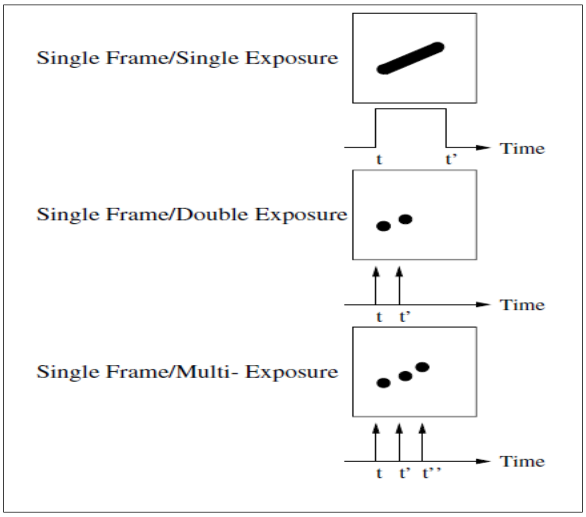

Figure 2.7 Different types of single frame exposures used in PIV recording. (Courtesy of Raffel *et al.*, "Particle image velocimetry" [25])

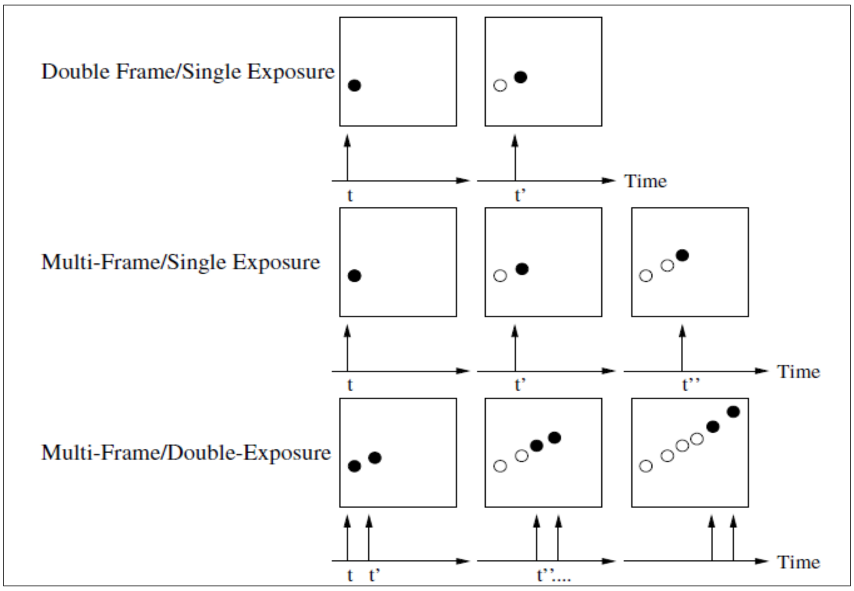

Figure 2.8 Different types of double and multi frame exposures used in PIV recording. (Courtesy of Raffel *et al.*, "Particle image velocimetry" [25])

2.2.2.5. Cross – correlation, adaptive correlation and interrogation areas

Cross – correlation is the statistical analysis algorithm used to calculate velocity of particles from double frame recording techniques. The particle displacement is measured and the final particle velocity is calculated taking into account the time between the double frames, Figure 2.9 shows the sequence of analysis in a typical PIV experiment. Cross – correlation accounts on using the Fast Fourier Transform to find the *highest probability* of the location of the tracer particle in the second frame relative to its location in the first frame and thus calculating the particle displacement [25] [27]. Cross – correlation is applied per each interrogation area and not for the whole imaged flow. The selection of the interrogation area is done on basis of the having maximum particle displacement not exceeding quarter of the interrogation area length in both {X} and {Y} directions [28]. Each interrogation area produces one vector. Each seed particle in the first frame is matched with a candidate seed particle in the second frame resulting in a displacement pattern for the whole interrogation window. The probability of correctness of the resulting pattern is high when nearly all vectors within the interrogation area are moving in the same direction. This process is then repeated until each seed particle from the first frame is compared to every seed particle in the second frame. For each seed particle alone, all probabilities are summed up where the point of highest probability becomes the location of this particular particle in the second frame. Figure 2.10 shows a visual representation of how seed particles candidates are selected (in black arrows) and how the final pattern is expected to look like (in green arrows). Figure 2.11 (left) shows the probability of correctness of the assumed matches for one seed particle and Figure 2.11 (right) shows the sum of probabilities for the same one seed particle after comparison to every particle in the second frame. An overlapping concept is applied in PIV analysis where interrogation areas next to each other are partially overlapped to increase the number of vectors in each direction and account for the possibility of having some seed particles crossing from one windows to the other [25]. Adaptive correlation, which is a commonly used analysis method for PIV analysis is an advanced version of the cross correlation. Adaptive correlation accommodates for an increased dynamic range and better image detection accuracy in cases where seeding is inhomogeneous and particle density is varying [29].

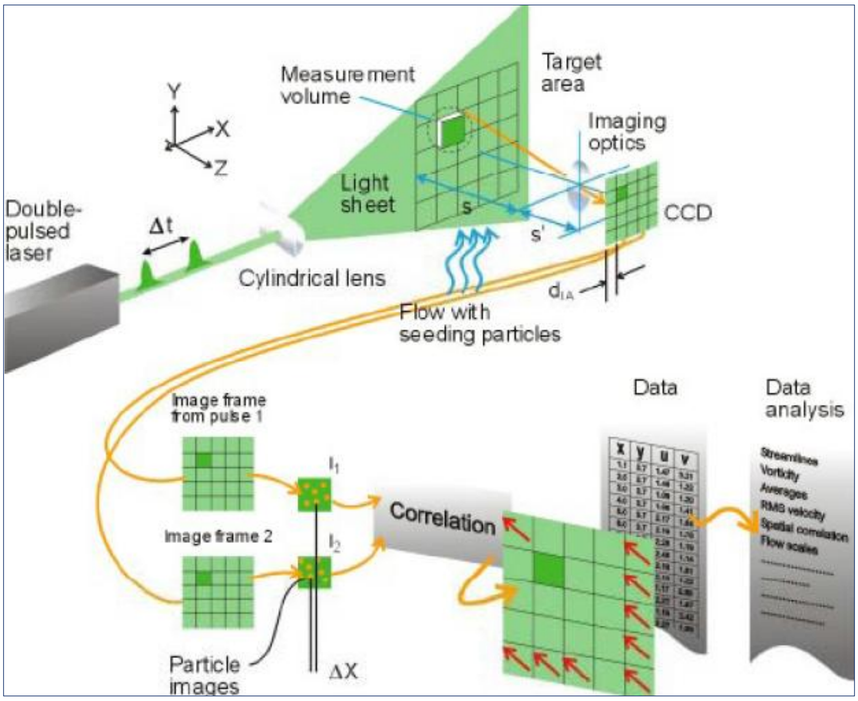

Figure 2.9 Sequence of analysis in a typical PIV experiment. (Courtesy of Dantec Dynamics [30])

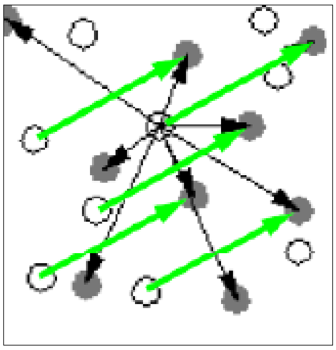

Figure 2.10 Selection of seed particles' candidates between the first and the second frame (black arrows) and the resulting pattern (green arrows) in one interrogation window. (Courtesy of the University of Maryland)

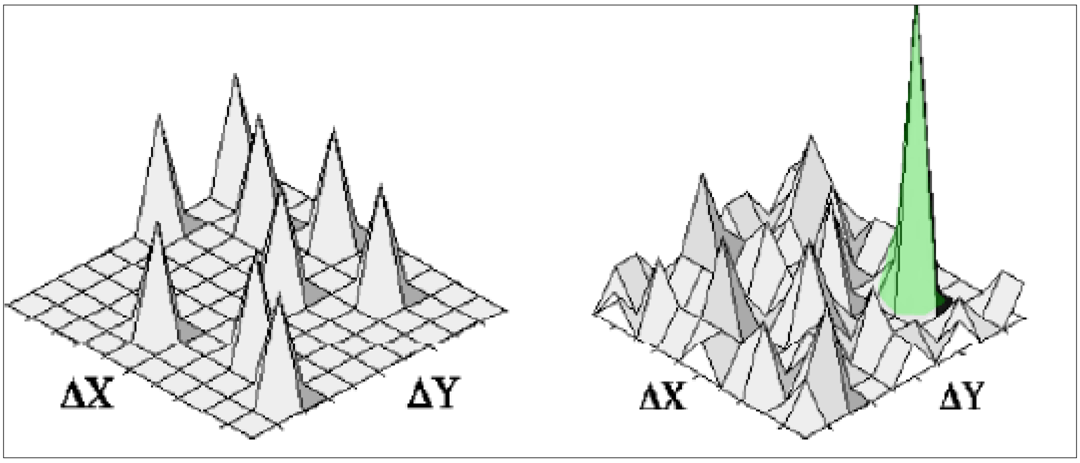

Figure 2.11 (Left) Probability of correctness of the matches of one seed particle from the first frame to candidate particles in the second frame. (Right) The final probability distribution for one seed particle after compared to every other particle in the second frame. (Courtesy of the University of Maryland)

Figure 2.12 shows how the probability distribution of a seed particle's velocity becomes more accurate as the number of seed particles increases. However, if the number of seed particles increases more than allowed (20 to 25 particles per interrogation area), it becomes hard to produce a peak in the probability distribution [25].

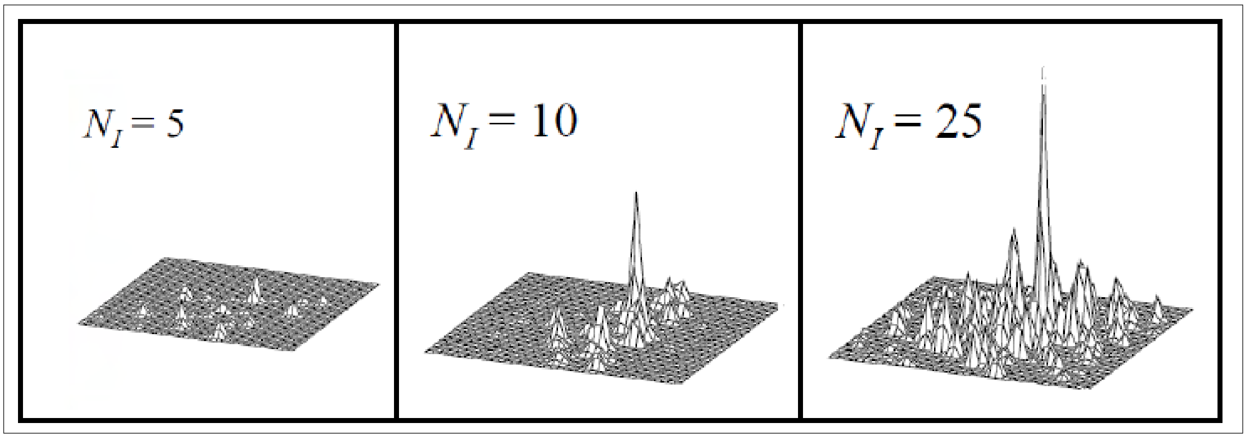

Figure 2.12 Increase in probability distribution accuracy of a seed particle's velocity as the number of seed particles within one interrogation window increases to a range of 20 to 25 particles per window. (Courtesy of Dantec Dynamics [30])

2.1.3. DeltaEC analysis software

DeltaEC (Design Environment for Low-Amplitude Thermoacoustic Energy Conversion) is a computer software designed to model thermoacoustic devices to study the performance of such devices and optimize their designs [31]. DeltaEC was built by Bill Ward, John Clark, and Greg Swift at the Los Alamos National Laboratory**,** USA**.** Version [6] of the software is the version used in this study.

DeltaEC uses a simple interface where it divides the thermoacoustic into segments where each segment represents a component in the system. Segments are of different kinds and each segment has its own input variables depending on the segment's type. DeltaEC also allows for variable input through text files. DeltaEC solves the wave and energy equation per each segment alone using the boundary conditions supplied through the input variables and then integrates the solution of all the segments throughout the whole modeled system. DeltaEC solves for only the axial spatial dimension where axial refers to the segment axis. DeltaEC assumes low amplitude acoustic approximation and sinusoidal time dependence.

DeltaEC solves the second order Helmholtz differential equation for the complex dynamic pressure amplitude as two coupled first order differential equations for complex dynamic pressure and complex volume flow rate amplitude. The solution is computed over each segment solving for dynamic pressure, volume flow rates and other variables that have matched values at the interface between each segment the following segment. For solution in stacks or stacks the energy equation is solved simultaneously with the adjusted wave equation to find the mean temperature profile of the flow.

DeltaEC solves using the shooting method numerical technique to converge for a set of variable and mixed boundary conditions allowing as well the definition of boundary conditions as functions of each other. DeltaEC can also accommodate for some non-linear effects appearing at high amplitude.

Of the common examples of used segments in DeltaEC is 'DUCT' , 'HEX' which stands for heat exchanger, 'STKRECT' AND 'STKSLAB' which define two different type of stacks, 'SURFACE' which is dummy segment to account for losses in the resonator tube. 'HARDEND' which simulated a hard were impedance is infinity, 'CONE' which defines a cone and 'VESPEAKER' which defines an electro-dynamic loudspeaker.

Phenomena normally associated with high drive, such as acoustic streaming, boundary layer turbulence, separation or reattachment are neglected in DeltaEC causing the model to over predict performance at high drive ratios. Good comparisons between model and experimental results have been reported for drive ratios near 4%, while poorer results have been obtained for drive ratios approaching 9% [32]. Additionally, DeltaEC does not properly consider the effects of abrupt geometrical changes, since the effects of boundary layer separation and reattachment downstream are neglected and it also does not consider heat conduction in the heat exchanger metal.

2.2. Basic photography terminology

The use of PIV as a measurement tool obliges a more than basic knowledge of the photography. Some terms are used in photography that go beyond daily use of cameras but in PIV are considered basic. Of which there is:

2.2.1. Focal length, optical zoom and field of view

The focal length is the distance in [mm] between the camera sensor/film and the optical center of the camera lens at the time when the subject is in focus. Optical zoom is the ratio between the maximum focal length and the minimum focal length of a lens. The field of view is the projection of the camera sensor/film size through the angle of view. The field of view is the horizontal and vertical dimension of the image [33]. Figure 2.13 shows a schematic illustrating focal length and field of view.

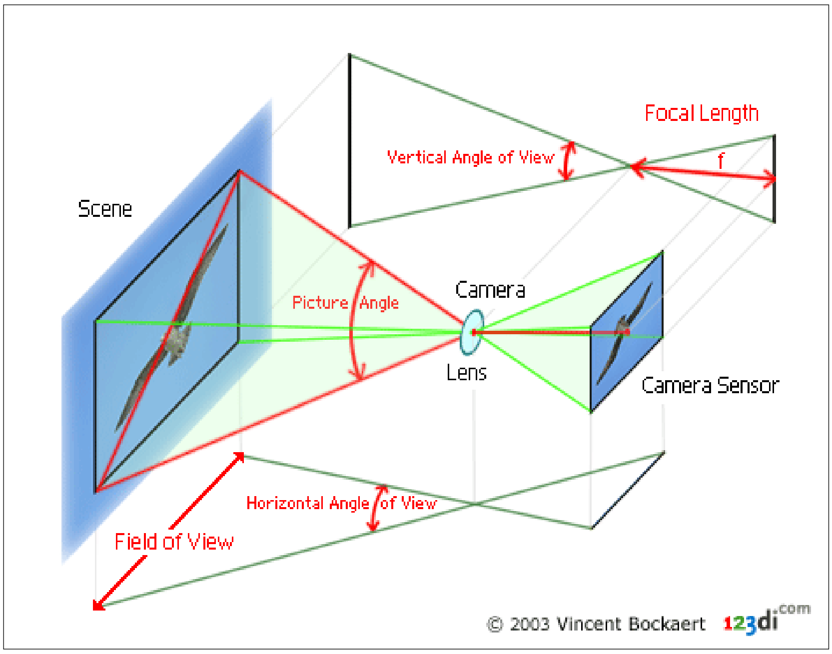

Figure 2.13 A schematic illustrating the focal length and the field of view in photography. (Courtesy of Digital Photography Review [34])

2.2.2. Prime lens

A prime lens is a photography lens that has one focal distance and cannot zoom in our out at the subject.

2.2.3. Subject distance

Subject distance is the real life distance between the subject and the camera lens.

2.2.4. Aperture

The aperture is the size of the opening in the camera lens that controls the amount of light passage to the camera sensor [33]. The larger the diameter of the opening (the aperture number) the more light is allowed. The resultant of dividing the focal length of a lens by the aperture diameter is called the (f-number) which is more practical in use for photographers. Thus, as the (f-number) decreases for the same focal length, the aperture decreases and the darker is the image becomes but with a better depth of field (Section 2.2.5).

2.2.5. Depth of field

Depth of field refers to the focus zone before and after the main focus plane. It expresses how far the background of a subject under focus remains sharp. Aperture, subject distance, focal length and sensor type affect the depth of field. For a larger aperture (small f number) shallow depth of field occurs, for a shorter subject distance shallow depth of field occurs and for shorter focal lengths larger depths of field occur [33].

2.2.6. Shutter speed

Shutter speed is the speed at which the camera sensor is exposed to light and then blocked again. Shutter speed is the reciprocal of the exposure time of the camera sensor to light. The higher the shutter speed the faster an image is captures [33]. It should be noted however that in the specific case of PIV the shutter speed and consequently the exposure time are controlled by the laser and the camera synchronization system.

2.2.7. Macro lens

A macro lens is a photography lens used to achieve magnification values higher than those achieved in daily close up photography where the details are mostly unseen by the naked eye [35].

2.2.8. Pixel depth

Pixel depth is the number of bits used to indicate the color of a single pixel in a bitmapped image or video frame buffer [36]. Color depth expresses how finely levels of color can be expressed or in other terms how fine color precision is in an image. In the use of grey scale PIV pixel depth defines the strength of the camera sensor in differentiating between white illuminated particles and black flow background.

Chapter 3. Characterization of electro-dynamic loudspeakers for thermoacoustic purposes

Commercial electro-dynamic loudspeakers are widely used in driving thermoacoustic refrigerators. They represent the source of acoustic energy input. They simplify the design and operation by providing direct source of acoustic energy input rather than using a thermoacoustic engine to drive a thermoacoustic refrigerator. They are inexpensive, widely available easy to control and they provide acoustic power over a wide range of frequencies but they suffer from very low electro-acoustic conversion efficiencies. A loudspeaker is composed of several components including magnets and diaphragms and others that work together to produce sound. Figure 3.1 shows an image of a Pioneer TS-G1013R loudspeaker that was used throughout this work.

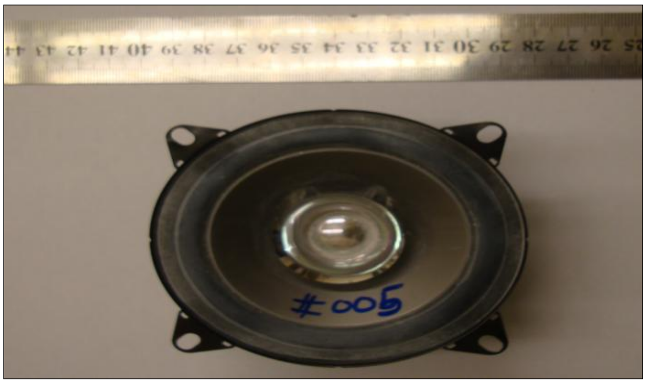

Figure 3.1 The Pioneer TS-G1013R loudspeaker

Figure 3.2 shows a cross section in a typical loudspeaker. Electric current flows through the voice coils and while in the presence of permanent magnets an electromagnetic field is produced forcing the cone (diaphragm) to move in a perpendicular direction to the gap field moving air particles back and forth and producing sound [37].

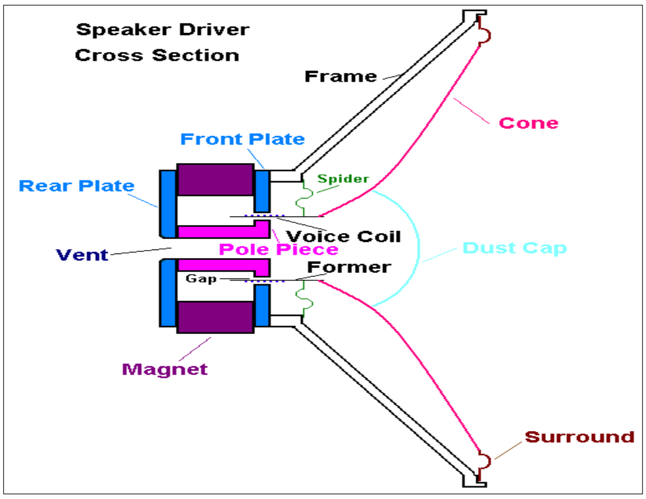

Figure 3.2 A cross section in a typical loudspeaker. (Courtesy of DJ society [38])

It becomes very useful to describe loudspeakers in analogy to electric circuits in order to facilitate the understanding of loudspeaker performance when subjected to acoustic loads. The electric-circuit analogy is shown in Figure 3.3 where the loudspeaker is represented electrically as three stages; the electrical circuit followed by the mechanical circuit and finally ending by the acoustical circuit [39]. Table 3.1 shows the definition of the electric symbols and their corresponding acoustical matches.

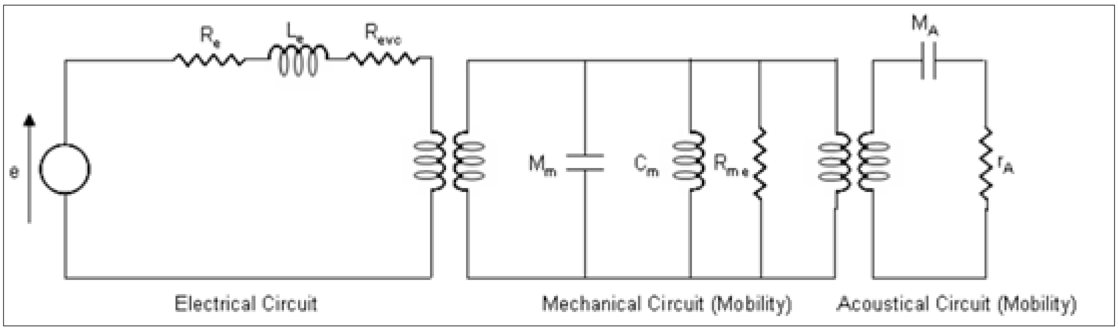

Figure 3.3 Electric circuit analogy of a loudspeaker. (Courtesy of Engineering Acoustics – Wiki books [40])

Table 3.1 Definition of symbols used in the electric circuit analogy of a loudspeaker and their matching acoustical elements.
(Courtesy of Engineering Acoustics – Wiki books [40])

	Electric symbol	**Electric function**	**Acoustic match**
Electrical circuit	e	Supply voltage	Supply voltage
	R_e	DC resistance	DC resistance
	L_e	Imaginary part of the voice coil inductance	Imaginary part of the voice coil inductance
	R_{evc}	Real part of the voice coil inductance	Real part of the voice coil inductance
Mechanical circuit	M_m	Electrical capacitance	Moving mass
	C_m	Electrical inductance	Compliance of the moving mass
	R_{me}	Electrical resistance	Suspension system
Acoustical circuit	M_A	Electrical capacitance	Air mass
	r_A	Electrical resistance	Radiation impedance

The objective of this chapter is to quantify some of the important parameters of the electro-dynamic speaker used. This is essential for full characterization of the thermoacoustic device built in order to understand its performance and to model the speaker numerically as part of modeling the device. DeltaEC is the software used to perform analytical modeling of the thermoacoustic refrigerator under study.

The parameters that characterize a loudspeaker are the effective cone area (A_{eff}), the DC-resistance (R_{DC}), the resonance frequency in the free field (f_o), the lumped stiffness (k), the lumped mass (m_o), the time constant (τ), the mechanical impedance (R_m), the electric impedance at resonance (Z_e), the electro-dynamic force factor (Bl product) which is the product of the magnet field strength in the voice coil gap and the length of wire in the magnetic field. In addition, the spectral behavior of real and imaginary parts of the impedance (Z) is measured and discussed.

3.1. Experimental setup and results

A Pioneer TS-G1013R loudspeaker, a Tektronix AFG 3021B function generator and a Tektronix TDS 2024B oscilloscope are connected in four different configurations to measure the different loudspeaker parameters. Multi-meters are also used to measure RMS voltages.

Prior to the measurements, the effective cone area (A_{eff}) was measured by measuring the diameter of the diaphragm and the DC-resistance (R_{DC}) was measured using a multi-meter when the speaker was turned-off.

The diameter of the speaker's diaphragm was found to be 86 mm. Thus the area becomes:

$$\mathrm{Aeff} = \frac{\pi}{4}\left(D^2\right) = \frac{\pi}{4}\left(0.086^2\right) = 0.0058\ \mathrm{m}^2 \qquad \textbf{Eq. 3.1}$$

The DC resistance of the loudspeaker was found to be 3.8 Ohms.

3.1.1. Setup configuration [A]

The setup configuration shown in Figure 3.4 was used to measure the resonance frequency (f_o) in the free-field, the lumped stiffness (k) and the lumped mass (m_o).

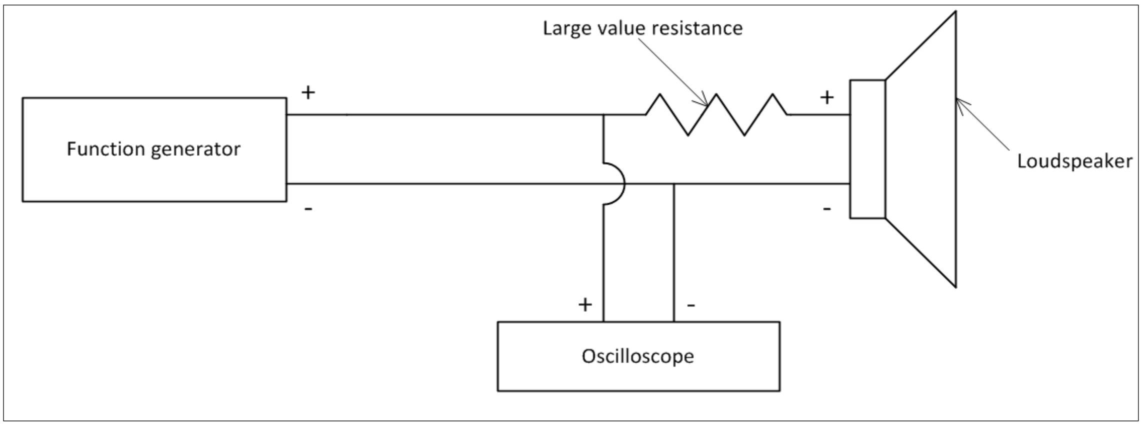

Figure 3.4 Setup configuration [A] to measure effective cone area (A_{eff}), the DC resistance (R_{DC}), the resonance frequency (f_o), the lumped stiffness (k) and the lumped mass (m_o) of a loudspeaker.

In order to measure above mentioned parameters, it is necessary to load the speaker’s diaphragm with a set of small loads. The weight of several nuts was measured in an incremental method starting with one nut and adding one nut at a time while weighing the nuts at each time a new nut was added Table 3.2. A regression line was constructed Figure 3.5 to determine the average nut mass. Fifteen nuts were weighed accordingly.

Table 3.2 The masses corresponding to added nuts

No. of nuts	Mass (gm)
1	2.15
2	4.34
3	6.45
4	8.64
5	10.79
10	21.49
15	32.39

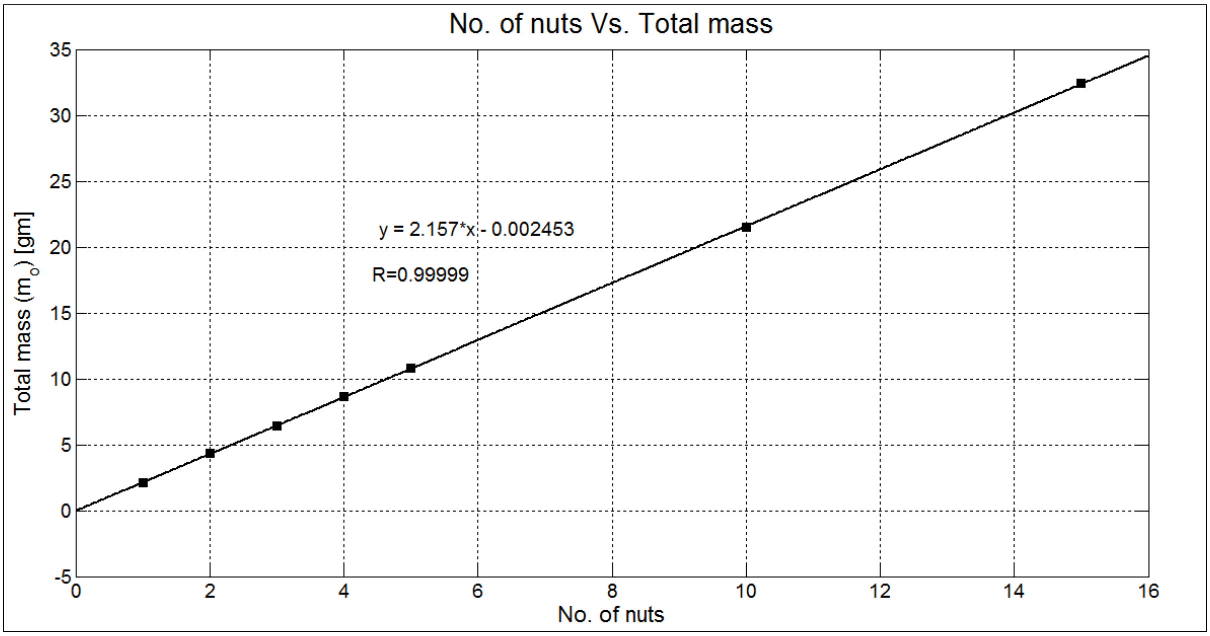

Figure 3.5 Regression between the number of nuts and the corresponding total mass

From the regression curve the average mass per nut is the slope of the regression line and is equal to 2.157 gm. Assuming the loudspeaker is a mass-spring system, the angular resonance frequency of the loudspeaker (ω_o) is defined as:

$$\omega_o = \sqrt{\frac{k}{m}} \quad \left[\frac{rad}{sec}\right] \qquad \textbf{Eq. 3.2}$$

where (m) is the total system mass in [kg]. The above equation thus yields:

$$2\pi f_o = \sqrt{\frac{k}{m}} \quad [rad/sec] \qquad \textbf{Eq. 3.3}$$

yielding;

$$4\pi^2 {f_o}^2 = \frac{k}{m} \quad [\frac{rad}{sec}]^2 \qquad \textbf{Eq. 3.4}$$

let

$$f_o = \frac{1}{T} \quad [Hz] \qquad \textbf{Eq. 3.5}$$

where (T) is the period of the acoustic wave produced in [sec].

thus;

$$\frac{4\pi^2}{T^2} = \frac{k}{m} \quad [\frac{rad}{sec}]^2 \qquad \textbf{Eq. 3.6}$$

$$\frac{T^2}{4\pi^2} = \frac{m}{k} \quad [\frac{rad}{sec}]^2 \qquad \textbf{Eq. 3.7}$$

To obtain the values of the lumped stiffness and the lumped mass, the mass of the loudspeaker was changed by adding nuts to its diaphragm. The mass of the nuts was calculated as the product of the number of nuts multiplied by the mass of one nut (previously determined from Figure 3.5). The function generator was operated at a five Volts peak-to-peak driving the loudspeaker. The change in the speaker mass causes a change in the resonance frequency. The new resonance frequency was looked for by sweeping through a range of frequencies and looking for the largest voltage. The current was assumed constant thanks to the current-limiting resistance attached in series to the speaker (100-Ohms resistance). Without using this resistance, it would have been necessary to measure both the voltage and the current and looking for the largest impedance. The total mass (m) in this case is the mass of the loudspeaker in addition to the added mass. Thus Eq. 3.7 yields:

$$\frac{T^2}{4\pi^2} = \frac{m_o + m_i}{k} \quad [\frac{rad}{sec}]^2 \qquad \textbf{Eq. 3.8}$$

where (m_i) represents the added mass in [kg].

Replicating Eq. 3.8 in a straight line form yields:

$$\frac{T^2}{4\pi^2} = \frac{m_o}{k} + m_i\left(\frac{1}{k}\right) \quad [\frac{rad}{sec}]^2 \qquad \textbf{Eq. 3.9}$$

where $\left(\frac{1}{k}\right)$ becomes the slope of the straight line.

let

$$\frac{T^2}{4\pi^2} = U \quad [sec]^2 \qquad \textbf{Eq. 3.10}$$

The values obtained from the experiment are shown below in Table 3.3.

Table 3.3 Values of resonance frequency in (Hz), wave period in (sec) and [U] in (sec^2) corresponding to changes in total mass of loudspeaker.

No. of nuts	Mass (kg)	Resonance Frequency (Hz)	Period (T) (sec)	U $(\mathbf{sec^2})$
0	0	99	0.010101	2.58446E-06
1	0.002156	79	0.012658	4.05869E-06
2	0.004312	68	0.014706	5.47801E-06
3	0.006468	60	0.016667	7.03619E-06
4	0.008624	55	0.018182	8.37365E-06
5	0.01078	51	0.019608	9.73868E-06
6	0.012936	48	0.020833	1.09941E-05

The free resonance frequency of the loudspeaker (f_o) is the frequency at zero added mass which was measured as 99 Hz. The regression line in Figure 3.6 describes the relation between the added mass of nuts (m_i) and the term (U) in Eq. 3.10 which corresponds to the period of the produced wave, the value of the stiffness was calculated using the slope value as:

$$k = \frac{1}{6.541 * 10^{-4}} = 1528.818\ \mathrm{N/m} \qquad \textbf{Eq. 3.11}$$

The value of the loudspeaker mass was calculated using the line intercept as:

$$m_o = 2.664 * 10^{-6} * 1528.818 = 0.004073\ \mathrm{kg} \qquad \textbf{Eq. 3.12}$$

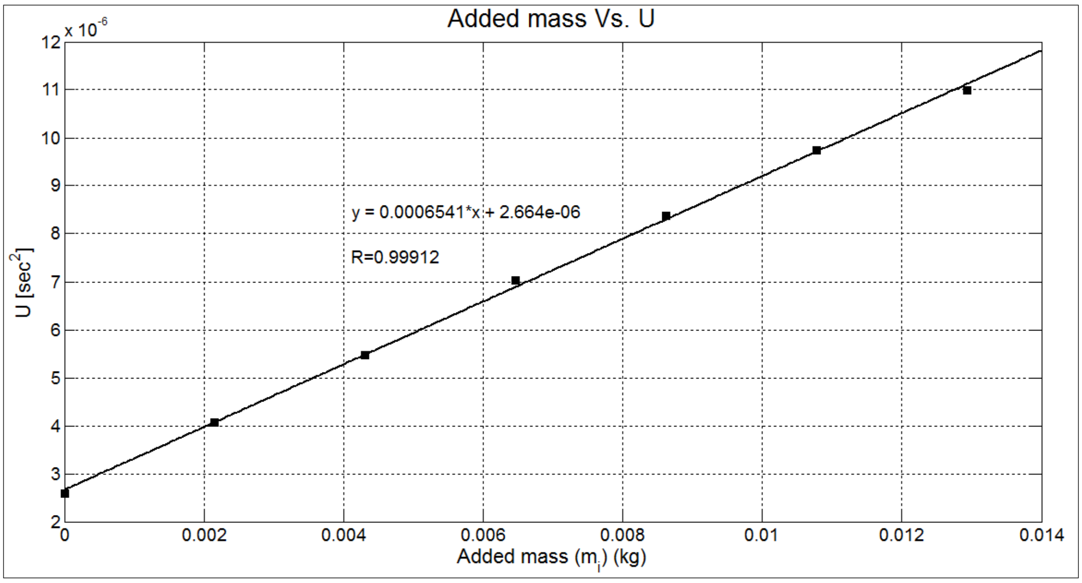

Figure 3.6 Regression between the added mass (m_i) in [gm] and (U) in [sec^2].

3.1.2. Setup configuration [B]

The setup configuration shown in Figure 3.7 is used for measuring the time constant (τ) and the mechanical damping (R_m). The Tektronix AFG 3021B function generator was connected in series directly to the Pioneer TS-G1013R loudspeaker and the Tektronix TDS 2024B oscilloscope was connected in parallel to the circuit.

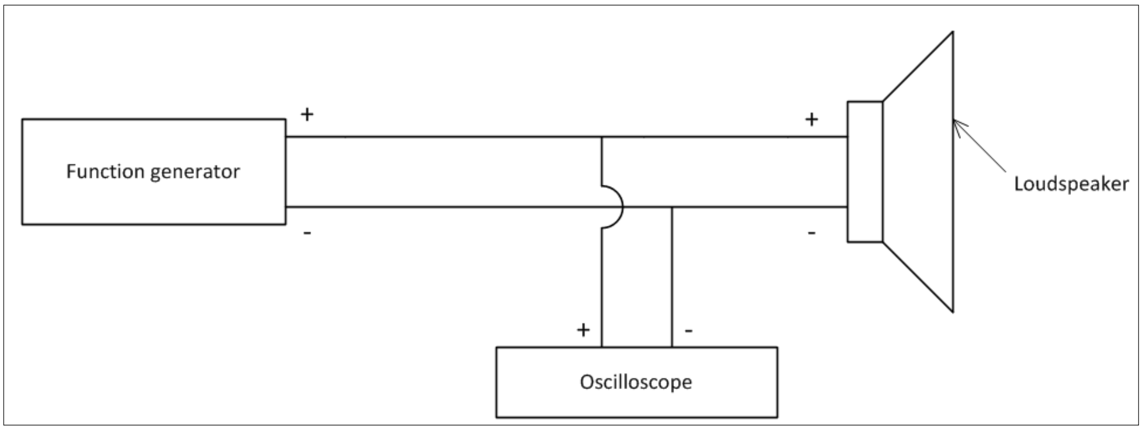

Figure 3.7 Setup configuration [B] to measure the time constant (τ) and the mechanical impedance (R_m) of a loudspeaker.

To measure the time constant and the mechanical damping the loudspeaker is to be operated at any amplitude and frequency and then shut down suddenly (by turning-off the function generator) while capturing the amplitude decay curve on the oscilloscope. Figure 3.8 shows the free decay curve of the loud speaker.

The frequency of the free decay is also the resonance frequency in the free field. As shown in Figure 3.8 two successive peak values of voltage are captures during the free decay cycle. These values are 0.03176 s and 0.04276 s. Eq. 3.14 shows the calculation of the free field resonance frequency using the free decay curve.

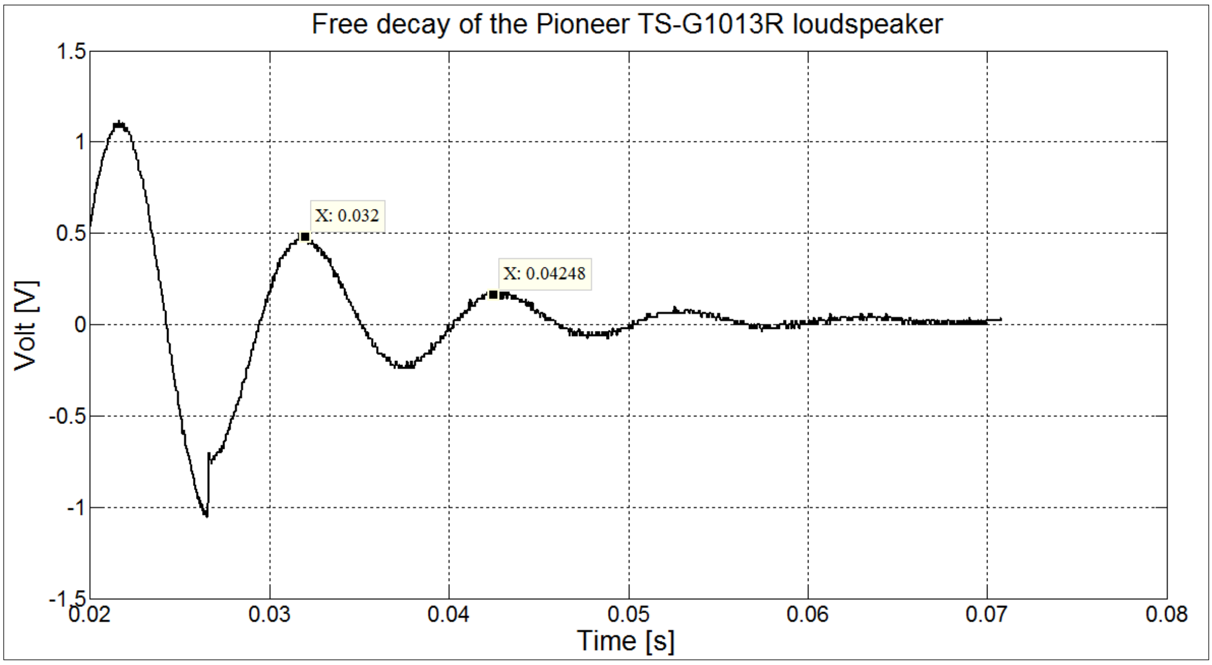

Figure 3.8 Free decay output of loudspeaker occurring after the sudden stop of input signal from the function generator

$$f_{\text{free decay}} = \frac{1}{\text{decay period}} = \frac{1}{0.0424 - 0.032} = 96.2\ \text{Hz} \qquad \textbf{Eq. 3.13}$$

The free decay resonance was found to be 96.2 Hz and is in good agreement with the value measured using the added mass technique (99 Hz).

The values obtained from the decay plot are used to plot a straight line graph from which the values of the time constant and the mechanical damping are obtained. In this experiment, the function generator was used to produce a signal of frequency 99 Hz and amplitude of five Volts peak-to-peak value. There is no certain reference in selecting the values of both variables; both values could be selected differently as the results are independent of them.

The voltage value is measured between consecutive peaks although these peaks are not of the same amplitude. The voltage measured for the first half cycle is the peak-to peak value between the first peak in the decay diagram and the following trough. The voltage representing the pressure amplitude can be written in equation form as follows:

$$V(t) = V_o e^{\left(\frac{-t}{\tau}\right)} \qquad [V] \qquad \textbf{Eq. 3.14}$$

yielding;

$$\ln V = \text{lv}\, V_o - t\left(\frac{1}{\tau}\right) \qquad [\ln V] \qquad \textbf{Eq. 3.15}$$

where $\left(\frac{1}{\tau}\right)$ is the slope of the line.

The values obtained from the decay curve are as shown in Table 3.4. The values of voltage obtained from the free decay curve at each half cycle and the corresponding logarithmic values of voltage.

Table 3.4 Values from the free decay curve.

No. of cycles	Time (sec) [No. of cycles x period]	Voltage (mV)	ln (V)
0.5	0.0050505	448	6.104793
1	0.010101	228	5.429346
1.5	0.0151515	148	4.997212
2	0.020202	120	4.787492
2.5	0.0252525	80	4.382027
3	0.030303	60	4.094345

From the graph Figure 3.9 the value of the time constant was determined as the inverse of the slope of the line where;

$$\tau = \frac{1}{75.83} = 0.0132 \text{ sec} \qquad \textbf{Eq. 3.16}$$

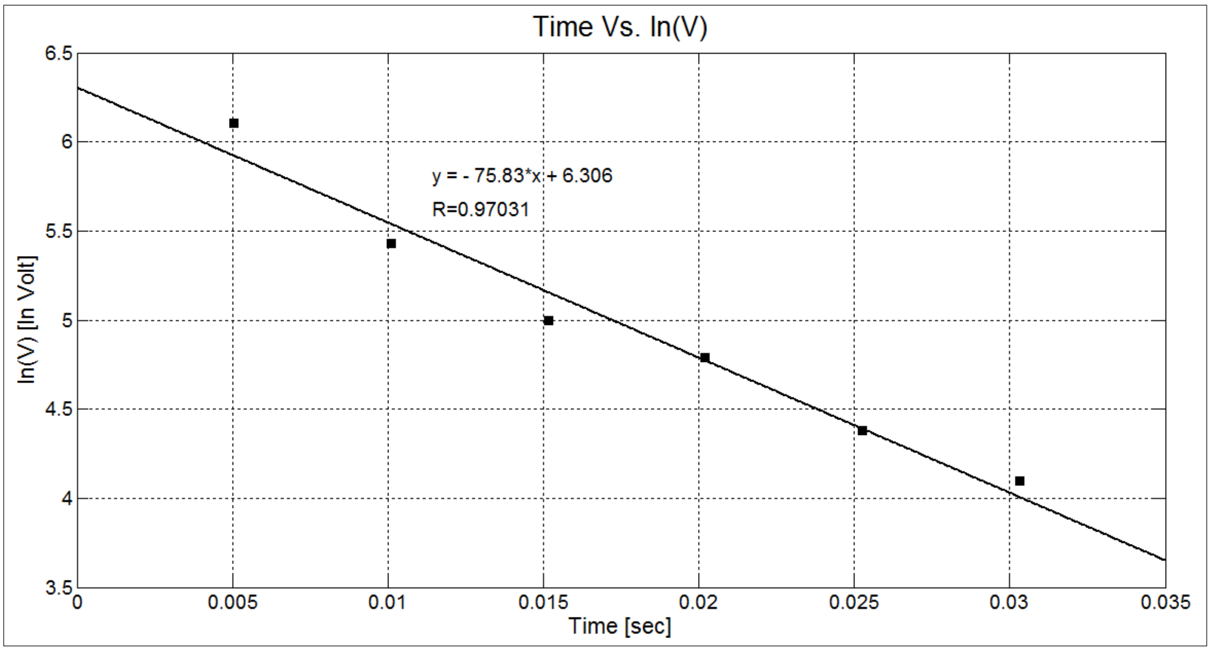

Figure 3.9 Regression between time in (sec) and the logarithmic value of voltage obtained from the free decay measurement of the loudspeaker.

To determine the value of the mechanical impedance (R_m), the definitions of the quality factor is used:

$$Q_{\text{factor}} = \frac{\omega_o\, m_o}{k} \quad [\text{sec}] \qquad \textbf{Eq. 3.17}$$

The other definition of the quality factor is:

$$Q_{factor} = \frac{\omega_o\,\tau}{2} \qquad [\mathrm{sec}] \qquad \textbf{Eq. 3.18}$$

equating Eq. 3.17 and Eq. 3.18;

$$\frac{1}{k_m} = \frac{\tau}{2m_o} \qquad [\frac{m}{N}] \qquad \textbf{Eq. 3.19}$$

thus the value of the mechanical impedance (R_m) becomes:

$$R_m = \frac{2m_o}{\tau} = \frac{2 * 0.004073}{0.0132} = 0.6172\ \mathrm{kg/sec} \qquad \textbf{Eq. 3.20}$$

3.1.3. Setup configuration [C]

The setup configuration shown in Figure 3.10 is used to calculate the electric impedance at resonance (Ze), the coupling coefficient (Bl) and the voice coil inductance (L). As shown the Tektronix AFG 3021B function generator, the Pioneer TS-G1013R loudspeaker and the current-limiting resistance (100-Ohms resistance) were connected in series. Two multi-meters were connected to the circuit, one of which is connected in parallel to the 100 Ohms resistance and the other is connected in parallel to the loudspeaker’s voice coil. The function generator was operated at a five Volts peak-to-peak value and at the free resonance frequency which was previously found to be 99 Hz. The voltages across the voice coil and the resistance and the exact value of the 100 Ohms resistance were first measured followed by the calculation of the other acoustic parameters.

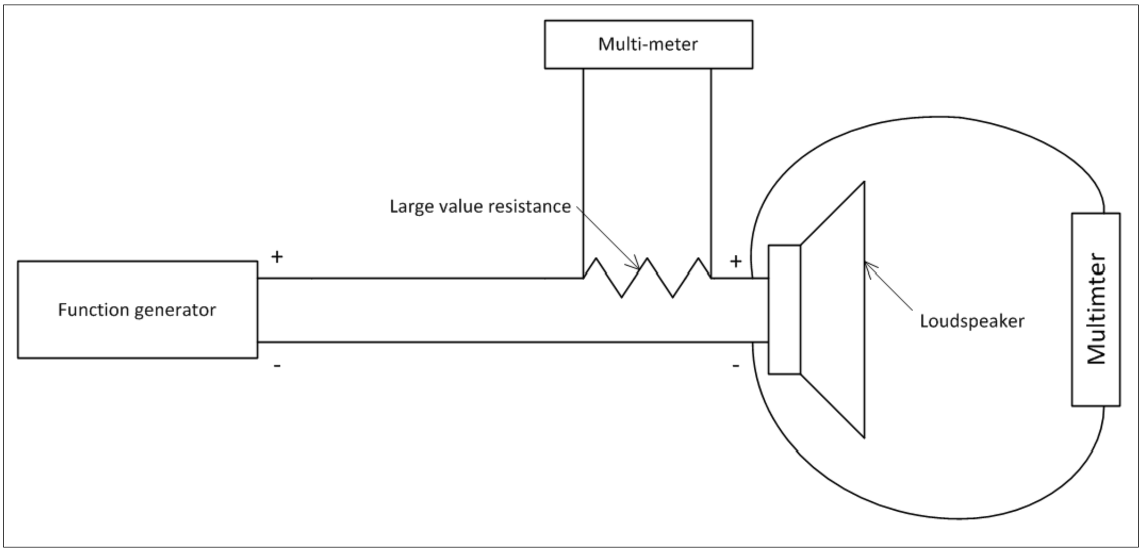

Figure 3.10 Setup configuration [C] to measure the coil voltage (V_c) and the voltage across the resistance (V_Ω) to calculate electric impedance at resonance (Ze), the coupling coefficient (Bl) and the voice coil inductance (L) of a loudspeaker.

The voltage across the loudspeaker coil (V_c) was found to be 0.696 V, while the voltage across the resistance (V_Ω) was found to be 4.23 V. Both were measured using multi-meters. The exact value of the resistance was found to be 100.1 ohms. Calculation procedures were as follows:

For the current (I) passing through the loudspeaker voice coil:

$$I = \frac{V_\Omega}{R_{high}} = \frac{4.22}{100.1} = 0.0426 \text{ A} \qquad \textbf{Eq. 3.21}$$

where (R_{high}) is the high value resistance.

For the electric impedance at resonance (Z_e):

$$Z_e = \frac{V_c}{I} = \frac{0.696}{0.0426} \approx 16\ \mathrm{Ohms} \tag*{\textbf{Eq. 3.22}}$$

For the coupling coefficient (Bl):

$$\mathrm{Bl} = \sqrt{(Z_e - R_{DC})R_m} = \sqrt{(16 - 3.8) * (0.6172)} = 2.744\ \ [\mathrm{Tesla.m}] \tag*{\textbf{Eq. 3.23}}$$

For the voice coil inductance (L):

$$L = \sqrt{\frac{{Z_e}^2 - {R_{DC}}^2}{{\omega_o}^2}} = \sqrt{\frac{{Z_e}^2 - {R_{DC}}^2}{(2 * \pi * f_o)^2}} = \sqrt{\frac{16^2 - 3.8^2}{(2 * \pi * 99)^2}} = 0.0249\ \mathrm{H} \tag*{\textbf{Eq. 3.24}}$$

Other methods [41] and [42] indicate that the value of the voice coil inductance should be calculated at a high frequency value (1000 Hz or more) where the loudspeaker’s electrical impedance (Z_e) becomes nearly completely reactive and inductance is dominant. However it will be shown later in chapter Chapter 5 that analytical models done using DeltaEC where the inductance was measured at the free resonance frequency were highly compatible to experimental results. Models done using other methods were unable to match the experimentally-measured pressures.

3.1.4. Setup configuration [D]:

The setup configuration shown in Figure 3.11 was used to plot the impedance versus the frequency. The setup is used to measure the acoustic impedance versus the frequency given that the acoustic impedance of a loudspeaker is a complex value where the resistance represents the real part and the reactance is the imaginary part [43]. A 385 Ohms resistance is connected in series to the Tektronix AFG 3021B function generator and the Pioneer TS-G1013R loudspeaker. The Tektronix TDS 2024B oscilloscope was connected in parallel to both the resistance and the loudspeaker voice coil to measure voltage for both components at the same time. The 385 Ohms the resistance added in this configuration was used as a current-measuring resistance. The work uses the fact that in pure resistances, voltage and current are in phase and dividing the voltage drop across the resistance yields the current. The used resistance had a power rating of five Watts to withstand the power flow through it.

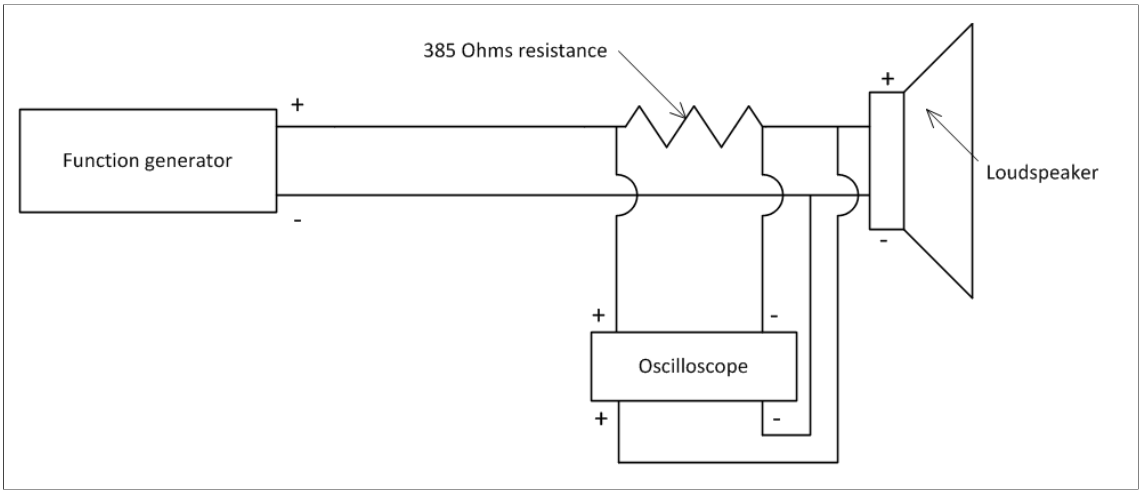

Figure 3.11 Setup configuration [D] to measure the voltage across a large power rating resistance and the loudspeaker and calculate the acoustic parameters necessary to plot the frequency versus the complex impedance of the loudspeaker (Z).

The oscilloscope was used to measure simultaneously the voltage signals across the speaker and across the resistance across a range of frequencies. This way the phase information of the voltage and current (and therefore the impedance) is captured.

The phase shift is calculated by manually detecting the time difference in [sec] between the voltage peaks of both the resistance and the loudspeaker that are appearing on the oscilloscope's screen. The time difference is then converted to an angular difference using simple cross multiplication. Knowing that 360^{o} of angle rotation are equivalent to one acoustic cycle whose time is the inverse of the frequency and knowing the actual time difference the phase is calculated as shown in Eq. 3.25:

$$\text{Phase angle} = \frac{\frac{1}{f}}{360 * \text{Measured time difference between peaks}} \quad [\text{Degrees}] \qquad \textbf{Eq. 3.25}$$

where (f) is the frequency in [Hz]. A sample of the results obtained from the measurements is shown in Table 3.5. The full results are shown in Appendix (A).

Table 3.5 Values of different parameters used in setup configuration [D] to plot the complex impedance vs. frequency

Frequency	**Loudspeaker peak -to- peak voltage**	**Resistance Peak -to- peak voltage**	**Loud -speaker Current**	**Loud -speaker Impedance**	**Phase shift**	**Re (Z)**	**Im(Z)**
f [Hz]	$V_{speaker}$ [V]	$V_{resistance}$ [V]	I [Ampere]	Z [Ohms]	φ [Degree]		
10	0.134	7.6	0.0197	6.7917	8.64	6.715	1.020
20	0.142	8.4	0.0218	6.5117	2.88	6.503	0.327
30	0.160	8.8	0.0228	7.0036	14.40	6.784	1.742
90	0.340	8.8	0.0228	14.8827	40.32	11.347	9.630
91	0.356	8.8	0.0228	15.5831	29.66	13.541	7.712
92	0.384	8.8	0.0228	16.8087	18.72	15.920	5.395
93	0.384	8.8	0.0228	16.8087	20.88	15.705	5.991
94	0.400	8.8	0.0228	17.5091	23.04	16.112	6.853
95	0.416	8.8	0.0228	18.2095	25.20	16.476	7.753
250	0.168	8.8	0.0228	7.3538	0.00	7.354	0.000
300	0.160	9	0.0234	6.8480	5.76	6.813	0.687
350	0.156	9	0.0234	6.6768	6.48	6.634	0.754
400	0.156	9	0.0234	6.6768	4.32	6.658	0.503
450	0.160	9	0.0234	6.8480	14.40	6.633	1.703
500	0.162	9	0.0234	6.9336	14.40	6.716	1.724
600	0.164	9	0.0234	7.0192	10.08	6.911	1.229
700	0.166	9	0.0234	7.1048	26.64	6.351	3.186
800	0.174	9	0.0234	7.4472	33.12	6.237	4.069
900	0.176	9	0.0234	7.5328	33.84	6.257	4.195
1000	0.182	8.8	0.0228	7.9666	28.80	6.981	3.838
1500	0.204	9	0.0234	8.7312	46.80	5.977	6.365
2000	0.232	8.8	0.0228	10.1553	57.60	5.441	8.574

The resultant plots in Figure 3.12, Figure 3.13 and Figure 3.14 show how the complex impedance behaves versus the frequency. It is observed how the real amplitude shows a peak at a frequency of 99 Hz and the imaginary part is zero at the same frequency. The amplitude is maximum at this resonance frequency. The results show excellent agreement with the literature [39].

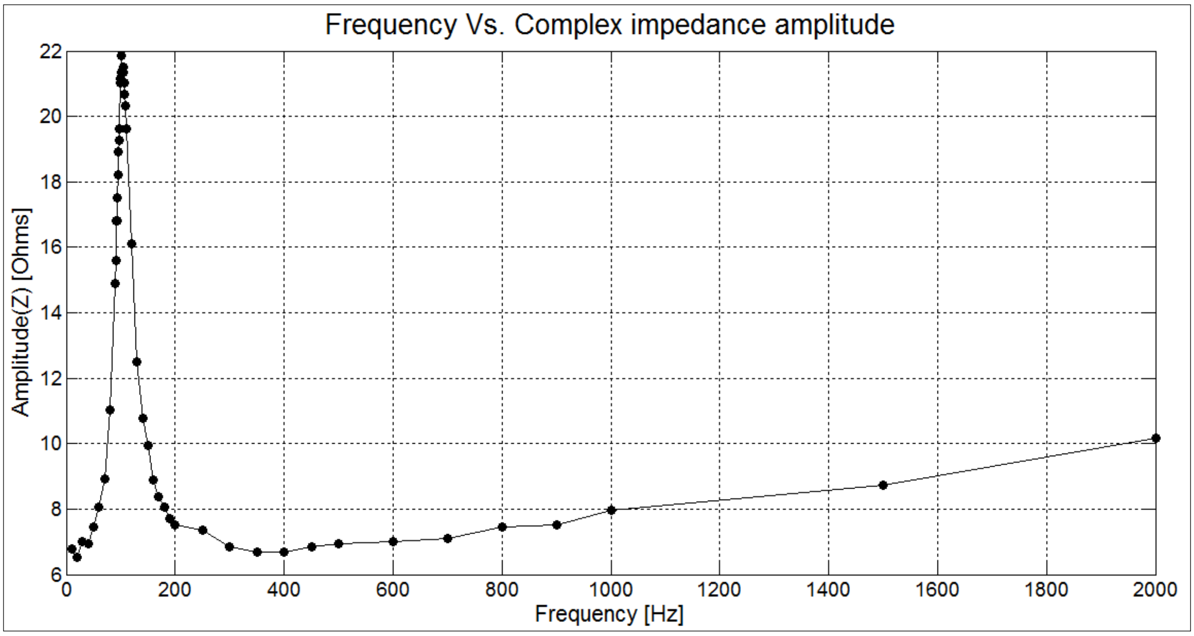

Figure 3.12 Frequency in [Hz] vs. the complex impedance (Z) amplitude of a loudspeaker in [Ohms].

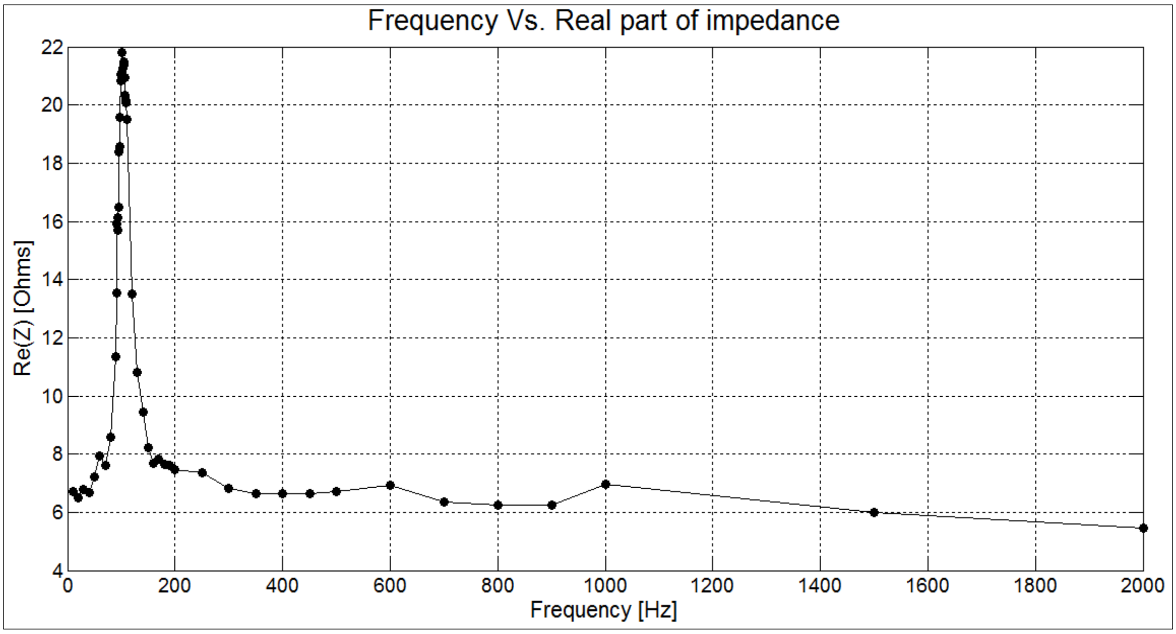

Figure 3.13 Frequency in [Hz] vs. the real part of the impedance (Z) of a loudspeaker in [Ohms].

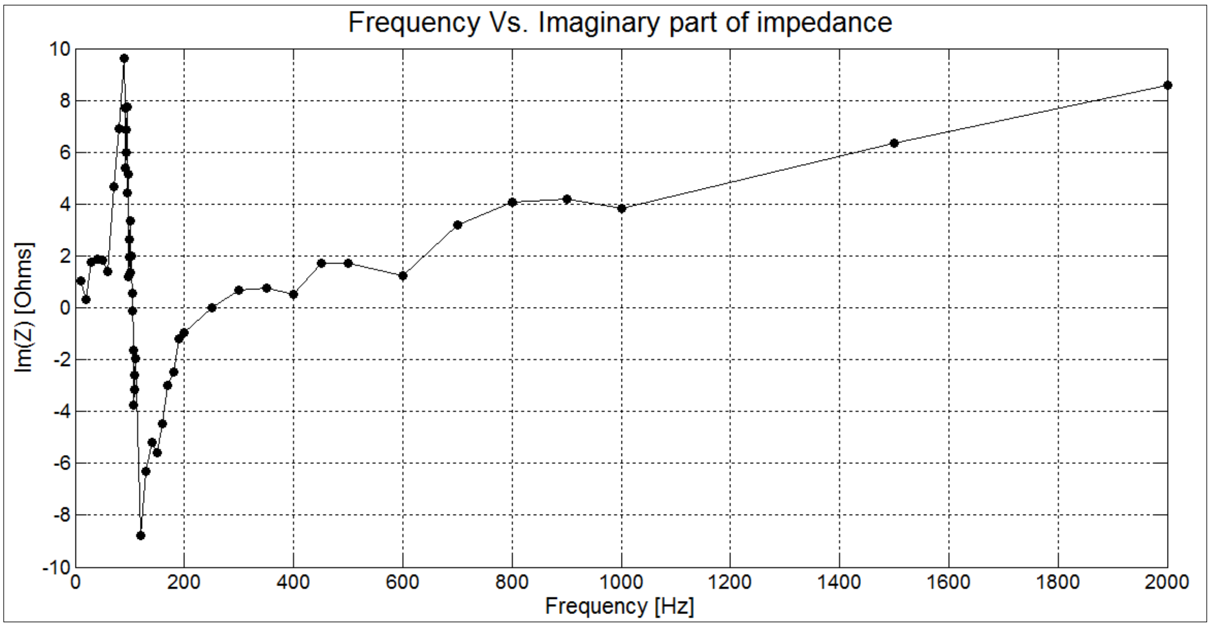

Figure 3.14 Frequency in [Hz] vs. the imaginary part of the impedance (Z) of a loudspeaker in [Ohms].

3.2. Results summary

The main parameters that characterize a loudspeaker for the sake of modeling it in DeltaEC for the Pioneer TS-G1013R loudspeaker were found to be:

- Effective cone area (A_{eff}) = 0.0058 m^2
- DC resistance (R_{DC}) = 3.8 Ohms
- Resonance frequency in the free field [Moving mass method] (f_o) = 99 Hz
- Resonance frequency in the free field [Free decay method] ($\mathbf{f_{free\ decay}}$) = 96.2 Hz
- Lumped stiffness (k) = 1528.818 N/m
- Lumped mass (m_o) = 0.004073
- Time constant (τ) = 0.0132 sec
- Mechanical impedance (R_m) = 0.6172 kg/sec
- Electric impedance at resonance (Z_e) =16 Ohms
- Coupling coefficient (Bl) = 2.744 Tesla.
- Voice coil inductance (L) = 0.0249 H

Chapter 4. Experimental setup

4.1. PIV and dynamic pressure measurement setup

One setup was used for all types of measurements; these are velocity, dynamic end pressure and spatial dynamic pressure distribution with only minor modifications at the hard end of the quartz resonator where microphones replaced the seeder to change from measuring velocity using seeding particles to measuring spatial and dynamic end pressure using condensate electret and piezo-resistive microphones. The hard end was constructed to be simply attached and removed from the resonator without causing leakage. All experiments were conducted with air at a mean pressure equal to the atmospheric pressure.

4.1.1. Laser system and CCD camera

As shown in Figure 4.1 which illustrates the main PIV setup components used to measure velocity with the seeder and air step at the hard end connected using a hose. As the main key to using PIV in measurements is to have the laser sheet perpendicular to the camera field of view, the laser sheet was directed in horizontal plane to light a horizontal cross section of the quartz resonator and the camera was placed in a vertical position pointing downwards. The laser used is a Litron Class 4 - Nd:YLF laser (Neodymium-doped yttrium lithium fluoride), of 527 nm wavelength, 150ns/CW pulse duration and a maximum output of 100W. The maximum triggering rate the laser can achieve is 10000 Hz.

The camera used was a Photron SA1.1 CCD camera with a maximum frame rate of 5400 frames/sec, a resolution of 1024x1024 Pixles^2 and a pixel depth value of 12 used along with a 60 mm Nikon AF macro prime lens with a maximum aperture diameter of 32. A prime lens does not support zooming. Zooming is attained by moving the whole camera body towards the subject (in this case the laser light sheet). Aperture diameter was adjusted to a value of 8 or 11 depending on the amount of light needed in the experiments. The camera zoom, the focus plane and the field of view and were adjusted differently as per experiment according to the targeted outcome of each experiment.

A National Instruments timer box of model number 80N77 was used for synchronization of laser light pulses and the CCD camera. The software used for control of equipment, measurements and analysis is Dantec Dynamics’ Dynamic Studio and the whole assembled PIV system was also supplied by Dantec Dynamics. A traverse mechanism was used to control the vertical motion of the camera as it provides high resolution of linear motion. All velocity measurements experiments were performed at a 2700 Hz laser triggering rate of and a 185μs duration between pulses and analyzed using the adaptive correlation technique at different interrogation area sizes according to the experiment conducted. All experiments were operated at an acoustic frequency that ranged from 100 Hz to 130 Hz, thus providing a range of 27 to 20 imaging captures per cycle. The 185μs value was determined experimentally as the most convenient value to accommodate for a wide range of velocity measured using interrogation areas of 32 X 32 pixels^2 and 16 X 16 pixels^2 such that the seed particles move a reasonable distance within the interrogation area.

The laser was operated at 85% intensity with the two energy buttons describing the energy of each laser head set to the value of nine. Figure 4.2 shows a real time picture of the PIV setup.

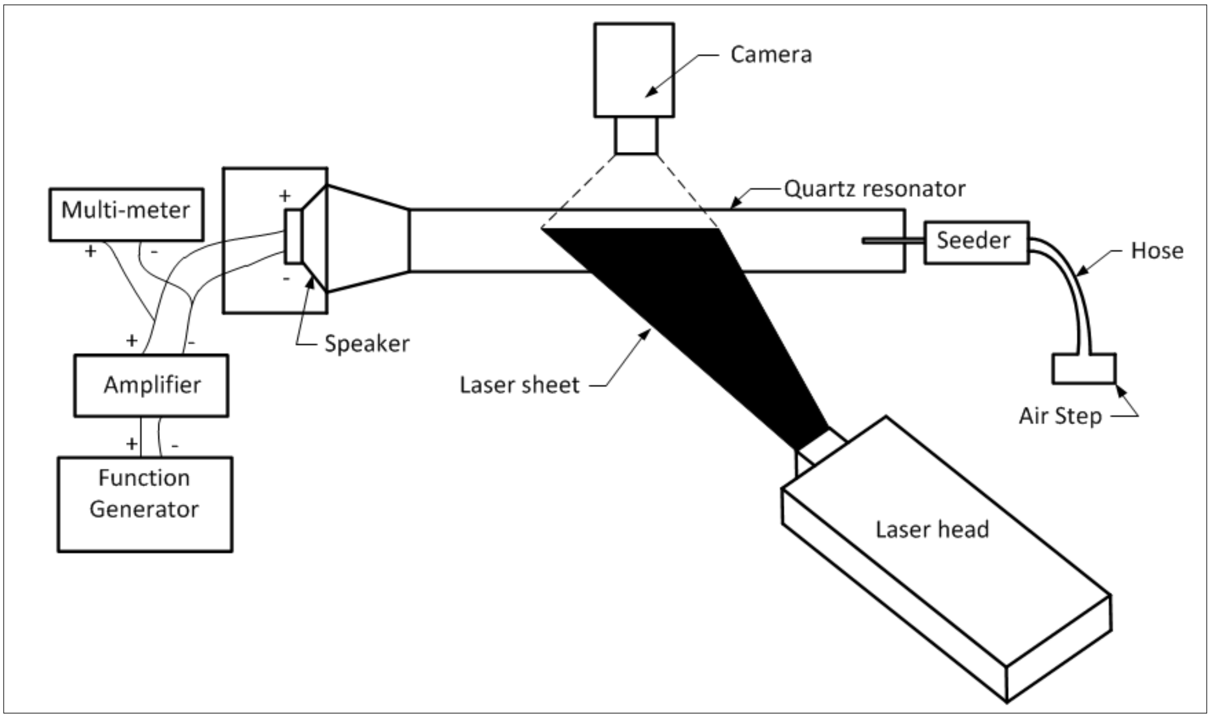

Figure 4.1 Schematic for the main PIV setup used to measure velocity with the seeder engaged at the hard end of the resonator to induce seeding tracer particles into the resonator tube. The seeder is replaced by a differential microphone and a condensate electret microphone fixtures to measure dynamic pressure.

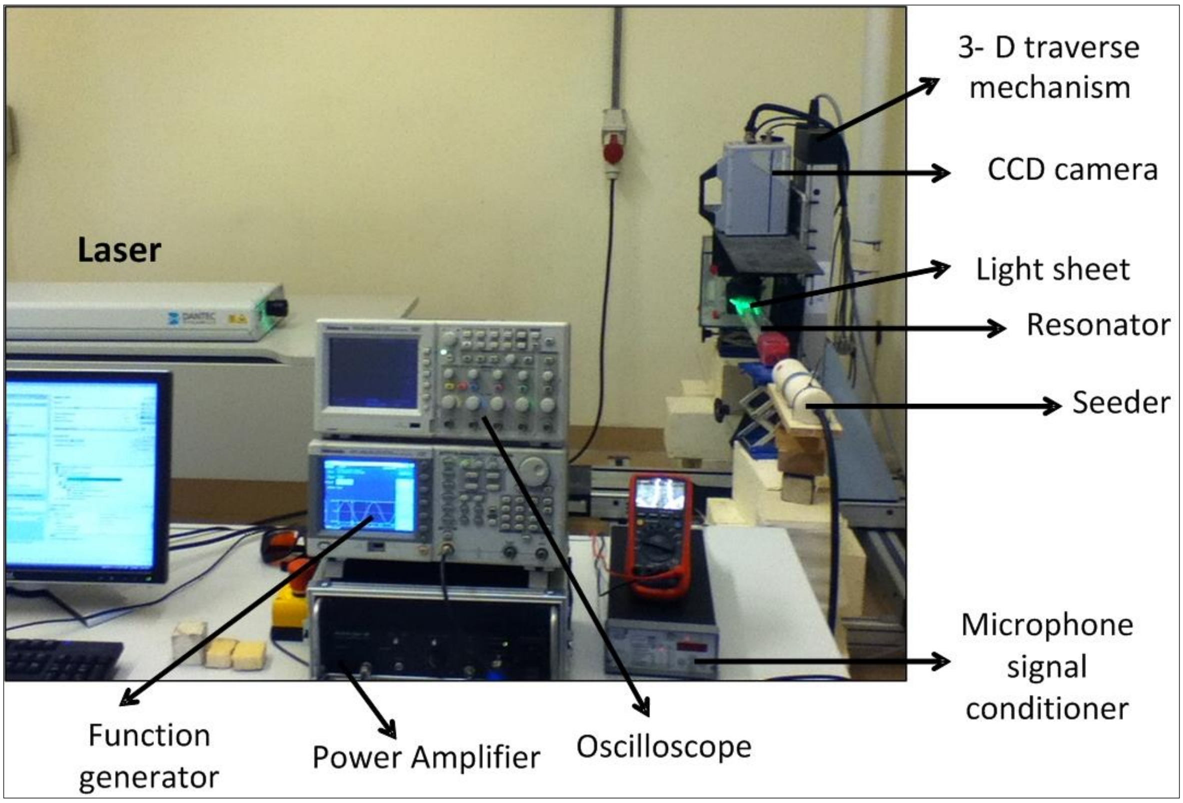

Figure 4.2 A real time picture of the PIV setup with the laser sheet directed towards the quartz resonator.

Calibration was done using a transparent plastic ruler with a white paper taped at its back and a simple aluminum bracket Figure 4.3 that was built to facilitate the process of calibration by directly clamping the device and the ruler on the quartz resonator. The ruler was placed just under the camera and an example of pixel to millimeter calibration was calculated as shown in Figure 4.4.

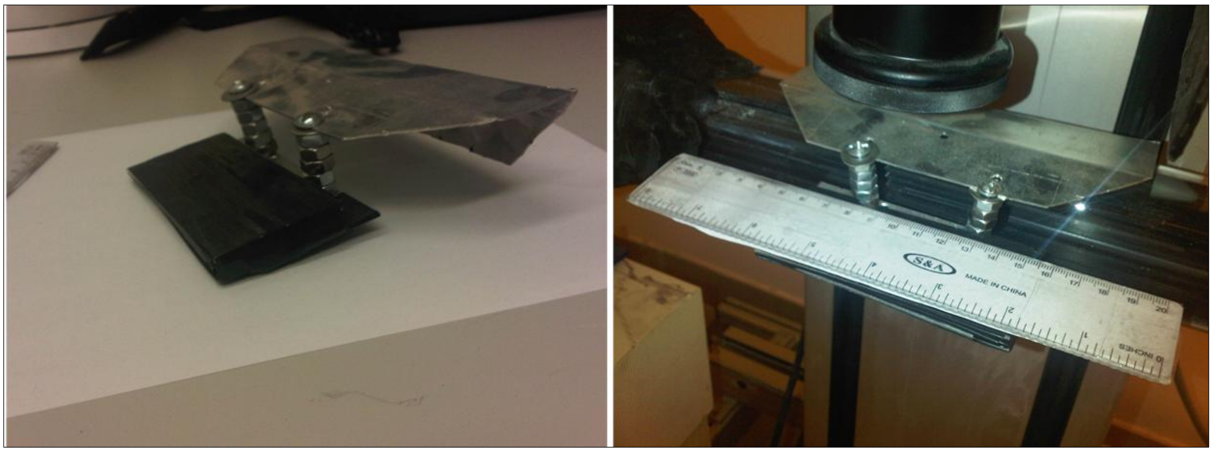

Figure 4.3 (Left) A simple aluminum bracket used to carry the ruler with white background for PIV calibration. (Right) the bracket carrying the ruler clamped on the quartz resonator with the CCD camera appearing in the top.

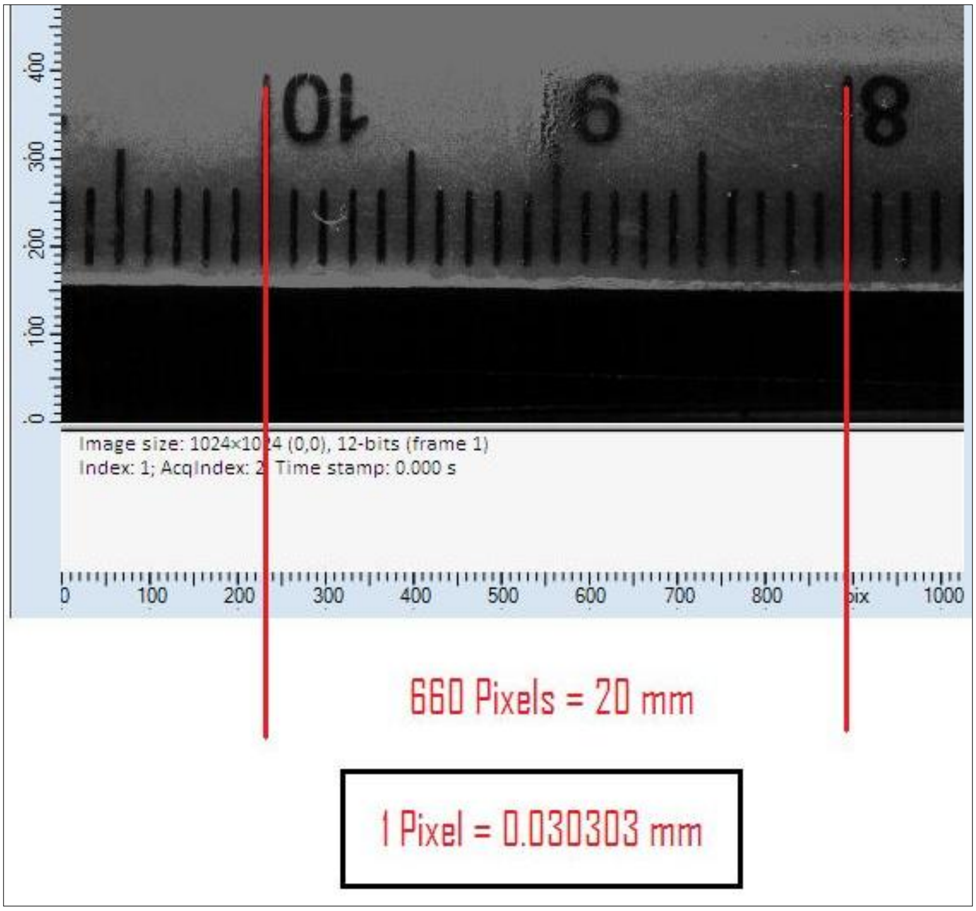

Image size: 1024×1024 (0,0), 12-bits (frame 1)
Index: 1; AcqIndex: 2 Time stamp: 0.000 s

Figure 4.4 Calibration of the PIV measurements for the thermoacoustic refrigerator with no stack.

4.1.2. The glass-quartz resonator

The thermoacoustic refrigerator was made of a quartz resonator tube glued to a glass pyramid-shaped cone connected at its end to a glass box that acts as a back volume for the Pioneer TS-G1013R loudspeaker. The back volume glass box has one of its faces made to slide through guides to allow for placing the speaker inside the box. The full dimensions of the glass-quartz resonator are shown in Figure 4.5 where the functional resonator length was 720 mm as it starts directly after the speaker's surface and along to the hard end of the resonator. The inner cross section of the quartz tube was 48x48 mm^2.

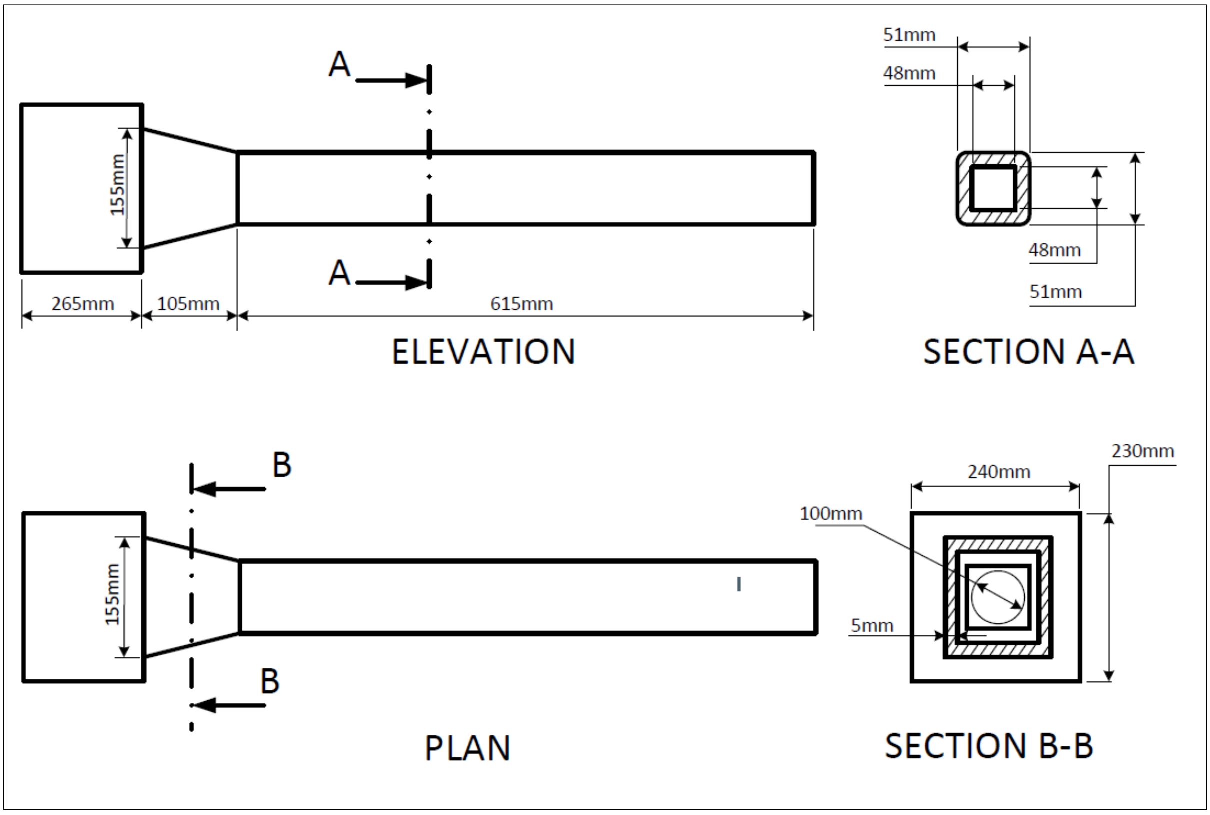

Figure 4.5 Detailed dimensions of the glass-quartz resonator showing the quartz resonator tube and the glass cone and back volume box.

4.1.3. The acoustic setup

The loudspeaker has a maximum power rating of 110 Watts and a nominal power rating of 20 Watts. The needed loudspeaker characteristics were defined in chapter Chapter 3. The Pioneer TS-G1013R loudspeaker was driven by a Tektronix AFG 3021B function generator through a B&K Amplifier Type 2743. The values of amplitude and frequency of the sound wave controlled by the function generator are changed according to each experiment's needs. The values of the amplifier were set to -20 dB as primary amplification and -9 dB as secondary. These values are not used to directly measure the output dynamic pressure but only as set values. A multi-meter was used to monitor the voltage at the output terminals of the amplifier to have a reference of the amplitude of acoustic signal flowing to the speaker and thus to the resonator. While placing a permanent microphone at the hard end of the resonator is the common method to monitor the dynamic pressure at the end of the resonator, the experimental setup couldn't accommodate for such placement thus replaced by measuring the RMS voltage input to speaker.

4.1.4. Seeding particles

The type of tracer particles used for velocity measurement experiments was DuPont's Ti-Pure R900 Titanium dioxide (TiO_2) seeding particles with a specific gravity value of four and a median particle size of 0.41μm. It is shown that the R900 is convenient for measuring velocity in air medium as the ratio of tracer particles speed to flow speed is extremely high [25] [26]. According to Eq. 2.5 the ratio of tracer particles speed to flow speed was calculated to be 3708 which was extremely convenient to conduct measurements. Appendix (B) shows a short MATLAB code used for calculating the ratio of tracer particles speed to flow speed. Figure 4.6 shows a schematic of the seeder used to generate homogenous particles into the flow. The device is a cylinder made into two halves and connected together by a threaded connection. The two halves were machined from inside to form a diverging opening towards the threaded connection. Seeding particles were dropped in the two halves before closing them together. As shown in Figure 4.1 the seeder was connected from one side to an air source which was an air step and a small tube is used to insert the seeding particles into the resonator. The key concept of the diverging-converging seeder is to distribute the input air homogenously over all seeding particles dropped in the seeder openings by diverging the input air flow and then produce a convenient amount of homogenously distributed seeding particles into the resonator by converging the flow again. The convenient amount is decided by the diameter of the output tube connected to the resonator and was determined by experiment. Figure 4.7 shows a picture of the seeder used showing the air hose at the right side of the picture and a small rubber tube on the left side to insert seeding particles into the resonator [25].

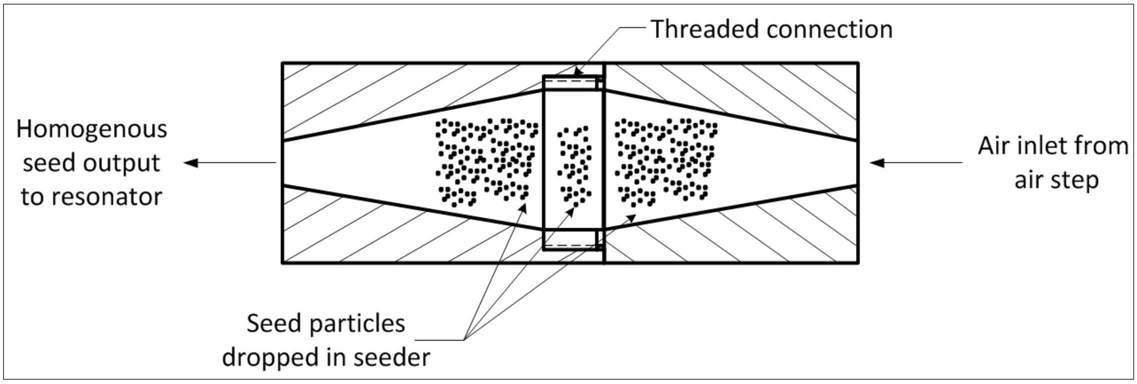

Figure 4.6 A cross-section of the seeder used to induce seeding tracer particles in the resonator tube.

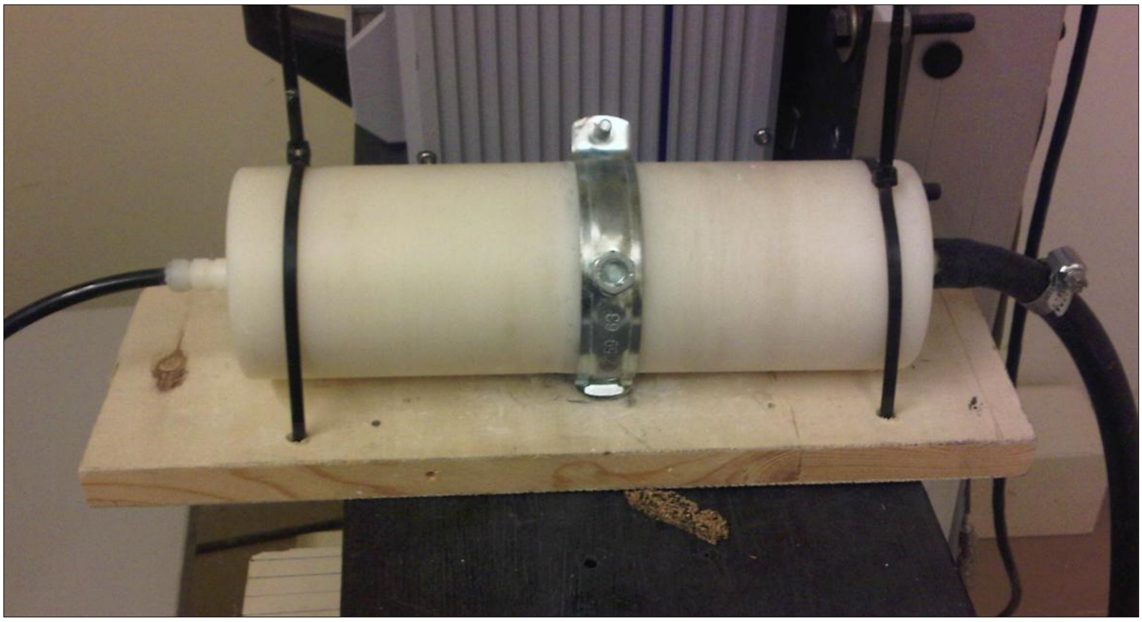

Figure 4.7 A picture of the seeder used to generate titanium dioxide particles into the quartz resonator to measure velocity using PIV.

4.1.5. Insertion of stacks

An L-shaped aluminum sheet with a thickness of 2 mm covered with black tape on its inner sides Figure 4.8 was used to act as a black background to the imaging plane which is a necessity in PIV measurements so that only white reflections from the seeding particles are imaged and nothing else. One of the coated-in-black sides faces the camera for this purpose and the other side was coated to absorb the light from the laser and prevent its reflection inside the resonator or refraction outwards.

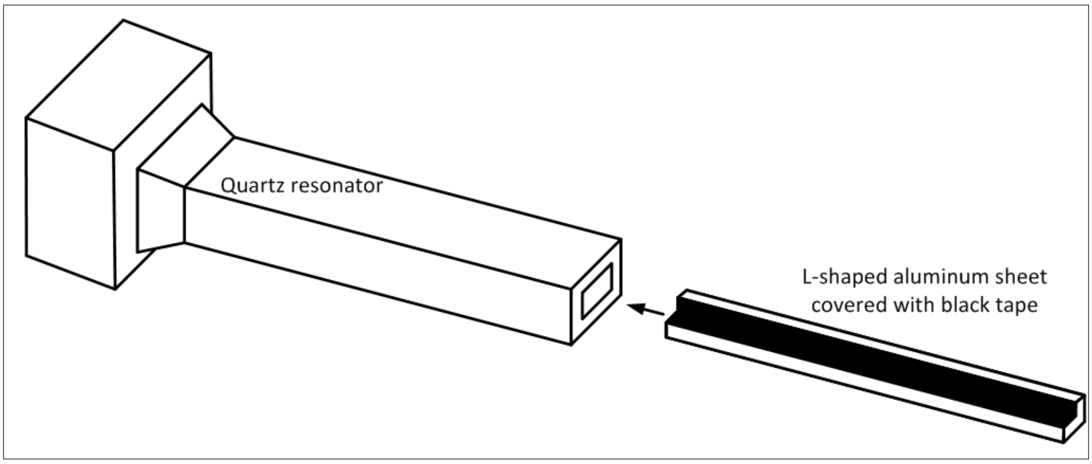

Figure 4.8 A schematic showing the insertion of the L-shaped aluminum sheet covered in black tape into the quartz resonator to act as a light absorption background for imaging.

4.1.6. Dynamic pressure measurement setups and sealing

The hard end of the resonator was designed for changing the measurement tools to measure velocity and dynamic pressure alternatively, to allow for cleaning the resonator after seeding particles' accumulation and to allow for insertion of different stacks to study the thermoacoustic phenomenon. A small plastic box of matching dimensions to the quartz resonator tube was fit to the hard end using plasticine (commercial clay) to be easily removed and placed again Figure 4.9. A hole was drilled at the backside of the plastic box to allow for inserting the different measuring equipment. For measuring velocity the fixture was the seeder output tube. For measuring spatial dynamic pressure distribution along the resonator's length the measurement fixture used was the electret microphone fixture Figure 4.10 where a condensate electret microphone was wired into a long copper tube and inserted through the hole in the plastic box to reach different locations along the resonator's length. For measuring the dynamic end pressure the measurement fixture used was the differential microphone fixture Figure 4.11 where an MEGGIT – 8510B-2 differential microphone with the range of 2 PSI and a sensitivity of 19.315 mV/kPa. A MEGGIT signal conditioner Model 136 was used to amplify the microphone's signal. A Tektronix TDS 2024B oscilloscope was used to measure the output signal of both spatial and dynamic end pressures. The differential microphone was fixed at the boundary between the inside of the resonator and the outside ambient to measure the dynamic pressure value at the hard end since the differential microphone's back vent requires to be in connection with the ambient pressure. As if it is placed inside the resonator, pressure oscillations occurring at the back vent will interfere with the measured oscillations. Unlike the condensate-electret microphone where such oscillations would have a minor effect.

Figure 4.9 The hard end of the quartz resonator showing the plastic box covering the tube end, the seeder output copper tube used to induce seeding particles into the resonator and plasticine (commercial clay) in pink covering the two interfaces of the resonator tube with the plastic box and the seeder tube with the plastic box.

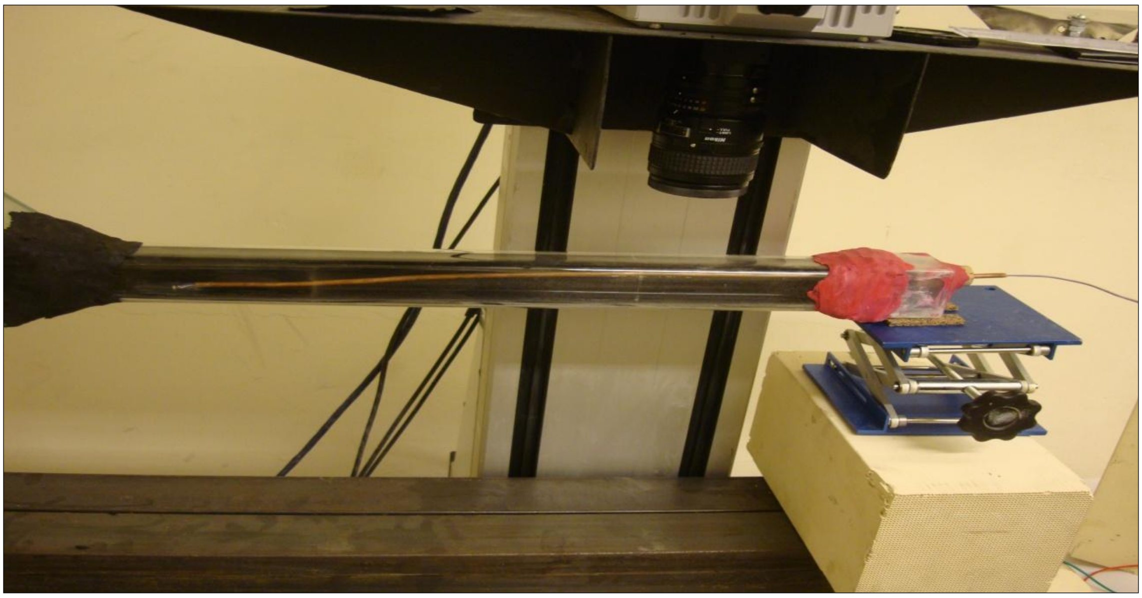

Figure 4.10 The spatial dynamic pressure measurement setup where the electret microphone is wired into a copper tube and placed at different locations inside the quartz resonator to measure spatial dynamic pressure.

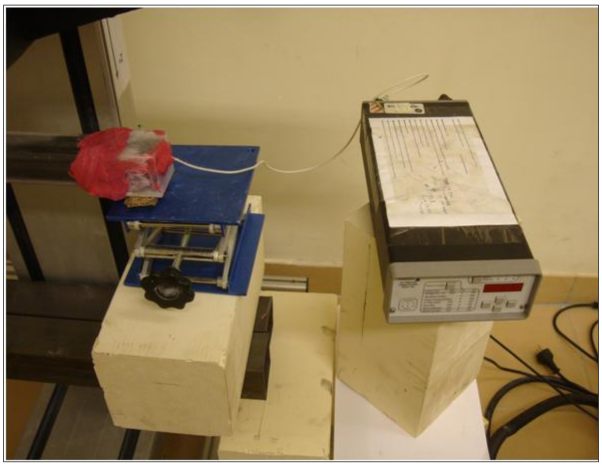

Figure 4.11 The dynamic end pressure measurement setup where the differential microphone is connected to its power supply and inserted into the quartz resonator at the interface between the inside of the resonator and the outside ambient.

Commercial clay has proven experimentally to be a very good leak prevention component with extremely high forming capabilities and also low cost. The plastic box was removed manually with the least effort and replaced again manually after changing the measurement fixture, cleaning or inserting/removing a stack. Clay was also used to leak proof different parts of the thermoacoustic refrigerator as shown in Figure 4.12.

Figure 4.12 Plasticine (commercial clay) covering several leakage point the quartz-glass thermoacoustic refrigerator.

For PIV experiments in general, conducting a successful measurement run requires the observance of a large number of measurement parameters in addition to the correct building of the experimental prototype. Table 4.1 lists a summary of measurement variables that were observed in velocity measurement experiments using PIV.

Table 4.1 A list of measurement variables to be observed within an acoustic-PIV measurement experiment.

Variable name and unit	Controlling device
Acoustics controlled variables	
Amplitude [V]	Function generator
Frequency [Hz]	Function generator
Amplification	Amplifier
Camera controlled variables	
Field of view	Lens
Zoom and focus	Lens
Shutter speed	Lens
PIV Hardware controlled variables	
Laser intensity	Laser power supply
The two laser heads’ energy	Laser power supply
Synchronization	Timer box
PIV software controlled variables	
Laser trigger rate	PIV software
Time between pulses	PIV software
Analysis technique	PIV software
Size of interrogation area	PIV software

4.2. Pitfalls in “Thermoacoustics – PIV” experimental setups

The use of PIV to measure velocity in thermoacoustic is rather a complex operation involving several parameters that need to be adjusted all together. In addition to the standard measurement variables mentioned in Table 4.1 other issues have to be carefully observed:

1 – The oscillating nature of the flow means that a wide range of positive and negative velocities have to be dealt with, including instances of near-zero velocity and instances of high acceleration or deceleration rates. This issue comes down to the proper selection of the time between pulses and the area of each interrogation window. For example, if the interrogation area is too large with respect to the motion of the seed particles, the PIV system cannot identify the motion accurately. On the other hand, if the interrogation area is too small with respect to the motion of the seed particles, the seed particles move from one area to another and the motion may not be traced. In this work, and with a calibration of 1 mm = 33 pixels, a seed particle moving at 10 m/s and analyzed using an interrogation area of 32 X 32 pixels^2 actually moved 20.6% of the interrogation area, allowing accurate measurement of the particle displacement without many seed particles moving from one area to another. At a 5 m/s, and using an interrogation area of 16 X 16 pixels^2, the seed particle would still move 20.6% of the interrogation area.

2 – The settling velocity Eq. 4.1 has to be negligible with respect to the actual flow velocities measured.

$$U_\infty = \frac{g * \left(d_p\right)^2 * (\rho_p - \rho_f)}{18 * \mu_f} \quad [m/s] \qquad \textbf{Eq. 4.1}$$

where; (g) is the gravitational constant in [m/s^2], (d_p) is the particle diameter in [m], (ρ_p) is the particle density in [kg/m^3], (ρ_f) is the fluid (gas) density and (μ_f) is the fluid’s (gas) viscosity.

Using seed particles of a mean diameter of 0.41 μm and density of 4000 kg/m^3 the settling velocity became 1.8 μm/s and the ratio of the measured velocity (10 m/s) to the settling velocity was around 5.5E5 times.

3 – Operation in a confined space causes several technical problems. First, the seed particles deposit on the resonator upper and bottom surfaces and create a layer between the flow and the CCD camera. This layer has to be removed regularly – without causing leaks during

operation - to obtain clear PIV images. Second, the seed particles hit the walls of the resonator causing flow structures unrelated to the oscillating flow pattern of thermoacoustics. One part of the solution to this issue was to introduce the seed parallel to the resonator axis (and not normal to it) such as to reduce the interaction between the resonator walls and the seed particles; and the other part was to operate the loud speaker for a convenient amount of time that is to be determined experimentally by observation according to the case under study before taking PIV images so that the oscillating flow dominates over any unrelated flow structures.

4 – Acoustic agglomeration [44] occurs because high amplitude oscillations cause the seed particles to collide with each other and agglomerate, causing the diameter to increase and forcing the seed particles to slip and eventually settle down. This issue practically placed a maximum on the power input to the speaker.

5 – Amplitude leakage occurs if the laser system misses the cycle peak point. This effect was reduced significantly by capturing more than 15 measurement points per cycle.

Recommendations for proper setup:

Certain recommendations should be taken into consideration when preparing a thermoacoustics-PIV measurement setup. Seeding selection is the most critical step in the whole measurement process. Literature provides tables that state different convenient seeding types for different flow mediums. Correct seeding selection allows for good flow following and large particle residing time. Selecting a seeder (seed generator) is the second step, for solid seeding particles the seeder provided in Figure 4.7.b. As for liquid seeding particles aerosol seed generators are a good choice. Some fog generators are used but these tend to produce a huge amount of non-homogenous seeding clouds which are by no means feasible for thermoacoustics. Liquid particles tend to precipitate on all inner sides of the resonator including the upper side, the seed generation process requires heating and a startup time and they require cleaning more frequently then solid particles, thus solid particles tend to be more convenient from the points of view of seeding sophistication and cleaning. The position of seeding particles entry is also important, when the tube transporting the particles into the resonator in placed perpendicular to the direction of the flow of the acoustic wave, more entry disturbances and vortex structures occur that take more time to settle down. It is better to place the inlet tube in a direction parallel to the acoustic wave flow to reduce entry disturbances. It is good practice to allow some time for seed residing and then induce a low amplitude acoustic wave for a small period of time followed by a small time before starting measurements. The low amplitude of the acoustic wave distributes the seeding particles homogenously throughout the resonator and helps in damping the seed entry disturbances. Some other practices imply the use of a high amplitude acoustic wave instead of a low amplitude one, but for the experiments mentioned in this document the low amplitude wave has shown much better results.

Finally it is very important to determine the outcomes of a PIV measurement before specifying all PIV components and initiating the measurement process. The PIV setup capabilities (laser trigger rate, camera trigger rate, focal length of the lens, seeding type) must be suitable to capture and analyze the targeted phenomenon.

Chapter 5. Study of the acoustic behavior of the thermoacoustic refrigerator (Experimental measurements versus numerical modeling)

The acoustic behavior of the thermoacoustic refrigerator was studied in two phases. The first was to validate the behavior of particle velocity and particle dynamic pressure which are the principal variables in any acoustic system. The validation process was done by comparing experimental and numerical values measured and computed on the thermoacoustic refrigerator with no stack or heat exchangers, thus not being a thermoacoustic device anymore but only an acoustic tube. No stack was placed in the resonator so as to remove any effect the stacks may have on the acoustic behavior. The validation process included comparing measured and numerical values for acoustic resonance frequency, spatial dynamic pressure distribution, spatial velocity distribution and dynamic end pressure values. The second phase was similar to the first phase except for adding meshed ceramic stacks of different porosities and lengths. DeltaEC software was used to compute all numerical values using the dimensions of the prototype and the speaker characteristics illustrated in Chapter Chapter 3, the PIV setup was used to measure the spatial velocity distribution, the electret microphone setup was used to measure the spatial dynamic pressure distribution and the differential microphone setup was used to measure the dynamic end pressure value. The numerical values were also obtained using DeltaEC.

Prior to acoustic measurements the maximum operating power capacity of the Pioneer TS-G1013R loudspeaker was calculated to avoid damage of the loudspeaker. As shown before in Figure 4.1 a multi-meter was used to measure the RMS voltage to the loudspeaker. Eq. 5.1 shows that acoustic power is the resultant of the product of voltage, electric current and the power factor ($cos\ \emptyset$). The power factor ($cos\ \emptyset$) is assumed to be unity:

$$\mathrm{Power_{max}} = \mathrm{V_{max}} * \mathrm{I}\ * \cos \emptyset\ [\mathrm{Watts}] \qquad \textbf{Eq. 5.1}$$

yielding;

$$\mathrm{Power_{max}} = \mathrm{V_{max}} * \frac{\mathrm{V_{max}}}{\mathrm{R_{DC}}} * \cos \emptyset\ \ [\mathrm{Watts}] \qquad \textbf{Eq. 5.2}$$

and

$$\mathrm{Power_{max}} = \frac{(\mathrm{V_{max}})^2}{\mathrm{R_{DC}}} * \cos \emptyset\ \ [\mathrm{Watts}] \qquad \textbf{Eq. 5.3}$$

thus;

$$\mathrm{V_{max}} = \sqrt{\mathrm{Power_{max}} * \mathrm{R_{DC}}} * \cos \emptyset\ = \sqrt{20 * 3.8} * 0.995\ = 8.6748\ [\mathrm{V}] \qquad \textbf{Eq. 5.4}$$

As shown in Eq. 5.4 the maximum voltage to speaker was found to be approximately 8.7 V. The acoustic system is composed of a function generator driving the loudspeaker through a power amplifier that only shows set values not direct gain values as illustrated in Chapter Chapter 4. Thus there was a need to determine the value of the driving voltage of the function generator that satisfies the maximum voltage to loudspeaker value. Through trial and error this value was determined to be 2.2 $V_{p\text{-}p}$ (peak-to-peak) which corresponds to a value of about 8 V delivered to the speaker thus attaining a value lower than that calculated in Eq. 5.4. All measurement runs were performed below the 2.2 $V_{p\text{-}p}$ value boundary.

The consistency of the loudspeaker's performance over time was tested by operating the loudspeaker for a continuous period of 30 minutes while measuring the voltage to the loudspeaker and the dynamic end pressure at the hard end of the resonator using the differential microphone setup. Additionally the speaker was turned off and on several times afterwards and left to operate for shorter periods of time to investigate the steadiness of the speaker's performance throughout different measurements. The function generator was operated at 0.7 $V_{p\text{-}p}$ which corresponded to 2.5 V_{rms} (root mean square) of voltage to loudspeaker. The dynamic end pressure value was measured around 600 Pa. The results of these tests showed constant values of voltage to speaker and dynamic end pressure with 1% deviation throughout the 30 minutes time period and the on and off short time periods.

For dynamic end pressure measurements the differential microphone output is measured as a peak-to-peak voltage on the Tektronix TDS 2024B oscilloscope. The corresponding values of dynamic pressure were computed by dividing over the microphone's sensitivity. The microphone's sensitivity is 19.315 mV/kPa, the gain used in the microphone signal conditioner was 100 and the value of dynamic end pressure obtained in DeltaEC is an amplitude value not a peak-to-peak value. Eq. 5.5 shows the conversion equation for the MEGGIT – 8510B-2 differential microphone used in dynamic end pressure measurements:

$$\text{Dynamic pressure amplitude } |P| = \frac{\text{Measured peak to peak value in Volts} * 1000 * 1000}{2 * \text{Gain} * \text{Sensitivity}}$$

Eq. 5.5

$$= V_{p-p} * 258.8662 \quad [\text{Pa}]$$

5.1. Validation of the acoustic behavior of a quartz resonator without a stack

5.1.1. Experimental results

5.1.1.1. Resonance frequency

Resonance frequency was measured using the differential microphone setup where the microphone was fixed at the hard end of the resonator and by sweeping through a range from frequencies starting near 50 Hz and up to 500 Hz, the frequency response function of the resonator system was obtained. The resonance frequency values are identified as frequency values corresponding to relative peak dynamic pressure amplitudes and are independent of the input dynamic pressure. The function generator was set to a value of one $V_{p\text{-}p}$ corresponding to 5 V_{rms} as voltage to loudspeaker value. The amplifier values were set to -20db and -9 dB. Table 5.1 shows the values of voltage measured using the oscilloscope where the peak values are shaded.

Table 5.1 Peak-to-peak pressure values in [V] obtained for frequency sweeping of the resonator.

Frequency [Hz]	V_{p-p} [V]	Frequency [Hz]	V_{p-p} [V]	Frequency [Hz]	V_{p-p} [V]
30	0.24	179	3.76	230	1.96
40	0.4	180	3.78	240	1.54
50	0.52	181	3.82	250	1.3
60	0.76	182	3.86	260	1.12
70	0.9	183	3.9	270	1
80	1.12	184	3.94	280	0.88
90	1.44	185	3.94	290	0.8
100	1.88	186	3.96	300	0.76
110	2.52	187	3.96	310	0.76
120	3.32	188	3.96	320	0.74
125	3.84	189	3.96	330	0.72
126	3.92	190	3.98	340	0.72
127	4	191	4.02	350	0.76
128	4.08	192	4.02	360	0.8
129	4.1	193	4	370	0.88
130	4.08	194	4	380	1.04
131	4.08	195	4	390	1.32
132	4.04	196	3.96	400	2.08
133	3.9	197	3.96	405	2.7
134	3.8	198	3.9	406	2.76
135	3.74	199	3.9	407	2.84
140	3.52	200	3.84	408	2.9
145	3.36	201	3.84	409	2.9
150	3.28	202	3.78	410	2.9
160	3.32	203	3.7	411	2.8
170	3.46	204	3.68	412	2.72
175	3.64	205	3.64	413	2.64
176	3.66	210	3.32	414	2.5
177	3.68	215	3		
178	3.7	220	2.68		

Figure 5.1 shows the frequency response function of the system where the values of peak amplitudes observed were 129 Hz, 191 Hz and 409 Hz. At a frequency of 129 Hz and a speed of sound of 343 m/s, the following calculations were performed:

$$c = \lambda f \quad [m/s] \qquad \textbf{Eq. 5.6}$$

where (c) is the speed of sound in [m/s], (λ) is the wave length in [m] and (f) is the frequency in [Hz].

yielding; $$\lambda = c/f = 343/129 = 2.66 \ [m] \qquad \textbf{Eq. 5.7}$$

thus; $$L_r/\lambda = 0.72/2.66 = 0.27 \approx 0.25 \qquad \textbf{Eq. 5.8}$$

where (L_r) is the length of the resonator from the loudspeaker's surface to the hard end.

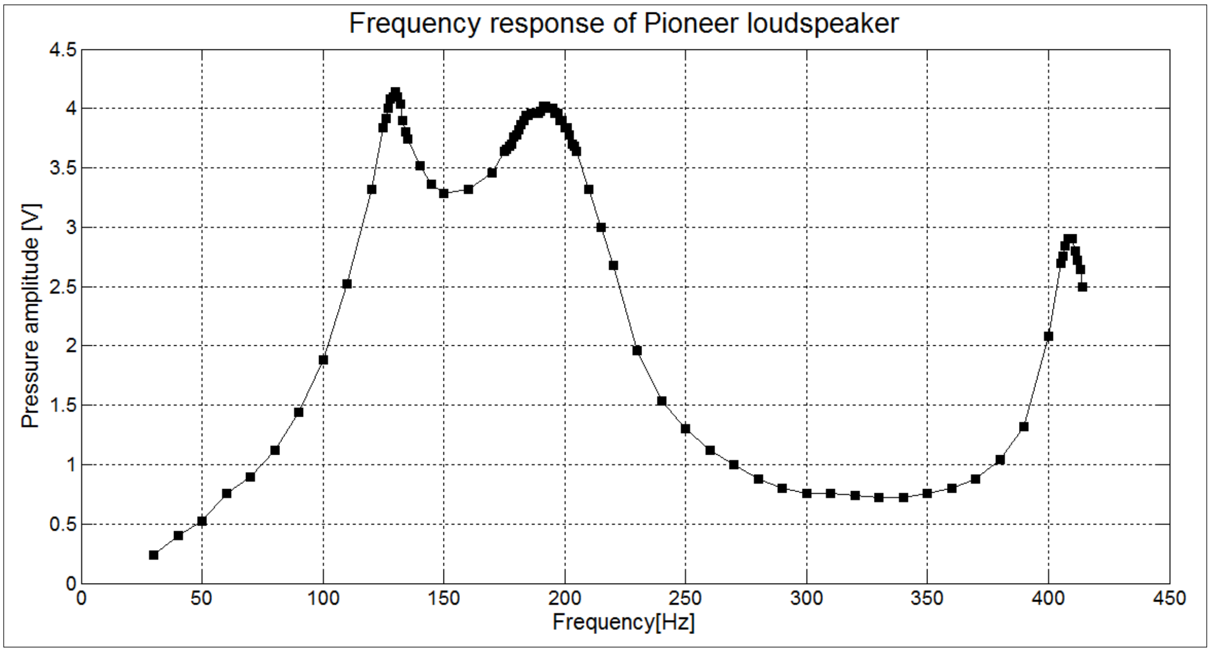

Figure 5.1 The frequency response of the Pioneer TS-G1013R loudspeaker measured using the dynamic end pressure measurement setup.

The result of the above calculations Eq. 5.8 states that the resonator operates at a quarter wave length mode at a frequency of 129 Hz. This argument is confirmed by the presence of a second peak at almost three times the value of the first frequency 409 Hz where the value of (L_r/λ) is calculated as follows:

$$\lambda_3 = c/f = 343/409 = 0.84 \ [m] \qquad \textbf{Eq. 5.9}$$

yielding; $$L_r/\lambda_3 = 0.72/0.84 = 0.85 \approx 0.75 \qquad \textbf{Eq. 5.10}$$

This was explained as a result of the large back volume at the loudspeaker's back side that doesn't act as a pure hard but as a soft end. The middle peak occurring at 191 Hz is the mechanical resonance of the speaker as affected by the acoustic impedance upstream and downstream of the speaker as stated by the frequency response chart supplied by the speaker manufacturer shown in Figure 5.2.

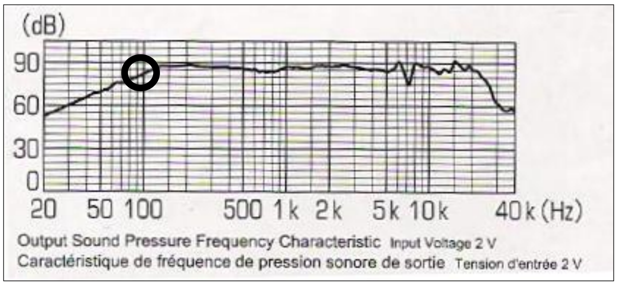

Figure 5.2 The frequency response chart provided by the Pioneer TS-G1013R loudspeaker manufacturer showing the end point of a slope where the speaker's response becomes nearly constant. This point indicates the resonance frequency of the loudspeaker when placed in a system with a back volume.

5.1.1.2. Dynamic end pressure

The function generator value was adjusted to 0.7 $V_{p\text{-}p}$ that corresponded to a 2.5 V_{rms} as voltage to speaker to generate the dynamic pressure. The function generator frequency was set to 129 Hz. The amplifier values were set to -20db and -9 dB. The dynamic end pressure value as measured through the oscilloscope was 2.24 $V_{p\text{-}p}$. Applying Eq. 5.5 to find the value of dynamic pressure in Pascal:

$$\text{Dynamic pressure amplitude } |P| = 2.24 * 258.8662 = 579.86 \pm 26 \quad [\text{Pa}] \qquad \textbf{Eq. 5.11}$$

5.1.1.3. Spatial dynamic pressure

Spatial dynamic pressure measurements were performed at a lower function generator voltage value than that used for dynamic end pressure and velocity measurements due to the limited capabilities of the electret microphone. The function generator value was adjusted to 0.08 $V_{p\text{-}p}$, that value was selected by trial and error until the electret microphone showed a full sinusoidal wave, the corresponding voltage to speaker was 0.5 V_{rms}. Figure 5.3 shows a calibration chart for the electret microphone that was developed by inserting both electret and differential microphones together from the hard end.

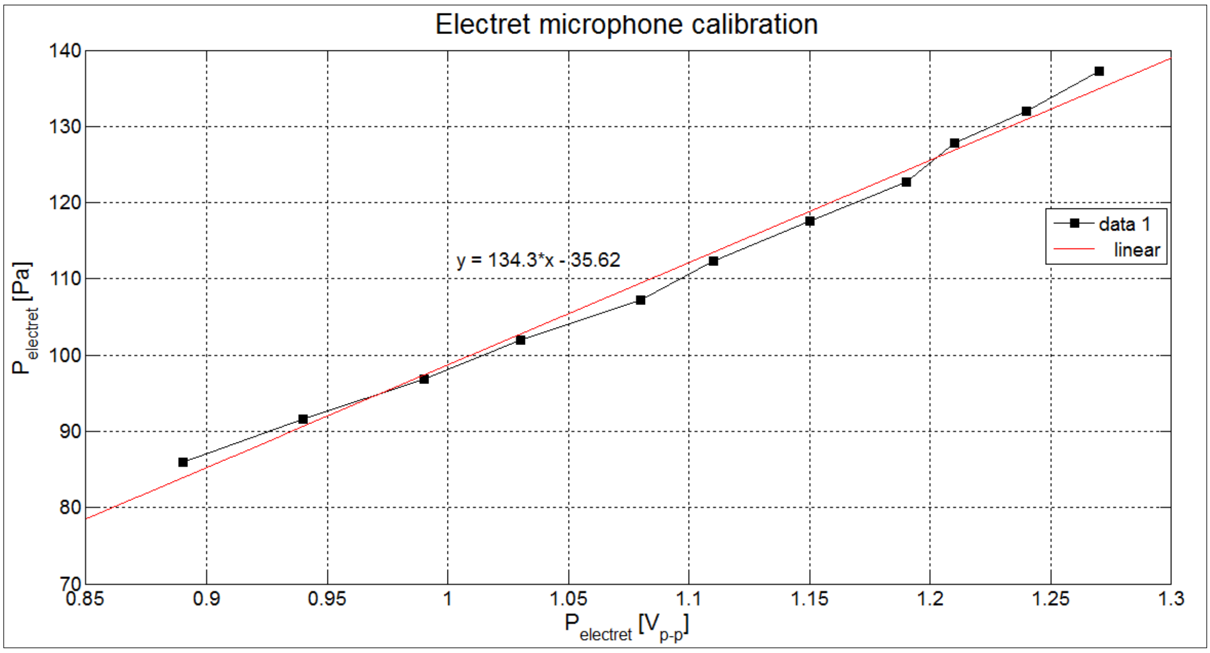

Figure 5.3 Calibration chart for electret microphone

The use of the calibration chart is to express the electret microphone measurement results in [Pa]. Eq. 5.12 shows the calibration equation of the electret microphone.

$$P_{electret} = (P_{electret}\,[V_{p-p}] * 134.3) - 35.621\ [Pa] \qquad \textbf{Eq. 5.12}$$

The function generator frequency was set to 129 Hz. The amplifier values were set to -20 dB and -9 dB. Table 5.2 shows the values obtained for spatial dynamic pressure measurements and Figure 5.4 shows the spatial plot.

Table 5.2 Values of dynamic pressure in [V] at different locations along the length of the resonator with no-stack.

Distance from outer edge of the back volume [m]	Dynamic pressure amplitude [V]
0.495	0.644 ± 0.1
0.545	0.752 ± 0.1
0.615	1.01 ± 0.1
0.66	1.12 ± 0.1
0.705	1.21 ± 0.1
0.76	1.28 ± 0.1
0.795	1.32 ± 0.1
0.83	1.36 ± 0.1
0.875	1.43 ± 0.1

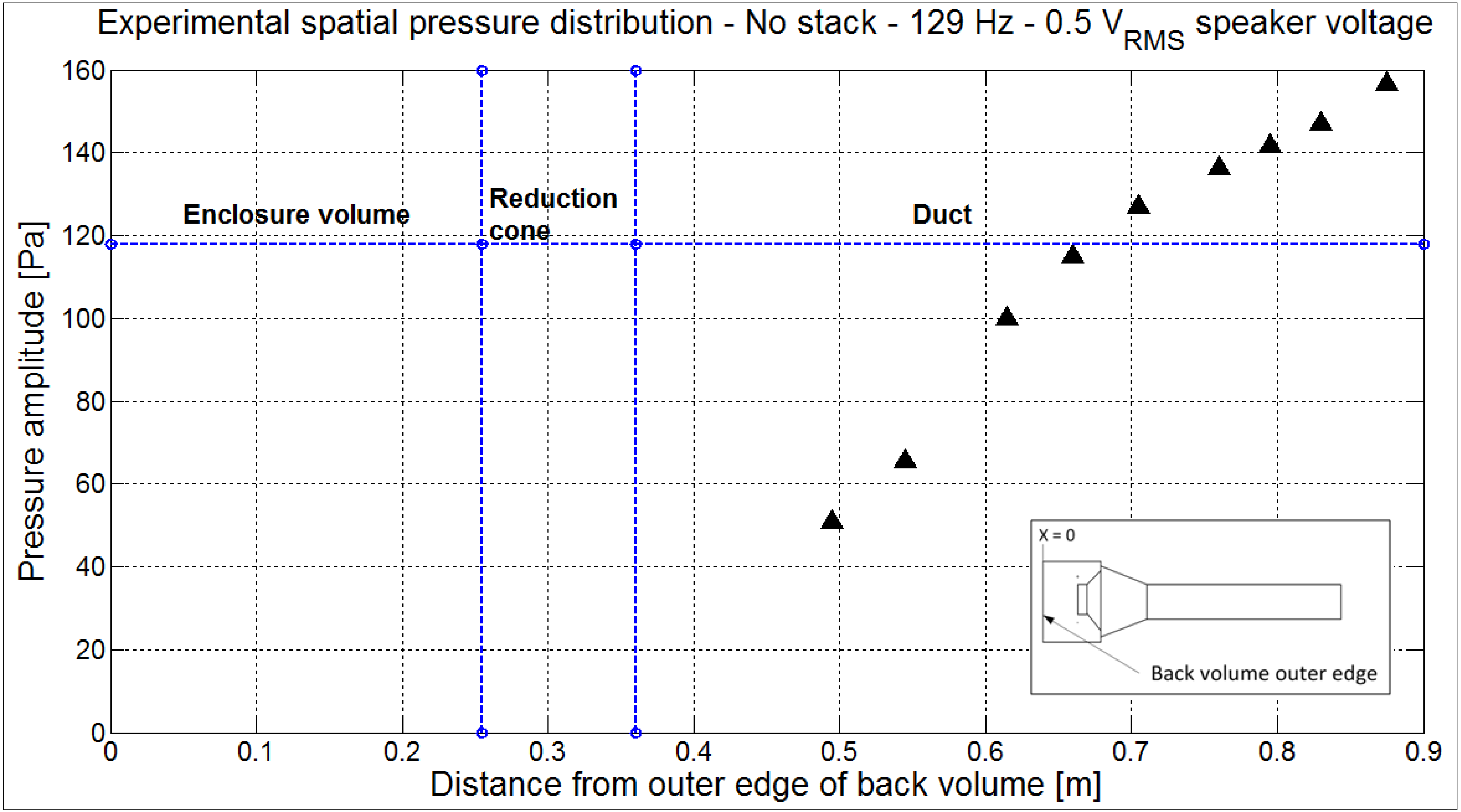

Figure 5.4 Spatial dynamic pressure distribution of the thermoacoustic refrigerator with no stack at 0.5 V_{rms} to speaker and 129 Hz frequency.

The spatial dynamic pressure measurements comply with the argument that the system runs in a quarter wave mode as a high dynamic pressure value is attained at the hard end and the amplitude tends to fade at the loudspeaker's end.

5.1.1.4. Spatial velocity

Spatial velocity was measured using the PIV measurement setup. The acoustic setup is the same as the dynamic end pressure and spatial dynamic pressure measurements. The PIV system was used to measure temporal velocity at several locations along the length of the resonator. At each measurement location 2728 images are taken at a rate of 2700 Hz giving a period of measurement of about one second. These images are double pulses and are produced as vector maps after adaptive correlation analysis is performed. Each vector map represents a point in time in the sinusoidal acoustic cycle. All the vectors in each map are then averaged to give one value of velocity per each point in time and plot the temporal behavior for each measurement location alone. Afterwards the full temporal cycle at each measurement point is plotted using the average values and the maximum amplitudes are extracted from the plots representing the dynamic pressure of each location. Finally the spatial distribution is plotted showing the maximum dynamic pressures along the axis of the resonator. In addition to the 2700 Hz trigger rate, the time between pulses was set to 185μs. The field of view was 31 X 31 mm^2. A sample of the raw images acquired is shown in Figure 5.5 indicating reasonable distribution of seed density per image. Adaptive correlation technique was used to analyze the raw images and produce vector maps using a 128x128 Pixels^2 interrogation area and a moving average filter. A sample series of vector maps representing the motion of air particles at a single location along the resonator throughout a complete acoustic cycle is shown in Figure 5.6.

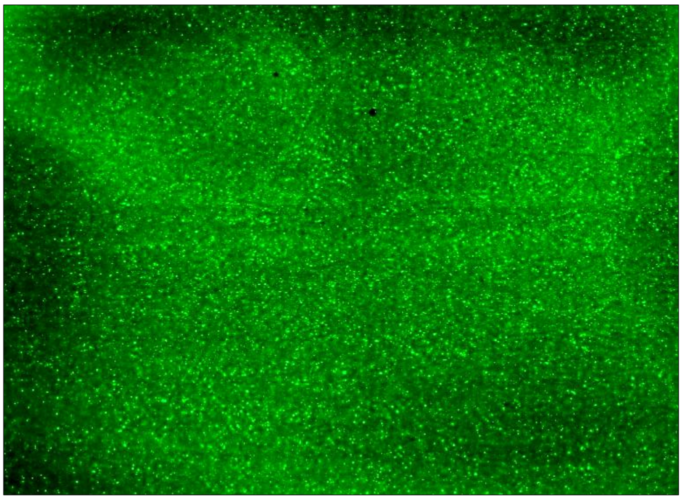

Figure 5.5 A sample raw image captured using the PIV measurement setup for measuring spatial velocity distribution of the thermoacoustic refrigerator.

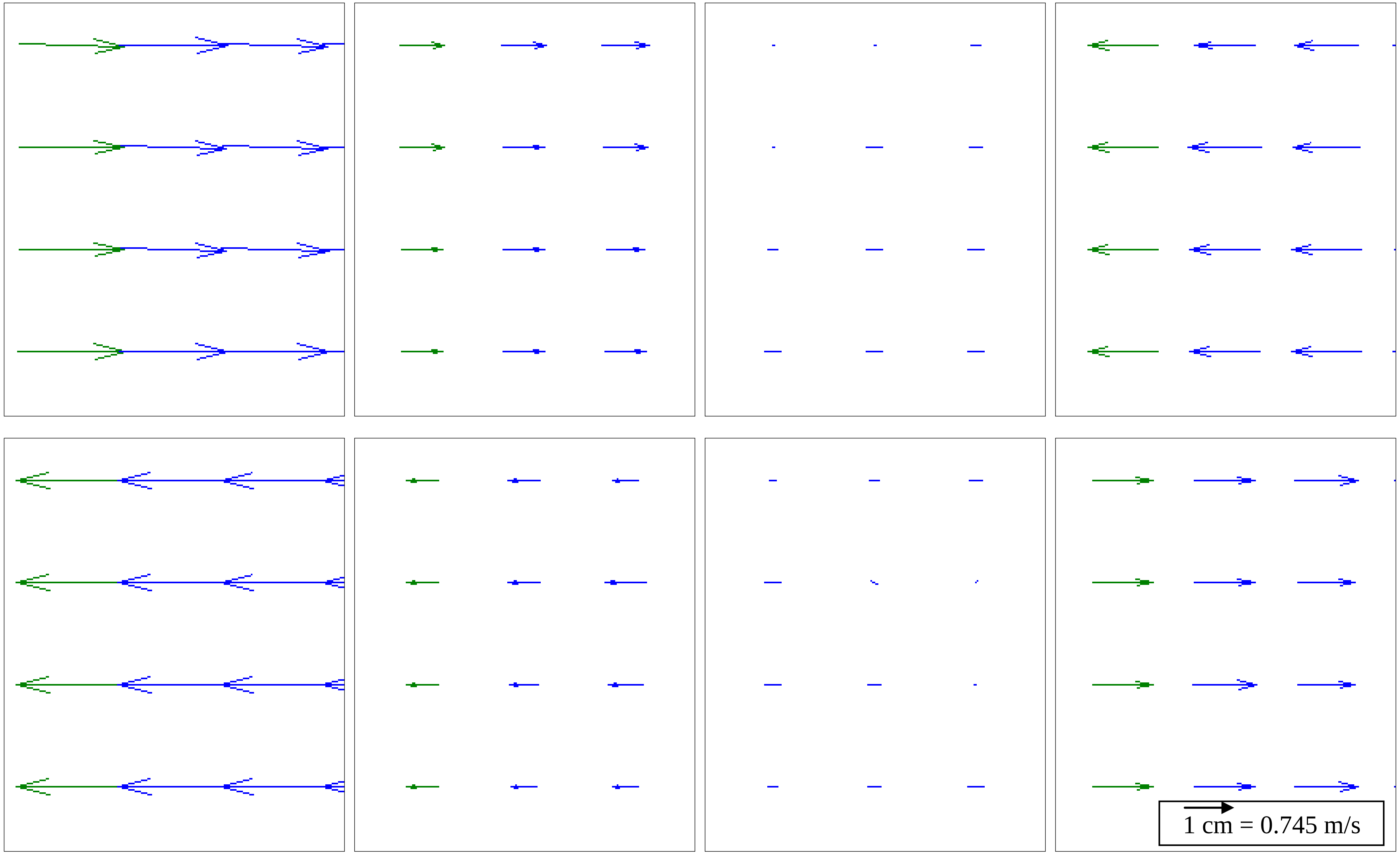

Figure 5.6 A sample series of vector maps analyzed using adaptive correlation technique showing the oscillatory particle motion that occurs in the thermoacoustic refrigerator with no stack.

Spatial analysis was performed using two MATLAB codes (Appendix C) where the analysis was performed on two stages using the two codes. The first code was used to write a part of the second code. That written part is responsible of reading the files exported from the PIV software having the values of vector velocities. The second code is used for averaging, selecting the maximum amplitudes at each measurement location, applying the conversion from pixel displacement to particle velocity in [m/s] and plotting the final spatial distribution. Figure 5.7 shows an example of the temporal velocity behavior of a single measurement location. Figure 5.8 shows the temporal velocity behavior at each measurement location and Figure 5.9 shows the final spatial plot where the measurement locations are referenced to the outermost edge of the prototype which is the outer edge of the back volume.

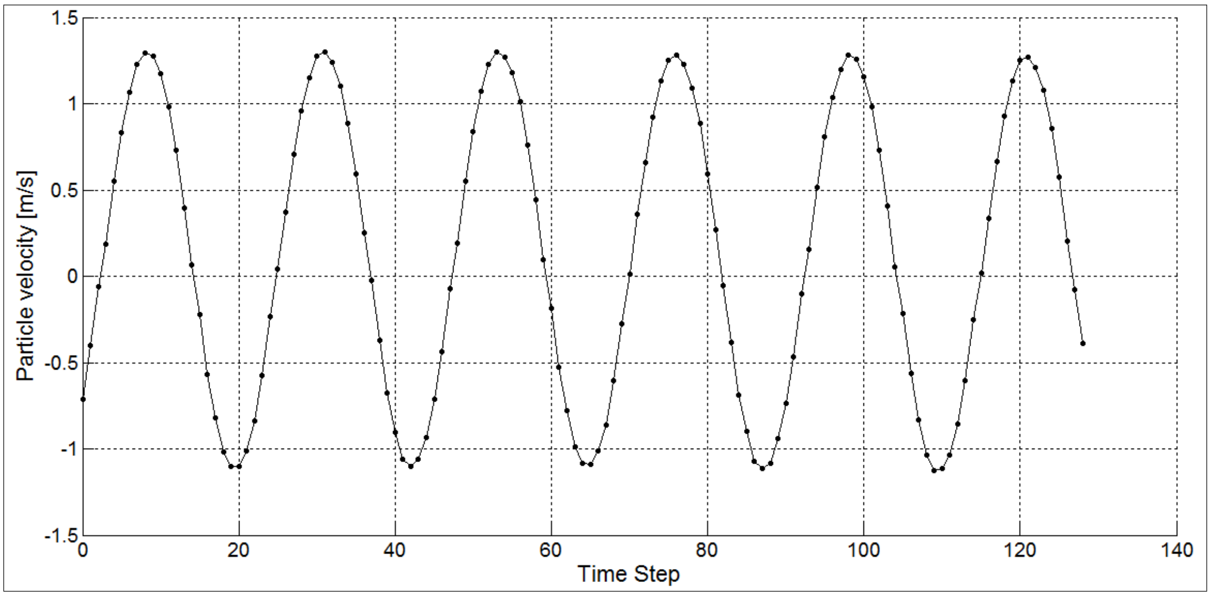

Figure 5.7 The temporal velocity behavior of air particles in the thermoacoustic refrigerator with no stack.

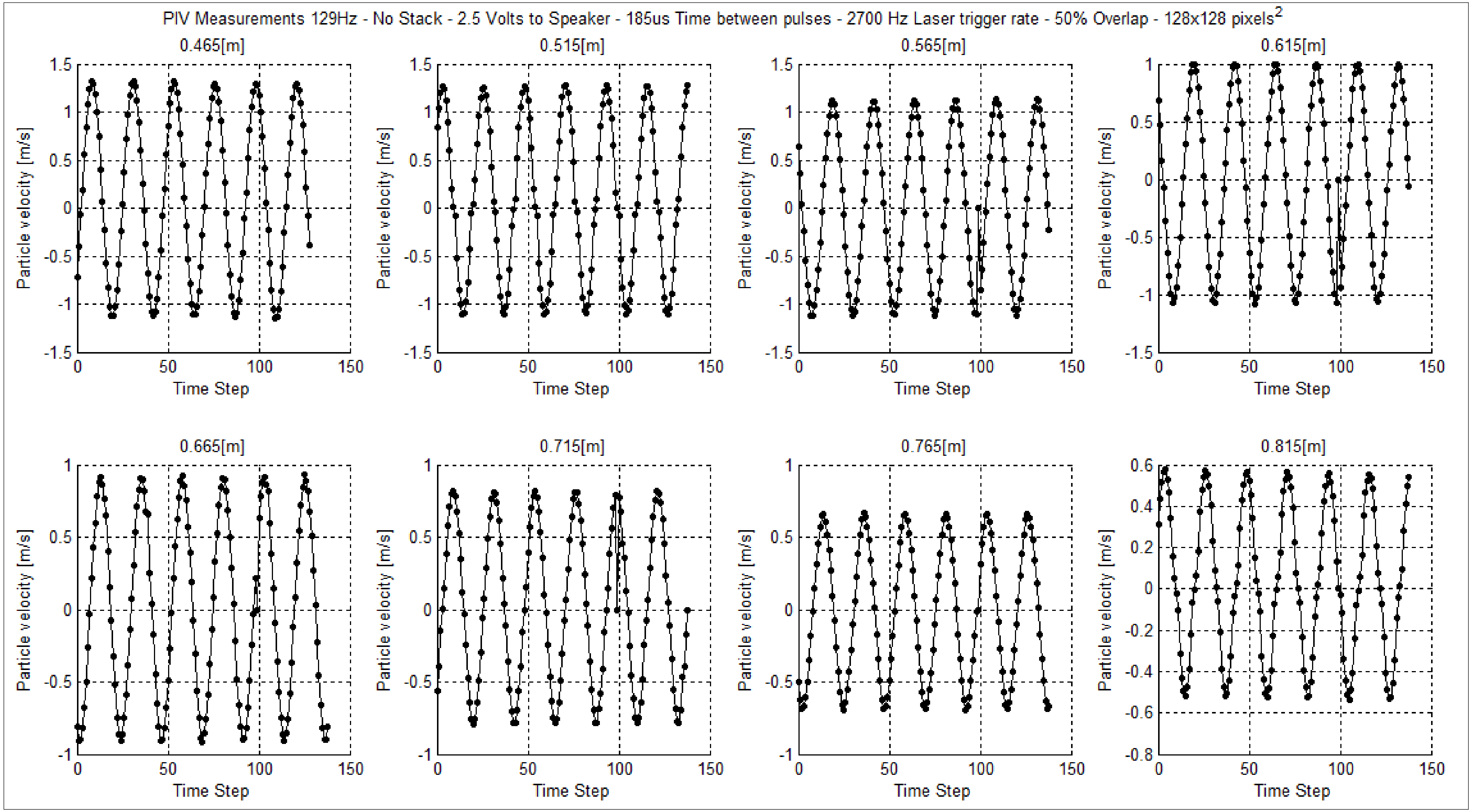

Figure 5.8 Temporal velocity behavior of air particles at different locations along the length of the resonator of the thermoacoustic refrigerator with no stack where the function generator was operated at 0.7 V_{p-p} corresponding to 2.5 V_{rms} and frequency 129 Hz.

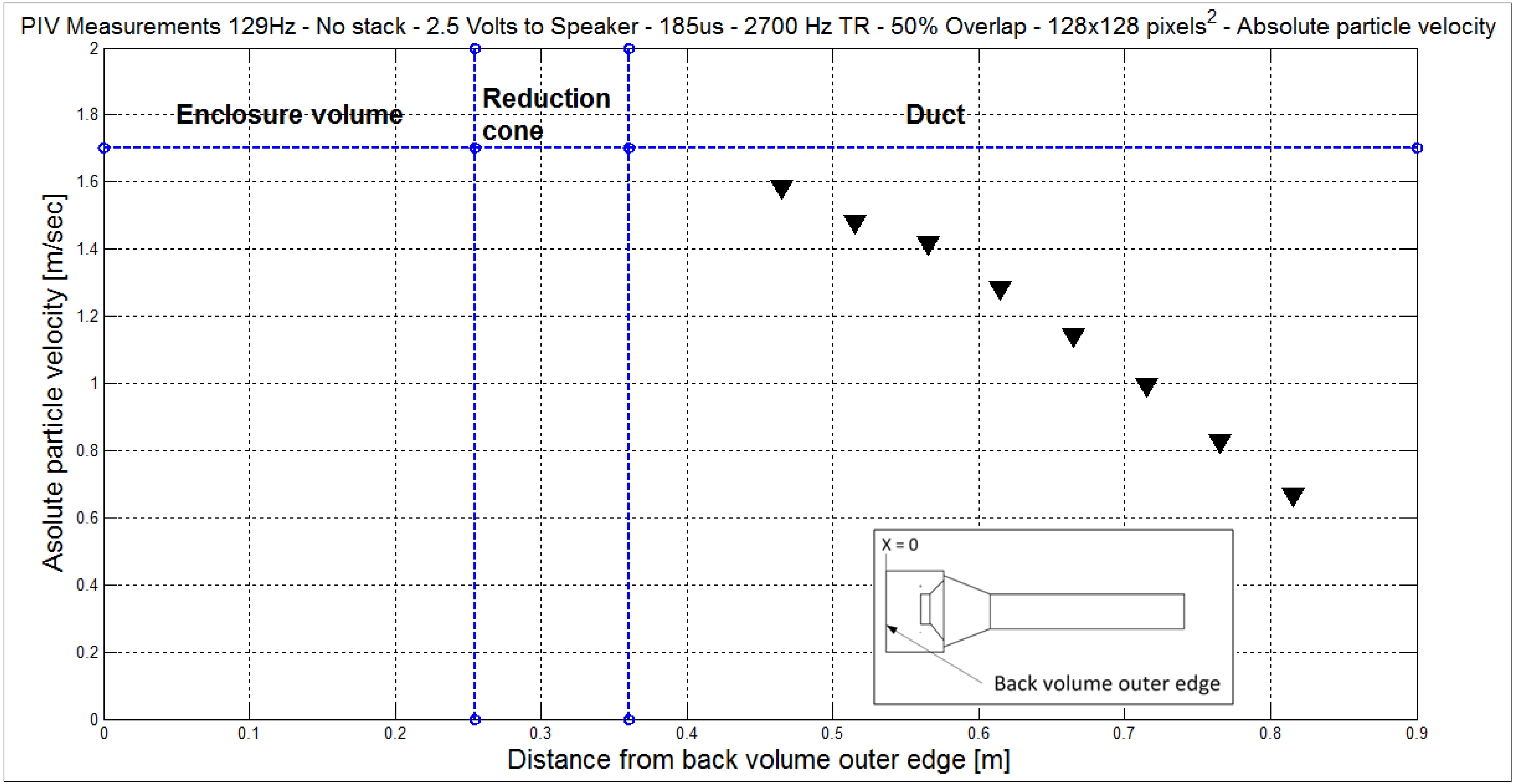

Figure 5.9 Spatial velocity distribution of air particles in a thermoacoustic refrigerator with no stack with 2.5 V_{rms} to speaker and 129 Hz frequency.

The velocity spatial distribution shows large amplitude at the loudspeaker's end and decreases along the resonator's length towards fading at the hard end. The velocity distribution also confirms the dynamic pressure measurement results stating that the thermoacoustic refrigerator is operating in a quarter wave length mode.

5.1.2. Numerical results

Numerical results are computed using DeltaEC software. Figure 5.10 shows the schematic of the thermoacoustic refrigerator as drawn by DeltaEC. Figure 5.11 shows the DeltaEC model for the thermoacoustic refrigerator with no stack. The model aims to simulate the experimental measurements to compare numerical and experimental results. The first segment in the model is the (Begin) segment where the operating gas was defined as air; the mean pressure was defined as atmospheric pressure and standard temperature as 304 Kelvin. The frequency and dynamic pressure are set as guesses to let DeltaEC compute their values. The (Begin) segment represents only a surface not a volume. The next segment is the (Duct) which represents the back volume of the speaker. The left column is for the input variables while the right column is for the output variables at each segment. The following segment is the (VE speaker) which defines the speaker's properties. These were previously illustrated in details in Chapter Chapter 3. One additional parameter is used in this segment which is the voltage amplitude applied on the speaker's terminals with symbol|V|. The voltage used in DeltaEC is the amplitude voltage which requires multiplying the 2.5 V_{rms} measured by the multi-meter by the square root of two to produce 3.535 V as shown in the figure. The following segment is the (Cone) segment where dimensions are dictated by the thermoacoustic refrigerator's detailed drawing Figure 4.5. Following is another (Duct) segment which represents the quartz tube with all its dimensions. Following is a (Surface) segment to accommodate for the viscous losses in the system and produce correct results. The final segment is the (Hard end) segment where it states that the value of impedance is infinity or the volume flow rate is zero to simulate a hard end. The two values of infinity at the hard end are a must to force the DeltaEC model to solve for finding the resonance frequency. Also as two targets are present two guesses must also be present for the software to start solving.

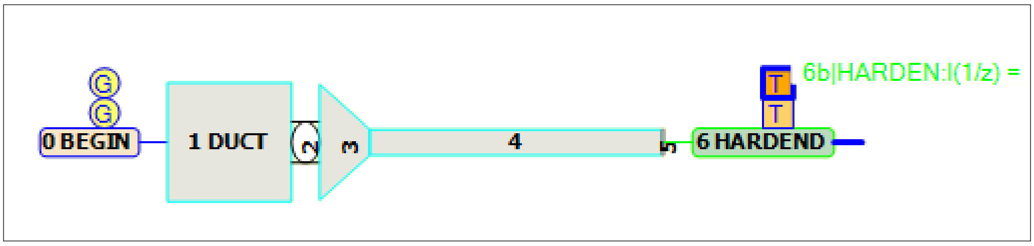

Figure 5.10 The thermoacoustic refrigerator with no stack schematic plotted by DeltaEC software.

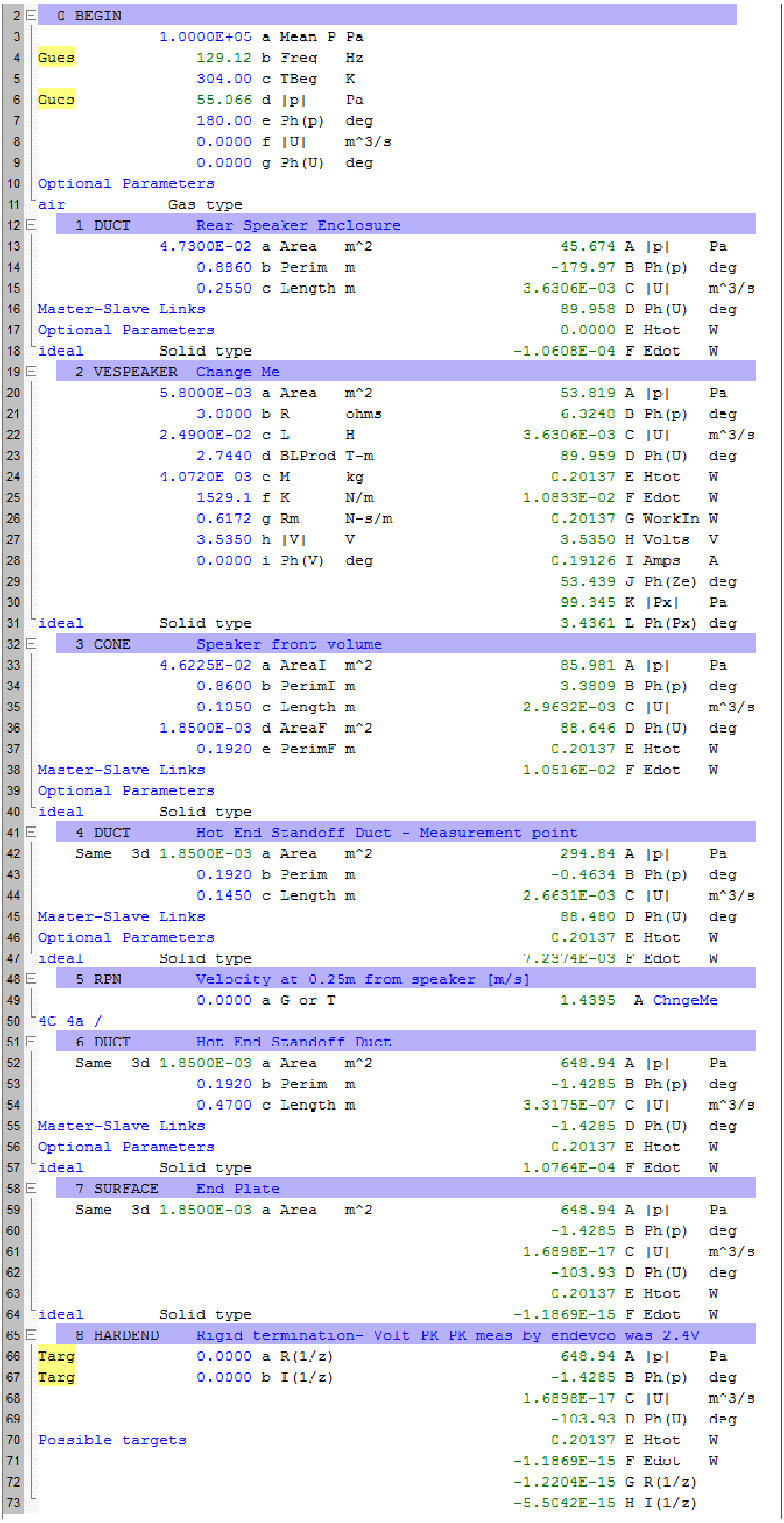

```
  0 BEGIN
             1.0000E+05 a Mean P Pa
Gues             129.12 b Freq   Hz
                 304.00 c TBeg   K
Gues             55.066 d |p|    Pa
                 180.00 e Ph(p)  deg
                 0.0000 f |U|    m^3/s
                 0.0000 g Ph(U)  deg
Optional Parameters
air           Gas type
    1 DUCT       Rear Speaker Enclosure
             4.7300E-02 a Area   m^2             45.674 A |p|     Pa
                 0.8860 b Perim  m              -179.97 B Ph(p)   deg
                 0.2550 c Length m           3.6306E-03 C |U|     m^3/s
Master-Slave Links                               89.958 D Ph(U)   deg
Optional Parameters                              0.0000 E Htot    W
ideal        Solid type                     -1.0608E-04 F Edot    W
    2 VESPEAKER  Change Me
             5.8000E-03 a Area   m^2             53.819 A |p|     Pa
                 3.8000 b R      ohms            6.3248 B Ph(p)   deg
             2.4900E-02 c L      H           3.6306E-03 C |U|     m^3/s
                 2.7440 d BLProd T-m             89.959 D Ph(U)   deg
             4.0720E-03 e M      kg             0.20137 E Htot    W
                 1529.1 f K      N/m         1.0833E-02 F Edot    W
                 0.6172 g Rm     N-s/m          0.20137 G WorkIn  W
                 3.5350 h |V|    V               3.5350 H Volts   V
                 0.0000 i Ph(V)  deg            0.19126 I Amps    A
                                                 53.439 J Ph(Ze)  deg
                                                 99.345 K |Px|    Pa
ideal        Solid type                          3.4361 L Ph(Px)  deg
    3 CONE       Speaker front volume
             4.6225E-02 a AreaI  m^2             85.981 A |p|     Pa
                 0.8600 b PerimI m               3.3809 B Ph(p)   deg
                 0.1050 c Length m           2.9632E-03 C |U|     m^3/s
             1.8500E-03 d AreaF  m^2             88.646 D Ph(U)   deg
                 0.1920 e PerimF m              0.20137 E Htot    W
Master-Slave Links                           1.0516E-02 F Edot    W
Optional Parameters
ideal        Solid type
    4 DUCT       Hot End Standoff Duct - Measurement point
    Same   3d 1.8500E-03 a Area  m^2             294.84 A |p|     Pa
                 0.1920 b Perim  m              -0.4634 B Ph(p)   deg
                 0.1450 c Length m           2.6631E-03 C |U|     m^3/s
Master-Slave Links                               88.480 D Ph(U)   deg
Optional Parameters                             0.20137 E Htot    W
ideal        Solid type                      7.2374E-03 F Edot    W
    5 RPN        Velocity at 0.25m from speaker [m/s]
                 0.0000 a G or T                 1.4395  A ChngeMe
4C 4a /
    6 DUCT       Hot End Standoff Duct
    Same   3d 1.8500E-03 a Area  m^2             648.94 A |p|     Pa
                 0.1920 b Perim  m              -1.4285 B Ph(p)   deg
                 0.4700 c Length m           3.3175E-07 C |U|     m^3/s
Master-Slave Links                              -1.4285 D Ph(U)   deg
Optional Parameters                             0.20137 E Htot    W
ideal        Solid type                      1.0764E-04 F Edot    W
    7 SURFACE    End Plate
    Same   3d 1.8500E-03 a Area  m^2             648.94 A |p|     Pa
                                                -1.4285 B Ph(p)   deg
                                             1.6898E-17 C |U|     m^3/s
                                                -103.93 D Ph(U)   deg
                                                0.20137 E Htot    W
ideal        Solid type                     -1.1869E-15 F Edot    W
    8 HARDEND    Rigid termination- Volt PK PK meas by endevco was 2.4V
Targ             0.0000 a R(1/z)                 648.94 A |p|     Pa
Targ             0.0000 b I(1/z)                -1.4285 B Ph(p)   deg
                                             1.6898E-17 C |U|     m^3/s
                                                -103.93 D Ph(U)   deg
Possible targets                                0.20137 E Htot    W
                                            -1.1869E-15 F Edot    W
                                            -1.2204E-15 G R(1/z)
                                            -5.5042E-15 H I(1/z)
```

Figure 5.11 DeltaEC model for the thermoacoustic refrigerator with no-stack at 2.5 V_{rms} to speaker and 129 Hz frequency.

5.1.2.1. Resonance frequency

The numerical resonance frequency of the fundamental mode was found to be 129.12 Hz.

5.1.2.2. Dynamic end pressure

The dynamic end pressure value was found to be 648.94 Pa

5.1.2.3. Spatial dynamic pressure

The numerically calculated spatial dynamic pressure plot is shown below in Figure 5.12.

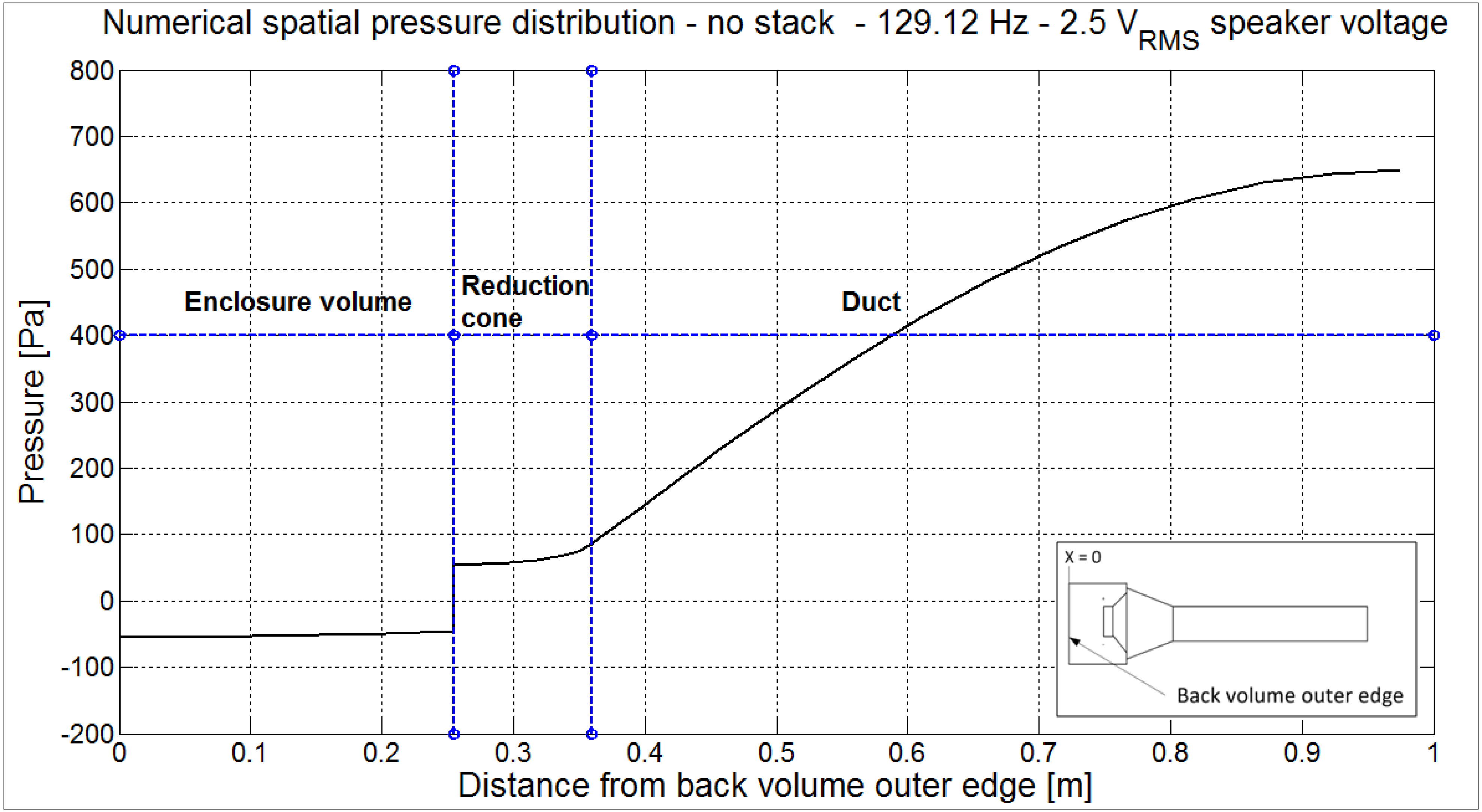

Figure 5.12 The numerically calculated spatial dynamic pressure plot without a stack.

5.1.2.4. Spatial velocity

The numerical spatial velocity plot is shown below in Figure 5.13

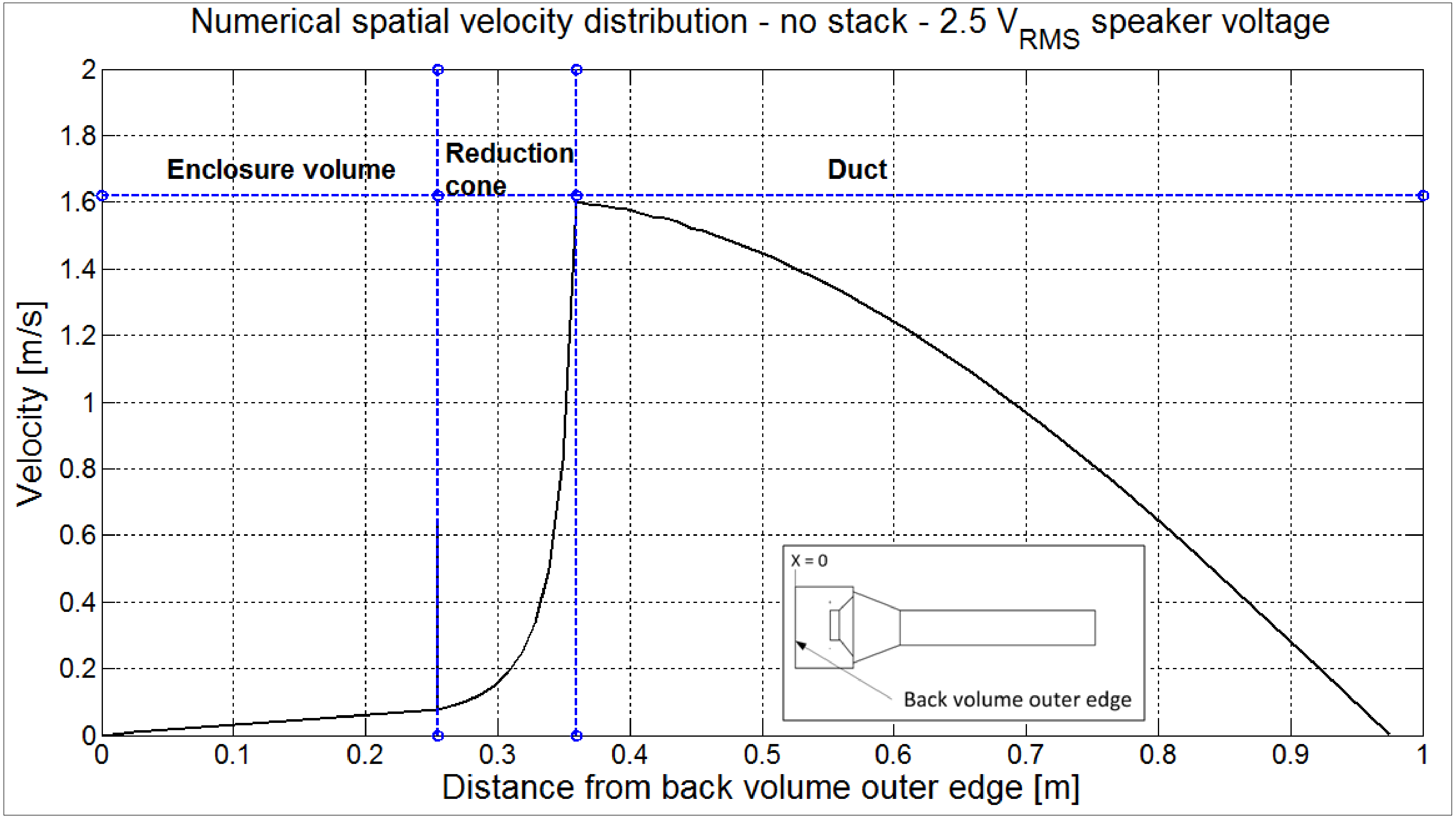

Figure 5.13 The numerical spatial velocity plot without a stack.

5.1.3. Comparison of experimental and numerical results

Table 5.3 shows a comparison between experimental and numerical results of the acoustical performance of the thermoacoustic refrigerator with no stack.

Table 5.3 A comparison between the experimental and numerical values measured and computed to validate the acoustic behavior of the thermoacoustic refrigerator without a stack. The parameters compared are resonance frequency, dynamic end pressure, spatial dynamic pressure distribution and spatial velocity distribution.

“No stack”	**Experimental results**	**Numerical results**
Resonance frequency [Hz]	129 ± 3	129.12
Dynamic end pressure [Pa]	579.86 ± 26	648.94
Velocity at 0.515 m from edge of back volume [m/s]	1.48 ± 0.025	1.4839

Experimental spatial dynamic pressure distribution

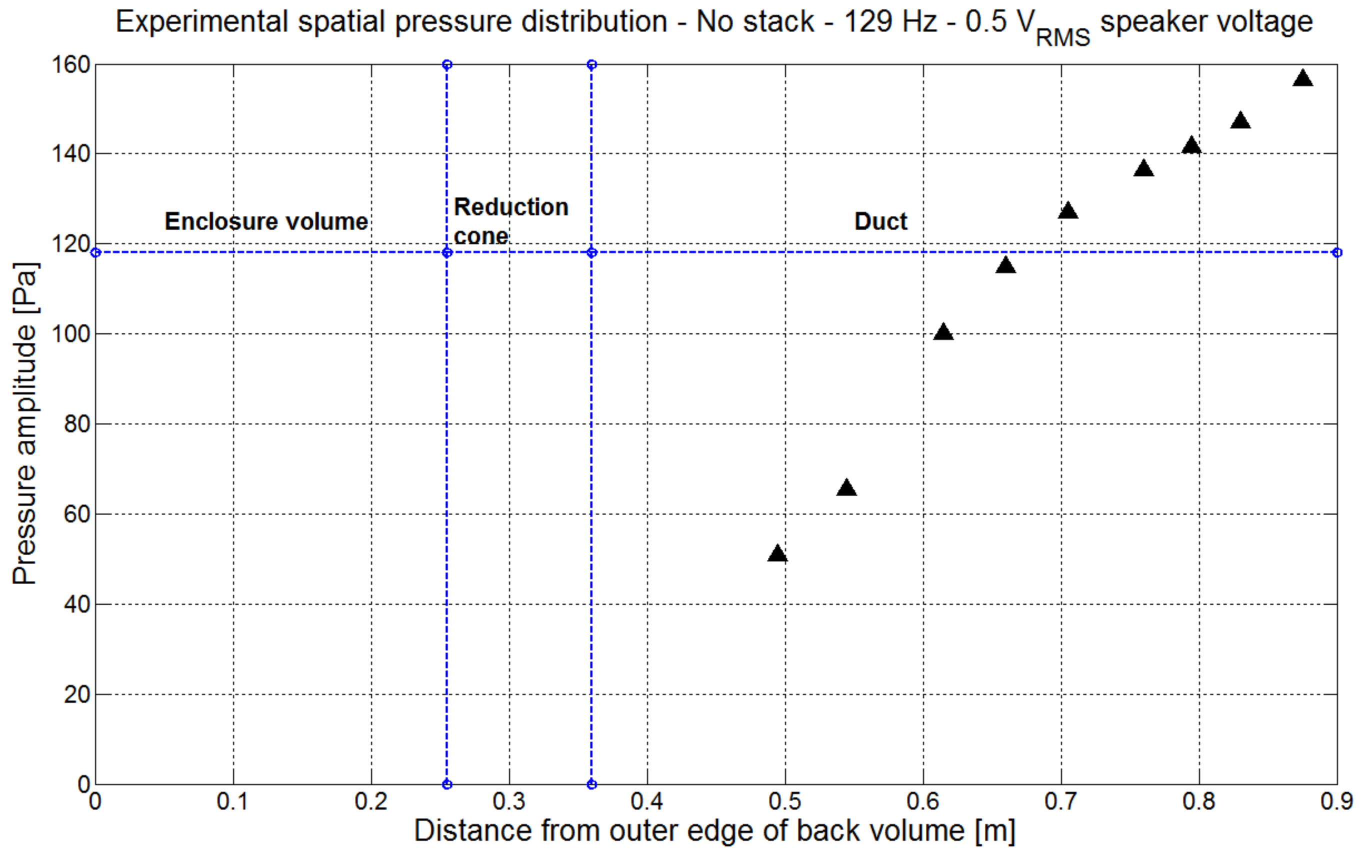

Table 5.3 (Continued)

Numerically calculated spatial dynamic pressure distribution
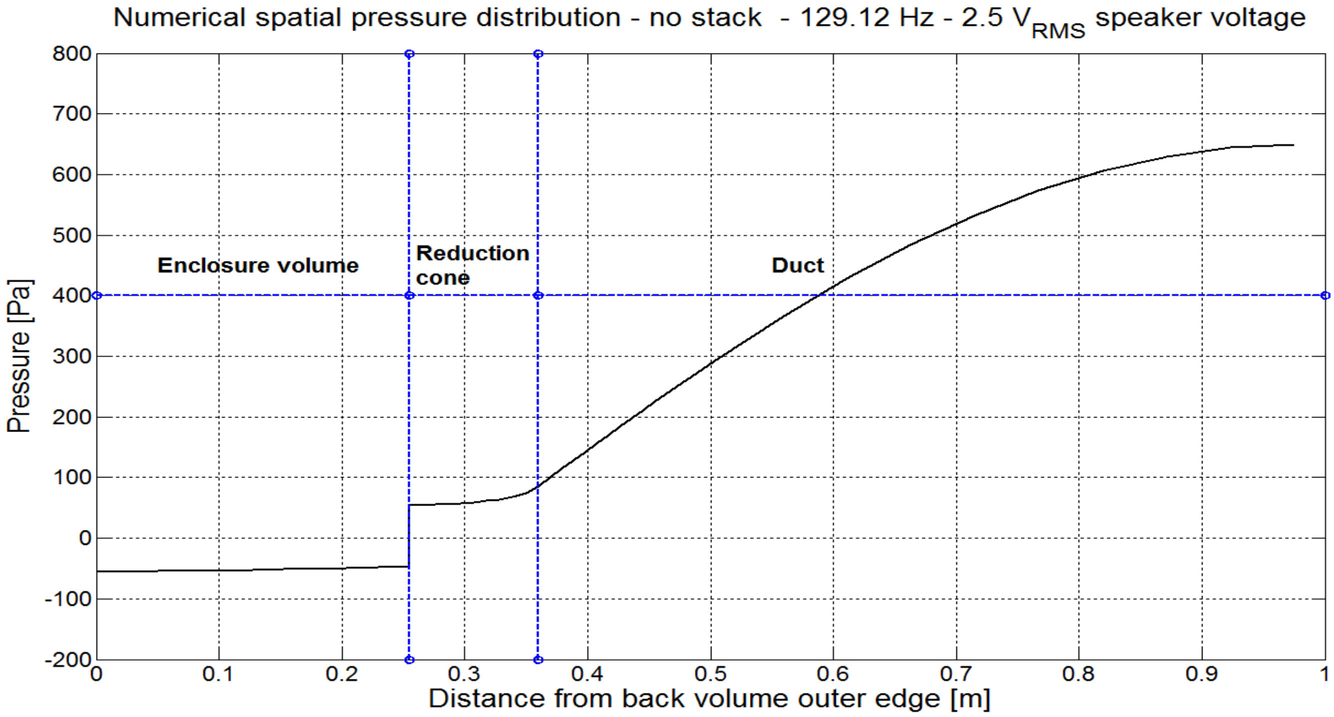
Experimental and numerical spatial velocity distribution
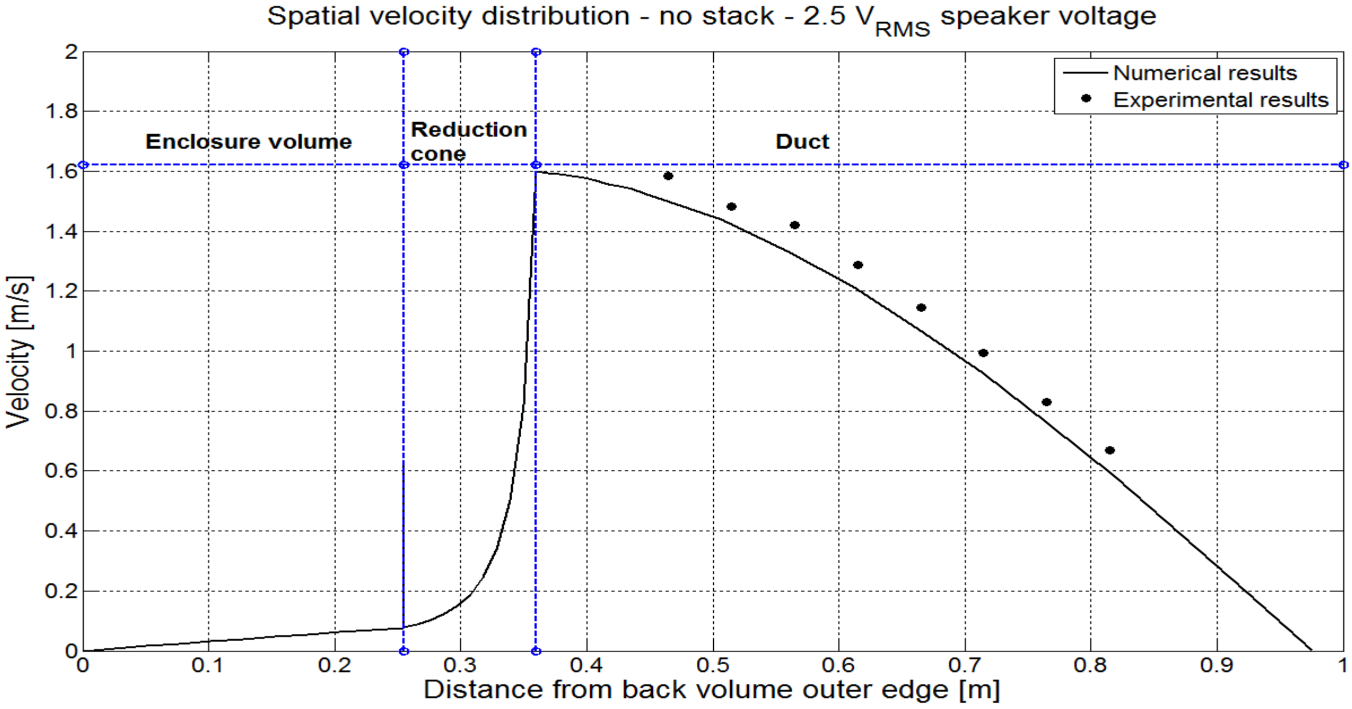

As shown through the results and the comparison table the experimental results are in good agreement with the numerical ones for all measured parameters. The fact that the thermoacoustic refrigerator is a standing wave refrigerator designated as a quarter wave system has been proven both by experiment and numerical modeling. The resonance frequency was found to be around 129 Hz, the dynamic end pressure averages around 615 Pa and the spatial dynamic pressure and velocity distributions were determined to characterize the thermoacoustic system as a whole from the acoustics' point of view. Figure 5.14 shows the numerical frequency response of the thermoacoustic refrigerator with no stack showing peaks at the mechanical resonance of the loudspeaker and at the fundamental and first harmonic frequency of the acoustic system. Table 5.4 shows a comparison between these numerical results and their corresponding experimental results confirming the good agreement between the numerical estimation and the experimental results of the acoustic behavior of the thermoacoustic refrigerator at no load.

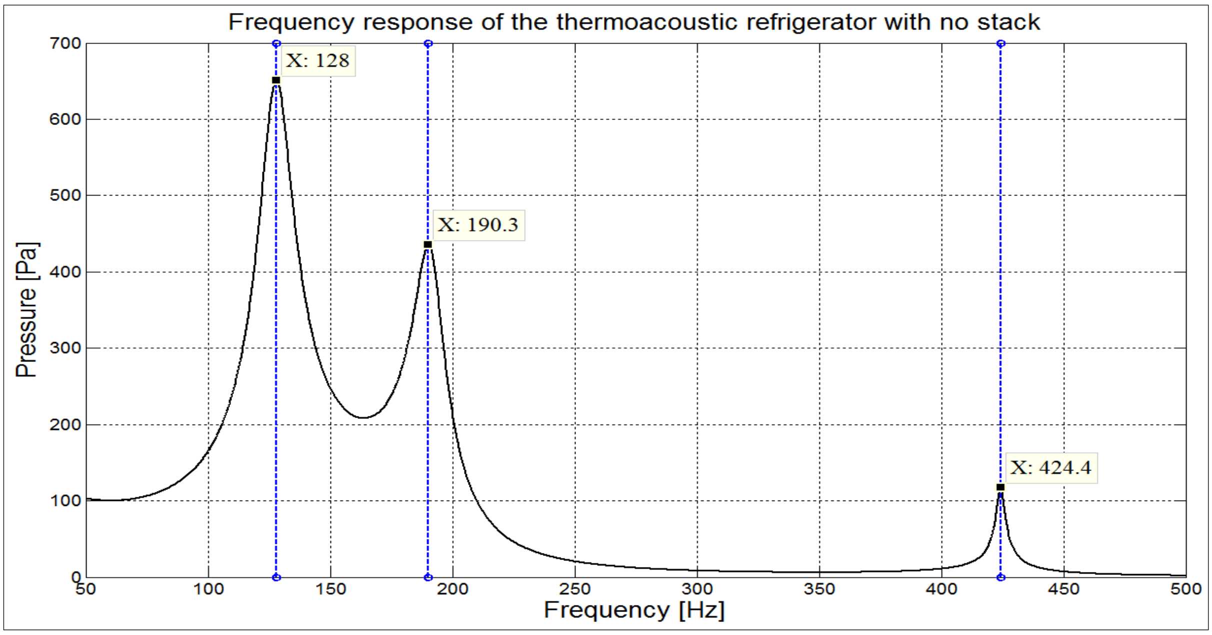

Figure 5.14 The numerical frequency response of the thermoacoustic refrigerator with no stack.

Table 5.4 Comparison of the estimated numerical and experimental values of resonance frequencies for the thermoacoustic refrigerator with no stack.

	Measured [Hz]	**Estimated [Hz]**
Mechanical resonance frequency of the speaker in the free field (Measured using microphone)	99	
Mechanical resonance frequency of the speaker in the free field (Measured using the free decay curve)	96.2	
Mechanical resonance frequency of the speaker in the free field (Calculated using the measured values of lumped mass and lumped stiffness)	97.5	
Mechanical resonance frequency of the speaker in the acoustic system	191	190.3
Fundamental acoustic frequency	129	128
First acoustic harmonic frequency	409	424.4

5.2. The study of the effect of changing stack configurations on dynamic pressure and velocity

The acoustic behavior of the thermoacoustic refrigerator was also studied after inserting stacks with different configurations into the resonator. The previous study performed with no stack was only to validate the numerical model against the experimental setup, but the presence of stacks as part of a thermoacoustic device is a necessity when looking into thermoacoustic effects. The main aim of this part of the study was to evaluate the effects that different stack porosities and lengths have on dynamic pressure and velocity.

The location of stacks' was determined using the validated numerical model of the thermoacoustic refrigerator with no-stack. An optimized location of the stack is where the product of the two principal acoustic variables – dynamic pressure and particle velocity – is maximum, in other words where the total acoustic power is maximum. Figure 5.15 shows the acoustic power plot as exported from DeltaEC. The zone of maximum acoustic power was located near the loudspeaker's end. Thus, all stacks with their different configurations were placed next to the loudspeaker.

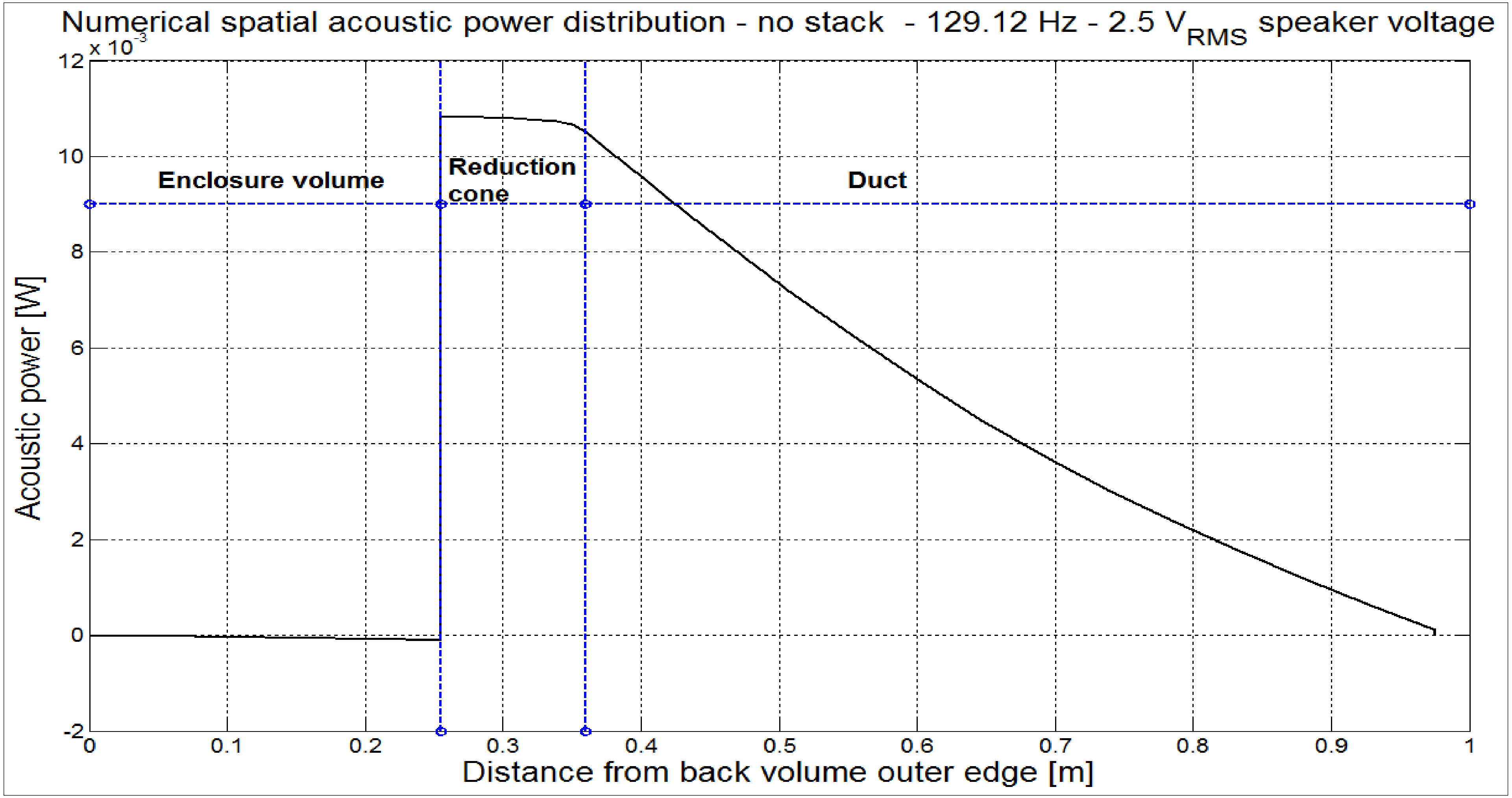

Figure 5.15 The acoustic power plot of the thermoacoustic refrigerator with no stack as exported from DeltaEC showing maximum value at the loudspeaker's end.

Figure 5.16 shows a schematic of the thermoacoustic refrigerator showing the location of stacks' placement. As the prototype structure implies the stacks could not be placed directly after the speaker due to the presence of the reducing pyramid-shaped cone, thus the stacks were placed at the closest point to the speaker after the cone which was the beginning of the quartz tube. The stacks used are meshed ceramic stacks with square channels and different porosities (100,200,400 and 600 cells per square inch) and lengths.

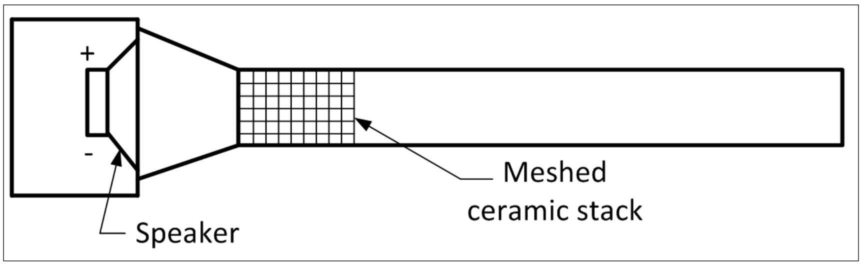

Figure 5.16 A schematic of the thermoacoustic refrigerator showing the stack location as close as possible to the speaker where the zone of maximum acoustic power exists.

Five different configurations of meshed ceramic stacks were used. Ceramics having high thermal capacity were chosen to allow for the gas temperature to fluctuate but not the stack temperature and low thermal conductivity to reduce the thermal conduction along the stack, thus being preferred in thermoacoustics as stack materials. A meshed stack is defined by the porosity, stack length and stack location. Figure 5.17 shows all four stack porosities (100 CPSI, 200 CPSI, 400 CPSI and 600 CPSI). Black plasticine (clay) was used to fix the stack to the aluminum sheet and to block the air gaps between the stack and the walls of the quartz resonator to prevent flow leakage. The image was taken after a measurement run was completed and the aluminum sheet was pulled out of the resonator. Table 5.5 shows the details of the five configurations of stacks used in the measurements. Some values in Table 5.5 are calculated to be used directly in numerical modeling with the DeltaEC software such as half the pore width, half the pore breadth and half the plate thickness.

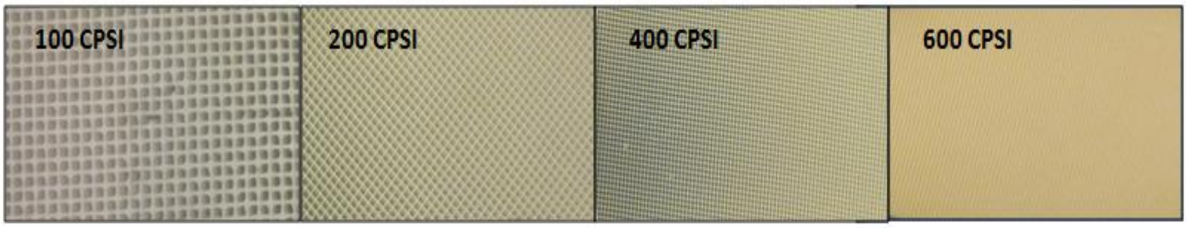

Figure 5.17 (From left to right) Real time pictures of ceramic stacks with different porosities 100 CPSI, 200 CPSI, 400 CPSI and 600 CPSI.

Table 5.5 Details of different meshed stack configurations used in studying the acoustic behavior of the thermoacoustic refrigerator.

	DeltaEC symbol	**100 CPSI**	**200 CPSI**	**400 CPSI**	**600 CPSI**	**600 CPSI Half length**
Run#		4A	4B	4C	4D	4E
Ceramic type		Celcor	Celcor	Celcor	Celcor	Celcor
Supplier		Chinese	Corning	Corning	Corning	Corning
Pore width/breadth [m]		0.001975	0.001542	0.001118	0.000961	0.000961
Half of pore width/breadth [m]	aa/bb	0.0009875	0.000771	0.000559	0.0004805	0.0004805
Plate thickness [m]		0.00055	0.000254	0.000152	0.000076	0.000076
Half of plate thickness [m]	L_{plate}	0.000275	0.000127	0.000076	0.000038	0.000038
Porosity (Gas area/Total area)	Gas A/A	0.611	0.737	0.774	0.858	0.858
Length [m]	Length	0.045	0.045	0.045	0.045	0.0225
Location of stack [m] Measured from edge of the stack to the outer edge of the back volume (Figure 5.18)		0.45	0.45	0.45	0.45	0.438

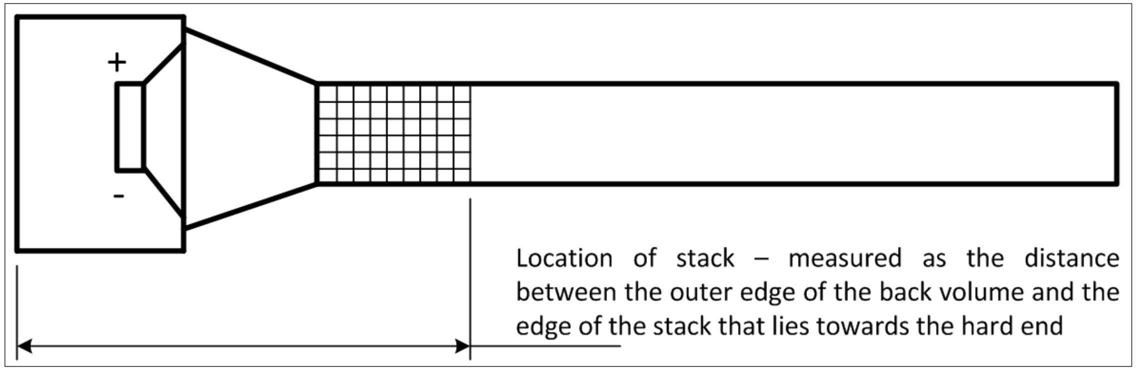

Location of stack – measured as the distance between the outer edge of the back volume and the edge of the stack that lies towards the hard end

Figure 5.18 Illustration of how the stack location was defined measuring the distance from outer edge of the back volume to the end of the stack's length.

5.2.1. Numerical and experimental results

For each stack configuration a DeltaEC model was developed and all experimental measurements performed in (Section 4) were also repeated for each configuration. Detailed DeltaEC models for each case are shown in (Appendix D) while comparison tables are furnished below to show the final experimental and numerical results.

Table 5.6 shows a comparison between the experimental and numerical results of Run# 4A.

Table 5.6 Comparison of experimental and numerical results of Run# 4A.

"100 CPSI - 0.045 m length"	**Experimental results**	**Numerical results**
Resonance frequency [Hz]	119 ± 3	125.41
Dynamic end pressure [Pa]	522.909 ± 26	555.47
Velocity at 0.515 m from edge of back volume [m/s]	1.21 ± 0.025	1.2103
Experimental spatial dynamic pressure distribution		
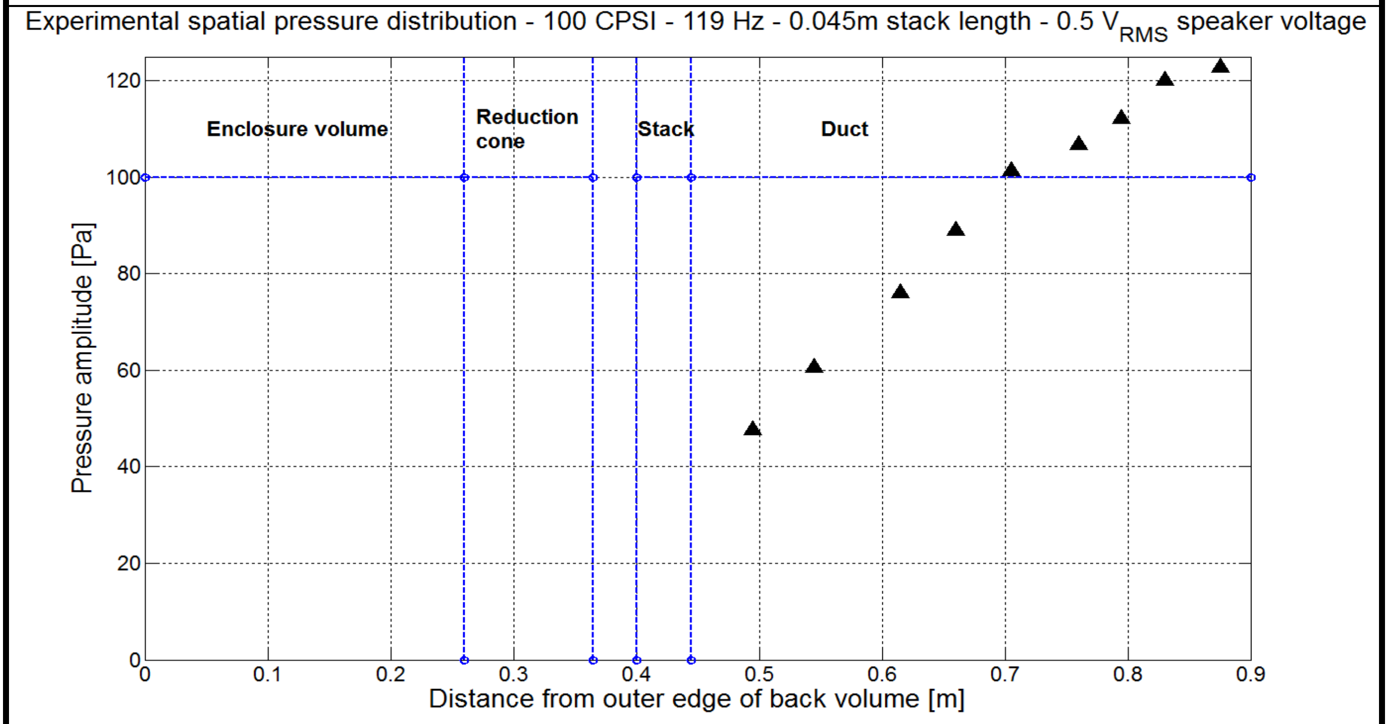		

Table 5.6 (Continued)

Numerically calculated spatial dynamic pressure distribution
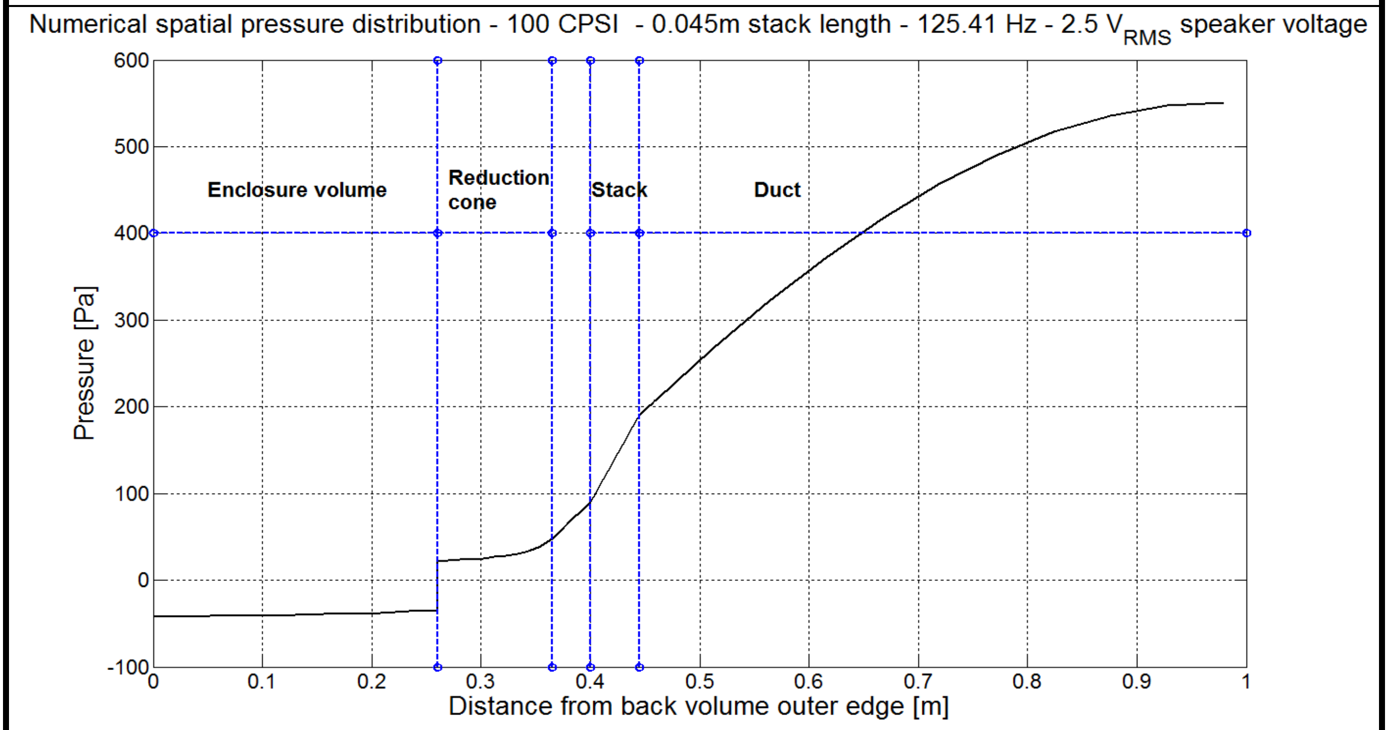
Experimental and numerical spatial velocity distribution
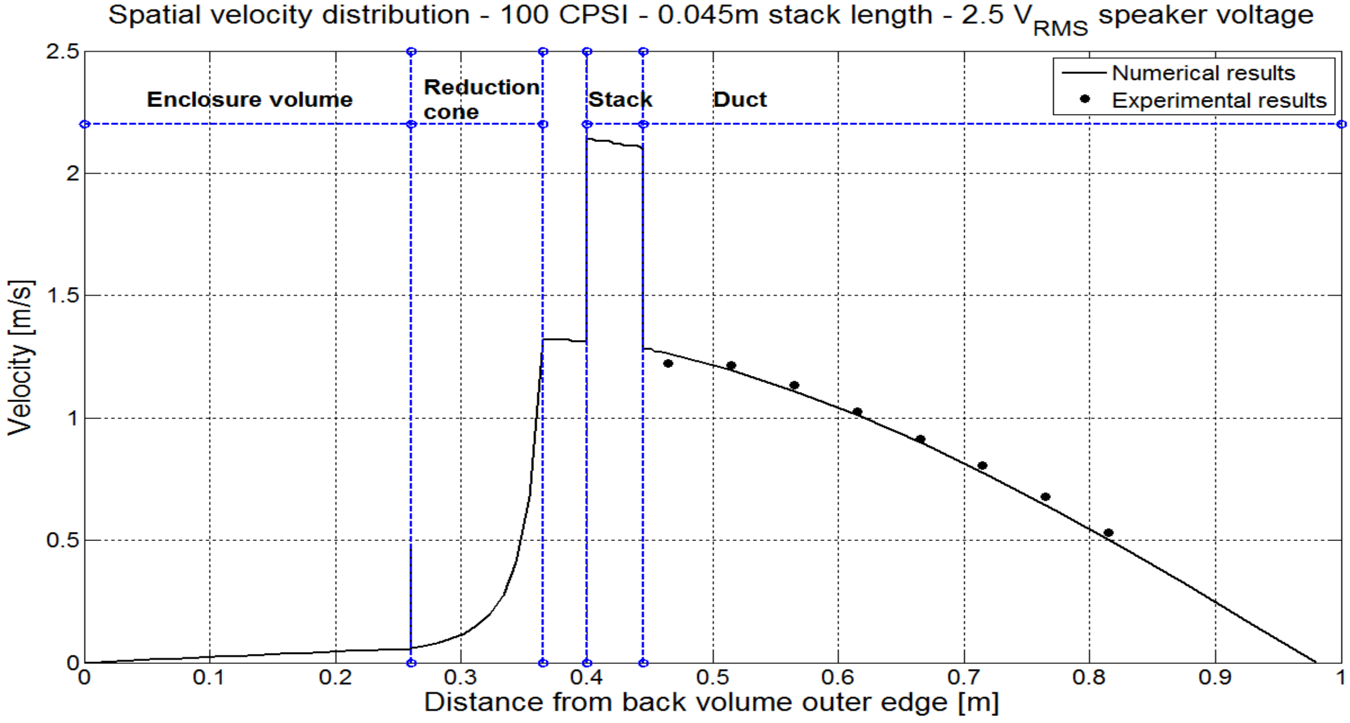

Table 5.7 shows a comparison between the experimental and numerical results of Run# 4B.

Table 5.7 Comparison of experimental and numerical results of Run# 4B.

"200 CPSI - 0.045 m length"	**Experimental results**	**Numerical results**
Resonance frequency [Hz]	119±3	126.65
Dynamic end pressure [Pa]	497.02 ± 26	523.11
Velocity at 0.515 m from edge of back volume [m/s]	1.16 ± 0.025	1.1461

Experimental spatial dynamic pressure distribution

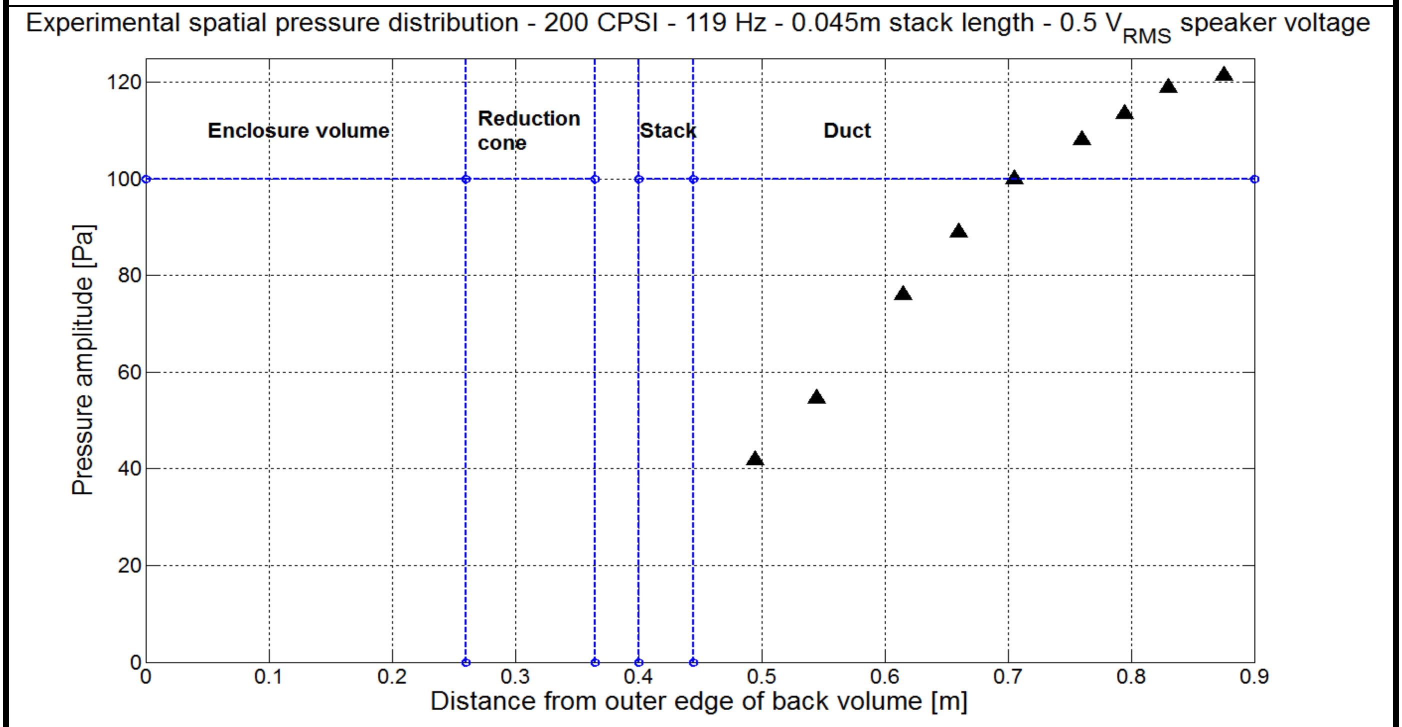

Numerically calculated spatial dynamic pressure distribution

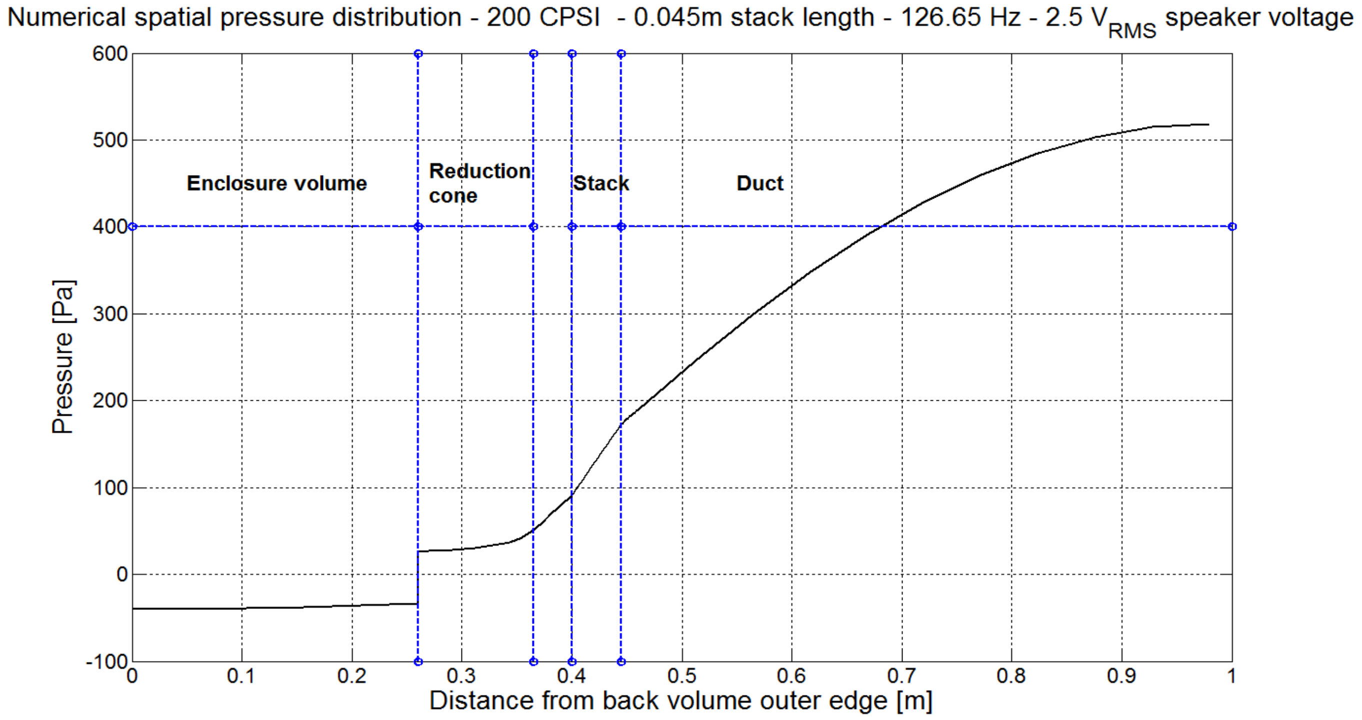

Table 5.7 (Continued)

Experimental and numerical spatial velocity distribution

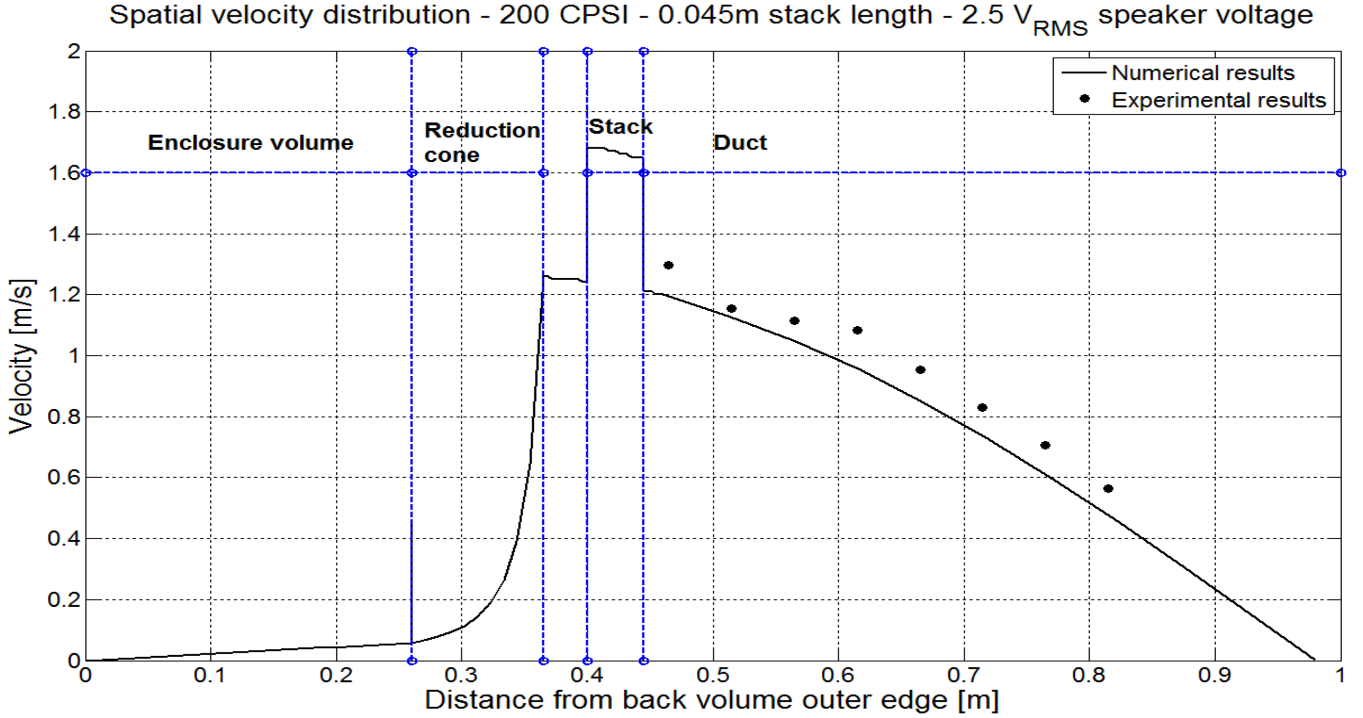

Table 5.8 shows a comparison between the experimental and numerical results of Run# 4C.

Table 5.8 Comparison of experimental and numerical results of Run# 4C.

“400 CPSI - 0.045 m length”	**Experimental results**	**Numerical results**
Resonance frequency [Hz]	120 ± 3	127.05
Dynamic end pressure [Pa]	481.49 ± 26	460.1
Velocity at 0.515 m from edge of back volume [m/s]	1.15 ± 0.025	1.0646
Experimental spatial dynamic pressure distribution		
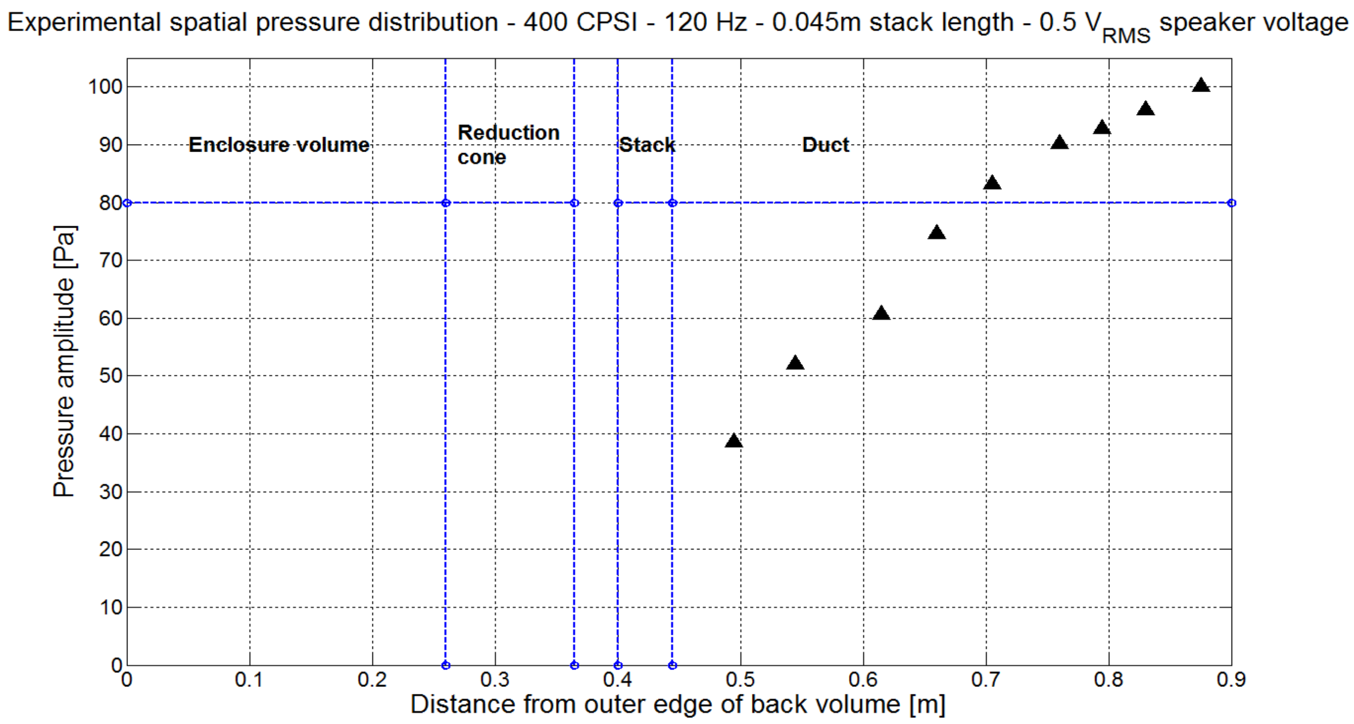		
Numerically calculated spatial dynamic pressure distribution		
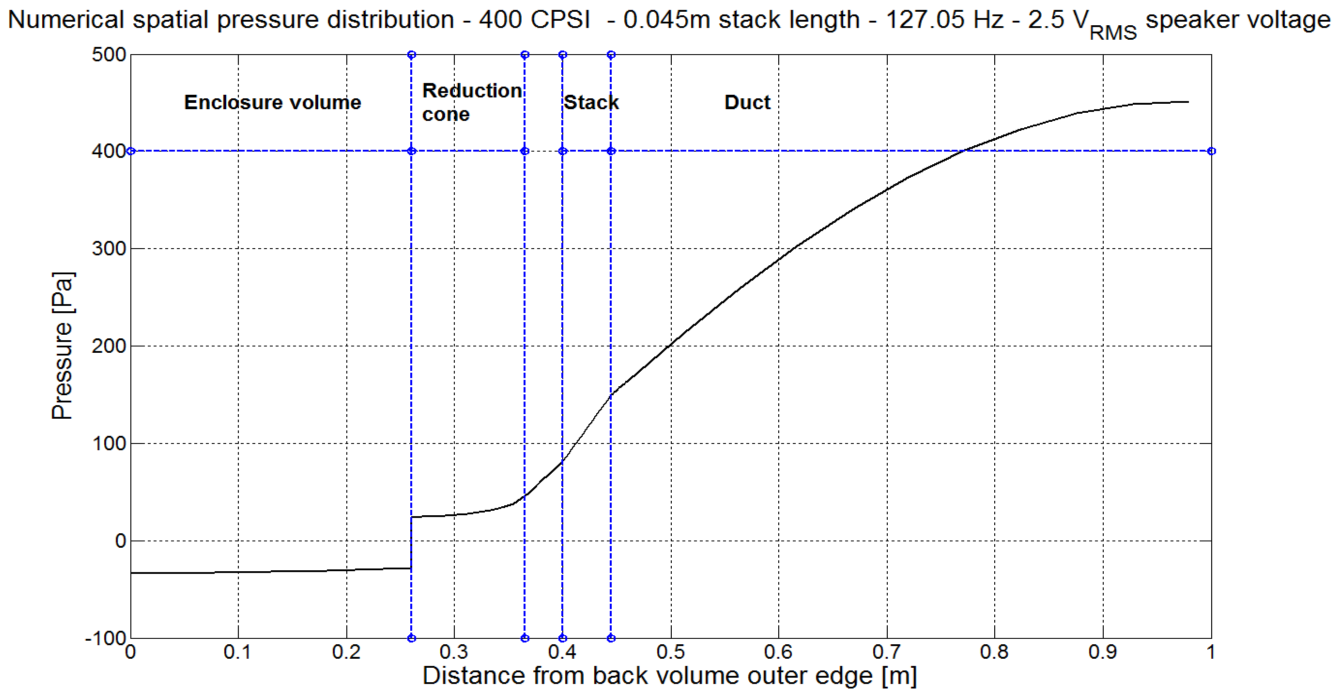		

Table 5.8 (Continued)

Experimental and numerical spatial velocity distribution
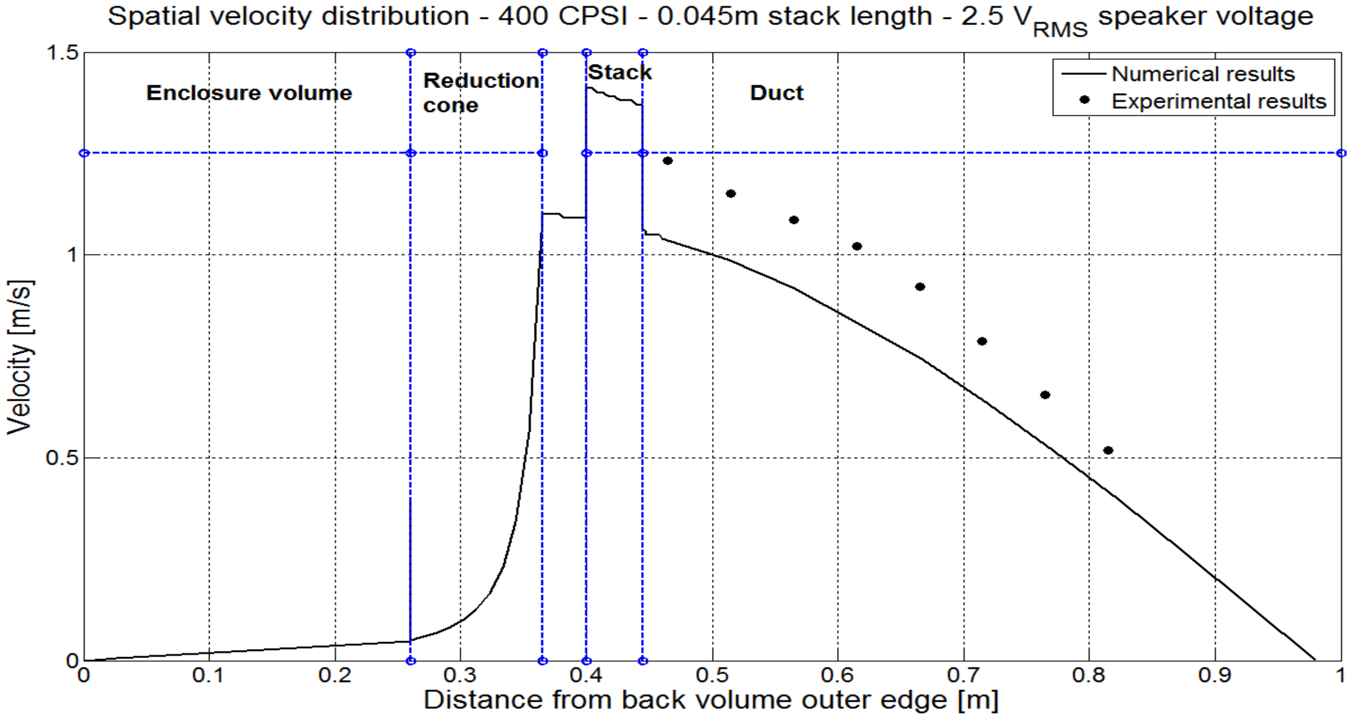

Table 5.9 shows a comparison between the experimental and numerical results Run# 4D.

Table 5.9 Comparison of experimental and numerical results of Run# 4D.

<table>
<tr><th>“600 CPSI - 0.045 m length”</th><th>Experimental results</th><th>Numerical results</th></tr>
<tr><td>Resonance frequency [Hz]</td><td>120 ± 3</td><td>128.18</td></tr>
<tr><td>Dynamic end pressure [Pa]</td><td>434.895 ± 26</td><td>432.46</td></tr>
<tr><td>Velocity at 0.515 m from edge of back volume [m/s]</td><td>1.03 ± 0.025</td><td>1.0058</td></tr>
<tr><td colspan="3"></td></tr>
<tr><td colspan="3">Experimental spatial dynamic pressure distribution</td></tr>
<tr><td colspan="3">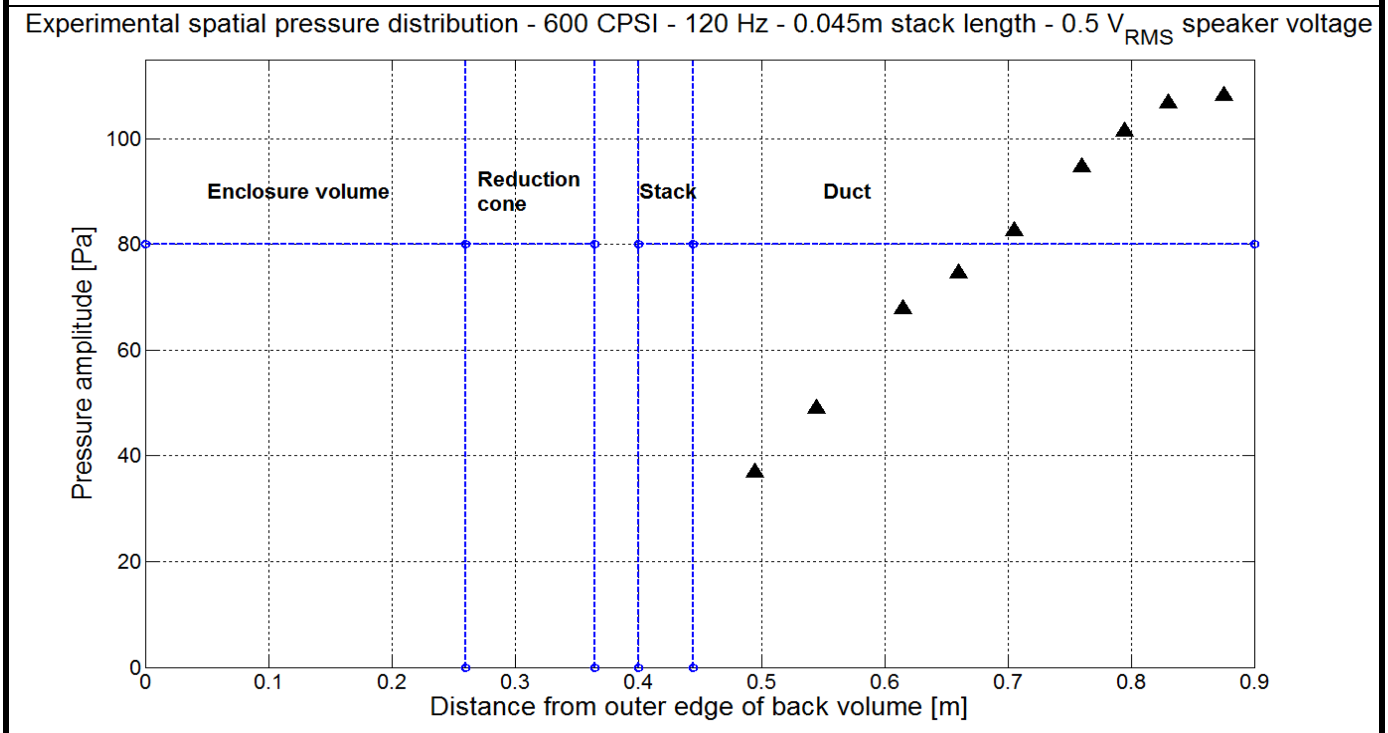
</td></tr>
<tr><td colspan="3">Numerically calculated spatial dynamic pressure distribution</td></tr>
<tr><td colspan="3">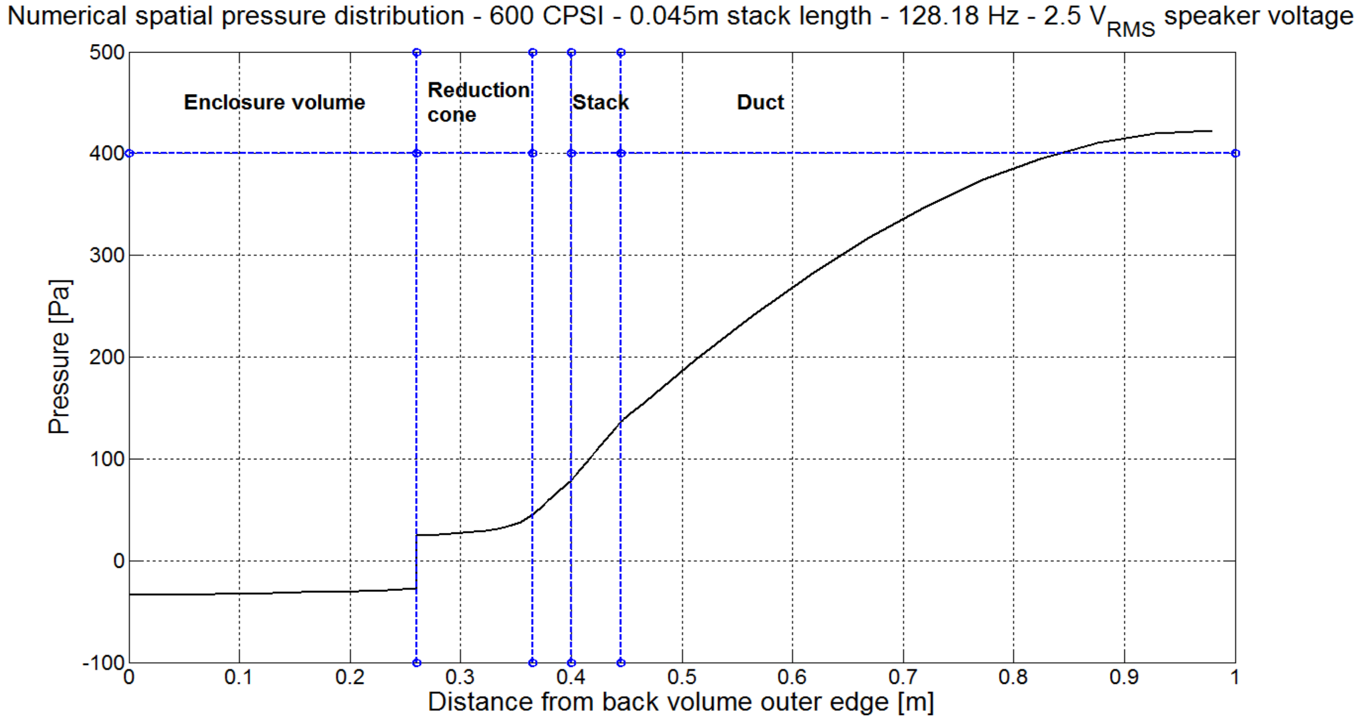
</td></tr>
</table>

Table 5.9 (Continued)

Experimental and numerical spatial velocity distribution
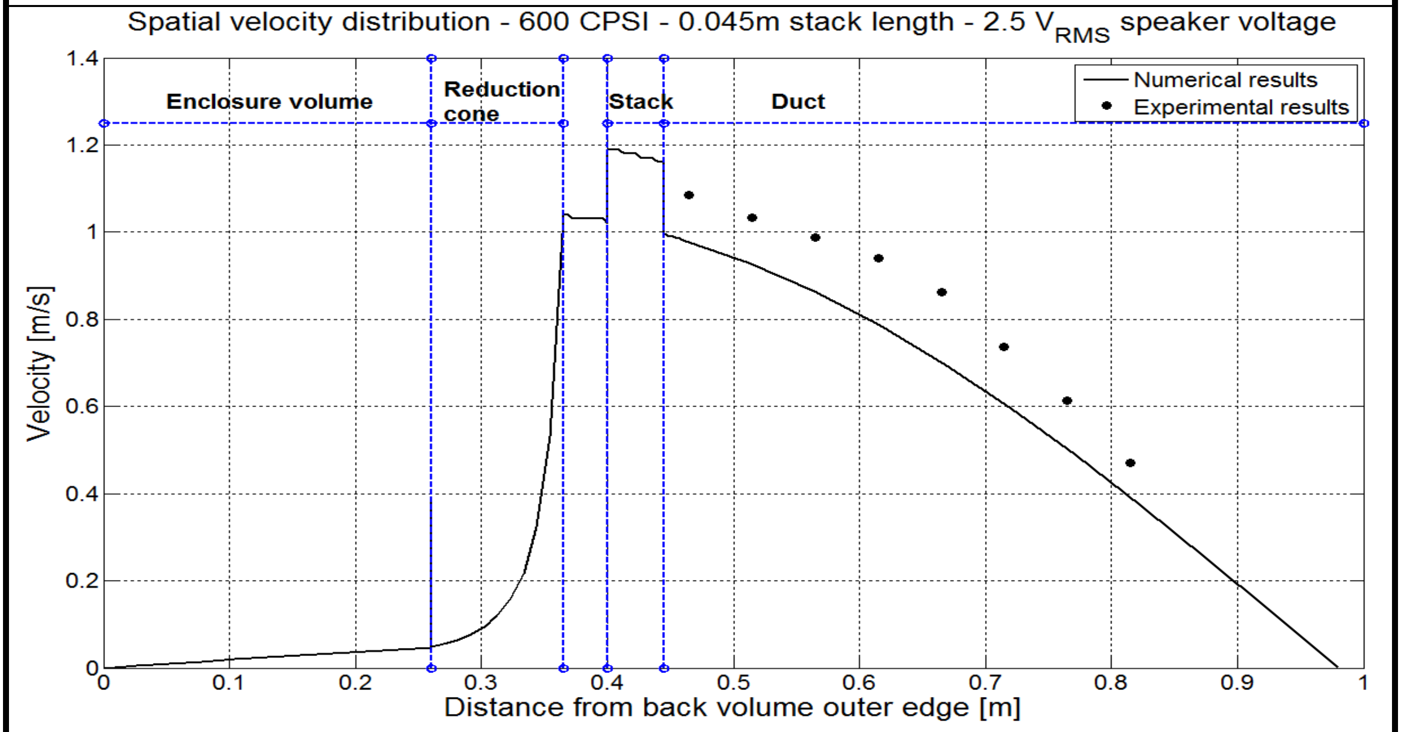

Table 5.10 shows a comparison between the experimental and numerical results of Run# 4E.

Table 5.10 Comparison of experimental and numerical results of Run# 4E.

"600 CPSI - 0.0225 m length"	**Experimental results**	**Numerical results**
Resonance frequency [Hz]	124 ± 3	128.34
Dynamic end pressure [Pa]	525.5 ± 26	523.97
Velocity at 0.515 m from edge of back volume [m/s]	1.16 ± 0.025	1.2192

Experimental spatial dynamic pressure distribution

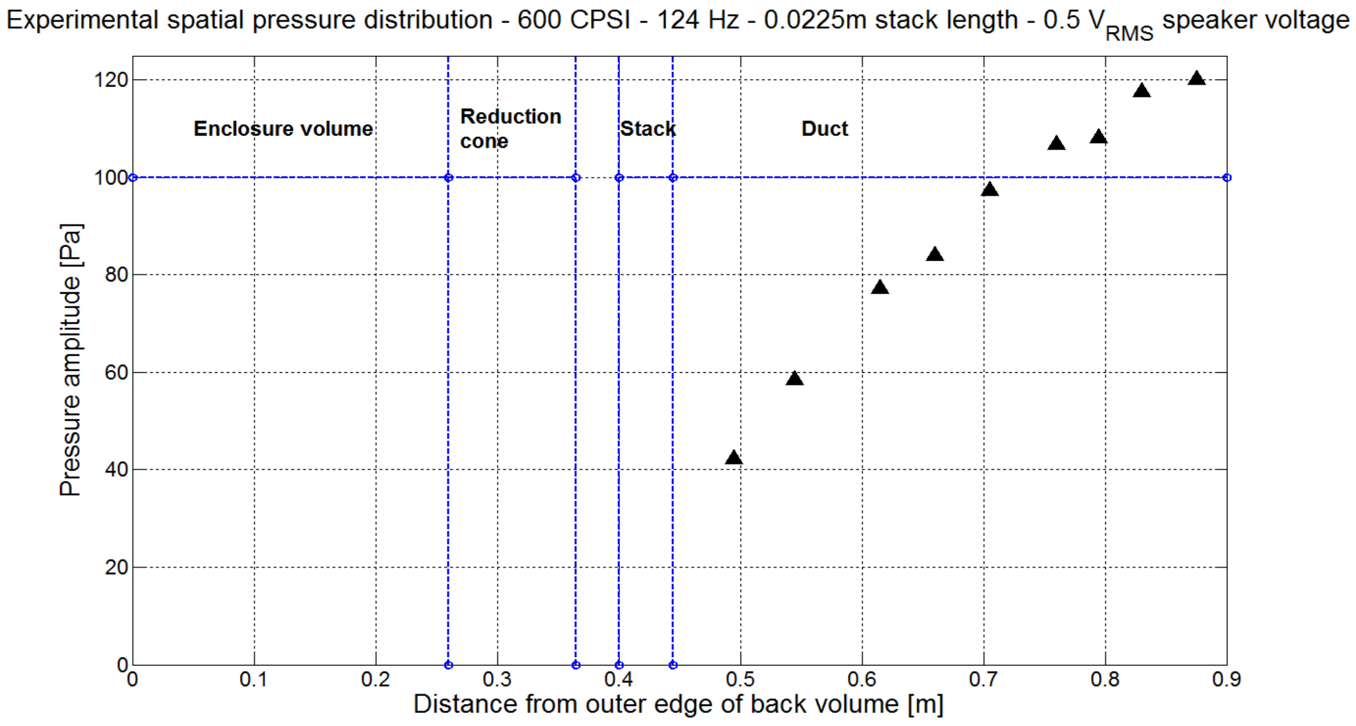

Numerically calculated spatial dynamic pressure distribution

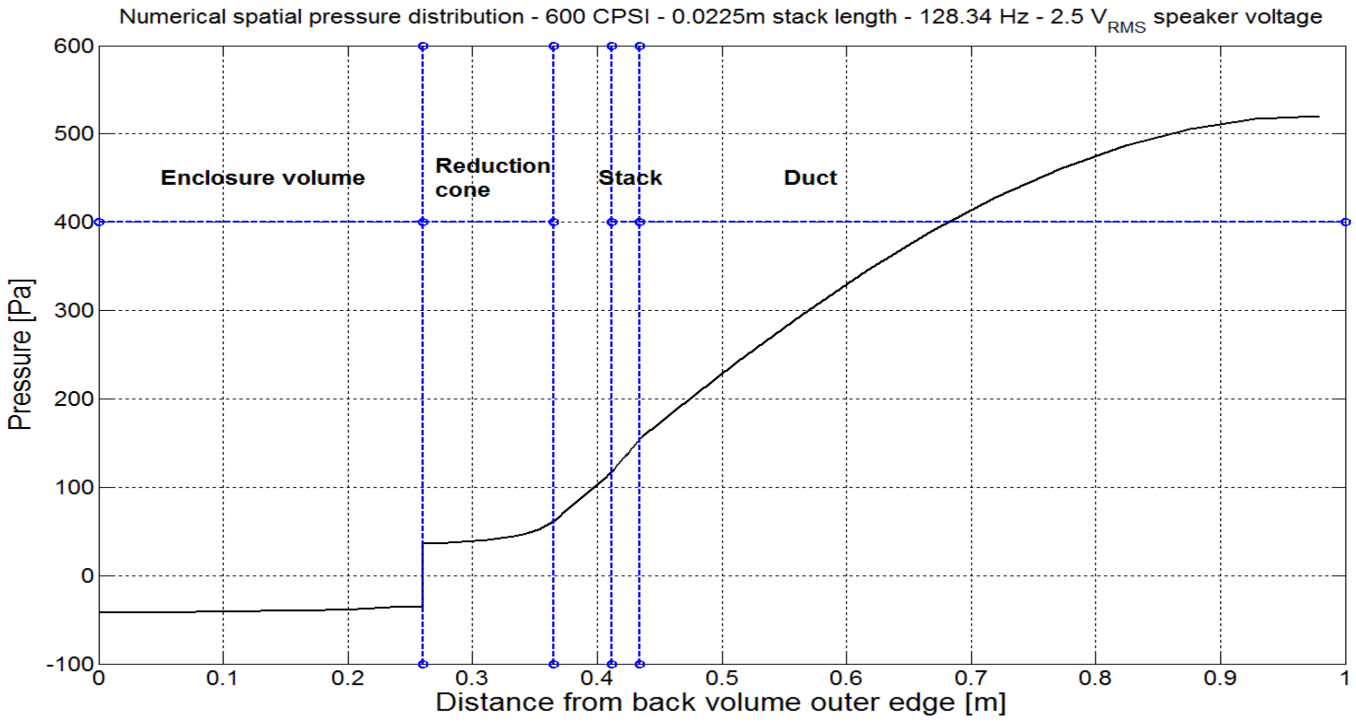

Table 5.10 (Continued)

Experimental and numerical spatial velocity distribution
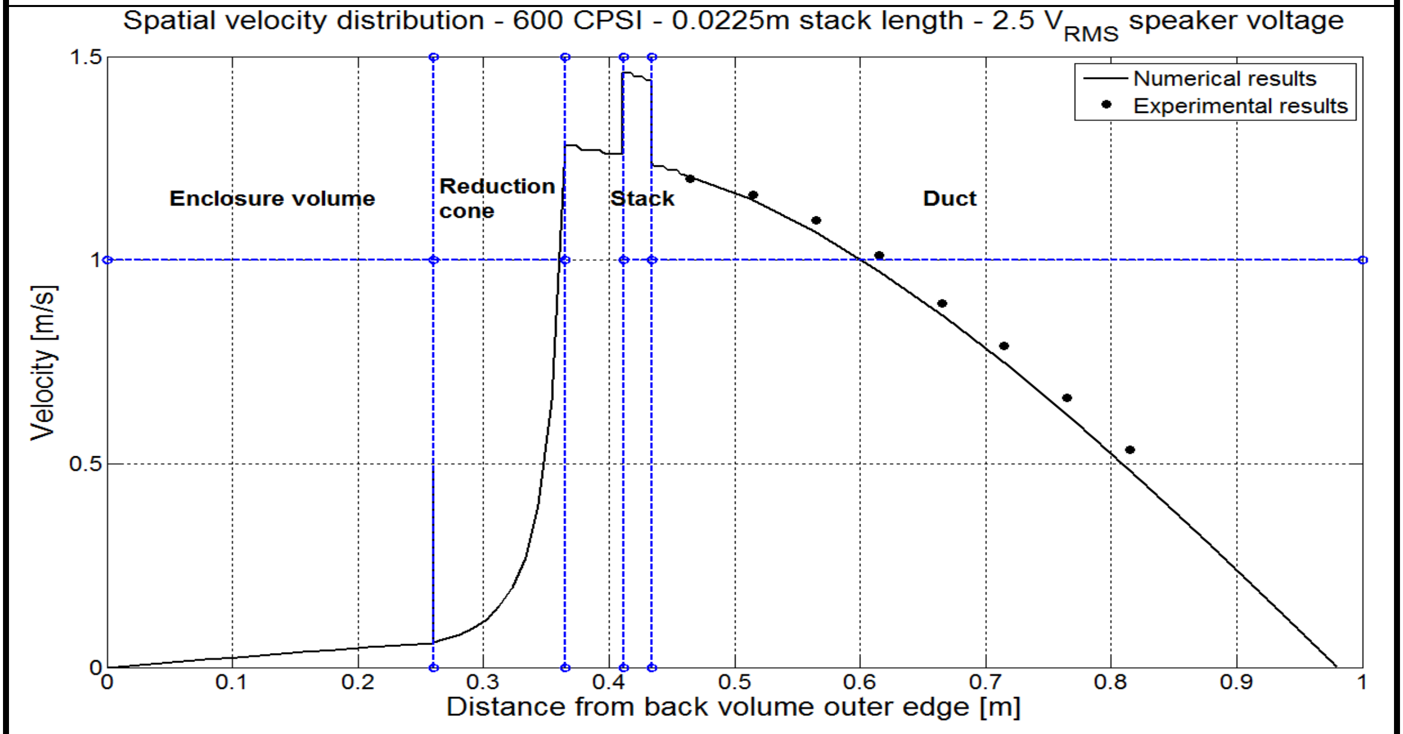

It is observed from the results of all cases introduced including the no-stack case that experimental results are in very good agreement with numerical ones. The values of frequency and end pressures are very close and the trends of spatial dynamic pressure and velocity are almost identical. Table 5.11 shows a list of measured frequencies for all configurations. Figure 5.19 shows a combined plot of the experimental spatial dynamic pressures of all stack configuration cases while Figure 5. shows the same plot but for spatial velocity.

Table 5.11 A list of experimental resonance frequencies of all runs.

Configuration	**Experimental resonance frequency [Hz]**
No stack	129 ± 3
100 CPSI	119 ± 3
200 CPSI	119 ± 3
400 CPSI	120 ± 3
600 CPSI	120 ± 3
600 CPSI – Half Length	124 ± 3

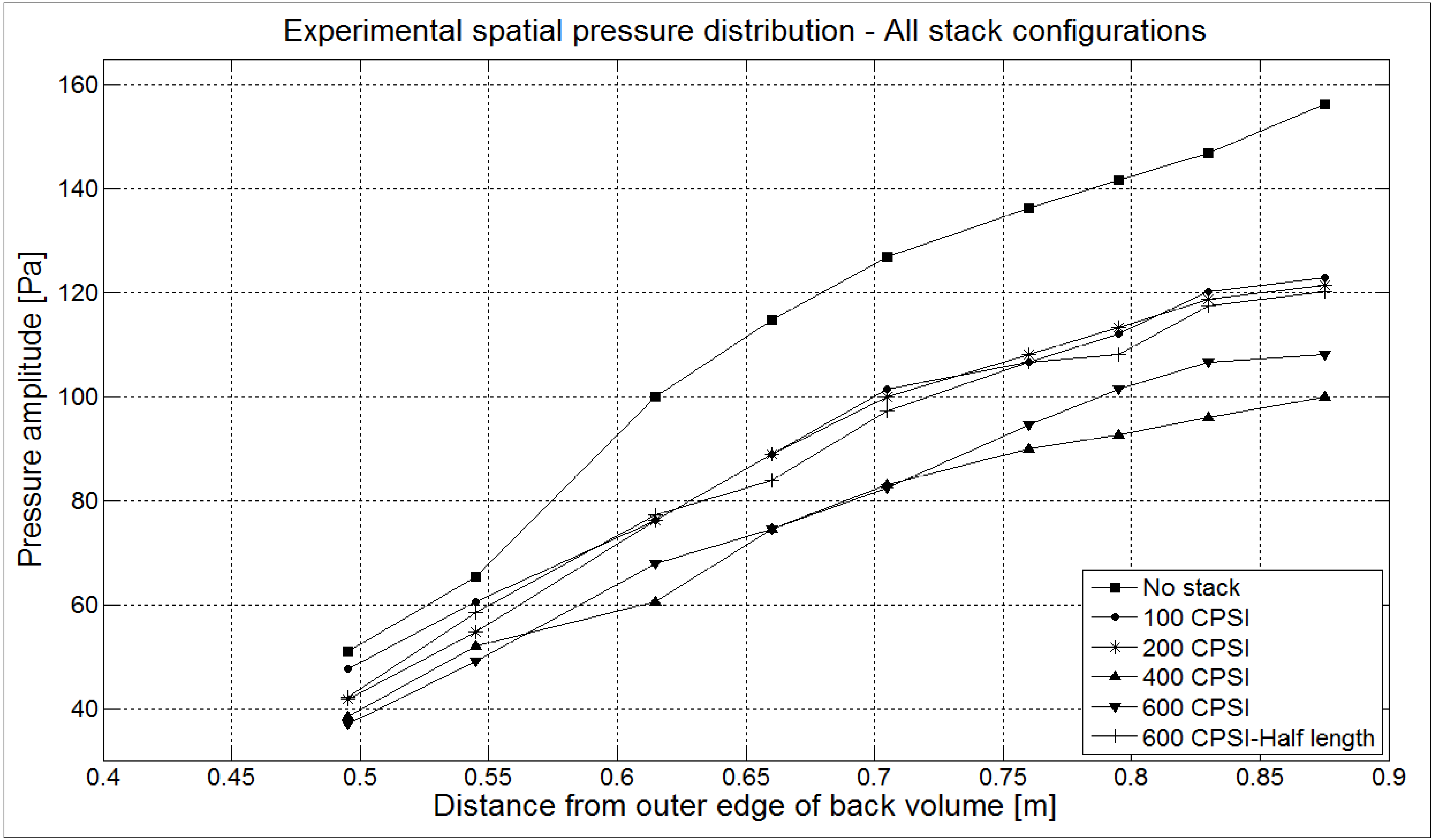

Figure 5.19 Combined plot of all experimental spatial dynamic pressure distributions.

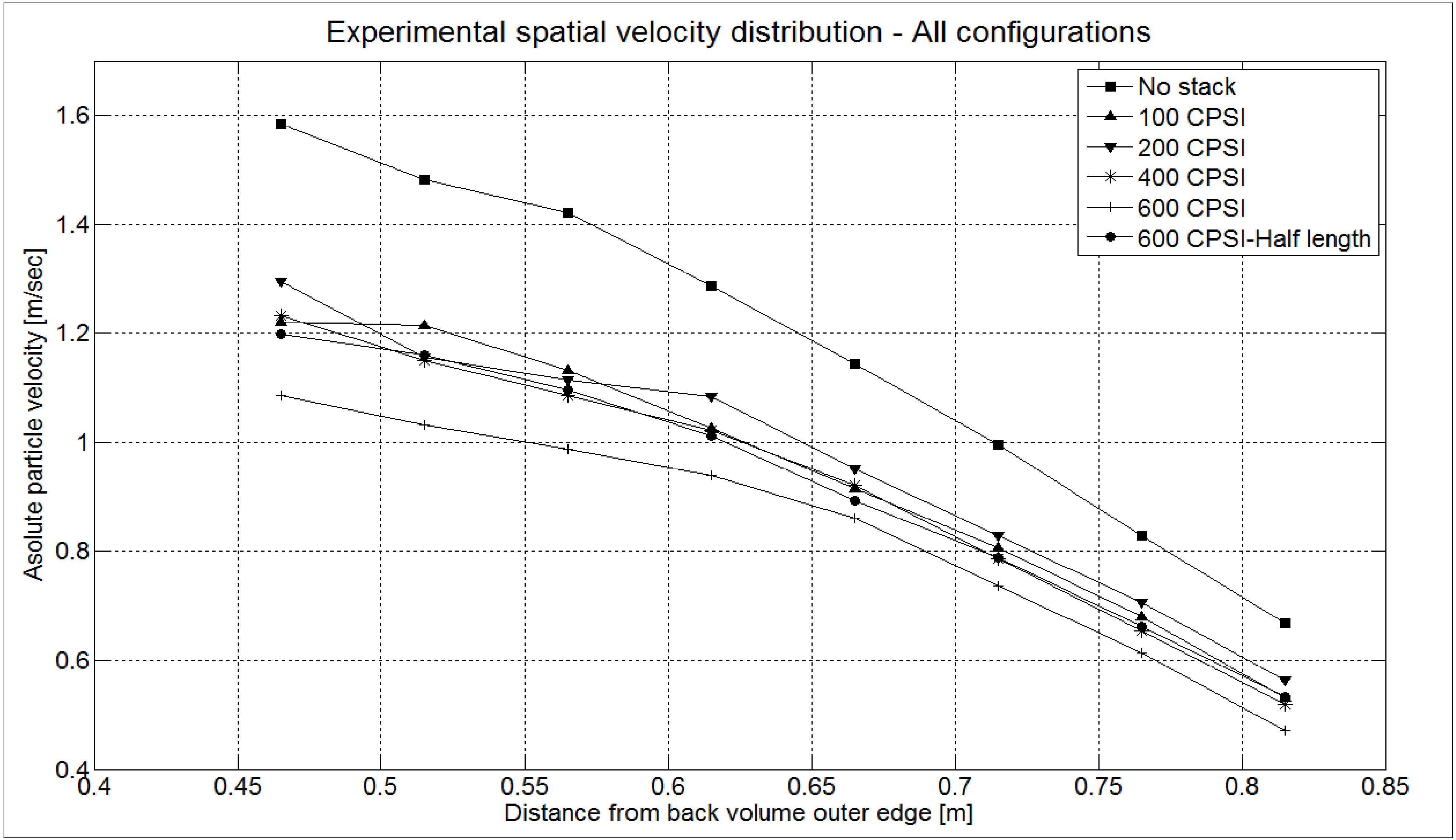

Figure 5.20 Combined plots of all experimental spatial velocity distributions.

Observing the results of frequency, spatial dynamic pressure and spatial velocity and comparing the results with different porosities of different configurations it was found that the insertion of the stacks components in general decreases both dynamic pressure and velocity values and accordingly acoustic power values along the length of the resonator while preserving the spatial trend obtained without the presence of stacks.

Additionally the numerical analysis showed that the behavior inside the stack channels is different from outside. As observed, the value of particle velocity increases greatly inside the stack channels breaking the trend of axial velocity yet replicating the trend but at higher amplitude. On the other hand, dynamic pressure was observed to take a linear trend inside the stack channels yet not breaking out from the axial dynamic pressure trend in a noticeable manner as velocity. This effect could be attributed to the sudden change in cross section from one large cross section to multiple smaller cross sections. Regarding velocity, the change in cross section should be regarded as a step down from the cross section of the resonator to the cross section of only one stack channel as the flow is forced to accommodate for the size of each channel alone. As for dynamic pressure, the change in cross section can be viewed from the blockage point of view thus the decrease in dynamic pressure amplitude is on a much smaller scale than the increase in velocity. However, the flow behavior inside the stack was not studied experimentally for meshed stacks and the observations are based only on numerical analysis.

It was also noticed that frequency, dynamic pressure and velocity are affected by changes in two main parameters; porosity viscous losses. As porosity increases the values of frequency, dynamic pressure and velocity are expected to increase. However, the increase in porosity is accompanied by an increase in the amount of viscous losses that occur due to friction resulting from the contact between the gas (air) parcels and the stack surfaces. This contact is increased as the number of cells per square inch increases and as the length of the stack increases. The value of contact friction is quantified as the wet area [m^2/$inch^2$] where this wet area is the product of the cell perimeter and the stack length per square inch. Figure 5. shows the dynamic end pressure values of each stack configuration compared to the wet area and Figure 5.22 shows the velocity values measured at 0.25 m from the speaker’s surface also compared to the wet area for each stack configuration.

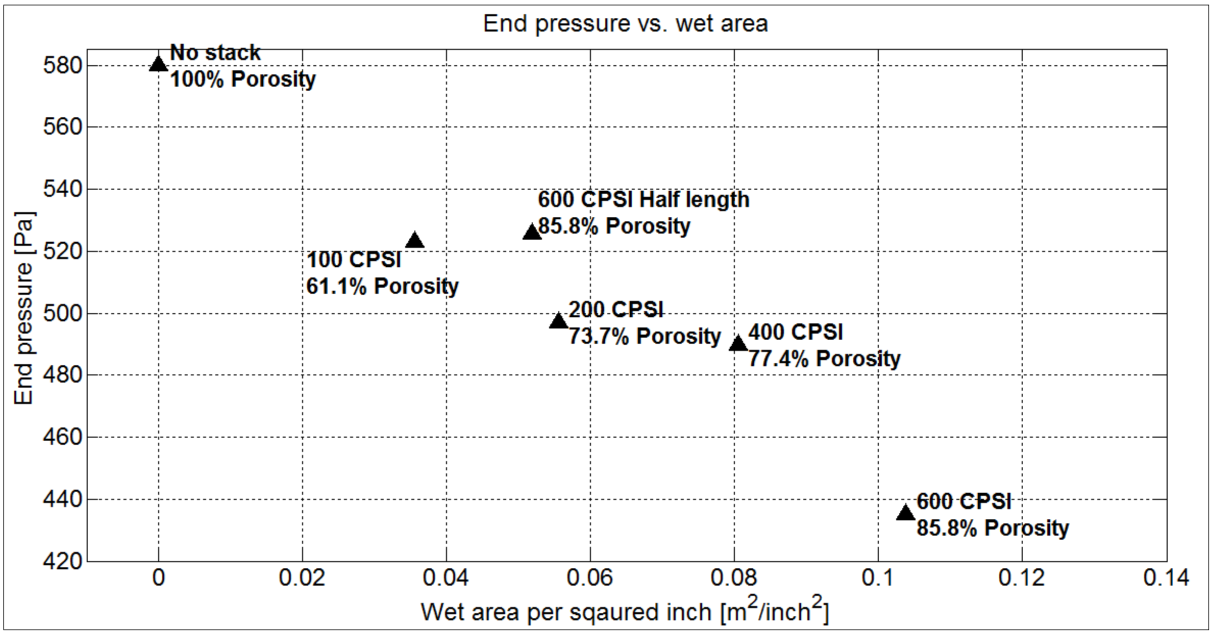

Figure 5.21 Dynamic end pressures of different stack configurations versus the wet area

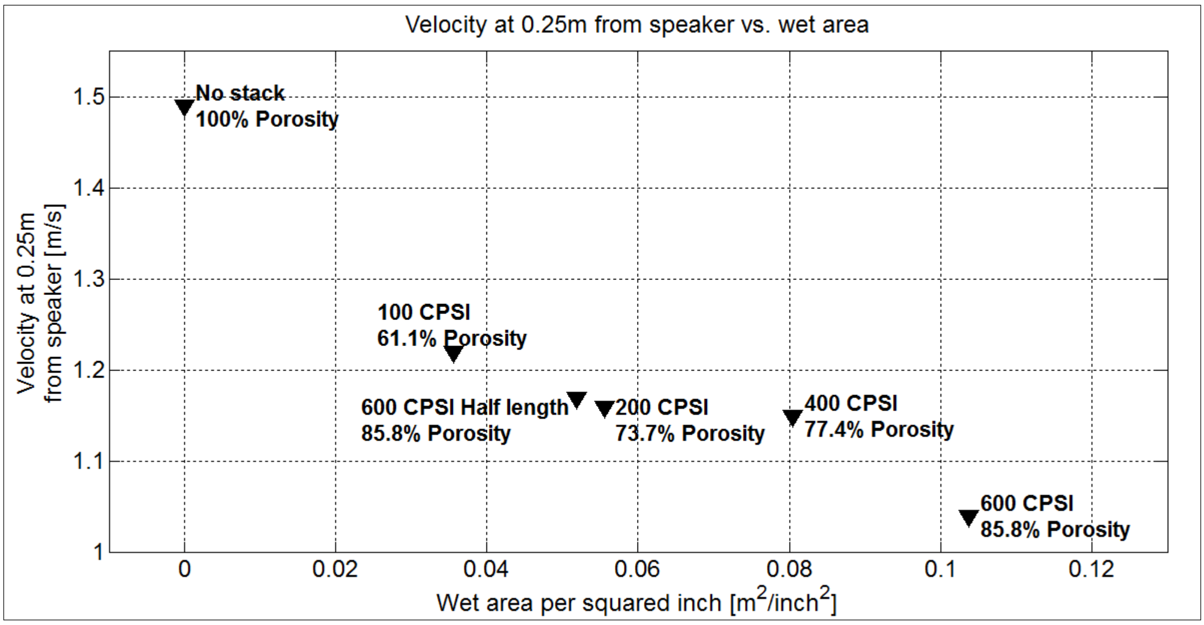

Figure 5.22 Velocity at 0.25 m from speaker's surface versus the wet area

As observed in Figure 5. and Figure 5.22 for experiments with meshed stacks; as porosity increases while maintaining stack length the values of the dynamic end pressure and velocity decrease unlike what is expected. Also, when the stack length is decreased to half its original length while maintaining the same porosity, pressure and velocity increase. Thus it is fair to say that it is the wet area of the meshed stack that dominates the acoustic losses of the thermoacoustic refrigerator not the porosity.

As for resonance frequency, looking at Table 5.5, Table 5.6, Table 5.7, Table 5.8, Table 5.9 and Table 5.10 while comparing values of experimental resonance frequencies to numerical ones; it becomes clear that the numerical data are not affected by the viscous losses showing that DeltaEC deals with stack elements as flow blockers and thermal exchange surfaces without taking into consideration the friction between the gas parcels and the stack surfaces (wet area), thus for the current configuration of the thermoacoustic refrigerator the numerical resonance frequency obtained through DeltaEC is only affected by change in porosity. Additionally, the measurements of the experimental values of resonance frequencies have shown that the thermoacoustic refrigerator in discussion has a bad quality factor leading to close values of resonance for stacks of close porosity values.

Chapter 6. Flow visualization in a thermoacoustic refrigerator

Flow visualization of the introduced thermoacoustic refrigerator was focused on two objectives. The first was to study the morphology of vortex formation at the vicinity of a set of parallel plates. This was done by using different configurations of the parallel plates set and changing the dynamic pressure. Observing the vortex formation in thermoacoustics in general is a step towards understanding the losses caused by vortex generation in thermoacoustic devices. Understanding how changing the stack components' configuration affects the formation of a vortex is essential. The second objective was to observe the flow physics inside the channels of a set of parallel plates at different stack configurations, dynamic pressure and under the effect of the vortex structures occurring at the edge of the plates of the stack.

For the purpose of studying the behavior of vortex structures at the edge of the plates aluminum plates were used, while for observations performed between the channels acrylic plates were used. Although aluminum and acrylic don't share the same good thermal properties of ceramic for use in thermoacoustics, but at the current scope of study the drive ratio used ranged from 0.73% to 1.84% with atmospheric pressure as the man pressure which is a very low value allowing for the thermal fluctuations occurring to be neglected.

All aluminum plates were of 6 mm thickness while the acrylic plates were 7 mm in thickness. All plates shared the same width and height, Figure 6.1 shows a detailed plate dimensions. Nuts of 3 mm thickness were used to separate the plates and were mounted on a bolt passing through identical holes in all connected plates. Figure 6.2 shows a top view of one of the parallel plate configurations from a top view showing one of the connecting bolts and the nuts in between the plates. The location of all stacks was at 0.465 m from the outer edge of the back volume. The definition of the location was previously illustrated in Figure 5.16.

Four different configurations of parallel plate sets were used; two aluminum and two acrylic. Each configuration was measured at two different values of dynamic pressure producing a total of eight measurements configurations. Aluminum plates do not allow light to pass through and were only used for imaging the vortex structures at the edge of the parallel plates. The aluminum stack plates were all covered in black tape to prevent reflection of laser light, glare and assure clear edge imaging. Unlike aluminum, acrylic plates allow the passage of laser light but the edge roughness of the acrylic plate itself produces a dead measurement zone at exactly the stack edge thus not allowing for measurements at the stack edge.

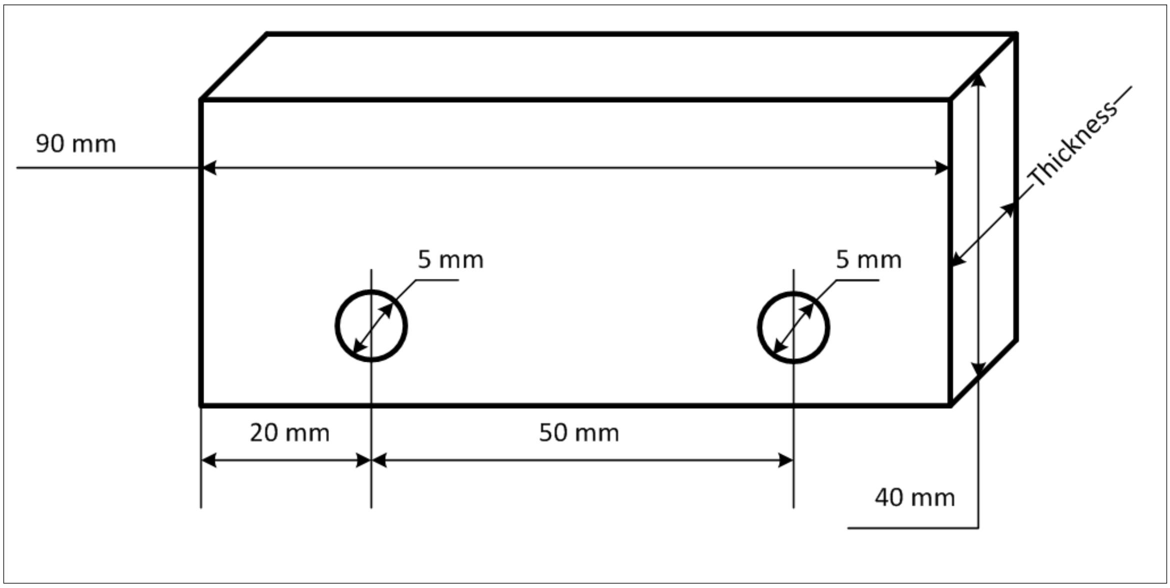

Figure 6.1 Detailed dimensions of aluminum and acrylic plates having different thicknesses.

Figure 6.2 Top view of one of the aluminum stack configurations showing the through bolt and the spacing nuts.

The plate thicknesses used throughout this work were selected such that the vortex size is detectable by the PIV camera lens. Figure 6.3, Figure 6.4, Figure 6.6 and Figure 6.5 show pictures of the four parallel plate configurations used.

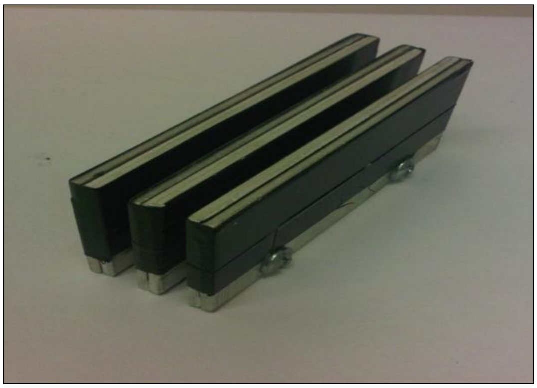

Figure 6.3 Aluminum – 3 plate configuration

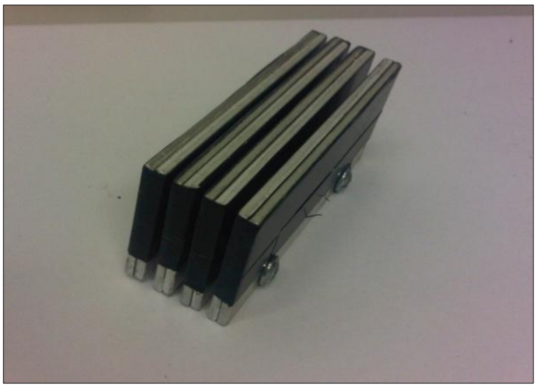

Figure 6.4 Aluminum – 4 plate configuration

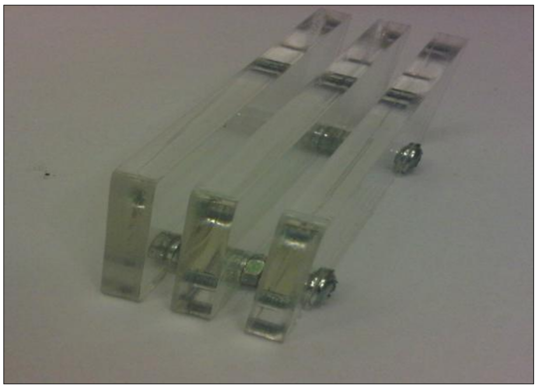

Figure 6.6 Acrylic – 3 plate configuration

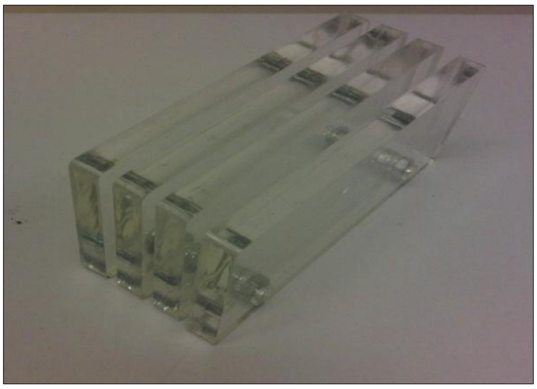

Figure 6.5 Acrylic – 4 plate configuration

In order to obtain the visualization measurement in a relatively quantitative form, fluid dimensionless numbers commonly used in fluid mechanics were used to characterize each measurement. The dimensionless numbers that are mostly used to describe flow physics in thermoacoustics are the Reynolds number (*Re*) which is used to characterize flow regimes as being laminar or turbulent, the Strouhal number (*St*), the Womersley number (*Wo*) and the Keulegan-Carpenter number (*KC*) [8] [11] [13] [19].

Eq. 6.1 through Eq. 6.4 show the mathematical definitions of these numbers.

The (Re) number equation as suggested by Aben [11]:

$$\mathrm{Re} = \frac{\mathrm{V_{Dim}} * \mathrm{D_p}}{\nu}$$ **Eq. 6.1**

where ($\mathrm{V_{Dim}}$) is the velocity value selected as a velocity scale in [m/sec], ($\mathrm{D_p}$) is the plate spacing selected as a length scale in [m] and (ν) is the kinematic viscosity in [m^2/sec].

For all visualization measurements (outside the stack or in the stack channels) the value of ($\mathrm{V_{Dim}}$) was measured at a distance of 6.5 mm away from the cold edge of the stack (the edge towards the hard end of the resonator). Aben [11] and Berson [8] have used this technique to measure the value of (V_{Dim}) while Mao [13] and Shi [15] used the value of the velocity at the edge of the stack.

The (St) number equation as suggested by Aben [11]:

$$St = \frac{f * D_p}{V_{Dim}} \qquad \textbf{Eq. 6.2}$$

For each measurement run a resonance frequency detection experiment (similar to that in Section 5.1.1.1) was performed to determine the resonance frequency and the dynamic end pressure is measured at the each case's dynamic pressure to determine the drive ratio.

The (Wo) number equation as suggested by Aben [11]:

$$Wo = \sqrt{(St) * (Re)} \qquad \textbf{Eq. 6.3}$$

The (KC) number equation as suggested by Aben [11]:

$$KC = \frac{V_{Dim}}{\omega * L_s} \qquad \textbf{Eq. 6.4}$$

where (ω) is the rotational frequency in [rad/sec] and (L_s) is the stack length in [m].

Two reasons decided choosing a point of measurement far away from the stack edge for the current measurement setup. The first was the reflection of the laser light sheet on the edges of the stacks due to manufacturing surface roughness causing zones of glare that produce unclear images. The second was the distortion in free stream velocities caused by the vortex structures occurring at the stack edges.

Calculating the value of (V_{Dim}) was done by selecting a portion of the vector map produced from the PIV velocity measurements where that portion is 6.5 mm away from the stack's cold edge. The 6.5 mm was converted to a pixel value using a calibration image. A 150 x 1024 Pixels^2 (3.5 x 20.48 mm^2) portion of the vector maps (orginially taken at 1024 x 1024 Pixels^2) produced from each run was taken as the calculation window where all vectors are averaged producing one single vector per map. The single vectors are then plotted to view their sinusoidal form and the maximum amplitudes are selected as the (V_{Dim}) values for each run. The reason for taking a smaller window of analysis than the full field of view is to approach a line or point velocity value. However the resultant sinusoidal plots of the selected 150 x 1024 Pixels^2 portion were not completely pure sinusoidal as some of the cases showed distortion effects in the sine wave, mostly at high drive ratios. Such distortion usually occurred when the vortex structures caused a larger disturbance in the flow field making the 6.5 mm not enough to secure measuring the value (V_{Dim}) without being disturbed by the effect of the vortex structures. However taking the measurement location farther than 6.5 mm would make the values of the calculated dimensionless numbers more related to the free stream flow than to the thermoacoustic effects. Additionally, the distorted plots showed sinusoidal-like results that could be traced to define the maximum amplitude with a bit of approximation. Figure 6.7 and Figure 6.8 show the temporal velocity behavior of each of the measured configurations analyzed using the 150 x 1024 Pixels^2 portion of the vector map.

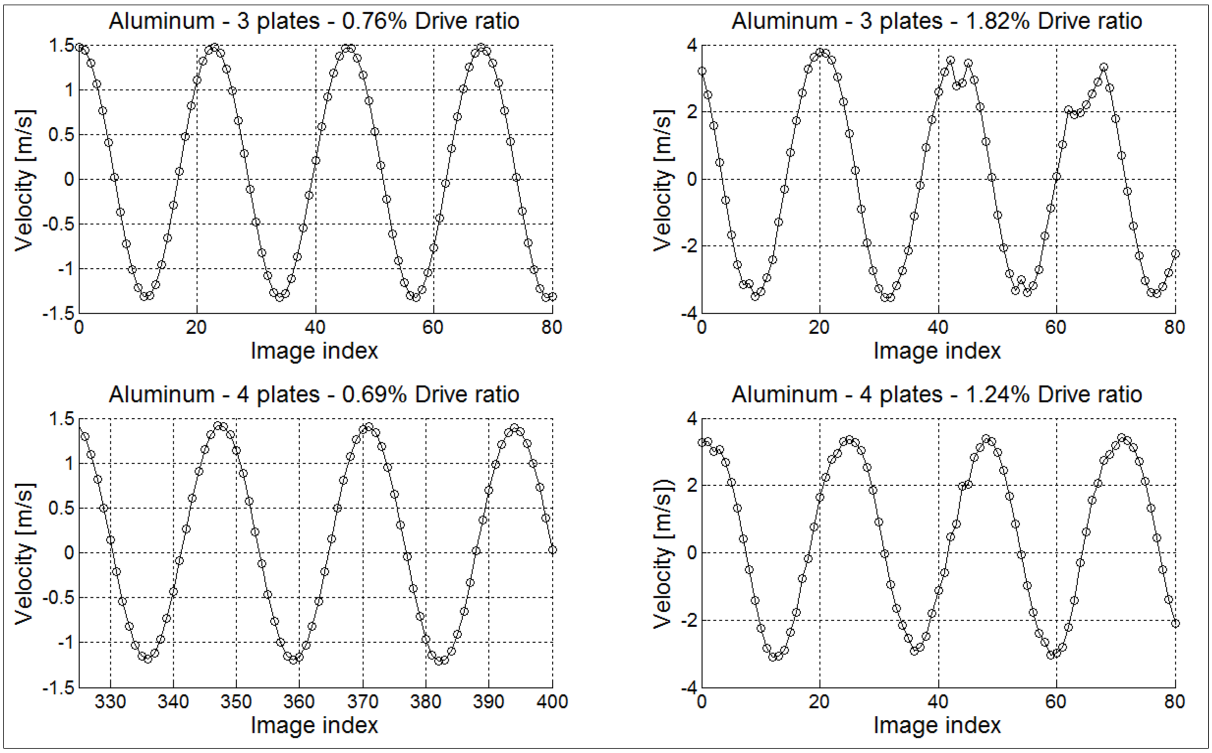

Figure 6.7 Temporal velocity distribution of air particles measured 6.5 mm away from the cold stack edge of aluminum parallel plate stacks imaged at 2700 Hz laser trigger rate and 185 μs time between pulses and analyzed using a 150 x 1024 Pixels^2 window out of 1024 x 1024 Pixels^2 .

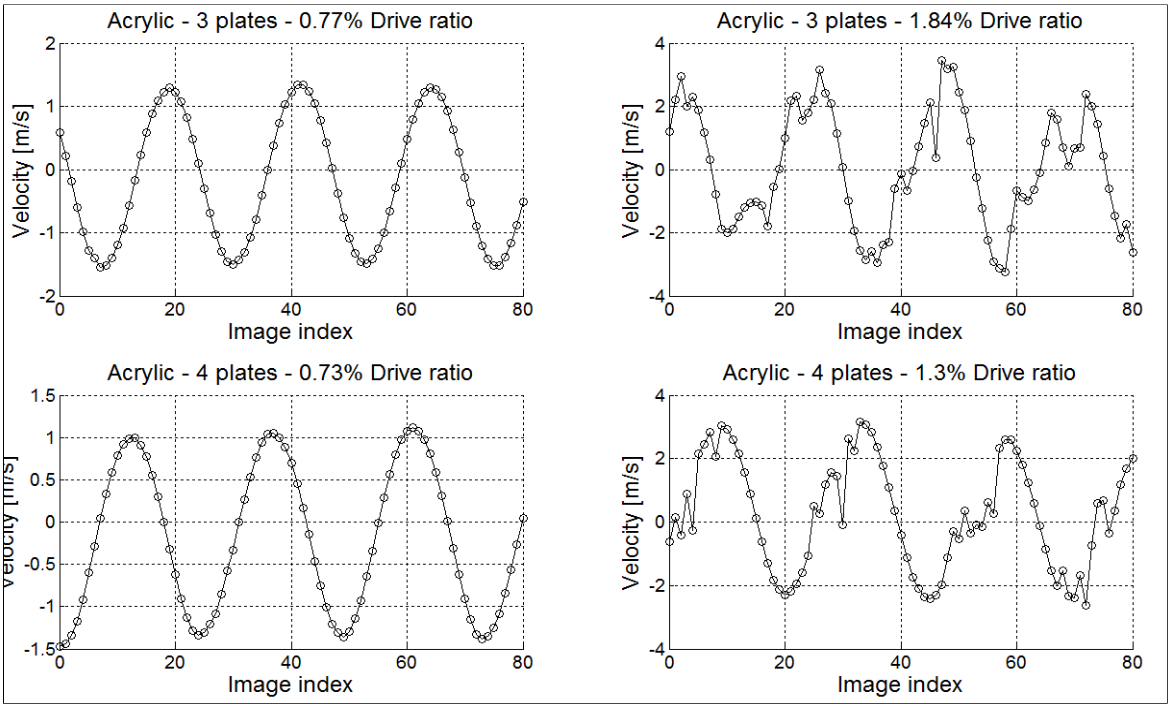

Figure 6.8 Temporal velocity distribution of air particles measured 6.5 mm away from the cold stack edge of acrylic parallel plate stacks and analyzed using a 150 x 1024 Pixels^2 window out of 1024 x 1024 Pixels^2 .

Table 6.1 shows the values of (V_{Dim}) calculated for all eight measurement configuration and the corresponding dimensionless numbers. The drive ratios used ranged from 0.73% as the lowest value up to 1.84% being the highest value. The selection of drive ratios was based on the need to have two different cases (one with low drive ratio and another with a higher one) for each stack configuration. The input signal from the function generator was 0.7 $V_{p\text{-}p}$ for the low drive ratio and 2.2 $V_{p\text{-}p}$ for the high drive ratio and both these inputs were fixed for all configurations. The 2.2 $V_{p\text{-}p}$ value is the maximum value the loudspeaker can attain for continuous operation. The change in the values of the drive ratios is a result of the different stack configurations that cause a change in the blockage value.

Table 6.1 Measurement configurations and the corresponding dimensionless numbers.

Run #	**Measurement configuration**	**(V_{Dim}) $[\frac{m}{sec}]$**	**Re**	**St**	**Wo**	**KC**
5A	Aluminum – 3 plates – 0.77% Drive ratio	1.4024	560	0.51	16.9	0.02
5B	Aluminum – 3 plates – 1.84% Drive ratio	3.6103	1444	0.2	16.9	0.05
5C	Aluminum – 4 plates – 0.73% Drive ratio	1.3083	523	0.53	16.7	0.02
5D	Aluminum – 4 plates – 1.3% Drive ratio	3.1781	1271	0.22	16.7	0.05
5E	Acrylic – 3 plates – 0.76% Drive ratio	1.42	662	0.59	19.7	0.02
5F	Acrylic – 3 plates – 1.82% Drive ratio	3.1583	1475	0.26	19.7	0.05
5G	Acrylic – 4 plates – 0.69% Drive ratio	1.2325	575	0.63	19.04	0.02
5H	Acrylic – 4 plates – 1.24% Drive ratio	2.7284	1273	0.28	19.04	0.04

Figure 6.9, Figure 6.13, Figure 6.16, Figure 6.19, Figure 6.22, Figure 6.25, Figure 6.28 and Figure 6.31 show selected raw images of the different measurement configurations. For (Section 6.2) the raw images are shown for the sake of illustrating vortex structures only as the main aim of this section is to study flow inside the stack channels. Figure 6.10, Figure 6.14, Figure 6.17, Figure 6.20, Figure 6.23, Figure 6.26, Figure 6.29 and Figure 6.32 show the temporal location of the analysis points in the acoustic cycle for each measurement configuration. Figure 6.11, Figure 6.15, Figure 6.18, Figure 6.21, Figure 6.24, Figure 6.27, Figure 6.30 and Figure 6.33 show a sequence of vector maps corresponding to these analysis points. The black areas that are bordered with circles and irregular shapes are the air gaps that occur at the core of vortex structures. The rectangular shapes on the right side of the raw images indicate the parallel plates. Each vector map is labeled with its index number in the acoustic cycle. In each figure there are eight vector maps, in the top four the flow is moving to the left towards the outside of the stack channels and into the free stream zone, this is the ejection stage. In the bottom four vector maps the flow is moving to the right and towards the inside of the parallel channels.

It was observed throughout all measurements that the peaks of vortex structures occur at the point where the flow velocity is zero and the flow changes direction and start returning back towards the plates’ direction. The part of the flow where the air particles start moving outside the stack into the resonator is called the ejection phase [15] referring to the flow or the air particles being ejected from inside the stack. All the vector maps shown in all measurement configurations are during the ejection phase. As observed in the vector maps; the vortex structures initiate as soon as the gas particles start to move outside the channels of the plates, and the vortex structures start to increase in size reaching the peak and then depending on the measurement configuration the vortex structures experience different events before the flow changes direction and during the return period and even after the air particles return back into the stack.

6.1. Flow visualization at the edge of a set of parallel aluminum plates stacks in a thermoacoustic refrigerator

6.1.1. Aluminum – 3 plates – 0.77% Drive ratio

Table 6.2 shows the measurement configuration for Run# 5A.

Table 6.2 Measurement configuration for Run# 5A.

Run# 5A: Aluminum – 3 plates – 0.77% Drive ratio		
Function generator settings	**Resonance frequency [Hz]**	119
	Function generator voltage [$V_{p\text{-}p}$]	0.7
	Amplifier settings	-20 dB, -9 dB
	Voltage to speaker [V_{rms}]	2.5
Measured dynamic pressure	**Drive ratio [%]**	0.77
Parallel plates' configuration	**Stack location from back volume [mm]**	465
	Plate length [mm]	90
	Plate thickness [mm]	6
	Plate spacing [mm]	6
	Volumetric porosity [Open area/Total area]	0.5
Dimensionless numbers	**Re**	560
	St	0.51
	Wo	16.9
	KC	0.02
PIV settings	**Laser trigger rate [Hz]**	2700
	Time between pulses [μs]	185
	Field of view [mm^2]	20 x 20
	Laser energy [mJ]	9
	Interrogation area size [$Pixels^2$]	32 x 32
	Overlap [%]	50
	Analysis technique	Adaptive correlation

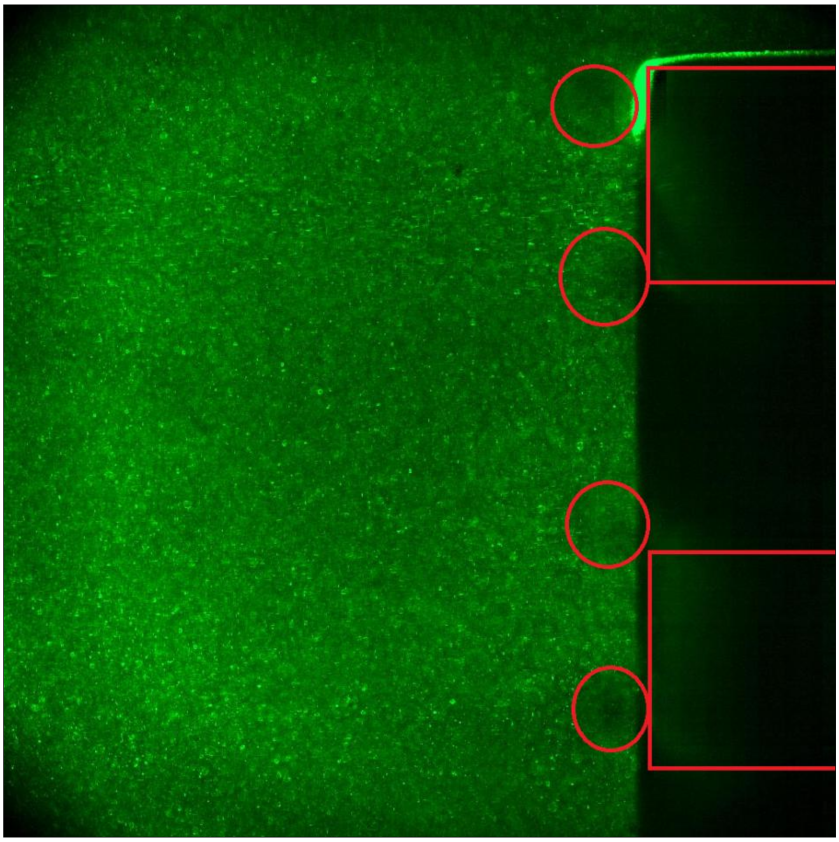

Figure 6.9 A selected raw image (index=17) from Run# 5A showing the air gaps inside vortex structures in red.

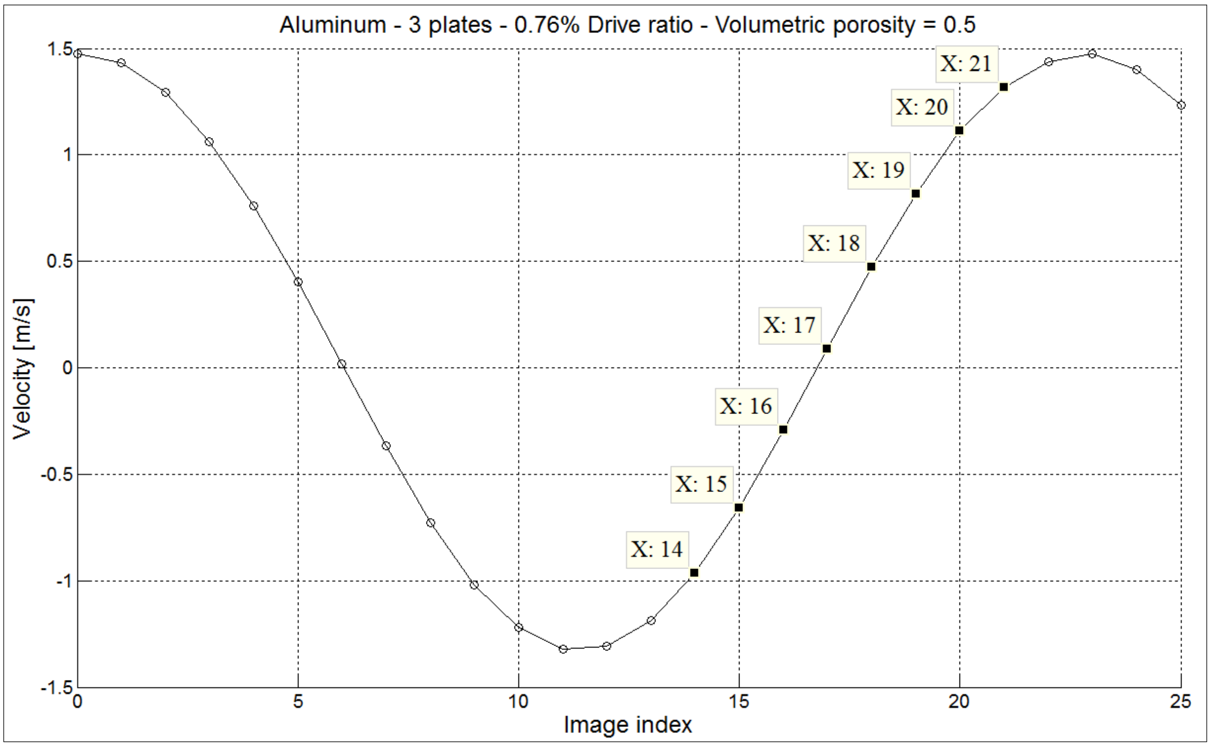

Figure 6.10 Part of the acoustic cycle from Run# 5A showing the indices of the vector maps shown in Figure 6.11.

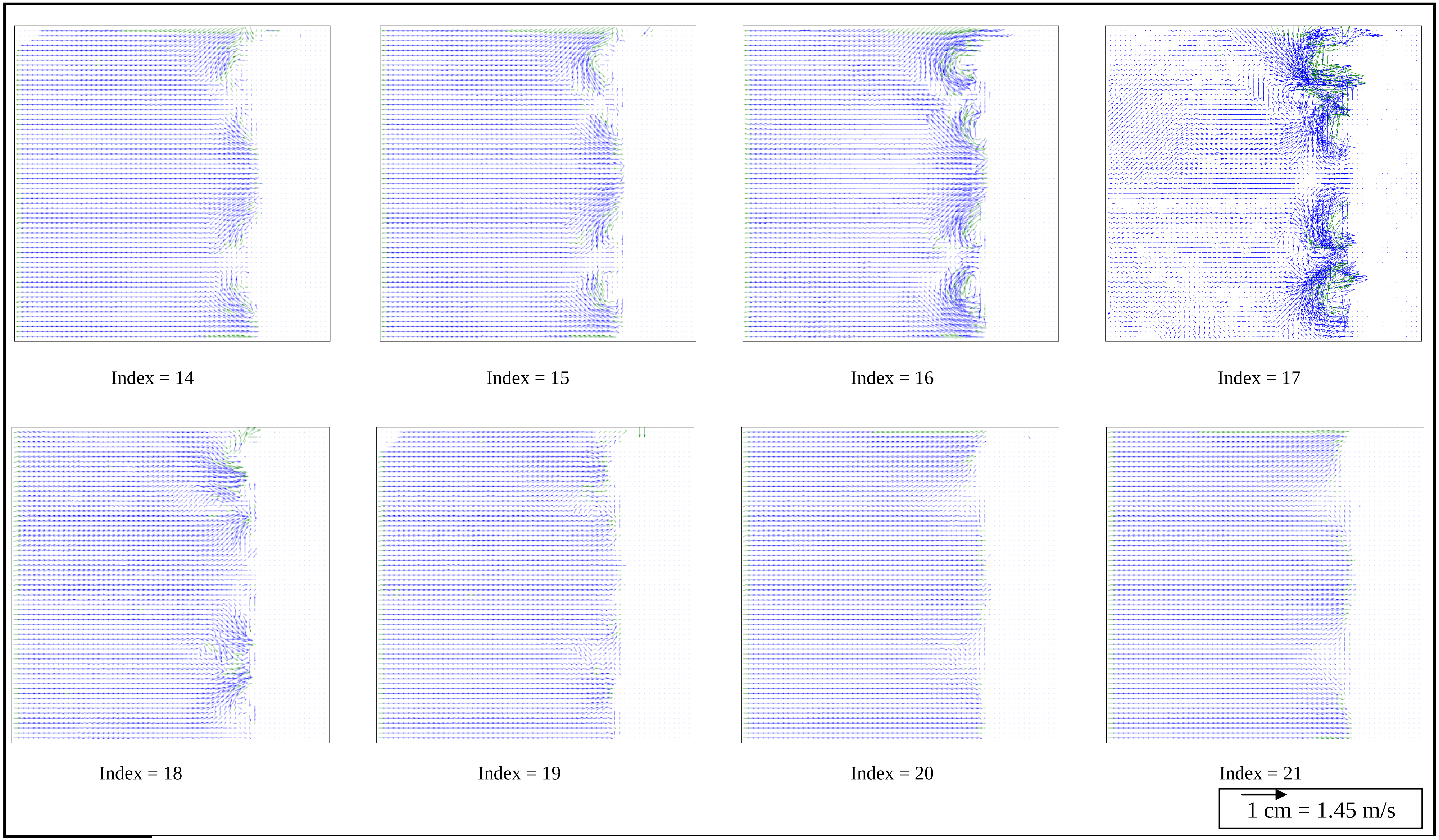
Index = 14

Index = 15

Index = 16

Index = 17

Index = 18

Index = 19

Index = 20

Index = 21

Figure 6.11 Vector maps of images having indices from 14 to 21 showing the development of vortex structures from Run# 5A.

It was observed that as soon as the extraction phase begins vortex structures begin to develop while moving in a direction away from the stack into the sudden expansion zone. The vortex structures occur exactly in-front of the stack walls in the sudden expansion zone. It is shown in Figure 6.11 in index 17 the peak development of the vortex structures with the air gaps inside them showing no vectors, these gaps are the ones circled in red as seen in Figure 6.9. Figure 6.12 shows an enlarged image of index 17 in Figure 6.11. Due to the oscillating nature of the sound wave vacuum occurs at the moment of sudden expansion of the flow. This sudden expansion is the one that occurs at the edges of the parallel plates where air particles from the plate channels move into the streaming flow part. Vacuum generates a centripetal force that forces the air particles to move in a curved path and form a vortex. Air gaps are formed in the core of the vortex as a result of particles grouping to follow the curved path of the vortex. It was also observed that the vortex structures affect only the region of the flow close to the parallel plates while away from the plates the flow was undisturbed.

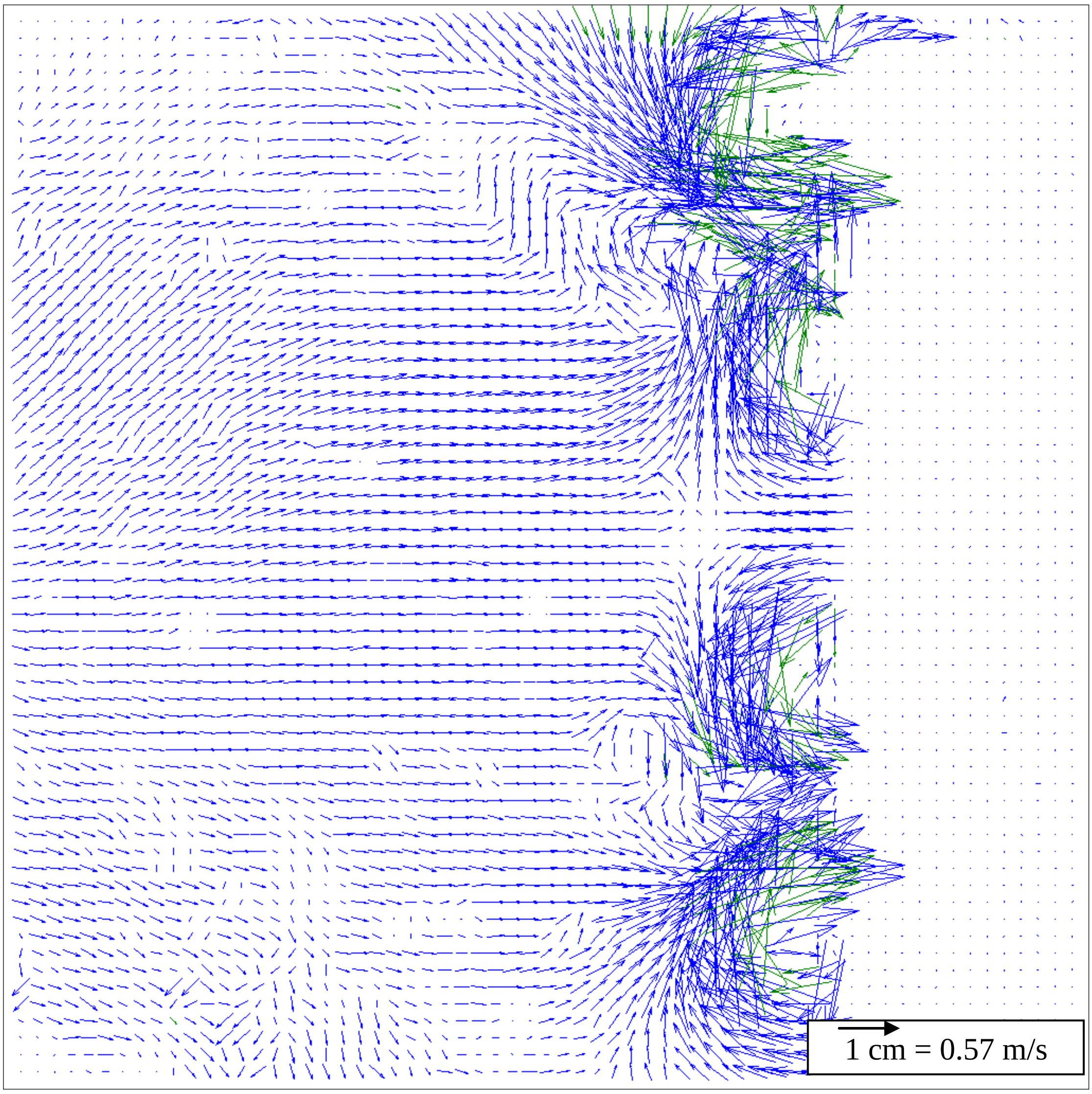

Figure 6.12 An enlarged image of index 17 in Figure 6.11

6.1.2. Aluminum – 3 plates – 1.84% Drive ratio

In order to investigate the effects of higher drive ratios, the drive ratio was increased from 0.77% to 1.84% at the same geometrical configuration of Run# 5A. Table 6.3 shows the measurement configuration for Run# 5B.

Table 6.3 Measurement configuration for Run# 5B.

Run# 5B: Aluminum – 3 plates – 1.84% Drive ratio		
Function generator settings	**Resonance frequency [Hz]**	119
	Function generator voltage [V]	2.2
	Amplifier settings	-20 dB, -9 dB
	Voltage to speaker [V_{rms}]	8
Measured dynamic pressure	**Drive ratio [%]**	1.84
Parallel plates' configuration	**Stack location from back volume [mm]**	465
	Plate length [mm]	90
	Plate thickness [mm]	6
	Plate spacing [mm]	6
	Volumetric porosity [Open area/Total area]	0.5
Dimensionless numbers	**Re**	1444
	St	0.2
	Wo	16.9
	KC	0.05
PIV settings	**Laser trigger rate [Hz]**	2700
	Time between pulses [μs]	185
	Field of view [mm^2]	20 x 20
	Laser energy [mJ]	9
	Interrogation area size [$Pixels^2$]	32 x 32
	Overlap [%]	50
	Analysis technique	Adaptive correlation

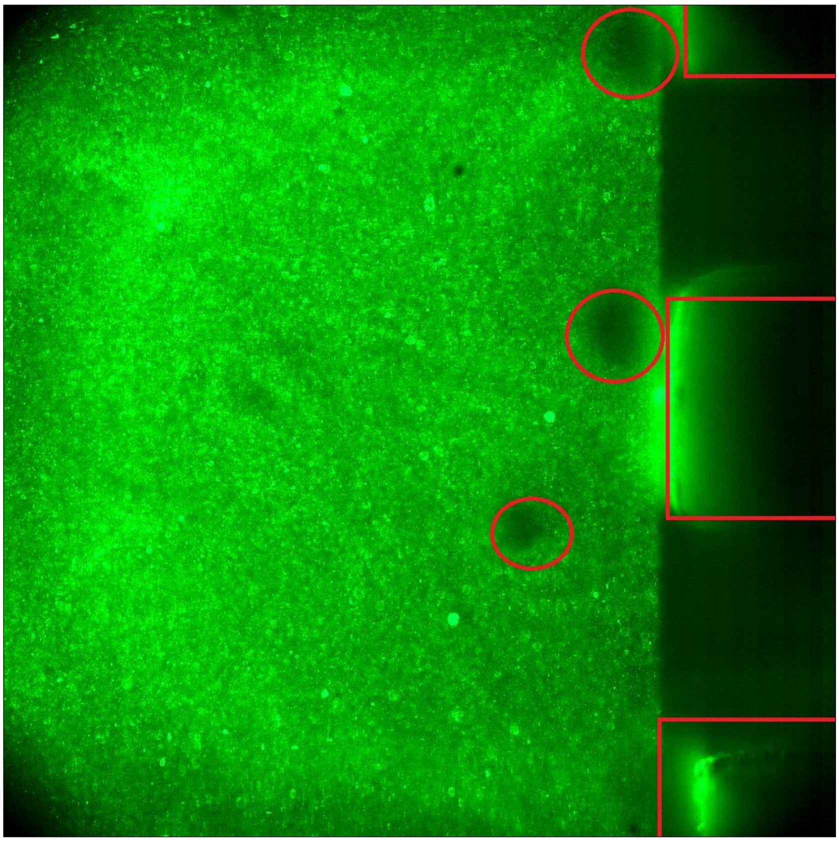

Figure 6.13 A selected raw image (index=37) from Run# 5B showing the air gaps inside vortex structures in red.

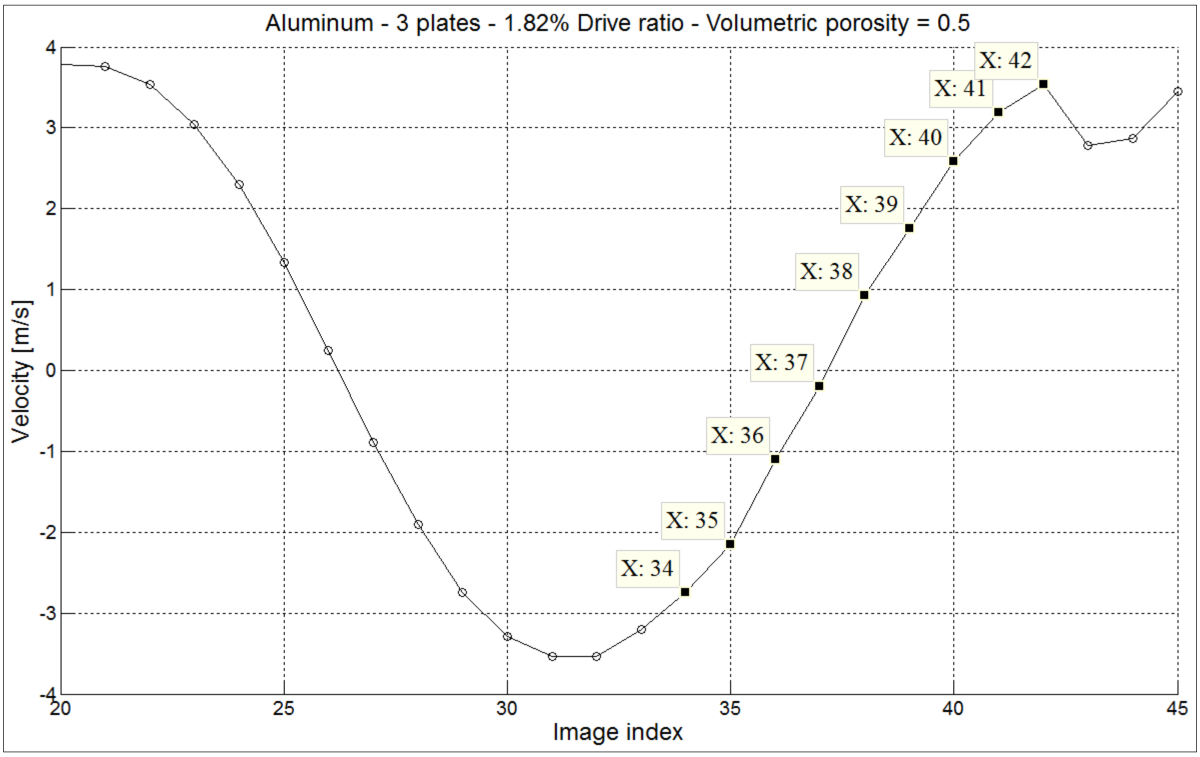

Figure 6.14 Part of the acoustic cycle from Run# 5B showing the indices of the vector maps shown in Figure 6.15.

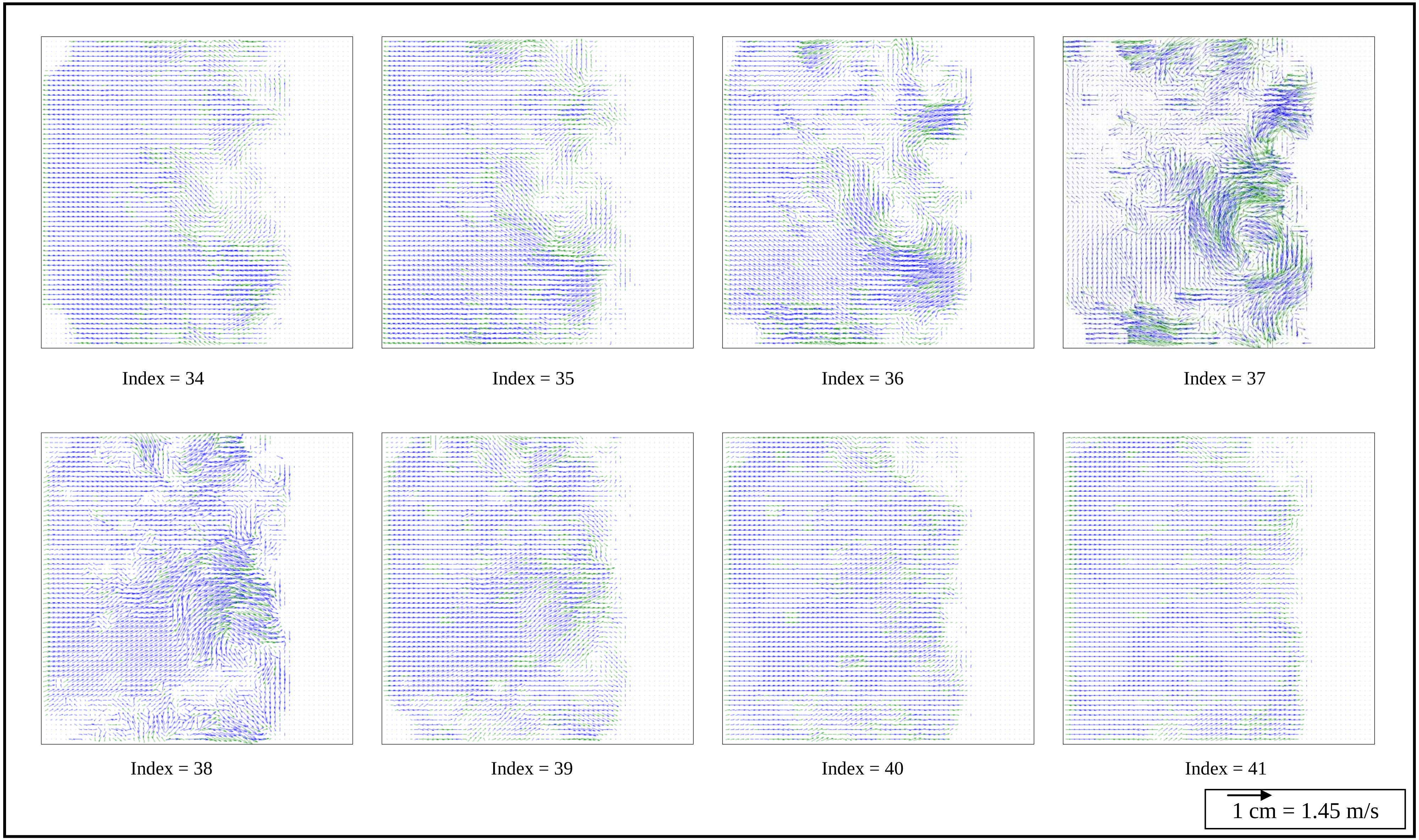

Index = 34

Index = 35

Index = 36

Index = 37

Index = 38

Index = 39

Index = 40

Index = 41

Figure 6.15 Vector maps of images having indices from 34 to 41 showing the development of vortex structures from Run# 5B.

At a higher drive ratio (1.84%) while preserving plate thickness and spacing, it was observed that the vortex structures are getting larger in size and thus causing a disturbance in a larger portion of flow measured as a displacement of the vortex structure away from the plate edges. Another interesting event was observed, which was the un-symmetry of the vortex structures around different place noticing one vortex leading the other.

6.1.3. Aluminum – 4 plates – 0.73% Drive ratio

Table 6.4 shows the measurement configuration for Run# 5C.

Table 6.4 Measurement configuration for Run# 5C.

Run# 5C: Aluminum – 4 plates – 0.73% Drive ratio		
Function generator settings	**Resonance frequency [Hz]**	116
	Function generator voltage [V]	0.7
	Amplifier settings	-20 dB, -9 dB
	Voltage to speaker [V_{rms}]	2.5
Measured dynamic pressure	**Drive ratio [%]**	0.73
Parallel plates' configuration	**Stack location from back volume [mm]**	465
	Plate length [mm]	90
	Plate thickness [mm]	6
	Plate spacing [mm]	3
	Volumetric porosity [Open area/Total area]	0.33
Dimensionless numbers	**Re**	262
	St	0.27
	Wo	8.34
	KC	0.02
PIV settings	**Laser trigger rate [Hz]**	2700
	Time between pulses [μs]	185
	Field of view [mm^2]	20 x 20
	Laser energy [mJ]	9
	Interrogation area size [$Pixels^2$]	32 x 32
	Overlap [%]	50
	Analysis technique	Adaptive correlation

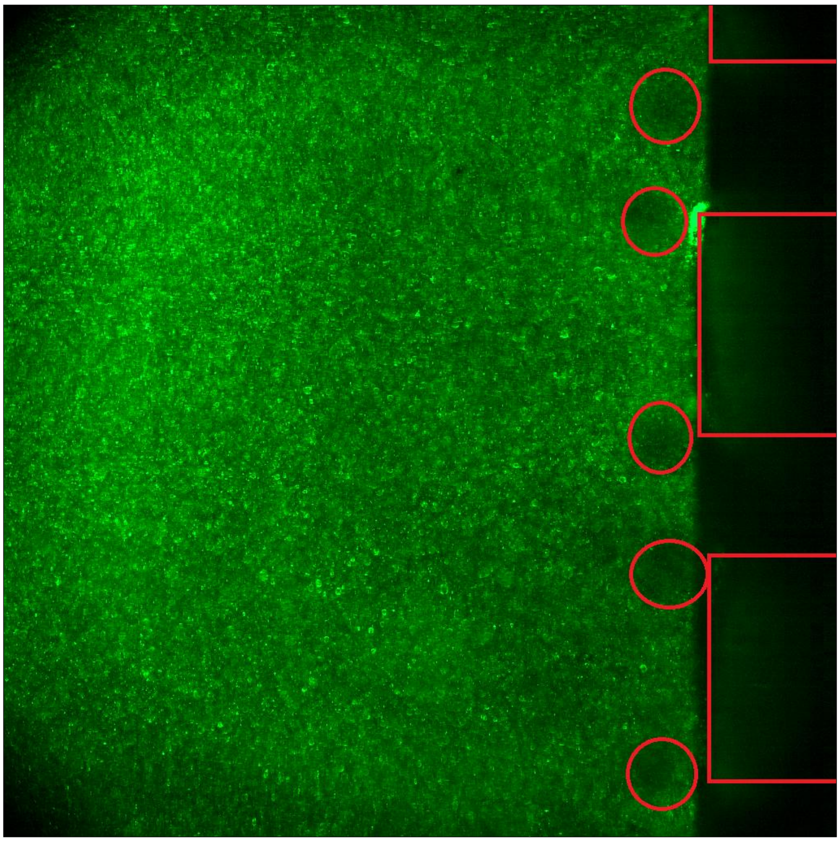

Figure 6.16 A selected raw image (index=10) from Run# 5C configuration showing the air gaps inside vortex structures in red.

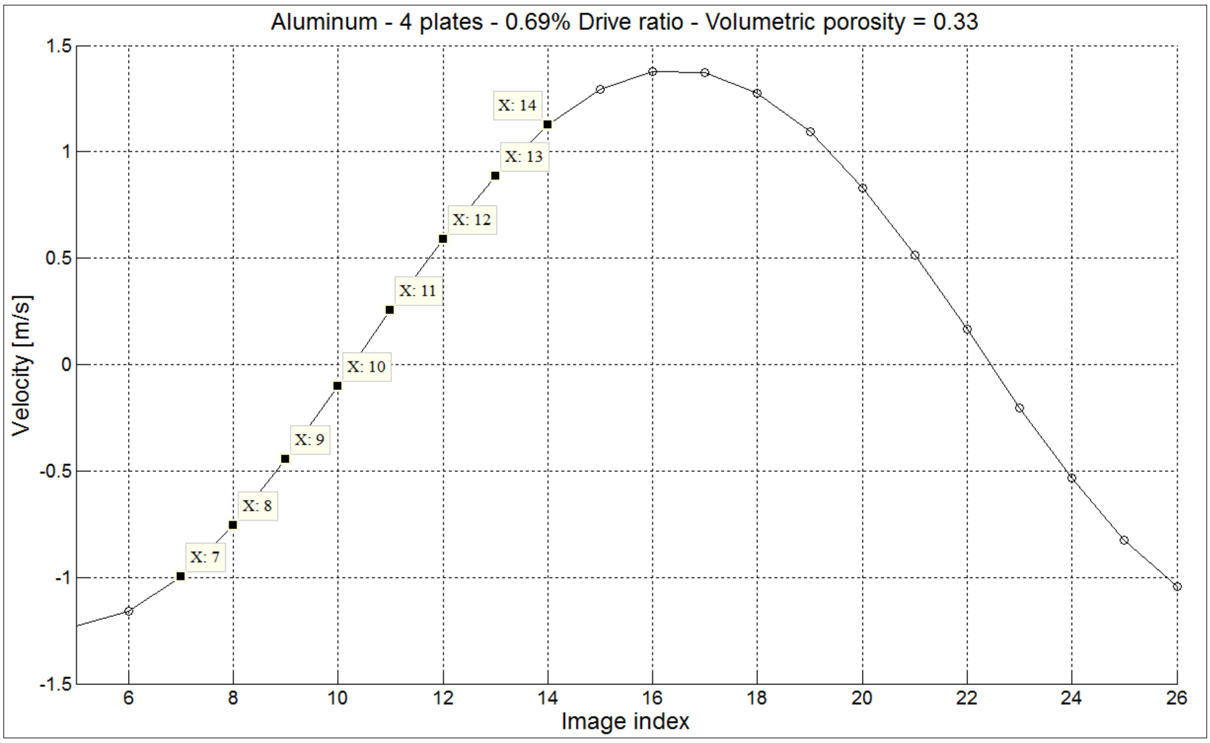

Figure 6.17 Part of the acoustic cycle of the from Run# 5C showing the indices of the vector maps shown in Figure 6.18.

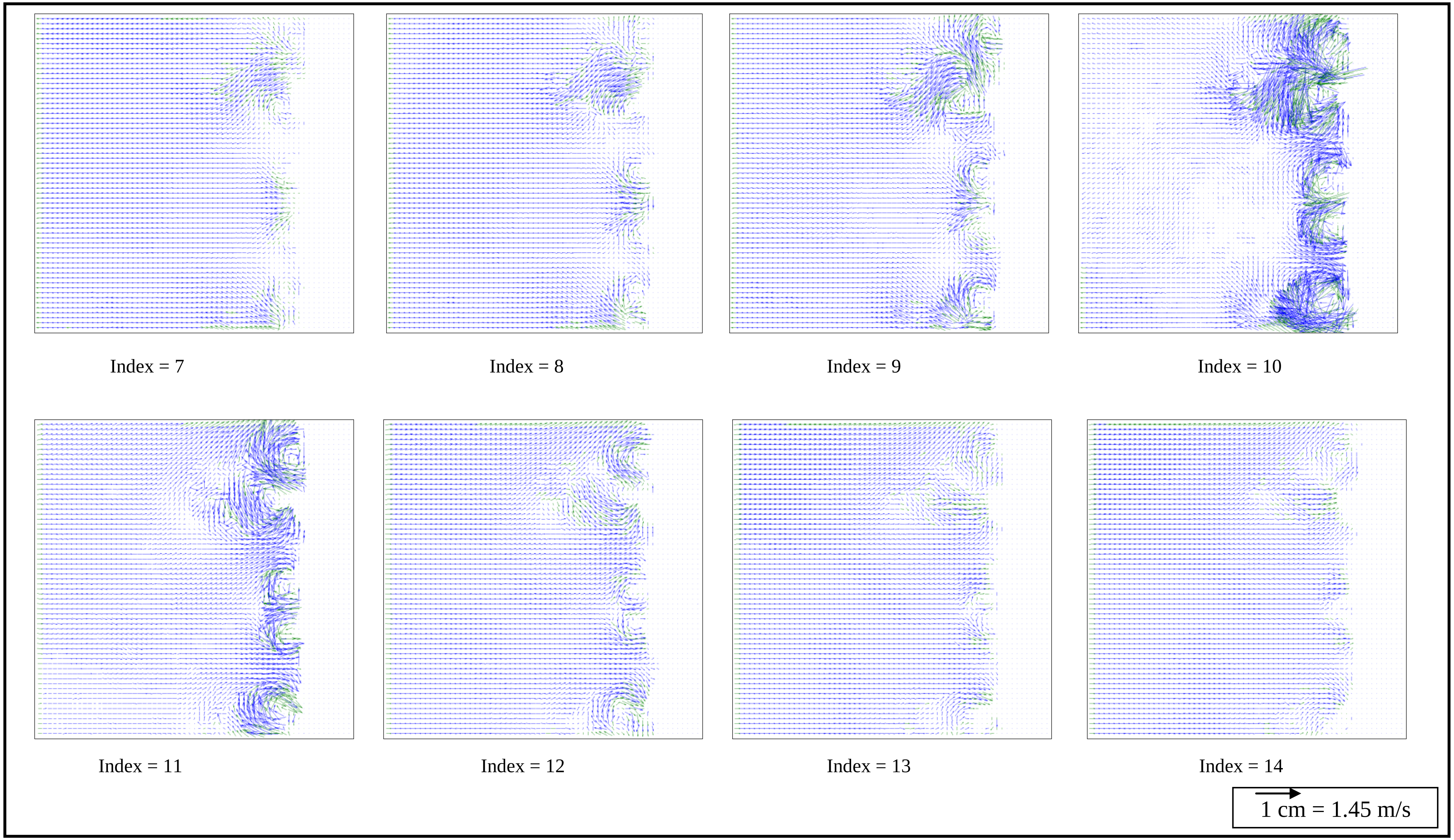

Index = 7

Index = 8

Index = 9

Index = 10

Index = 11

Index = 12

Index = 13

Index = 14

Figure 6.18 Vector maps of images having indices from 7 to 14 showing the development of vortex structures from Run# 5C.

Changing the plate spacing while returning to the value of the lower drive ratio (0.73%); similar vector maps were observed to those of Run# 5A but as plates close towards each other the vortex structures from different channels begin to interact with each other.

6.1.4. Aluminum – 4 plates – 1.3% Drive ratio

In order to investigate the effects of higher drive ratios, the drive ratio was increased from 0.73% to 1.3% at the same geometrical configuration of Run# 5C. Table 6.5 shows the measurement configuration for Run# 5D.

Table 6.5 Measurement configuration for Run# 5D.

Run# 5D: Aluminum – 4 plates – 1.3% Drive ratio		
Function generator settings	**Resonance frequency [Hz]**	116
	Function generator voltage [V]	2.2
	Amplifier settings	-20 dB, -9 dB
	Voltage to speaker [V_{rms}]	8
Measured dynamic pressure	**Drive ratio [%]**	1.3
Parallel plates’ configuration	**Stack location from back volume [mm]**	465
	Plate length [mm]	90
	Plate thickness [mm]	6
	Plate spacing [mm]	3
	Volumetric porosity [Open area/Total area]	0.33
Dimensionless numbers	**Re**	636
	St	0.11
	Wo	8.3
	KC	0.05
PIV settings	**Laser trigger rate [Hz]**	2700
	Time between pulses [μs]	185
	Field of view [mm^2]	20 x 20
	Laser energy [mJ]	9
	Interrogation area size [$Pixels^2$]	32 x 32
	Overlap [%]	50
	Analysis technique	Adaptive correlation

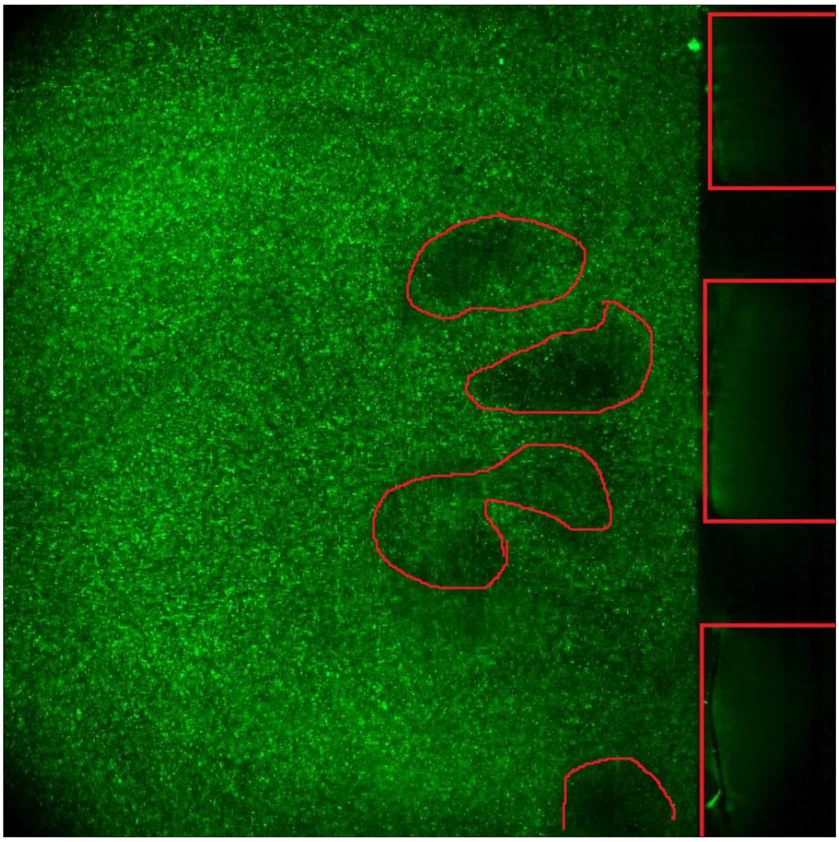

Figure 6.19 A selected raw image (index=19) from Run# 5D showing the air gaps inside vortex structures in red.

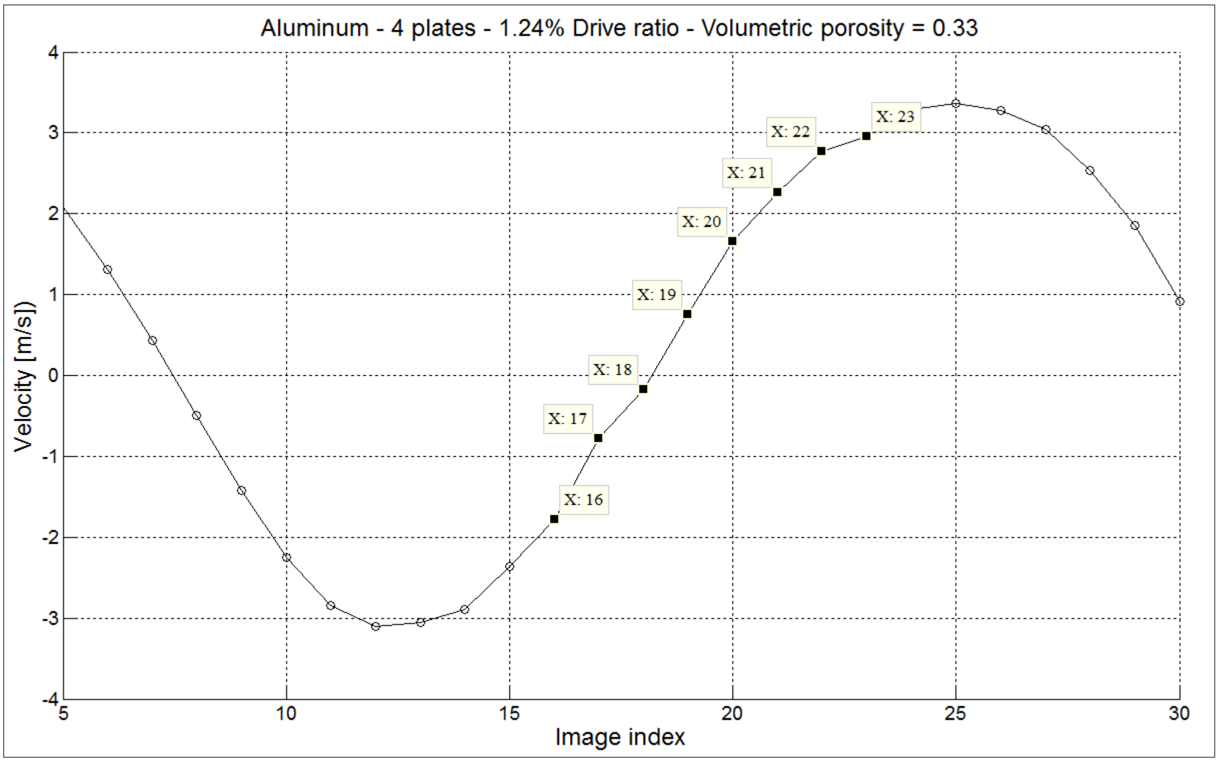

Figure 6.20 Part of the acoustic cycle from Run# 5D showing the indices of the vector maps shown in Figure 6.21.

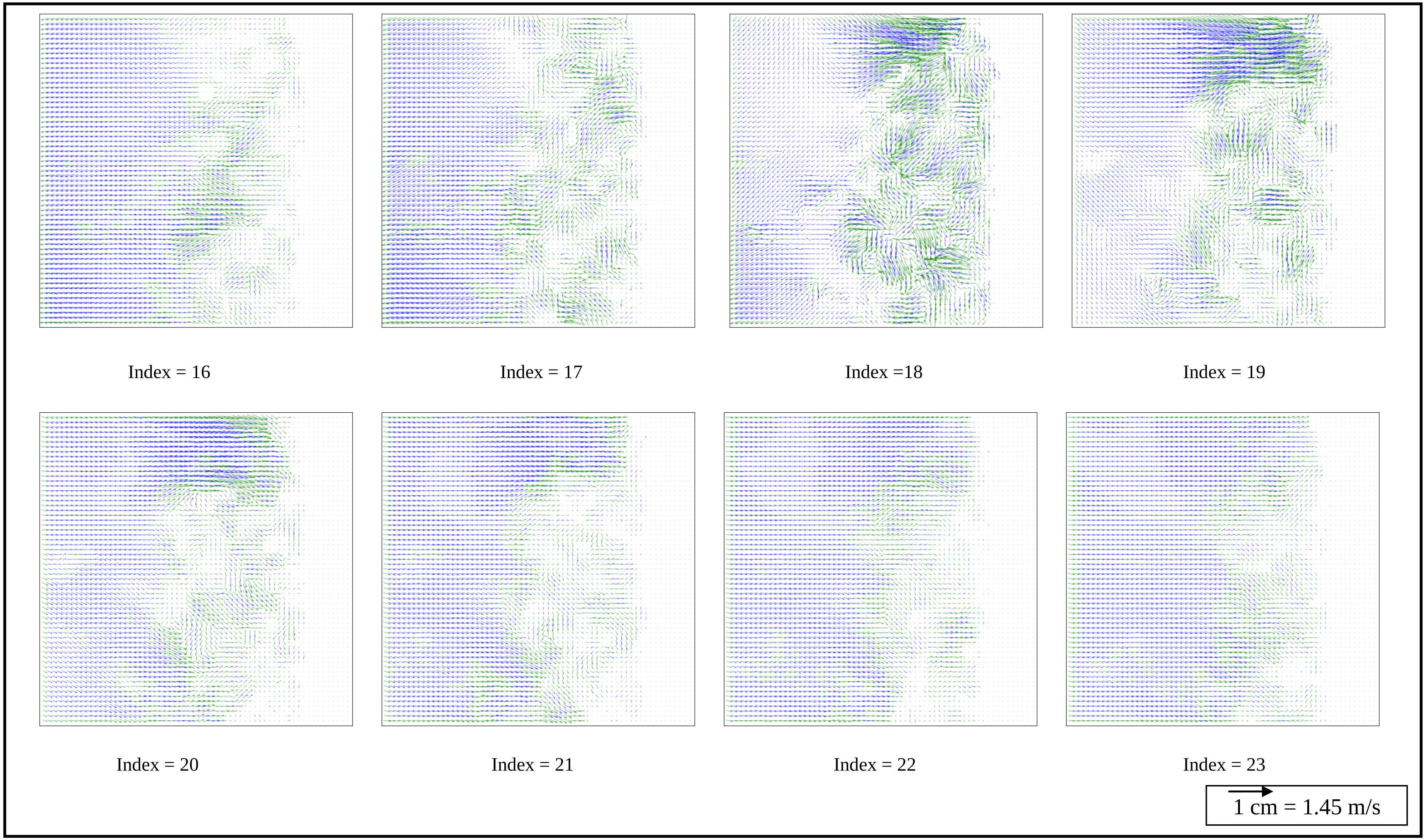

Index = 16

Index = 17

Index =18

Index = 19

Index = 20

Index = 21

Index = 22

Index = 23

Figure 6.21 Vector maps of images having indices from 16 to 23 showing the development of vortex structures from Run# 5D.

Changing the drive ratio to 1.3% and maintaining the smaller plate spacing caused large disturbances to occur throughout a larger portion of the flow. It was observed that vortex structures have increased in size and displaced to a farther distance (same observation as in Run# 5B) but with additional interaction between the vortex structures causing the formation of secondary complex structures composed of two vortex structures interacting together. It was observed that the structures sharing the same channel are the ones who interact. Additionally, these interactions cause an extended disturbance into the flow zone beyond the plate's edge into the flow in displacements that were farther than those observed in Run# 5B.

In higher drive ratio oscillations the flow disturbance is seen in a larger number of frames per cycle due to the large displacement of vortex structures occurring due to high dynamic pressure where the vortex structures take a longer time to develop.

As seen in Figure 6.21, no vortex shedding was observed, however it was noticed during measurements that at high amplitudes vortex structures tend to shed but at the edge of shedding the structures is pulled back into the plates; premises leaving no traces of disturbance outside the stack channels.

It was concluded that the increase in dynamic pressure amplitude initially increases the displacement of the air particles at constant frequency. The increase in displacement causes the formation of larger vortex structures and more disturbances in the flow beyond the plate edge and into the free stream flow. The decrease in plate spacing causes vortex structures to interact with each other and form complex structures. The combination of increasing dynamic pressure amplitude and decreasing plate spacing increase the amount of disturbances in a complex behavior. However at all drive ratios used in this work (Ranging from 0.73% to 1.84%) whatever disturbance occurred in the free stream zone was pulled back into the plates' premises as the flow changed direction.

6.2. Flow visualization inside the channels of a parallel plate acrylic stacks in a thermoacoustic refrigerator

The use of acrylic plates allowed for the passage of laser light through the plates and consequently the visualization of the flow in between the parallel plates.

6.2.1. Acrylic – 3 plates – 0.76% Drive ratio

Table 6.6 shows the measurement configuration for Run# 5E.

Table 6.6 Measurement configuration for Run# 5E.

Run# 5E: Acrylic – 3 plates – 0.76% Drive ratio		
Function generator settings	**Resonance frequency [Hz]**	119
	Function generator voltage [V]	0.7
	Amplifier settings	-20 dB, -9 dB
	Voltage to speaker [V_{rms}]	2.5
Measured dynamic pressure	**Drive ratio [%]**	0.76
Parallel plates' configuration	**Stack location from back volume [mm]**	465
	Plate length [mm]	90
	Plate thickness [mm]	7
	Plate spacing [mm]	6
	Volumetric porosity [Open area/Total area]	0.4615
Dimensionless numbers	**Re**	568
	St	0.5
	Wo	16.9
	KC	0.02
PIV settings	**Laser trigger rate [Hz]**	2700
	Time between pulses [μs]	185
	Field of view [mm^2]	20 x 20
	Laser energy [mJ]	9
	Interrogation area size [$Pixels^2$]	32 x 32
	Overlap [%]	50
	Analysis technique	Adaptive correlation

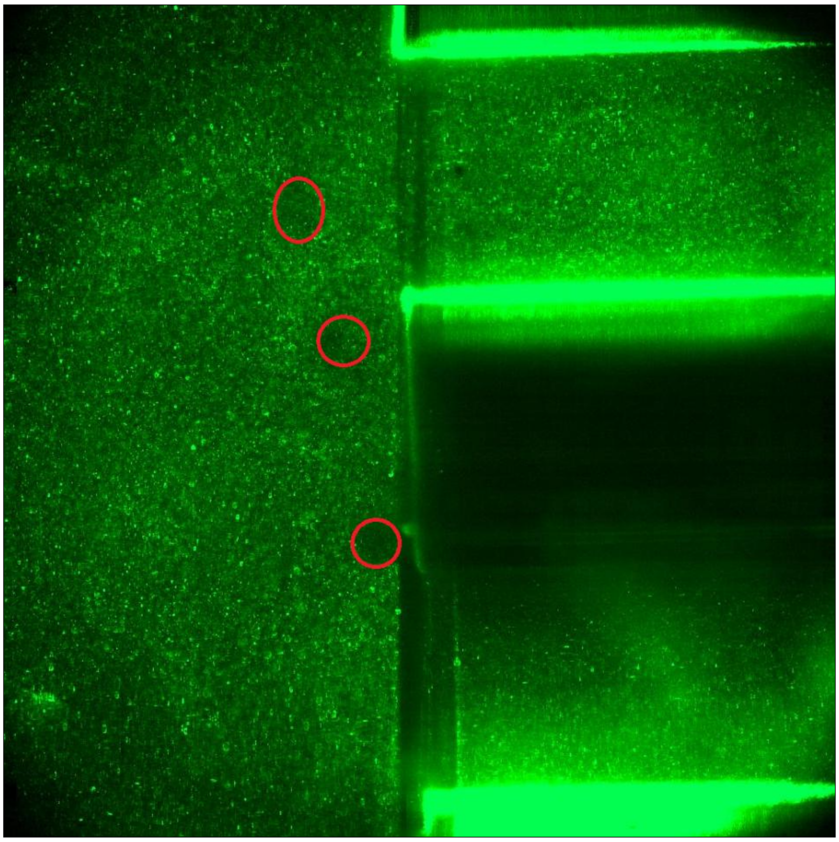

Figure 6.22 A selected raw image (index=13) from Run# 5E showing the air gaps inside vortex structures in red.

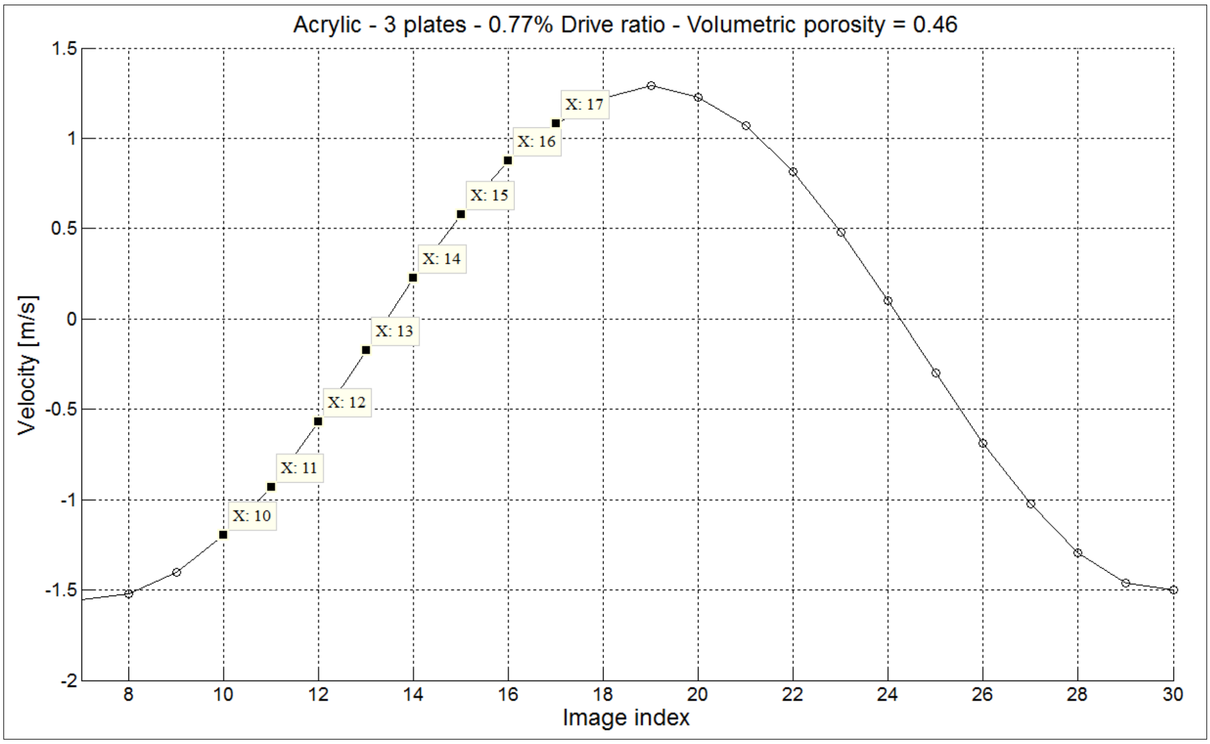

Figure 6.23 Part of the acoustic cycle from Run# 5E showing the indices of the vector maps shown in Figure 6.24.

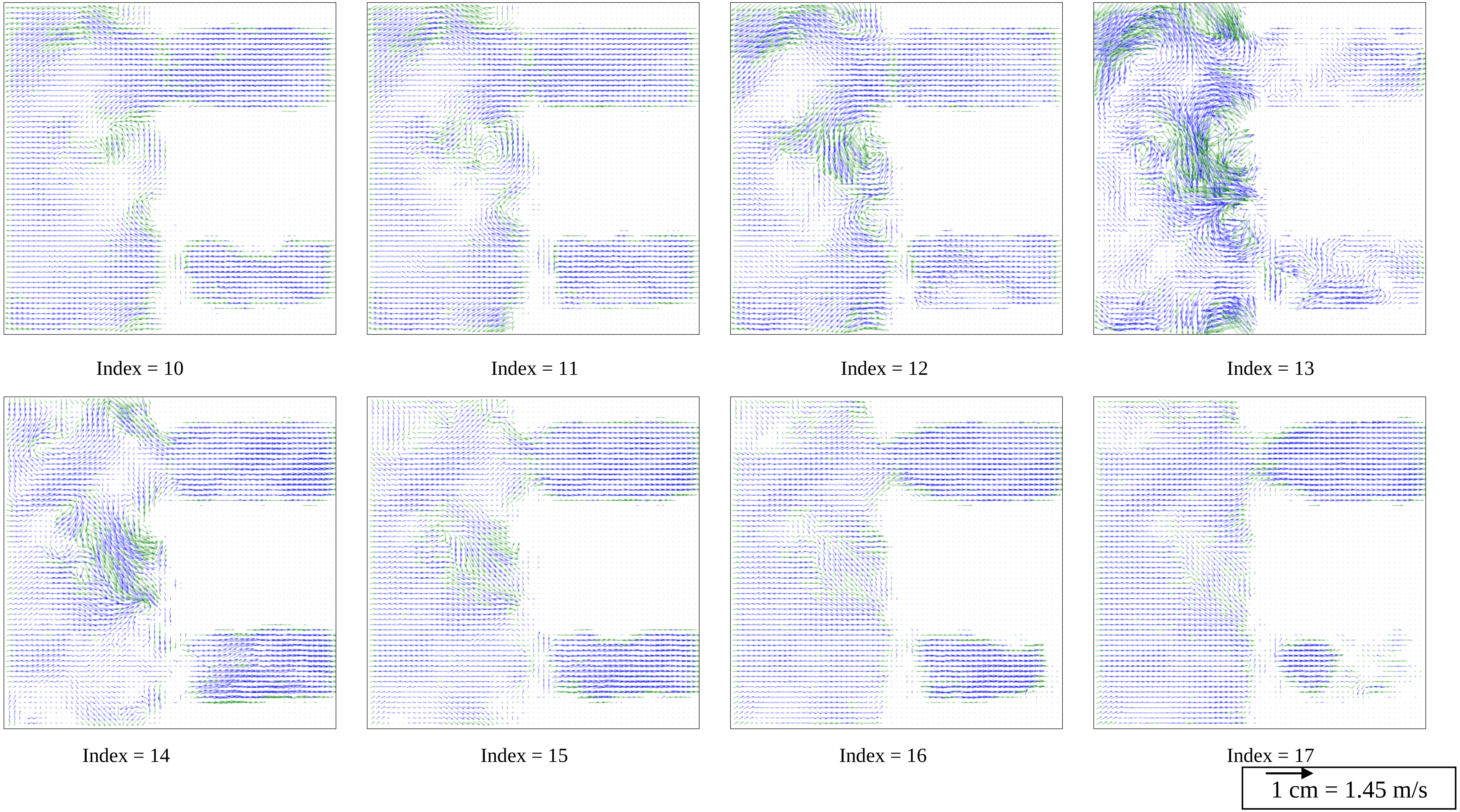
Index = 10
Index = 11
Index = 12
Index = 13
Index = 14
Index = 15
Index = 16
Index = 17

Figure 6.24 Vector maps of images having indices from 10 to 17 showing the development of vortex structures from Run# 5E.

It was observed that at the lower drive ratio (0.76%) the flow in between the plates is undisturbed at all points in the acoustic cycle.

6.2.2. Acrylic – 3 plates – 1.82% Drive ratio

In order to investigate the effects of higher drive ratios, the drive ratio was increased from 0.76% to 1.82% at the same geometrical configuration of Run# 5E. Table 6.7 shows the measurement configuration for Run# 5F.

Table 6.7 Measurement configuration for Run# 5F.

Run# 5F: Acrylic – 3 plates – 1.82% Drive ratio		
Function generator settings	**Resonance frequency [Hz]**	119
	Function generator voltage [V]	2.2
	Amplifier settings	-20 dB, -9 dB
	Voltage to speaker [V_{rms}]	8
Measured dynamic pressure	**Drive ratio [%]**	1.82
Parallel plates' configuration	**Stack location from back volume [mm]**	465
	Plate length [mm]	90
	Plate thickness [mm]	7
	Plate spacing [mm]	6
	Volumetric porosity [Open area/Total area]	0.4615
Dimensionless numbers	**Re**	1263
	St	0.26
	Wo	16.9
	KC	0.05
PIV settings	**Laser trigger rate [Hz]**	2700
	Time between pulses [μs]	185
	Field of view [mm^2]	20 x 20
	Laser energy [mJ]	9
	Interrogation area size [$Pixels^2$]	32 x 32
	Overlap [%]	50
	Analysis technique	Adaptive correlation

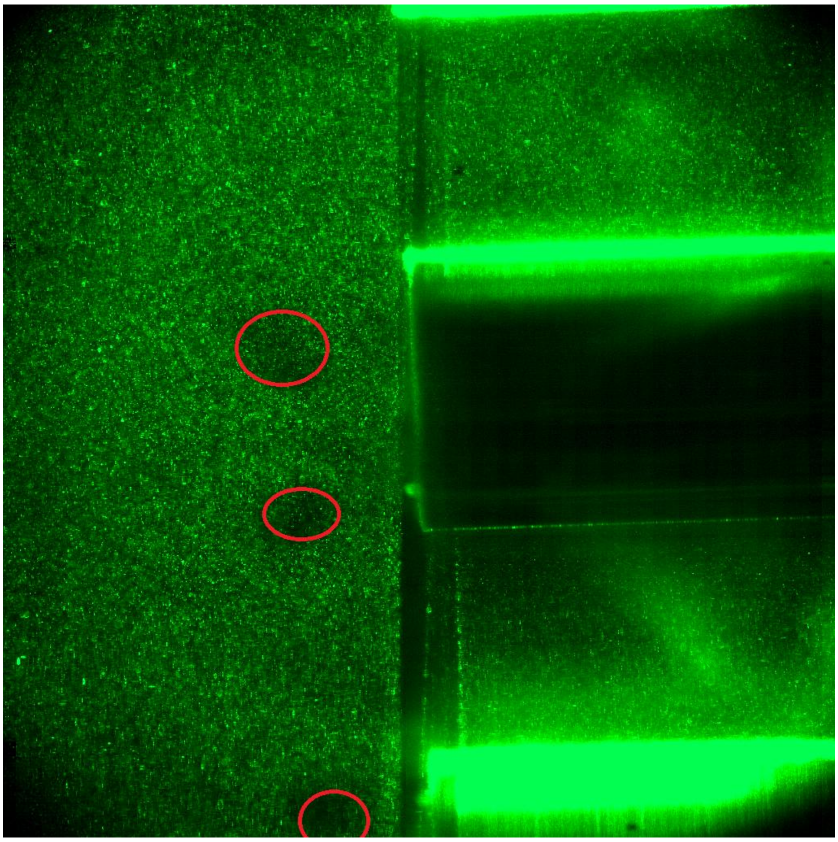

Figure 6.25 A selected raw image (index=18) from Run# 5F showing the air gaps inside vortex structures in red.

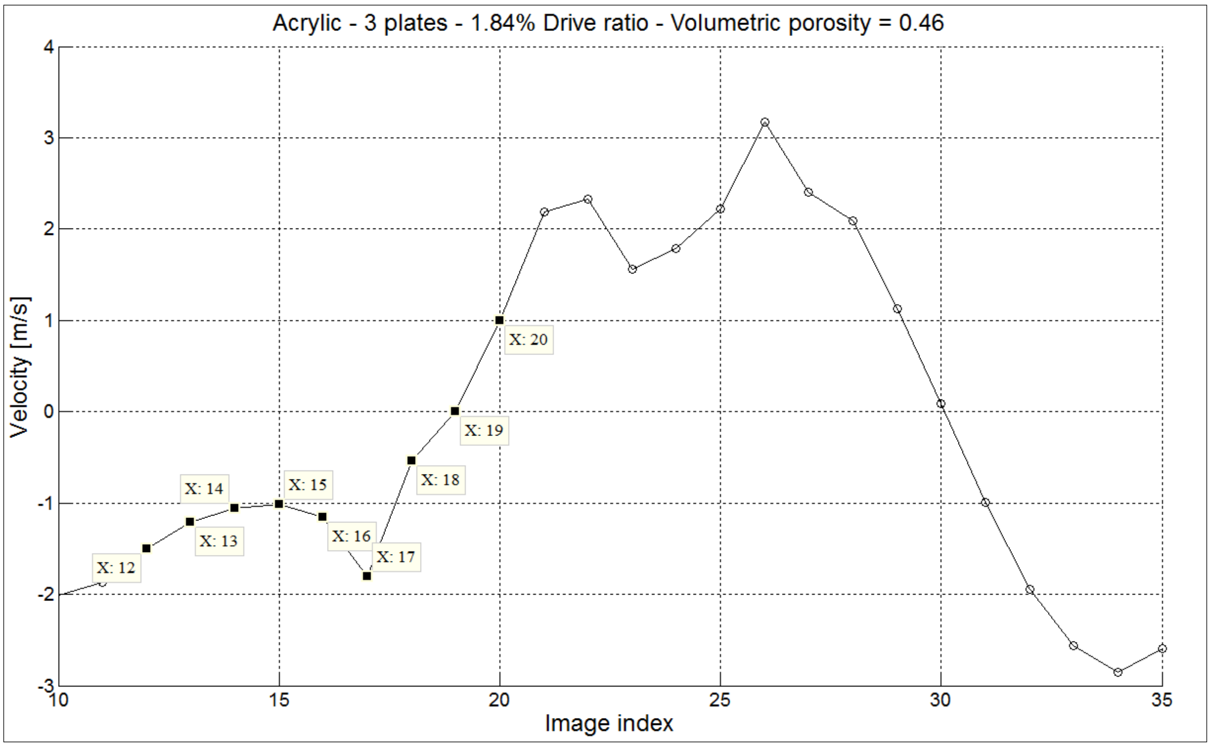

Figure 6.26 Part of the acoustic cycle from Run# 5F showing the indices of the vector maps shown in Figure 6.27.

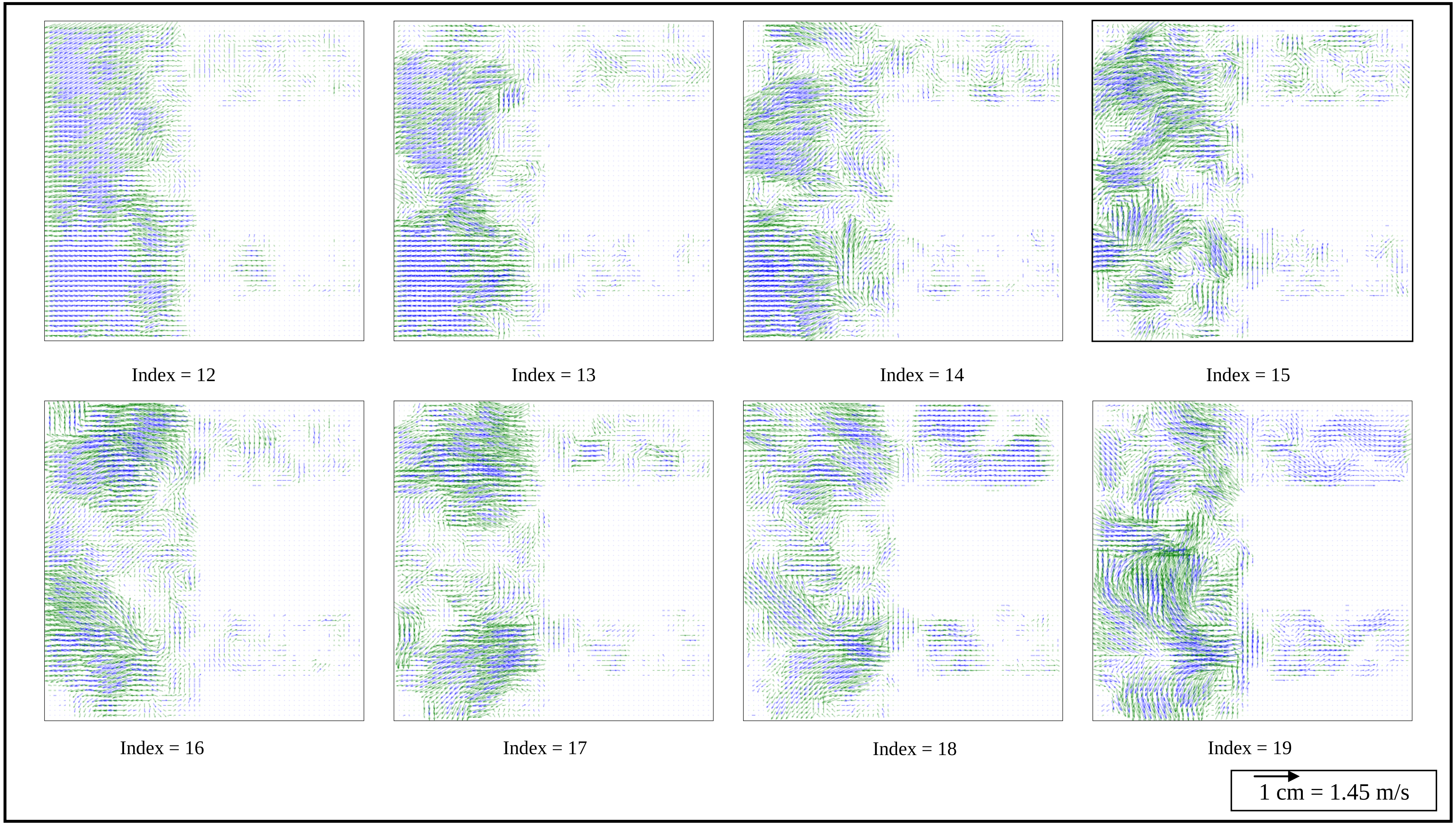

Figure 6.27 Vector maps of images having indices from 12 to 19 showing the development of vortex from Run# 5F.

After increasing the drive ratio to 1.82% while preserving the plate spacing it was observed that the flow in between the plates is disturbed when the vortex structures are pulled into the channels between the plates after returning from the ejection phase, but when the vortex structures are being developed outside the plates’ premises the flow in the channels is undisturbed. It was observed in the vortex maps in Figure 6.27 that when the vortex structures are pulled back into the channels most of the flow in undisturbed but some disturbances occur near the plate’s edge. These disturbances were related to the edge effect of the acrylic plates, where laser light is not allowed to pass through the edge of the plate leaving dark areas that produce error in vector maps’ computation.

6.2.3. Acrylic – 4 plates – 0.69% Drive ratio

Table 6.8 shows the measurement configuration for Run# 5G.

Table 6.8 Measurement configuration for Run# 5G.

Run# 5G: Acrylic – 4 plates – 0.69% Drive ratio		
Function generator settings	**Resonance frequency [Hz]**	111
	Function generator voltage [V]	0.7
	Amplifier settings	-20 dB, -9 dB
	Voltage to speaker [V_{rms}]	2.5
Measured dynamic pressure	**Drive ratio [%]**	0.69
Parallel plates’ configuration	**Stack location from back volume [mm]**	465
	Plate length [mm]	90
	Plate thickness [mm]	7
	Plate spacing [mm]	3
	Volumetric porosity [Open area/Total area]	0.3
Dimensionless numbers	**Re**	247
	St	0.27
	Wo	8.16
	KC	0.02
PIV settings	**Laser trigger rate [Hz]**	2700
	Time between pulses [μs]	185
	Field of view [mm^2]	20 x 20
	Laser energy [mJ]	9
	Interrogation area size [$Pixels^2$]	32 x 32
	Overlap [%]	50
	Analysis technique	Adaptive correlation

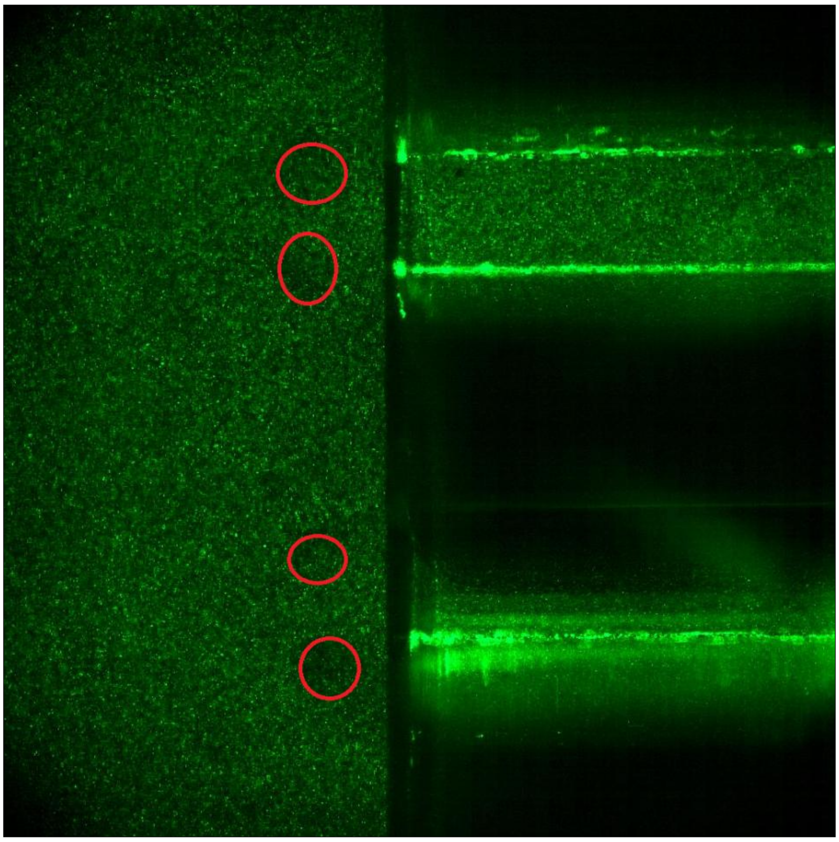

Figure 6.28 A selected raw image (index=6) from Run# 5G showing the air gaps inside vortex structures in red.

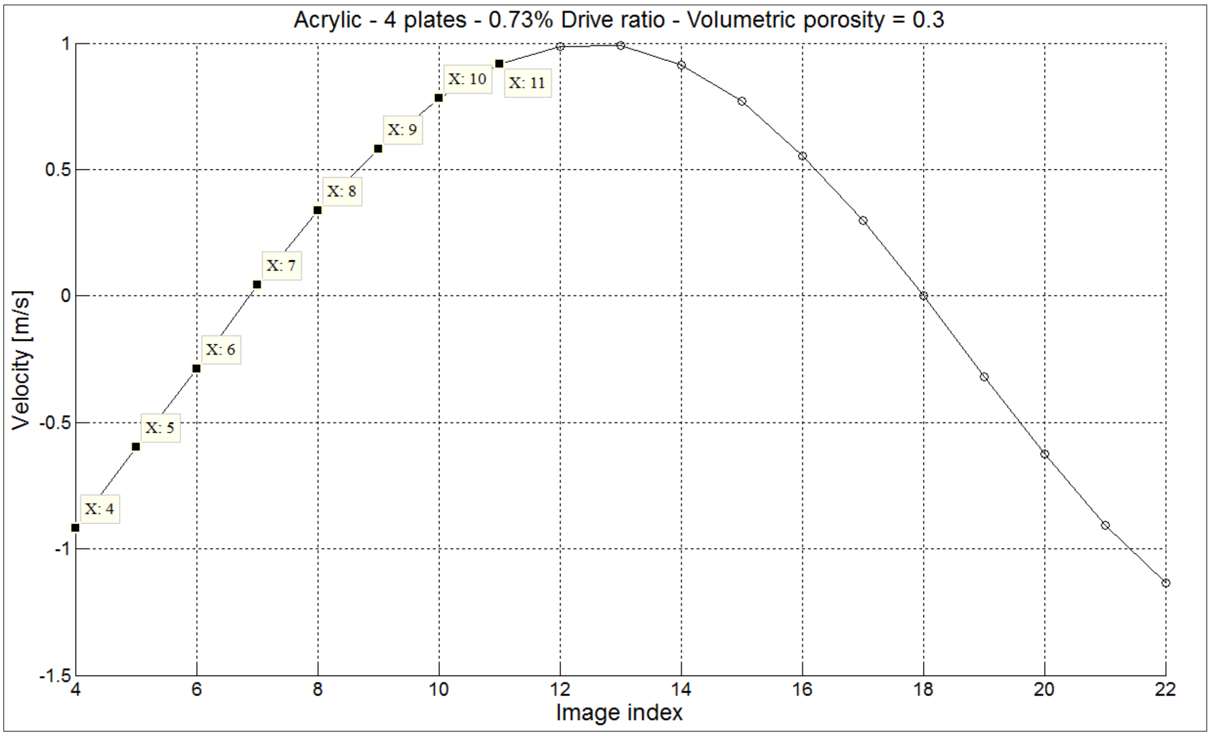

Figure 6.29 Part of the acoustic cycle from Run# 5G showing the indices of the vector maps shown in Figure 6.30

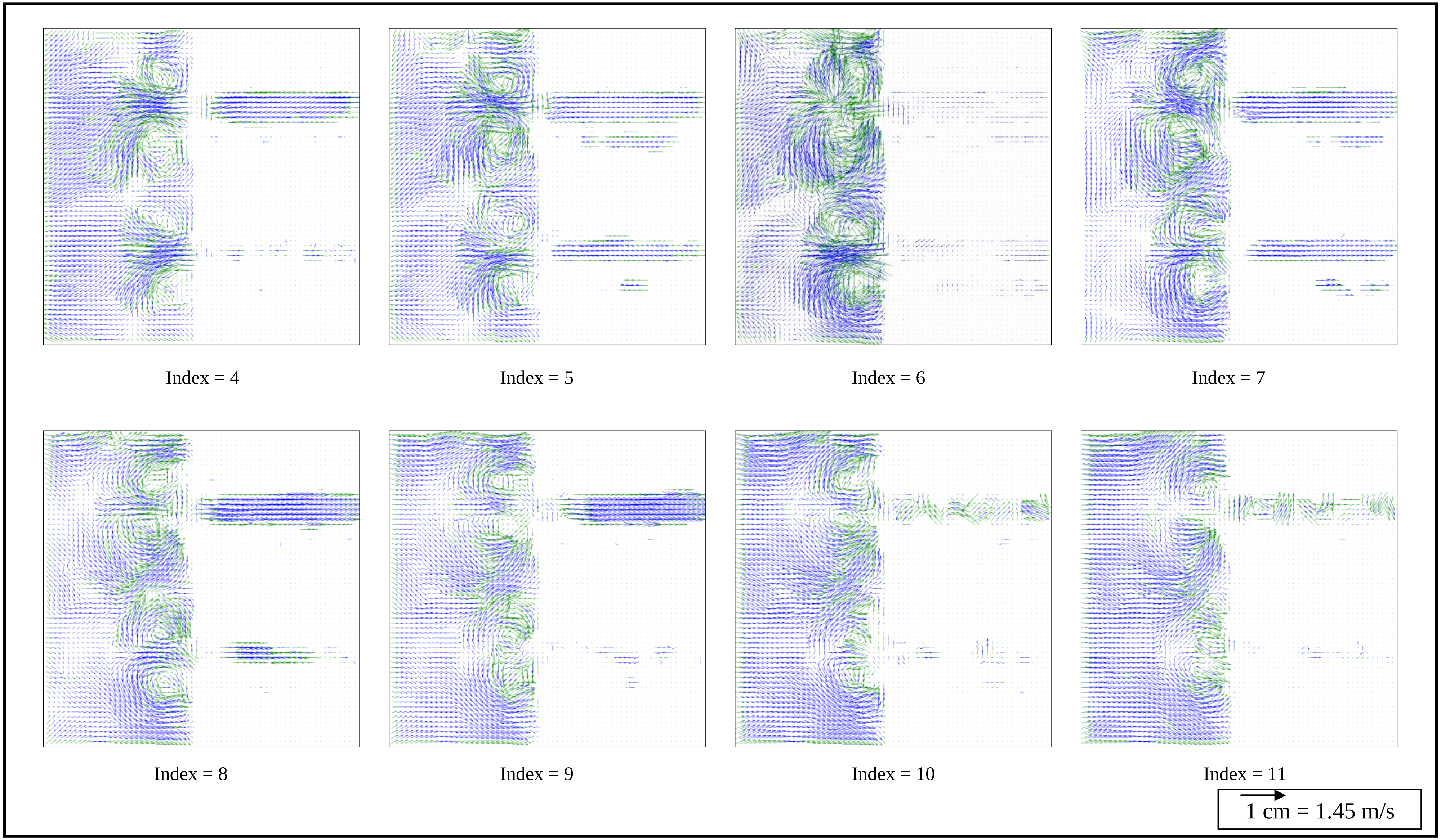

Index = 4

Index = 5

Index = 6

Index = 7

Index = 8

Index = 9

Index = 10

Index = 11

Figure 6.30 Vector maps of images having indices from 4 to 11 showing the development of vortex structures from Run# 5G.

Changing the plate spacing while returning to lower drive ratio (0.69%); it was confirmed that at low dynamic pressure the flow remains undisturbed all along. The cause of the few vectors occurring in the lower stack channel is attributed to glare effect rising from the reflection of the laser light sheet on the acrylic plate.

6.2.4. Acrylic – 4 plates – 1.24% Drive ratio

In order to investigate the effects of higher drive ratios, the drive ratio was increased from 0.69% to 1.24% at the same geometrical configuration of Run# 5G. Table 6.9 shows the measurement configuration for Run# 5H.

Table 6.9 Measurement configuration for Run# 5H

Run# 5H: Acrylic – 4 plates – 1.24% Drive ratio		
Function generator settings	**Resonance frequency [Hz]**	111
	Function generator voltage [V]	2.2
	Amplifier settings	-20 dB, -9 dB
	Voltage to speaker [V_{rms}]	8
Measured dynamic pressure	**Drive ratio [%]**	1.24
Parallel plates' configuration	**Stack location from back volume [mm]**	465
	Plate length [mm]	90
	Plate thickness [mm]	7
	Plate spacing [mm]	3
	Volumetric porosity [Open area/Total area]	0.3
Dimensionless numbers	**Re**	546
	St	0.12
	Wo	8.2
	KC	0.04
PIV settings	**Laser trigger rate [Hz]**	2700
	Time between pulses [μs]	185
	Field of view [mm^2]	20 x 20
	Laser energy [mJ]	9
	Interrogation area size [$Pixels^2$]	32 x 32
	Overlap [%]	50
	Analysis technique	Adaptive correlation

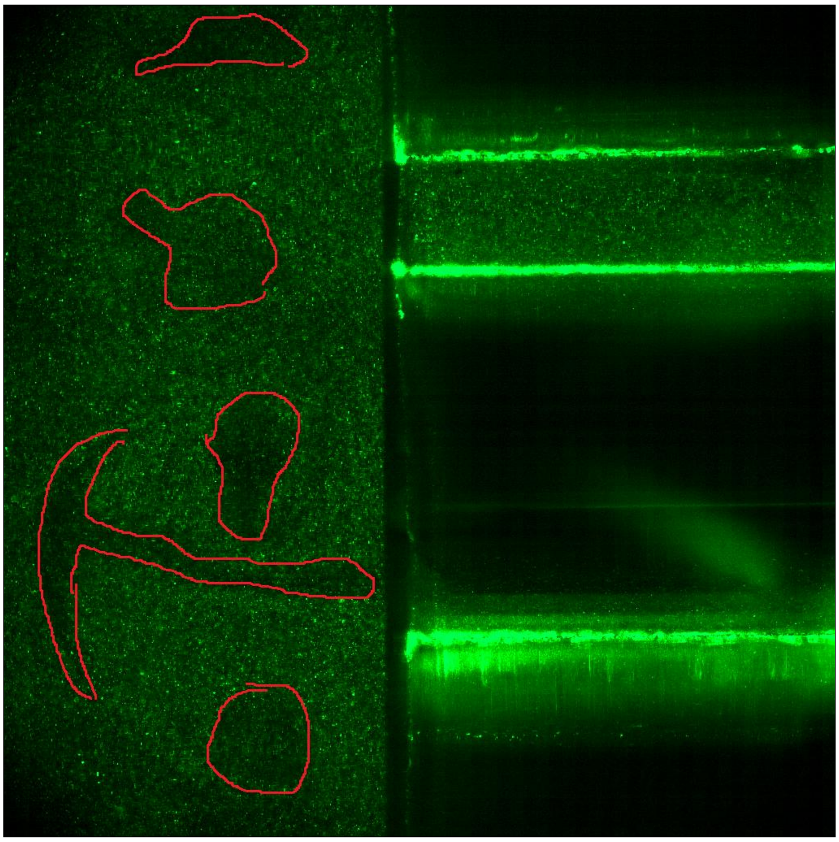

Figure 6.31 A selected raw image (index=3) from Run# 5H showing the air gaps inside vortex structures in red.

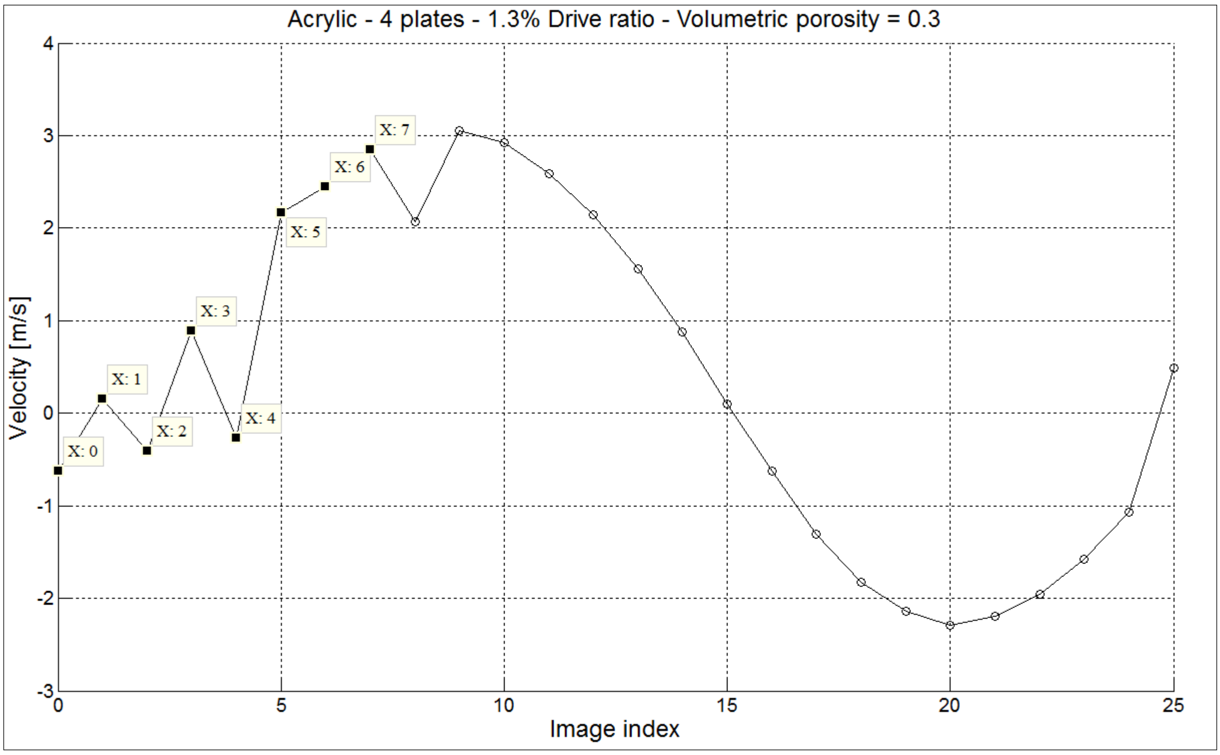

Figure 6.32 Part of the acoustic cycle from Run# 5H showing the indices of the vector maps shown in Figure 6.33.

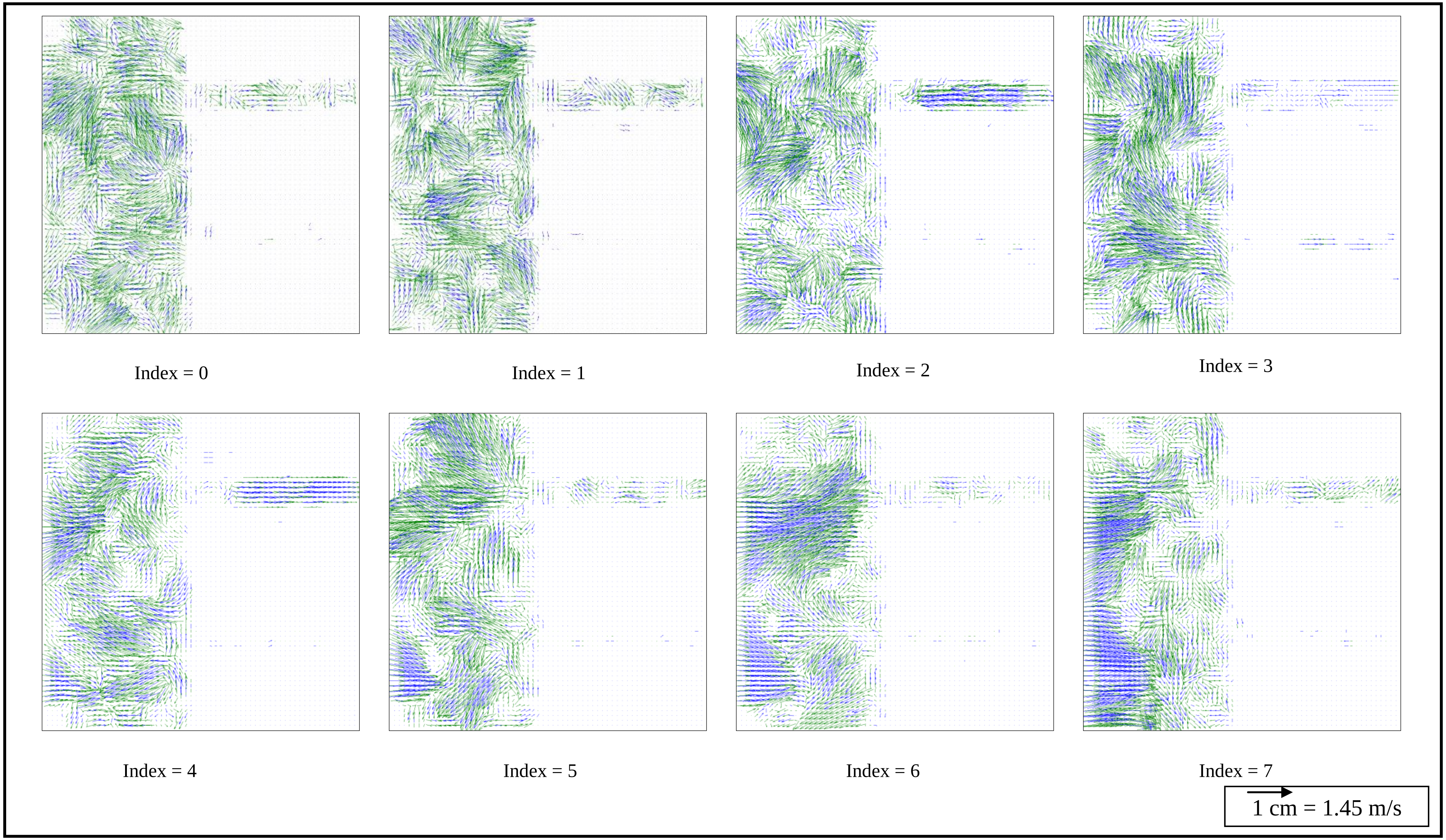

Figure 6.33 Vector maps of images having indices from 0 to 7 showing the development of vortex structures from Run# 5H.

Maintaining the small plate spacing and increasing the drive ratio (1.24%); it was observed that the amount of disturbance in between the plates is much greater than that observed at the lower drive ratio (0.69%) and even at a higher drive ratio but with larger plate spacing (Run# 5F). This was attributed to the smaller channel width that forces the vortex structures to interact together and produce greater disturbance even though the drive ratio is lower.

Chapter 7. **Summary and conclusions**

- Characterization of different properties of an electro-dynamic loudspeaker was performed. The parameters measured and estimated were the effective cone area (A_{eff}), the DC resistance (R_{DC}), the damped mechanical resonance frequency in the free field (f_o), the lumped stiffness (k), the lumped mass (m_o), the time constant (τ), the mechanical impedance (R_m), the electric impedance at resonance (Z_e), the coupling coefficient (Bl), the voice coil inductance (L) and the spectral behavior of impedance (Z). These parameters were used to simulate the performance of the electro-dynamic speaker as part of a thermoacoustic refrigerator system using DeltaEC software

- A prototype of a thermoacoustic refrigerator was built, operated and tested at no load. The prototype consisted of a loudspeaker, a quartz resonator and a meshed ceramic stack. The prototype was operated without heat exchangers. The dynamic pressure and air parcel velocity in part of the resonator were measured using microphones and PIV respectively. These measurements were made without stacks and with stacks of different porosities and lengths to quantify the blockage caused by the stack. The measurements indicated how changes in the stack parameters affect dynamic pressure, air parcel velocity and operating acoustic frequency. It was observed that the increase in stack length or porosity decreases the dynamic pressure, the air parcel velocity and slightly decreases the acoustic frequency. For example, an increase in stack porosity from 0% to 61% causes a decrease in dynamic pressure from 580 Pa to 523 Pa and a decrease in air parcel velocity from 1.4 m/s to 1.2 m/s. However further increase in porosity from 61% to 74% causes smaller decrease in velocity and pressure (from 1.2 m/s to 1.16 m/s and from 523 Pa to 479 Pa). The measured pressures and velocities were compared to simulations made by DeltaEC and reasonable agreements were found to be within 10% in pressure and 8% in velocity.

- The thermoacoustic refrigerator was operated with a set of parallel plates of different plate thicknesses and plate separations in order to visualize, using PIV the flow morphology at the plate edges and inside the gap between the plates in eight different configurations. Aluminum plates were used in four different configurations to visualize the flow pattern at the edges of the plates and acrylic plates were used in four different configurations to visualize the flow pattern inside the stack. The temporal parcel velocity behavior was recorded for each configuration. In general, the results showed that the higher the dynamic pressure the larger the core of the vortex is in terms of diameter and the larger is the disturbance away from the plate edges. The vortex size is always proportional to the plate thickness. It was also observed that decreasing the plate spacing has the effect of increasing the flow disturbance forcing the vortex structures generated near each other to interact and to form complex flow structures and increase the disturbance zone. The flow visualization inside the stack showed that the flow remains undisturbed in the channels between the stack plates as long as the amplitude is relatively low (0.69%, 0.73%, 0.76% and 0.78%). For higher drive ratios (1.24%, 1.3%, 1.82% and 1.84%), the flow becomes disturbed in the channels when vortex structures are pulled back inside the parallel plates' zone.

- The temporal behavior of the vortex generated in the thermoacoustic refrigerator was studied. It was observed that the vortex structure starts to initiate in the beginning of the rising half of the acoustic cycle. The vortex initiation starts at a maximum flow velocity and keeps increasing in size while decreasing in flow velocity till the flow velocity value reaches zero without affecting the vortex size. The flow then starts to increase in velocity while maintaining direction and also maintaining increase in vortex size. The maximum vortex size is reached at the end of the rising half of the acoustic cycle (i.e. when the flow starts to change direction again) and is accompanied by reaching the maximum velocity again but in the other direction. The falling half of the acoustic cycle experiences the same velocity behavior of the rising half cycle but with the diminishing of the vortex size.

- Vortex shedding was not observed. However, some outcomes showed vortex generates that were about to shed but were pulled back into the channels of the parallel plate sets. Through visual inspection, the existence of vortex shedding was observed to be a function of both the operating frequency and the dynamic pressure amplitude. Vortex shedding would occur if the period of the acoustic cycle is less than the time needed for a vortex to fully develop. The larger a vortex is, the more time it needs to fully develop. Thus, if the dynamic pressure is high and the frequency is high, the vortex size is large, the time it needs to fully develop is long and the period of the acoustic cycle is much less leading at the end to shedding.

Chapter 8. Recommendations and future work

- Decreasing the stack plate length allowing the observation of coupled flow structures that occur when the vortices of a new half acoustic cycle generated at plate edges interact with those generated from the previous half cycle that are propagating in between the plates.

- Flow visualization for complete thermoacoustic refrigerators (or engines) having heat exchanger components not just stacks.

- Flow visualization for *aerodynamic* plate edges to study the formation of vortex structures and entrance effects.

- Flow visualization of vortex structures occurring at the vicinity of meshed stacks with typical porosities (100 CPSI, 200 CPSI, 400 CPSI and 600 CPSI).

- Quantifying the effects of vortex generation on the overall energy conversion efficiency.

Bibliography

[1] D. Hann and C. Greated, "The measurement of flow velocity and acoustic particle velocity using particle image velocimetry," *Meas. Sci. Tecnol*, vol. 8, pp. 1517-1522, 1997.

[2] A. Tonddast-Navaei and D. Sharp, "PIV study of standing waves in a resonant air column," 2008.

[3] A. Fischer, E. Sauvage, and I. Röhle, "Acoustic PIV: Measurements of the acoustic particle velocity using synchronized PIV-technique," in *14th Int Symp on Applications of Laser Techniques to Fluid Mechanics*, Lisbon, Portugal, 2008.

[4] M. Nabavi, K. Siddiqui, and J. Dargahi, "Measurement of the acoustic velocity field of nonlinear standing waves using the synchronized PIV technique," *Experimental Thermal and Fluid Science*, vol. 33, pp. 123–131, 2008.

[5] K. Siddiqui and M. Nabavi, "Measurement of the acoustic velocity characteristics in a standing-wave tube using out of phase PIV," *Flow measurement and instrumentation*, vol. 19, pp. 364-369, 2008.

[6] Y. Rafat and L. Mongeau, "Time-resolved Particle Image Velocimetry of the flow in an acoustic standing wave tube," in *Proceedings of 20th International Congress on Acoustics, ICA 2010*, Sydney, Australia, 2010.

[7] P. Blanc-Benon, E. Besnoin, and O. Knio, "Experimental and computational visualization of the flow field in a thermoacoustic stack," *C. R. Mecanique*, vol. 331, pp. 17–24, 2003.

[8] A. Berson, M. Michard, and P. Blanc-Benon, "Measurement of acoustic velocity in the stack of a thermoacoustic refrigerator using particle image velocimetry," *Heat Mass Transfer*, vol. 44, pp. 1015–1023, 2008.

[9] X. Mao, D. Marx, and A. Jaworski, "PIV studies of coherent structures generated at the end of a stack of parallel plates in a standing wave acoustic field,"*Experiments in Fluids*, vol. 45, no. 5, pp. 833–846, 2008.

[10] P. Debesse, D. Baltean-Carlèsa, F. Lusseyra, and M.X. François, "Experimental analysis of nonlinear phenomena in a thermoacousitc system," in *Nonlinear Acoustics—Fundamentals and Applications (ISNA 18), 18th International Symposium*.

[11] P. Aben, P. Bloemen, and J. Zeegers, "2-D PIV measurements of oscillatory flow around parallel plates," *Exp Fluids*, vol. 46, pp. 631–641, 2009.

[12] A. Jaworski, X. Mao, X. Mao, and Z. Yu, "Entrance effects in the channels of the parallel plate stack in oscillatory flow conditions," *Experimental Thermal and Fluid Science*, vol. 33, pp. 495–502, 2009.

[13] X. Mao, L. Shi, and A. Jaworski, "Non-dimensional parameters controlling the behavior of oscillatory flows around stacks of parallel plates in thermoacoustic devices," in *The 16th Internationl Congress on Sound and Vibration*, Krakow, Poland, 2009.

[14] L. Shi, Z. Yu, and A. Jaworski, "Vortex formation at the end of the parallel-plate stack in the standing-wave thermoacosutic device," in *The 16th International Congress on Sound and Vibration*, Krakow, Poland, 2009.

[15] L. Shi, Z. Yu, A. Jaworski, and A. Abduljalil, "Vortex shedding at the end of parallel-plate thermoacoustic stack in the oscillatory flow conditions," *World Academy of Science, Engineering and Technology*, vol. 49, 2009.

[16] H. Babaei and K. Siddiqui, "Investigation of the streaming flow patterns in a thermoacosutic device using PIV," in *Proceedings of the ASME 2010 3rd Joint US-European Fluids Engineering summer Meeting and 8th International Conference on Nanochannles, Microshcannels and minichannels*, Montreal, Canada, 2010.

[17] X. Mao and A. Jawroski, "Application of particle image velocimetry measurement techniques to study turbulence characterisitcs of oscillatory flows around parallel-plate structures in thermoacoustic devices," *Meas. Sci. Technol*, vol. 21, 2010.

[18] L. Shi, Z. Yu, and A. Jaworski, "Application of laser-based instrumentation for measurement of time-resolved temperature and velocity fields in the thermoacoustic system," *International Journal of Thermal Sciences*, vol. 49, p. 2010.

[19] L. Shi, Z. Yu, and A. Jaworski, "et al., Vortex shedding flow patterns and their transitions in oscillatory flows past parallel-plate thermoacoustic stacks," *Experimental Thermal and Fluid Science*, vol. 34, pp. 954–965, 2010.

[20] T. Rossing, *Springer Handbook of acoustic*, Rossing, Ed. New York,USA: Springer Science + Business Media, 2007.

[21] F. Everest and K. Pohlmann, *Master handbook of acoustics*, 5th ed.: McGraw Hill, 2009.

[22] G. Swift, *Thermoacoustics: A unifying perspective for some engines and refrigerators*.: Los Alamos National Laboratory, 2001.

[23] Wikipedia. Wikipedia. [Online]. http://en.wikipedia.org/wiki/Thermoacoustics

[24] G. Swift, "Thermocaoustic engines and refrigerators," *Physics Today*, pp. 22-36, July 1995.

[25] M. Raffel, C. Willert, S. Wereley, and J. Kompenhans, *Particle Image Velocimetry*, Second, Ed. New York: Springer Berlin Heidelberg, 2007.

[26] A. Melling, "Tracer particles and seeding for particle image velocimetry," *Meas. Sci. Technol.*, vol. 8, pp. 1406-1416, 1997.

[27] Tornblom, O. - KTH(Royal Institute of Technology Sweden), "Introduction course in particle image velocimetry," 2004.

[28] A. Prasad, "Particle image velocimetry - review article," *Current Science*, vol. 79, 2000.

[29] J. Kitzhofer, F. Ergin, and V. Jaunet, "2D Least Squares Matching applied to PIV Challenge data (Part 1)," in *16th Int Symp on Applications of Laser Techniques to Fluid Mechanics*, Lisbon, Portugal, 2012.

[30] Dantec Dynamics. [Online]. www.dantecdynamics.com

[31] G. Swift. Thermoacoustics. [Online]. www.lanl.gov/thermoacoustics

[32] G. Swift, "Analysis and performance of a large thermoacoustic engine," *J. Aouct. Soc. AM*, vol. 92, no. 3, pp. 1551-1563, 1992.

[33] Bockaert. Digital Photography Review.[Online]
http://www.dpreview.com/learn/?/Glossary/

[34] Digital Photography Review. [Online]. www.drreview.com

[35] Nikon Inc. Nikon USA. [Online]. http://www.nikonusa.com/Learn-And-Explore/Nikon-Camera-Technology/gnhy8b3m/1/Macro-Lenses.html

[36] Wikipedia. Wikipedia. [Online]. http://en.wikipedia.org/wiki/Color_depth

[37] V. Dickason, *Loudspeaker design cookbook*, 7th ed. Peterborough, New Hampshire: Audio Amatuer Press, 2006.

[38] DJ Society. [Online]. www.djsociety.org

[39] wikibooks.org. (2010) wikibooks. [Online].
http://en.wikibooks.org/wiki/Engineering_Acoustics/Moving_Coil_Loudspeaker

[40] Engineering Acoustics - Wikibooks. [Online].
http://en.wikibooks.org/wiki/Engineering_Acoustics/Moving_Coil_Loudspeaker

[41] Weber. (1998) Weber VST. [Online]. http://www.webervst.com/spkrcalc/para.htm

[42] Elliott. (2007) Elliott Sound Products. [Online]. http://sound.westhost.com/tsp.htm

[43] Walker. (2012) Wikipedia. [Online]. http://en.wikipedia.org/wiki/Acoustic_impedance

[44] Texas Austin SPL. (2012) uTexas. [Online].
http://www.arlut.utexas.edu/spl/industrial.html

Appendix A Measurement results of setup configuration [D] used for plotting acoustic impedance versus frequency.

Frequency	**Period**	**Loudspeaker peak -to- peak voltage**	**Resistance Peak -to- peak voltage**	**Loudspeaker Current**	**Loudspeaker Impedance**	**Time difference**	**Phase shift**	**Re (Z)**	**Im(Z)**
f [Hz]	**1/f [sec]**	**$V_{speaker}$ [V]**	**$V_{resistance}$ [V]**	**I [Ampere]**	**Z [Ohms]**	**t [sec]**	**φ [Degree]**		
10	0.1000	0.134	7.6	0.0197	6.7917	0.0524	8.64	6.715	1.020
20	0.0500	0.142	8.4	0.0218	6.5117	0.0254	2.88	6.503	0.327
30	0.0333	0.160	8.8	0.0228	7.0036	0.0180	14.40	6.784	1.742
40	0.0250	0.162	9	0.0234	6.9336	0.0136	15.84	6.670	1.893
50	0.0200	0.170	8.8	0.0228	7.4414	0.0108	14.40	7.208	1.851
60	0.0167	0.184	8.8	0.0228	8.0542	0.0088	10.08	7.930	1.410
70	0.0143	0.204	8.8	0.0228	8.9296	0.0084	31.68	7.599	4.690
80	0.0125	0.252	8.8	0.0228	11.0307	0.0076	38.88	8.587	6.924
90	0.0111	0.340	8.8	0.0228	14.8827	0.0068	40.32	11.347	9.630
91	0.0110	0.356	8.8	0.0228	15.5831	0.0064	29.66	13.541	7.712
92	0.0109	0.384	8.8	0.0228	16.8087	0.0060	18.72	15.920	5.395
93	0.0108	0.384	8.8	0.0228	16.8087	0.0060	20.88	15.705	5.991
94	0.0106	0.400	8.8	0.0228	17.5091	0.0060	23.04	16.112	6.853

Frequency	**Period**	**Loudspeaker peak -to- peak voltage**	**Resistance Peak -to- peak voltage**	**Loudspeaker Current**	**Loudspeaker Impedance**	**Time difference**	**Phase shift**	**Re (Z)**	**Im(Z)**
f [Hz]	**1/f [sec]**	**$V_{speaker}$ [V]**	**$V_{resistance}$ [V]**	**I [Ampere]**	**Z [Ohms]**	**t [sec]**	**φ [Degree]**		
95	0.0105	0.416	8.8	0.0228	18.2095	0.0060	25.20	16.476	7.753
96	0.0104	0.432	8.8	0.0228	18.9098	0.0056	13.54	18.385	4.426
97	0.0103	0.440	8.8	0.0228	19.2600	0.0056	15.55	18.555	5.164
98	0.0102	0.448	8.8	0.0228	19.6102	0.0052	3.46	19.575	1.182
99	0.0101	0.472	8.6	0.0223	21.1412	0.0052	5.33	21.050	1.963
100	0.0100	0.480	8.8	0.0228	21.0109	0.0052	7.20	20.845	2.633
101	0.0099	0.488	8.8	0.0228	21.3611	0.0052	9.07	21.094	3.368
102	0.0098	0.488	8.6	0.0223	21.8579	0.0050	3.60	21.815	1.372
103	0.0097	0.488	8.8	0.0228	21.3611	0.0050	5.40	21.266	2.010
104	0.0096	0.488	8.8	0.0228	21.3611	0.0048	-0.29	21.361	-0.107
105	0.0095	0.480	8.6	0.0223	21.4995	0.0048	1.44	21.493	0.540
106	0.0094	0.480	8.8	0.0228	21.0109	0.0046	-4.46	20.947	-1.635
107	0.0093	0.472	8.8	0.0228	20.6607	0.0044	-10.51	20.314	-3.769
108	0.0093	0.464	8.8	0.0228	20.3105	0.0044	-8.93	20.064	-3.152
109	0.0092	0.464	8.8	0.0228	20.3105	0.0044	-7.34	20.144	-2.596

Frequency	Period	Loudspeaker peak -to- peak voltage	Resistance Peak -to- peak voltage	Loudspeaker Current	Loudspeaker Impedance	Time difference	Phase shift	Re (Z)	Im(Z)
f [Hz]	1/f [sec]	$V_{speaker}$ [V]	$V_{resistance}$ [V]	I [Ampere]	Z [Ohms]	t [sec]	φ [Degree]		
110	0.0091	0.448	8.8	0.0228	19.6102	0.0044	-5.76	19.511	-1.968
120	0.0083	0.368	8.8	0.0228	16.1084	0.0034	-33.12	13.491	-8.802
130	0.0077	0.292	9	0.0234	12.4976	0.0032	-30.24	10.797	-6.294
140	0.0071	0.252	9	0.0234	10.7856	0.0030	-28.80	9.451	-5.196
150	0.0067	0.232	9	0.0234	9.9296	0.0027	-34.20	8.213	-5.581
160	0.0063	0.208	9	0.0234	8.9024	0.0026	-30.24	7.691	-4.483
170	0.0059	0.196	9	0.0234	8.3888	0.0026	-20.88	7.838	-2.990
180	0.0056	0.188	9	0.0234	8.0464	0.0025	-18.00	7.653	-2.486
190	0.0053	0.180	9	0.0234	7.7040	0.0025	-9.00	7.609	-1.205
200	0.0050	0.176	9	0.0234	7.5328	0.0024	-7.20	7.473	-0.944
250	0.0040	0.168	8.8	0.0228	7.3538	0.0020	0.00	7.354	0.000
300	0.0033	0.160	9	0.0234	6.8480	0.0017	5.76	6.813	0.687
350	0.0029	0.156	9	0.0234	6.6768	0.0015	6.48	6.634	0.754
400	0.0025	0.156	9	0.0234	6.6768	0.0013	4.32	6.658	0.503
450	0.0022	0.160	9	0.0234	6.8480	0.0012	14.40	6.633	1.703

Frequency	**Period**	**Loudspeaker peak -to- peak voltage**	**Resistance Peak -to- peak voltage**	**Loudspeaker Current**	**Loudspeaker Impedance**	**Time difference**	**Phase shift**	**Re (Z)**	**Im(Z)**
f [Hz]	**1/f [sec]**	**$V_{speaker}$ [V]**	**$V_{resistance}$ [V]**	**I [Ampere]**	**Z [Ohms]**	**t [sec]**	**φ [Degree]**		
500	0.0020	0.162	9	0.0234	6.9336	0.0011	14.40	6.716	1.724
600	0.0017	0.164	9	0.0234	7.0192	0.0009	10.08	6.911	1.229
700	0.0014	0.166	9	0.0234	7.1048	0.0008	26.64	6.351	3.186
800	0.0013	0.174	9	0.0234	7.4472	0.0007	33.12	6.237	4.069
900	0.0011	0.176	9	0.0234	7.5328	0.0007	33.84	6.257	4.195
1000	0.0010	0.182	8.8	0.0228	7.9666	0.0006	28.80	6.981	3.838
1500	0.0007	0.204	9	0.0234	8.7312	0.0004	46.80	5.977	6.365
2000	0.0005	0.232	8.8	0.0228	10.1553	0.0003	57.60	5.441	8.574

Appendix B MATLAB code for calculating the ratio of tracer particles' speed to flow speed.

```
close all, clear all,clc

% Calculation of the ratio of particle response time to period of acoustic
% wave
rhom=1.2;       % Density of fluid
rhop=4000;       % Density of particle
D=0.41e-6;       % Particle diameter
mu=1.5e-5;      % Kinematic viscosity of fluid
freq=150;       % Operating frequency (20 Hz + Maximum resonance)
gamma=rhop/rhom;
tp=(gamma-1)*(D^2)/18/mu;%Particle response time
tf=1/freq;               %Period of acoustic wave
disp(['Ratio of Flow Velocity to Particle Velocity = ' num2str(tf/tp)])
```

Appendix C MATLAB code for performing spatial analysis of velocities measured using PIV.

Code (1): File name displayer: Used to write a part in the second code that is responsible for reading the files exported from the PIV software

```
close all,clear all, clc

% This code is used to write the first lines of the "Plotter" code that are
% responsible for reading the ".csv" files exported from the PIV
% software Dynamic Studio. For each measurement location around 2700 images
% are taken, each image is a 1024x1024 pixels2 in size. For an
% interrogation area of 128x128 pixles2 with 50% overlap, the number of
% vectors per map is 256 maps. Each vector map is exported as a single
% ".csv" file. Thus a large number of files is exported and each has to
% imported into MATLAB individually. Files' reading is done through [for]
% loops due to their large number. The values above the loops are the
% location of the measurement along the resonator’s length measured from
% the loudspeaker.



% Each loop builds a filename and the code that reads the file. The
% filename is written manually as exported from the PIV software
% and the numbers of zeros in the filename depend on the image number.
% For example in the loop from 1:10 only one vacancy is required in the
% file name so one zero is removed from the original six and five remain.
% For the loop from 11:100 two vacancies are required in the filename so
% two zeros are removed.

% The values (11,0) at the end of code line represent the number of the
% cell in the excel file that MATLAB will start reading the values from.
% The exported files include information at the beginning and the vector
% values start from cell no. 11 in column no. 1


%200

for i=1:10
    disp(['M200(:,' num2str(i) ')=csvread(''200.2wmoqgxv.00000' num2str(i-
1)
        '.csv'',11,0);'])
end

for i=11:100
    disp(['M200(:,' num2str(i) ')=csvread(''200.2wmoqgxv.0000' num2str(i-1)
'.csv'',11,0);'])
end

for i=101:139
    disp(['M200(:,' num2str(i) ')=csvread(''200.2wmoqgxv.000' num2str(i-1)
'.csv'',11,0);'])
end


%250
```

```
for i=1:10
    disp(['M250(:,' num2str(i) ')=csvread(''250.2wmowms8.00000' num2str(i-
1) '.csv'',11,0);'])
end

for i=11:99
    disp(['M250(:,' num2str(i) ')=csvread(''250.2wmowms8.0000' num2str(i-1)
'.csv'',11,0);'])
end

for i=101:139
    disp(['M250(:,' num2str(i) ')=csvread(''250.2wmowms8.000' num2str(i-1)
'.csv'',11,0);'])
end


%300

for i=1:10
    disp(['M300(:,' num2str(i) ')=csvread(''300.2wmp0x4w.00000' num2str(i-
1) '.csv'',11,0);'])
end

for i=11:99
    disp(['M300(:,' num2str(i) ')=csvread(''300.2wmp0x4w.0000' num2str(i-1)
'.csv'',11,0);'])
end

for i=101:139
    disp(['M300(:,' num2str(i) ')=csvread(''300.2wmp0x4w.000' num2str(i-1)
'.csv'',11,0);'])
end


%350

for i=1:10
    disp(['M350(:,' num2str(i) ')=csvread(''350.2wmp4h29.00000' num2str(i-
1) '.csv'',11,0);'])
end

for i=11:99
    disp(['M350(:,' num2str(i) ')=csvread(''350.2wmp4h29.0000' num2str(i-1)
'.csv'',11,0);'])
end

for i=101:139
    disp(['M350(:,' num2str(i) ')=csvread(''350.2wmp4h29.000' num2str(i-1)
'.csv'',11,0);'])
end


%400
for i=1:10
    disp(['M400(:,' num2str(i) ')=csvread(''400.2wmp8bb4.00000' num2str(i-
1) '.csv'',11,0);'])
end

for i=11:99
    disp(['M400(:,' num2str(i) ')=csvread(''400.2wmp8bb4.0000' num2str(i-1)
'.csv'',11,0);'])
end
```

```
for i=101:139
    disp(['M400(:,' num2str(i) ')=csvread(''400.2wmp8bb4.000' num2str(i-1)
'.csv'',11,0);'])
end

%450
for i=1:10
    disp(['M450(:,' num2str(i) ')=csvread(''450.2wmpd9nr.00000' num2str(i-
1) '.csv'',11,0);'])
end

for i=11:99
    disp(['M450(:,' num2str(i) ')=csvread(''450.2wmpd9nr.0000' num2str(i-1)
'.csv'',11,0);'])
end

for i=101:139
    disp(['M450(:,' num2str(i) ')=csvread(''450.2wmpd9nr.000' num2str(i-1)
'.csv'',11,0);'])
end

%500
for i=1:10
    disp(['M500(:,' num2str(i) ')=csvread(''500.2wmph1yf.00000' num2str(i-
1) '.csv'',11,0);'])
end

for i=11:99
    disp(['M500(:,' num2str(i) ')=csvread(''500.2wmph1yf.0000' num2str(i-1)
'.csv'',11,0);'])
end

for i=101:139
    disp(['M500(:,' num2str(i) ')=csvread(''500.2wmph1yf.000' num2str(i-1)
'.csv'',11,0);'])
end
```

Code (2): Plotter: Used in averaging vector maps, plotting temporal acoustic behavior at each location, selecting maximum amplitudes, applying calibration and plotting the final spatial plot. For space saving purposes some lines that are repeated and do not affect the code illustration are removed. These removed lines are part of the result of the first code “File name displayer”.

```
close all, clear all, clc

% The following lines are the output of the first code "Filename Displayer"
% These lines are used to read the files exported from the PIV software
% that contain the velocity vector values.


% The vector values are imported into matrices where each column represents
% a point in the acoustic cycle and the following columns represents the
% following point in the cycle. Each matrix then contains the all the
% values of one measurement point (e.g. M200 contains all the acoustic
cycle
% values at 200 mm from the loudspeaker)


M200(:,1)=csvread('200.2wmoqgxv.000000.csv',11,0);
M200(:,2)=csvread('200.2wmoqgxv.000001.csv',11,0);
M200(:,3)=csvread('200.2wmoqgxv.000002.csv',11,0);
M200(:,4)=csvread('200.2wmoqgxv.000003.csv',11,0);
M200(:,5)=csvread('200.2wmoqgxv.000004.csv',11,0);
M200(:,6)=csvread('200.2wmoqgxv.000005.csv',11,0);
M200(:,7)=csvread('200.2wmoqgxv.000006.csv',11,0);
M200(:,8)=csvread('200.2wmoqgxv.000007.csv',11,0);
M200(:,9)=csvread('200.2wmoqgxv.000008.csv',11,0);
M200(:,10)=csvread('200.2wmoqgxv.000009.csv',11,0);
M200(:,11)=csvread('200.2wmoqgxv.000010.csv',11,0);
M200(:,12)=csvread('200.2wmoqgxv.000011.csv',11,0);
M200(:,13)=csvread('200.2wmoqgxv.000012.csv',11,0);
M200(:,14)=csvread('200.2wmoqgxv.000013.csv',11,0);
M200(:,15)=csvread('200.2wmoqgxv.000014.csv',11,0);
M250(:,1)=csvread('250.2wmowms8.000000.csv',11,0);
M250(:,2)=csvread('250.2wmowms8.000001.csv',11,0);
M250(:,3)=csvread('250.2wmowms8.000002.csv',11,0);
M250(:,4)=csvread('250.2wmowms8.000003.csv',11,0);
M250(:,5)=csvread('250.2wmowms8.000004.csv',11,0);
M250(:,6)=csvread('250.2wmowms8.000005.csv',11,0);
M250(:,7)=csvread('250.2wmowms8.000006.csv',11,0);
M250(:,8)=csvread('250.2wmowms8.000007.csv',11,0);
M250(:,9)=csvread('250.2wmowms8.000008.csv',11,0);
M250(:,10)=csvread('250.2wmowms8.000009.csv',11,0);
M250(:,11)=csvread('250.2wmowms8.000010.csv',11,0);
M250(:,12)=csvread('250.2wmowms8.000011.csv',11,0);
M250(:,13)=csvread('250.2wmowms8.000012.csv',11,0);
M250(:,14)=csvread('250.2wmowms8.000013.csv',11,0);
M250(:,15)=csvread('250.2wmowms8.000014.csv',11,0);
M300(:,1)=csvread('300.2wmp0x4w.000000.csv',11,0);
M300(:,2)=csvread('300.2wmp0x4w.000001.csv',11,0);
M300(:,3)=csvread('300.2wmp0x4w.000002.csv',11,0);
M300(:,4)=csvread('300.2wmp0x4w.000003.csv',11,0);
M300(:,5)=csvread('300.2wmp0x4w.000004.csv',11,0);
M300(:,6)=csvread('300.2wmp0x4w.000005.csv',11,0);
M300(:,7)=csvread('300.2wmp0x4w.000006.csv',11,0);
M300(:,8)=csvread('300.2wmp0x4w.000007.csv',11,0);
```

```
M300(:,9)=csvread('300.2wmp0x4w.000008.csv',11,0);
M300(:,10)=csvread('300.2wmp0x4w.000009.csv',11,0);
M300(:,11)=csvread('300.2wmp0x4w.000010.csv',11,0);
M300(:,12)=csvread('300.2wmp0x4w.000011.csv',11,0);
M300(:,13)=csvread('300.2wmp0x4w.000012.csv',11,0);
M300(:,14)=csvread('300.2wmp0x4w.000013.csv',11,0);
M300(:,15)=csvread('300.2wmp0x4w.000014.csv',11,0);
M350(:,1)=csvread('350.2wmp4h29.000000.csv',11,0);
M350(:,2)=csvread('350.2wmp4h29.000001.csv',11,0);
M350(:,3)=csvread('350.2wmp4h29.000002.csv',11,0);
M350(:,4)=csvread('350.2wmp4h29.000003.csv',11,0);
M350(:,5)=csvread('350.2wmp4h29.000004.csv',11,0);
M350(:,6)=csvread('350.2wmp4h29.000005.csv',11,0);
M350(:,7)=csvread('350.2wmp4h29.000006.csv',11,0);
M350(:,8)=csvread('350.2wmp4h29.000007.csv',11,0);
M350(:,9)=csvread('350.2wmp4h29.000008.csv',11,0);
M350(:,10)=csvread('350.2wmp4h29.000009.csv',11,0);
M350(:,11)=csvread('350.2wmp4h29.000010.csv',11,0);
M350(:,12)=csvread('350.2wmp4h29.000011.csv',11,0);
M350(:,13)=csvread('350.2wmp4h29.000012.csv',11,0);
M350(:,14)=csvread('350.2wmp4h29.000013.csv',11,0);
M350(:,15)=csvread('350.2wmp4h29.000014.csv',11,0);
M400(:,1)=csvread('400.2wmp8bb4.000000.csv',11,0);
M400(:,2)=csvread('400.2wmp8bb4.000001.csv',11,0);
M400(:,3)=csvread('400.2wmp8bb4.000002.csv',11,0);
M400(:,4)=csvread('400.2wmp8bb4.000003.csv',11,0);
M400(:,5)=csvread('400.2wmp8bb4.000004.csv',11,0);
M400(:,6)=csvread('400.2wmp8bb4.000005.csv',11,0);
M400(:,7)=csvread('400.2wmp8bb4.000006.csv',11,0);
M400(:,8)=csvread('400.2wmp8bb4.000007.csv',11,0);
M400(:,9)=csvread('400.2wmp8bb4.000008.csv',11,0);
M400(:,10)=csvread('400.2wmp8bb4.000009.csv',11,0);
M400(:,11)=csvread('400.2wmp8bb4.000010.csv',11,0);
M400(:,12)=csvread('400.2wmp8bb4.000011.csv',11,0);
M400(:,13)=csvread('400.2wmp8bb4.000012.csv',11,0);
M400(:,14)=csvread('400.2wmp8bb4.000013.csv',11,0);
M400(:,15)=csvread('400.2wmp8bb4.000014.csv',11,0);
M450(:,1)=csvread('450.2wmpd9nr.000000.csv',11,0);
M450(:,2)=csvread('450.2wmpd9nr.000001.csv',11,0);
M450(:,3)=csvread('450.2wmpd9nr.000002.csv',11,0);
M450(:,4)=csvread('450.2wmpd9nr.000003.csv',11,0);
M450(:,5)=csvread('450.2wmpd9nr.000004.csv',11,0);
M450(:,6)=csvread('450.2wmpd9nr.000005.csv',11,0);
M450(:,7)=csvread('450.2wmpd9nr.000006.csv',11,0);
M450(:,8)=csvread('450.2wmpd9nr.000007.csv',11,0);
M450(:,9)=csvread('450.2wmpd9nr.000008.csv',11,0);
M450(:,10)=csvread('450.2wmpd9nr.000009.csv',11,0);
M450(:,11)=csvread('450.2wmpd9nr.000010.csv',11,0);
M450(:,12)=csvread('450.2wmpd9nr.000011.csv',11,0);
M450(:,13)=csvread('450.2wmpd9nr.000012.csv',11,0);
M450(:,14)=csvread('450.2wmpd9nr.000013.csv',11,0);
M450(:,15)=csvread('450.2wmpd9nr.000014.csv',11,0);
M500(:,1)=csvread('500.2wmph1yf.000000.csv',11,0);
M500(:,2)=csvread('500.2wmph1yf.000001.csv',11,0);
M500(:,3)=csvread('500.2wmph1yf.000002.csv',11,0);
M500(:,4)=csvread('500.2wmph1yf.000003.csv',11,0);
M500(:,5)=csvread('500.2wmph1yf.000004.csv',11,0);
M500(:,6)=csvread('500.2wmph1yf.000005.csv',11,0);
M500(:,7)=csvread('500.2wmph1yf.000006.csv',11,0);
M500(:,8)=csvread('500.2wmph1yf.000007.csv',11,0);
M500(:,9)=csvread('500.2wmph1yf.000008.csv',11,0);
M500(:,10)=csvread('500.2wmph1yf.000009.csv',11,0);
M500(:,11)=csvread('500.2wmph1yf.000010.csv',11,0);
M500(:,12)=csvread('500.2wmph1yf.000011.csv',11,0);
M500(:,13)=csvread('500.2wmph1yf.000012.csv',11,0);
```

```
M500(:,14)=csvread('500.2wmph1yf.000013.csv',11,0);
M500(:,15)=csvread('500.2wmph1yf.000014.csv',11,0);
M550(:,1)=csvread('550.2wmpmqvl.000000.csv',11,0);
M550(:,2)=csvread('550.2wmpmqvl.000001.csv',11,0);
M550(:,3)=csvread('550.2wmpmqvl.000002.csv',11,0);
M550(:,4)=csvread('550.2wmpmqvl.000003.csv',11,0);
M550(:,5)=csvread('550.2wmpmqvl.000004.csv',11,0);
M550(:,6)=csvread('550.2wmpmqvl.000005.csv',11,0);
M550(:,7)=csvread('550.2wmpmqvl.000006.csv',11,0);
M550(:,8)=csvread('550.2wmpmqvl.000007.csv',11,0);
M550(:,9)=csvread('550.2wmpmqvl.000008.csv',11,0);
M550(:,10)=csvread('550.2wmpmqvl.000009.csv',11,0);
M550(:,11)=csvread('550.2wmpmqvl.000010.csv',11,0);
M550(:,12)=csvread('550.2wmpmqvl.000011.csv',11,0);
M550(:,13)=csvread('550.2wmpmqvl.000012.csv',11,0);
M550(:,14)=csvread('550.2wmpmqvl.000013.csv',11,0);
M550(:,15)=csvread('550.2wmpmqvl.000014.csv',11,0);


% The following commands define the sizes of the matrices which represent
% the number of images to accommodate for different numbers of images if
% present

s200=size(M200);s250=size(M250);s300=size(M300);
s350=size(M350);s400=size(M400);s450=size(M450);
s500=size(M500);s550=size(M550);

% The following commands are responsible for averaging the values of each
% vector map to produce one value for each point in the acoustic cycle

r200=mean(M200);r250=mean(M250);r300=mean(M300);
r350=mean(M350);r400=mean(M400);r450=mean(M450);
r500=mean(M500);r550=mean(M550);

% The following commands are used to build the x-axis matrix using the
% number of images for each measurement location

t200=0:s200(2)-1;t250=0:s250(2)-1;t300=0:s300(2)-1;
t350=0:s350(2)-1;t400=0:s400(2)-1;t450=0:s450(2)-1;
t500=0:s500(2)-1;t550=0:s550(2)-1;

% The following commands plot the temporal acoustic behavior at each
location and
% proceed with presenting the selection tool for the user to select the
% maximum amplitudes for each location

figure, grid on, hold on, plot(t200,r200,'k'),xlabel('Time Step'),
ylabel('Particle displacement (Pixel)'),title('200mm')
[j1,y1]=ginput(6);y1=abs(y1);y1m=mean(y1);

figure; grid on, hold on, plot(t250,r250,'k'),xlabel('Time Step'),
ylabel('Particle displacement (Pixel)'),title('250mm')
[j2,y2]=ginput(6);y2=abs(y2);y2m=mean(y2);

figure; grid on, hold on, plot(t300,r300,'k'),xlabel('Time Step'),
ylabel('Particle displacement (Pixel)'),title('300mm')
[j3,y3]=ginput(6);y3=abs(y3);y3m=mean(y3);

figure, grid on, hold on, plot(t350,r350,'k'),xlabel('Time Step'),
ylabel('Particle displacement (Pixel)'),title('350mm')
[j4,y4]=ginput(6);y4=abs(y4);y4m=mean(y4);
```

```
figure; grid on, hold on, plot(t400,r400,'k'),xlabel('Time Step'),
ylabel('Particle displacement (Pixel)'),title('400mm')
[j5,y5]=ginput(6);y5=abs(y5);y5m=mean(y5);

figure; grid on, hold on, plot(t450,r450,'k'),xlabel('Time Step'),
ylabel('Particle displacement (Pixel)'),title('450mm')
[j6,y6]=ginput(6);y6=abs(y6);y6m=mean(y6);

figure; grid on, hold on, plot(t500,r500,'k'),xlabel('Time Step'),
ylabel('Particle displacement (Pixel)'),title('500mm')
[j7,y7]=ginput(6);y7=abs(y7);y7m=mean(y7);

figure; grid on, hold on, plot(t550,r550,'k'),xlabel('Time Step'),
ylabel('Particle displacement (Pixel)'),title('550mm')
[j8,y8]=ginput(6);y8=abs(y8);y8m=mean(y8);



% Measurement locations for the final spatial plot
x=[0.465 0.515 0.565 0.615 0.665 0.715 0.765 0.815];

% Averaging and normalizing the maximum velocity amplitudes that were
% selected manually
ym=[y1m y2m y3m y4m y5m y6m y7m y8m];
ymax=max(ym);
ym=ym./ymax;



%Plotting all temporal results in one figure
figure
subplot(2,4,1);grid on, hold on, plot(t200,r200,'-o'),xlabel('Time
Step'),ylabel('Particle displacement (Pixel)'),title('x=200mm')
subplot(2,4,2);grid on, hold on, plot(t250,r250,'-o'),xlabel('Time
Step'),ylabel('Particle displacement (Pixel'),title('x=250mm')
text(-100,13,'PIV Measurements 129Hz - No Stack - 2.5 Volts to Speaker -
20us - 2700 Hz TR - 50% Overlap - 128x128 pixels^2')
subplot(2,4,3);grid on, hold on, plot(t300,r300,'-o'),xlabel('Time
Step'),ylabel('Particle displacement (Pixel'),title('x=300mm')
subplot(2,4,4);grid on, hold on, plot(t350,r350,'-o'),xlabel('Time
Step'),ylabel('Particle displacement (Pixel'),title('x=350mm')
subplot(2,4,5);grid on, hold on, plot(t400,r400,'-o'),xlabel('Time
Step'),ylabel('Particle displacement (Pixel'),title('x=400mm')
subplot(2,4,6);grid on, hold on, plot(t450,r450,'-o'),xlabel('Time
Step'),ylabel('Particle displacement (Pixel'),title('x=450mm')
subplot(2,4,7);grid on, hold on, plot(t500,r500,'-o'),xlabel('Time
Step'),ylabel('Particle displacement (Pixel'),title('x=500mm')
subplot(2,4,8);grid on, hold on, plot(t550,r550,'-o'),xlabel('Time
Step'),ylabel('Particle displacement (Pixel'),title('x=550mm')

%Plot normalized standing wave only
                       %Relative
figure,plot(x,ym,'*'),xlabel('Distance from speaker
[mm]'),ylabel('Normalized Amplitude'),xlim([100 600]),ylim([0 1.2])
title('PIV Measurements 129Hz - No Stack - 2.5 Volts to Speaker - 185us -
2700 Hz TR - 50% Overlap - 128x128 pixels^2 - Normalized values')



%Plot actual particle displacement
j=[y1m y2m y3m y4m y5m y6m y7m y8m];
figure,plot(x,j,'*'),xlabel('Distance from speaker [mm]'),ylabel('Particle
displacement [pixels]'),xlim([100 600])
title('PIV Measurements 129Hz - No Stack - 2.5 Volts to Speaker - 185us -
2700 Hz TR - 50% Overlap - 128x128 pixels^2 - Particle displacement')
```

```matlab
%Plot actual velocity values
p2mm=0.030303;%One pixel in mm calibration
tbp=185e-6;%Time between pulses
trans=p2mm/1000/tbp;
v_NoStack_0=j.*trans;
figure,plot(x,v_NoStack_0,'o'),xlabel('Distance from speaker
[mm]'),ylabel('Absolute particle velocity [m/sec]'),xlim([150 600]),ylim([0
16]),hold on
title('PIV Measurements 129Hz - No Stack - 2.5 Volts to Speaker - 185us -
2700 Hz TR - 50% Overlap - 128x128 pixels^2 - Absolute particle velocity')
```

Appendix D Detailed numerical DeltaEC models of the different stack configurations presented in chapter 0.

❖ Numerical DeltaEC model of the 100 CPSI – 0.045 mm length configuration

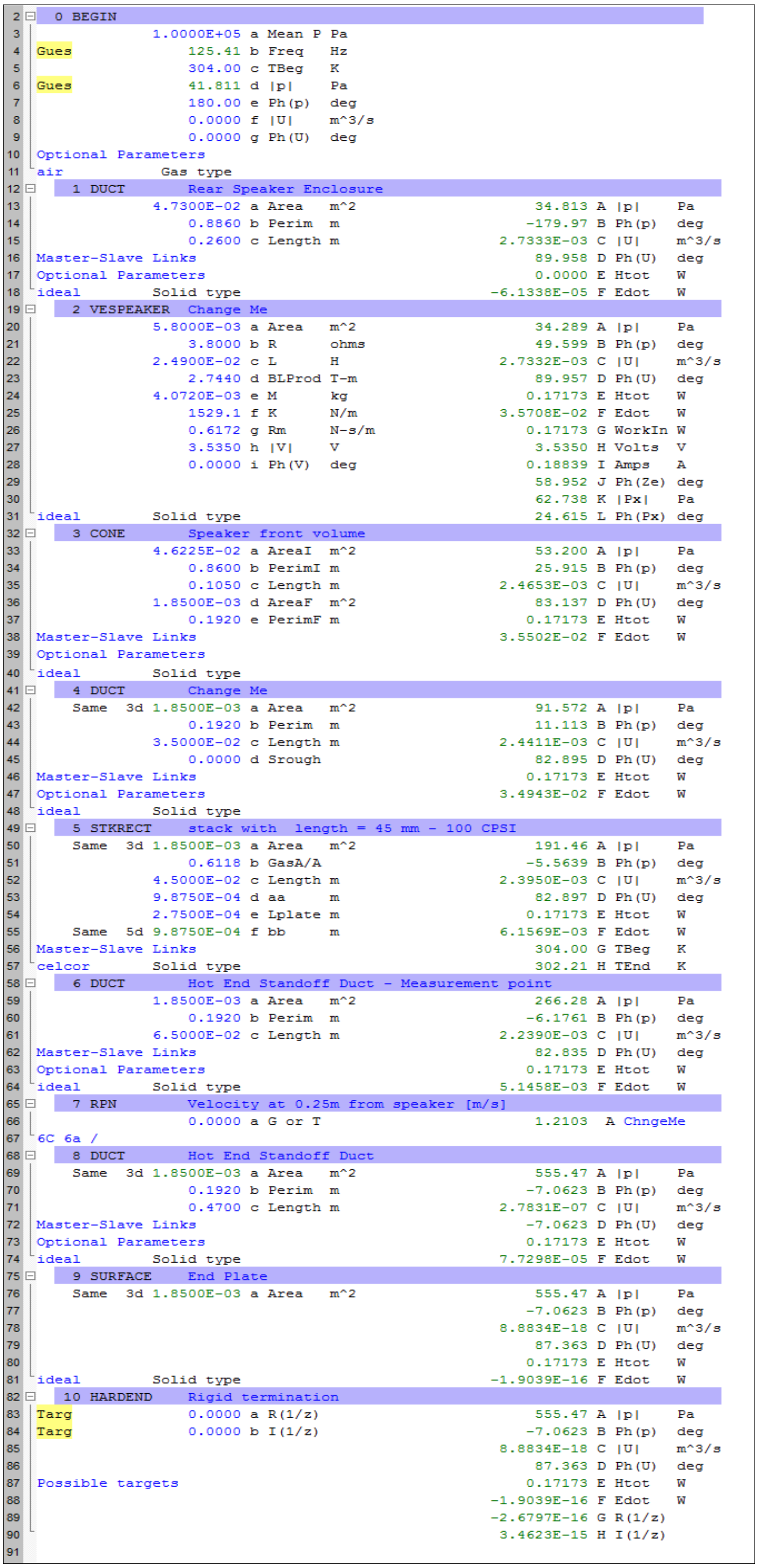

```
  0 BEGIN
             1.0000E+05 a Mean P Pa
Gues             125.41 b Freq   Hz
                 304.00 c TBeg   K
Gues             41.811 d |p|    Pa
                 180.00 e Ph(p)  deg
                 0.0000 f |U|    m^3/s
                 0.0000 g Ph(U)  deg
Optional Parameters
air           Gas type
    1 DUCT           Rear Speaker Enclosure
             4.7300E-02 a Area   m^2                  34.813 A |p|    Pa
                 0.8860 b Perim  m                   -179.97 B Ph(p)  deg
                 0.2600 c Length m                2.7333E-03 C |U|    m^3/s
Master-Slave Links                                    89.958 D Ph(U)  deg
Optional Parameters                                   0.0000 E Htot   W
ideal        Solid type                          -6.1338E-05 F Edot   W
    2 VESPEAKER  Change Me
             5.8000E-03 a Area   m^2                  34.289 A |p|    Pa
                 3.8000 b R      ohms                 49.599 B Ph(p)  deg
             2.4900E-02 c L      H                2.7332E-03 C |U|    m^3/s
                 2.7440 d BLProd T-m                  89.957 D Ph(U)  deg
             4.0720E-03 e M      kg                  0.17173 E Htot   W
                 1529.1 f K      N/m              3.5708E-02 F Edot   W
                 0.6172 g Rm     N-s/m               0.17173 G WorkIn W
                 3.5350 h |V|    V                    3.5350 H Volts  V
                 0.0000 i Ph(V)  deg                 0.18839 I Amps   A
                                                      58.952 J Ph(Ze) deg
                                                      62.738 K |Px|   Pa
ideal        Solid type                               24.615 L Ph(Px) deg
    3 CONE           Speaker front volume
             4.6225E-02 a AreaI  m^2                  53.200 A |p|    Pa
                 0.8600 b PerimI m                    25.915 B Ph(p)  deg
                 0.1050 c Length m                2.4653E-03 C |U|    m^3/s
             1.8500E-03 d AreaF  m^2                  83.137 D Ph(U)  deg
                 0.1920 e PerimF m                   0.17173 E Htot   W
Master-Slave Links                                3.5502E-02 F Edot   W
Optional Parameters
ideal        Solid type
    4 DUCT           Change Me
    Same  3d 1.8500E-03 a Area   m^2                  91.572 A |p|    Pa
                 0.1920 b Perim  m                    11.113 B Ph(p)  deg
             3.5000E-02 c Length m                2.4411E-03 C |U|    m^3/s
                 0.0000 d Srough                      82.895 D Ph(U)  deg
Master-Slave Links                                   0.17173 E Htot   W
Optional Parameters                               3.4943E-02 F Edot   W
ideal        Solid type
    5 STKRECT        stack with  length = 45 mm - 100 CPSI
    Same  3d 1.8500E-03 a Area   m^2                  191.46 A |p|    Pa
                 0.6118 b GasA/A                     -5.5639 B Ph(p)  deg
             4.5000E-02 c Length m                2.3950E-03 C |U|    m^3/s
             9.8750E-04 d aa     m                    82.897 D Ph(U)  deg
             2.7500E-04 e Lplate m                   0.17173 E Htot   W
    Same  5d 9.8750E-04 f bb     m                6.1569E-03 F Edot   W
Master-Slave Links                                    304.00 G TBeg   K
celcor       Solid type                               302.21 H TEnd   K
    6 DUCT           Hot End Standoff Duct - Measurement point
             1.8500E-03 a Area   m^2                  266.28 A |p|    Pa
                 0.1920 b Perim  m                   -6.1761 B Ph(p)  deg
             6.5000E-02 c Length m                2.2390E-03 C |U|    m^3/s
Master-Slave Links                                    82.835 D Ph(U)  deg
Optional Parameters                                  0.17173 E Htot   W
ideal        Solid type                           5.1458E-03 F Edot   W
    7 RPN            Velocity at 0.25m from speaker [m/s]
                 0.0000 a G or T                      1.2103  A ChngeMe
6C 6a /
    8 DUCT           Hot End Standoff Duct
    Same  3d 1.8500E-03 a Area   m^2                  555.47 A |p|    Pa
                 0.1920 b Perim  m                   -7.0623 B Ph(p)  deg
                 0.4700 c Length m                2.7831E-07 C |U|    m^3/s
Master-Slave Links                                   -7.0623 D Ph(U)  deg
Optional Parameters                                  0.17173 E Htot   W
ideal        Solid type                           7.7298E-05 F Edot   W
    9 SURFACE        End Plate
    Same  3d 1.8500E-03 a Area   m^2                  555.47 A |p|    Pa
                                                     -7.0623 B Ph(p)  deg
                                                  8.8834E-18 C |U|    m^3/s
                                                      87.363 D Ph(U)  deg
                                                     0.17173 E Htot   W
ideal        Solid type                          -1.9039E-16 F Edot   W
   10 HARDEND        Rigid termination
Targ             0.0000 a R(1/z)                      555.47 A |p|    Pa
Targ             0.0000 b I(1/z)                     -7.0623 B Ph(p)  deg
                                                  8.8834E-18 C |U|    m^3/s
                                                      87.363 D Ph(U)  deg
Possible targets                                     0.17173 E Htot   W
                                                 -1.9039E-16 F Edot   W
                                                 -2.6797E-16 G R(1/z)
                                                  3.4623E-15 H I(1/z)
```

❖ Numerical DeltaEC model of the 200 CPSI – 0.045 mm length configuration

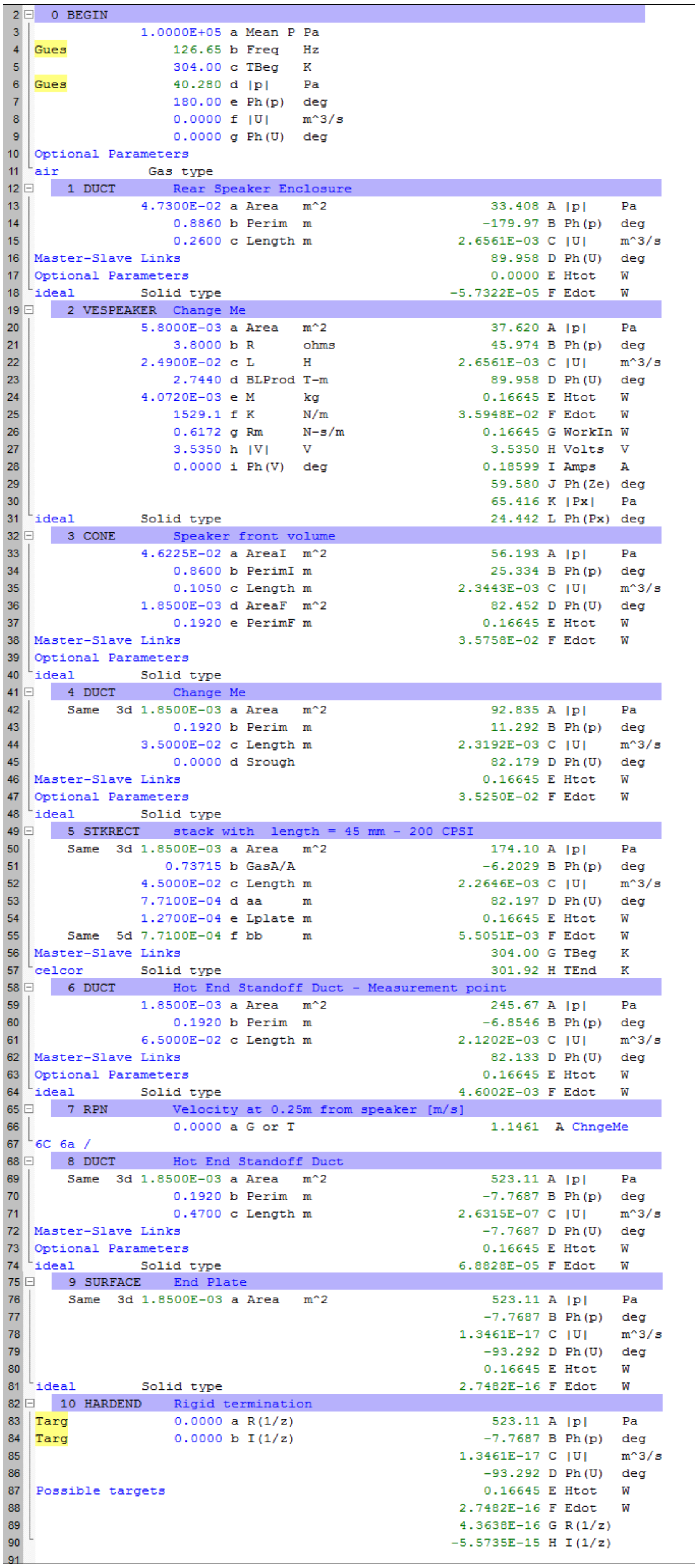

```
  0 BEGIN
             1.0000E+05 a Mean P Pa
Gues             126.65 b Freq   Hz
                 304.00 c TBeg   K
Gues             40.280 d |p|    Pa
                 180.00 e Ph(p)  deg
                 0.0000 f |U|    m^3/s
                 0.0000 g Ph(U)  deg
Optional Parameters
air           Gas type
    1 DUCT       Rear Speaker Enclosure
             4.7300E-02 a Area   m^2                    33.408 A |p|    Pa
                 0.8860 b Perim  m                     -179.97 B Ph(p)  deg
                 0.2600 c Length m                  2.6561E-03 C |U|    m^3/s
Master-Slave Links                                      89.958 D Ph(U)  deg
Optional Parameters                                     0.0000 E Htot   W
ideal        Solid type                            -5.7322E-05 F Edot   W
    2 VESPEAKER  Change Me
             5.8000E-03 a Area   m^2                    37.620 A |p|    Pa
                 3.8000 b R      ohms                   45.974 B Ph(p)  deg
             2.4900E-02 c L      H                  2.6561E-03 C |U|    m^3/s
                 2.7440 d BLProd T-m                    89.958 D Ph(U)  deg
             4.0720E-03 e M      kg                    0.16645 E Htot   W
                 1529.1 f K      N/m                3.5948E-02 F Edot   W
                 0.6172 g Rm     N-s/m                 0.16645 G WorkIn W
                 3.5350 h |V|    V                      3.5350 H Volts  V
                 0.0000 i Ph(V)  deg                   0.18599 I Amps   A
                                                        59.580 J Ph(Ze) deg
                                                        65.416 K |Px|   Pa
ideal        Solid type                                 24.442 L Ph(Px) deg
    3 CONE       Speaker front volume
             4.6225E-02 a AreaI  m^2                    56.193 A |p|    Pa
                 0.8600 b PerimI m                      25.334 B Ph(p)  deg
                 0.1050 c Length m                  2.3443E-03 C |U|    m^3/s
             1.8500E-03 d AreaF  m^2                    82.452 D Ph(U)  deg
                 0.1920 e PerimF m                     0.16645 E Htot   W
Master-Slave Links                                  3.5758E-02 F Edot   W
Optional Parameters
ideal        Solid type
    4 DUCT       Change Me
    Same  3d 1.8500E-03 a Area   m^2                    92.835 A |p|    Pa
                 0.1920 b Perim  m                      11.292 B Ph(p)  deg
             3.5000E-02 c Length m                  2.3192E-03 C |U|    m^3/s
                 0.0000 d Srough                        82.179 D Ph(U)  deg
Master-Slave Links                                     0.16645 E Htot   W
Optional Parameters                                 3.5250E-02 F Edot   W
ideal        Solid type
    5 STKRECT    stack with  length = 45 mm - 200 CPSI
    Same  3d 1.8500E-03 a Area   m^2                    174.10 A |p|    Pa
                0.73715 b GasA/A                       -6.2029 B Ph(p)  deg
             4.5000E-02 c Length m                  2.2646E-03 C |U|    m^3/s
             7.7100E-04 d aa     m                      82.197 D Ph(U)  deg
             1.2700E-04 e Lplate m                     0.16645 E Htot   W
    Same  5d 7.7100E-04 f bb     m                  5.5051E-03 F Edot   W
Master-Slave Links                                      304.00 G TBeg   K
celcor       Solid type                                 301.92 H TEnd   K
    6 DUCT       Hot End Standoff Duct - Measurement point
             1.8500E-03 a Area   m^2                    245.67 A |p|    Pa
                 0.1920 b Perim  m                     -6.8546 B Ph(p)  deg
             6.5000E-02 c Length m                  2.1202E-03 C |U|    m^3/s
Master-Slave Links                                      82.133 D Ph(U)  deg
Optional Parameters                                    0.16645 E Htot   W
ideal        Solid type                             4.6002E-03 F Edot   W
    7 RPN        Velocity at 0.25m from speaker [m/s]
                 0.0000 a G or T                        1.1461  A ChngeMe
6C 6a /
    8 DUCT       Hot End Standoff Duct
    Same  3d 1.8500E-03 a Area   m^2                    523.11 A |p|    Pa
                 0.1920 b Perim  m                     -7.7687 B Ph(p)  deg
                 0.4700 c Length m                  2.6315E-07 C |U|    m^3/s
Master-Slave Links                                     -7.7687 D Ph(U)  deg
Optional Parameters                                    0.16645 E Htot   W
ideal        Solid type                             6.8828E-05 F Edot   W
    9 SURFACE    End Plate
    Same  3d 1.8500E-03 a Area   m^2                    523.11 A |p|    Pa
                                                       -7.7687 B Ph(p)  deg
                                                    1.3461E-17 C |U|    m^3/s
                                                       -93.292 D Ph(U)  deg
                                                       0.16645 E Htot   W
ideal        Solid type                             2.7482E-16 F Edot   W
   10 HARDEND    Rigid termination
Targ             0.0000 a R(1/z)                        523.11 A |p|    Pa
Targ             0.0000 b I(1/z)                       -7.7687 B Ph(p)  deg
                                                    1.3461E-17 C |U|    m^3/s
                                                       -93.292 D Ph(U)  deg
Possible targets                                       0.16645 E Htot   W
                                                    2.7482E-16 F Edot   W
                                                    4.3638E-16 G R(1/z)
                                                   -5.5735E-15 H I(1/z)
```

❖ Numerical DeltaEC model of the 400 CPSI – 0.045 mm length configuration

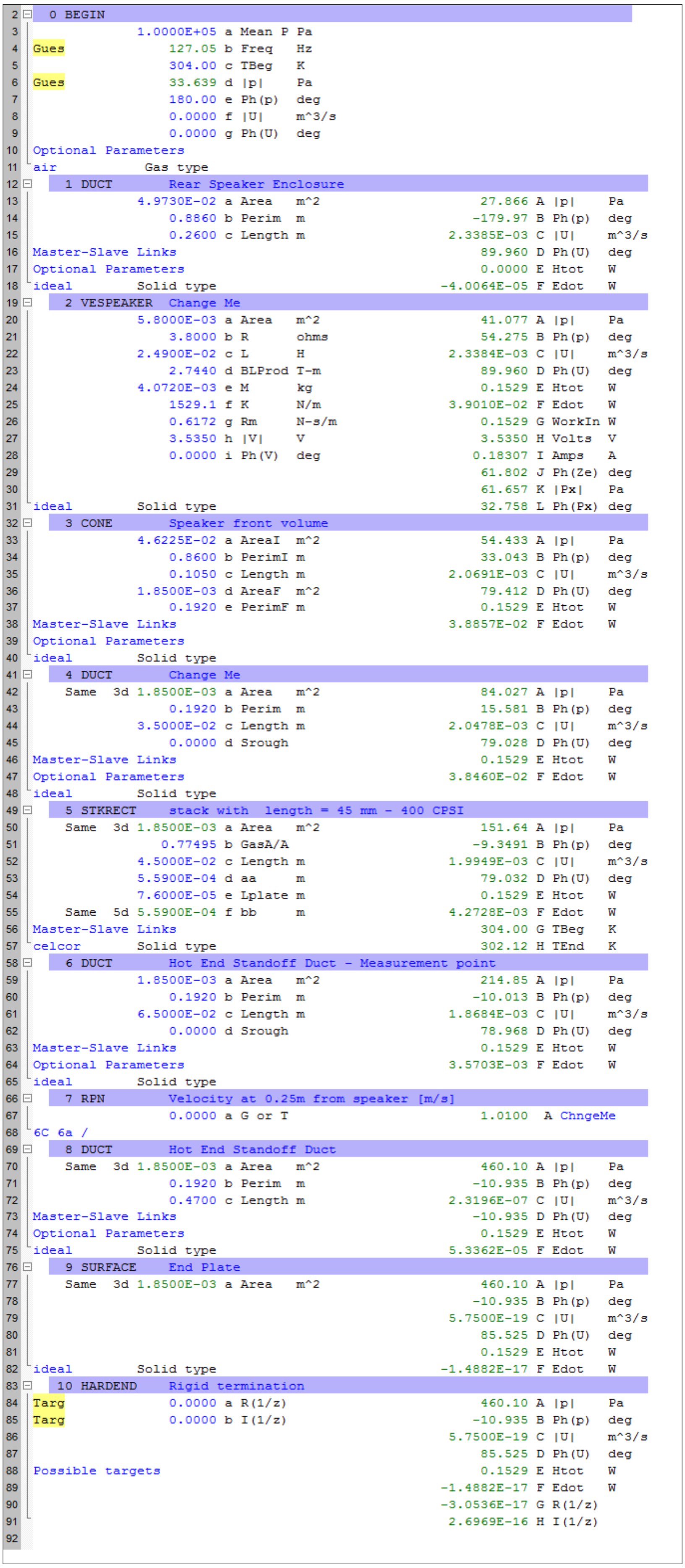

```
 0 BEGIN
              1.0000E+05 a Mean P Pa
Gues              127.05 b Freq    Hz
                  304.00 c TBeg    K
Gues              33.639 d |p|     Pa
                  180.00 e Ph(p)   deg
                  0.0000 f |U|     m^3/s
                  0.0000 g Ph(U)   deg
Optional Parameters
air              Gas type
   1 DUCT           Rear Speaker Enclosure
              4.9730E-02 a Area    m^2                     27.866 A |p|     Pa
                  0.8860 b Perim   m                      -179.97 B Ph(p)   deg
                  0.2600 c Length  m                   2.3385E-03 C |U|     m^3/s
Master-Slave Links                                         89.960 D Ph(U)   deg
Optional Parameters                                        0.0000 E Htot    W
ideal             Solid type                         -4.0064E-05 F Edot    W
   2 VESPEAKER   Change Me
              5.8000E-03 a Area    m^2                     41.077 A |p|     Pa
                  3.8000 b R       ohms                    54.275 B Ph(p)   deg
              2.4900E-02 c L       H                   2.3384E-03 C |U|     m^3/s
                  2.7440 d BLProd  T-m                     89.960 D Ph(U)   deg
              4.0720E-03 e M       kg                      0.1529 E Htot    W
                  1529.1 f K       N/m                 3.9010E-02 F Edot    W
                  0.6172 g Rm      N-s/m                   0.1529 G WorkIn  W
                  3.5350 h |V|     V                       3.5350 H Volts   V
                  0.0000 i Ph(V)   deg                    0.18307 I Amps    A
                                                           61.802 J Ph(Ze)  deg
                                                           61.657 K |Px|    Pa
ideal             Solid type                               32.758 L Ph(Px)  deg
   3 CONE           Speaker front volume
              4.6225E-02 a AreaI   m^2                     54.433 A |p|     Pa
                  0.8600 b PerimI  m                       33.043 B Ph(p)   deg
                  0.1050 c Length  m                   2.0691E-03 C |U|     m^3/s
              1.8500E-03 d AreaF   m^2                     79.412 D Ph(U)   deg
                  0.1920 e PerimF  m                       0.1529 E Htot    W
Master-Slave Links                                     3.8857E-02 F Edot    W
Optional Parameters
ideal             Solid type
   4 DUCT           Change Me
     Same   3d 1.8500E-03 a Area    m^2                    84.027 A |p|     Pa
                  0.1920 b Perim   m                       15.581 B Ph(p)   deg
              3.5000E-02 c Length  m                   2.0478E-03 C |U|     m^3/s
                  0.0000 d Srough                          79.028 D Ph(U)   deg
Master-Slave Links                                         0.1529 E Htot    W
Optional Parameters                                    3.8460E-02 F Edot    W
ideal             Solid type
   5 STKRECT        stack with  length = 45 mm - 400 CPSI
     Same   3d 1.8500E-03 a Area    m^2                    151.64 A |p|     Pa
                 0.77495 b GasA/A                         -9.3491 B Ph(p)   deg
              4.5000E-02 c Length  m                   1.9949E-03 C |U|     m^3/s
              5.5900E-04 d aa      m                       79.032 D Ph(U)   deg
              7.6000E-05 e Lplate  m                       0.1529 E Htot    W
     Same   5d 5.5900E-04 f bb      m                   4.2728E-03 F Edot    W
Master-Slave Links                                         304.00 G TBeg    K
celcor            Solid type                               302.12 H TEnd    K
   6 DUCT           Hot End Standoff Duct - Measurement point
              1.8500E-03 a Area    m^2                     214.85 A |p|     Pa
                  0.1920 b Perim   m                      -10.013 B Ph(p)   deg
              6.5000E-02 c Length  m                   1.8684E-03 C |U|     m^3/s
                  0.0000 d Srough                          78.968 D Ph(U)   deg
Master-Slave Links                                         0.1529 E Htot    W
Optional Parameters                                    3.5703E-03 F Edot    W
ideal             Solid type
   7 RPN            Velocity at 0.25m from speaker [m/s]
                  0.0000 a G or T                          1.0100  A ChngeMe
6C 6a /
   8 DUCT           Hot End Standoff Duct
     Same   3d 1.8500E-03 a Area    m^2                    460.10 A |p|     Pa
                  0.1920 b Perim   m                      -10.935 B Ph(p)   deg
                  0.4700 c Length  m                   2.3196E-07 C |U|     m^3/s
Master-Slave Links                                        -10.935 D Ph(U)   deg
Optional Parameters                                        0.1529 E Htot    W
ideal             Solid type                           5.3362E-05 F Edot    W
   9 SURFACE        End Plate
     Same   3d 1.8500E-03 a Area    m^2                    460.10 A |p|     Pa
                                                          -10.935 B Ph(p)   deg
                                                       5.7500E-19 C |U|     m^3/s
                                                           85.525 D Ph(U)   deg
                                                           0.1529 E Htot    W
ideal             Solid type                          -1.4882E-17 F Edot    W
  10 HARDEND        Rigid termination
Targ              0.0000 a R(1/z)                          460.10 A |p|     Pa
Targ              0.0000 b I(1/z)                         -10.935 B Ph(p)   deg
                                                       5.7500E-19 C |U|     m^3/s
                                                           85.525 D Ph(U)   deg
Possible targets                                           0.1529 E Htot    W
                                                      -1.4882E-17 F Edot    W
                                                      -3.0536E-17 G R(1/z)
                                                       2.6969E-16 H I(1/z)
```

❖ Numerical DeltaEC model of the 600 CPSI – 0.045 mm length configuration

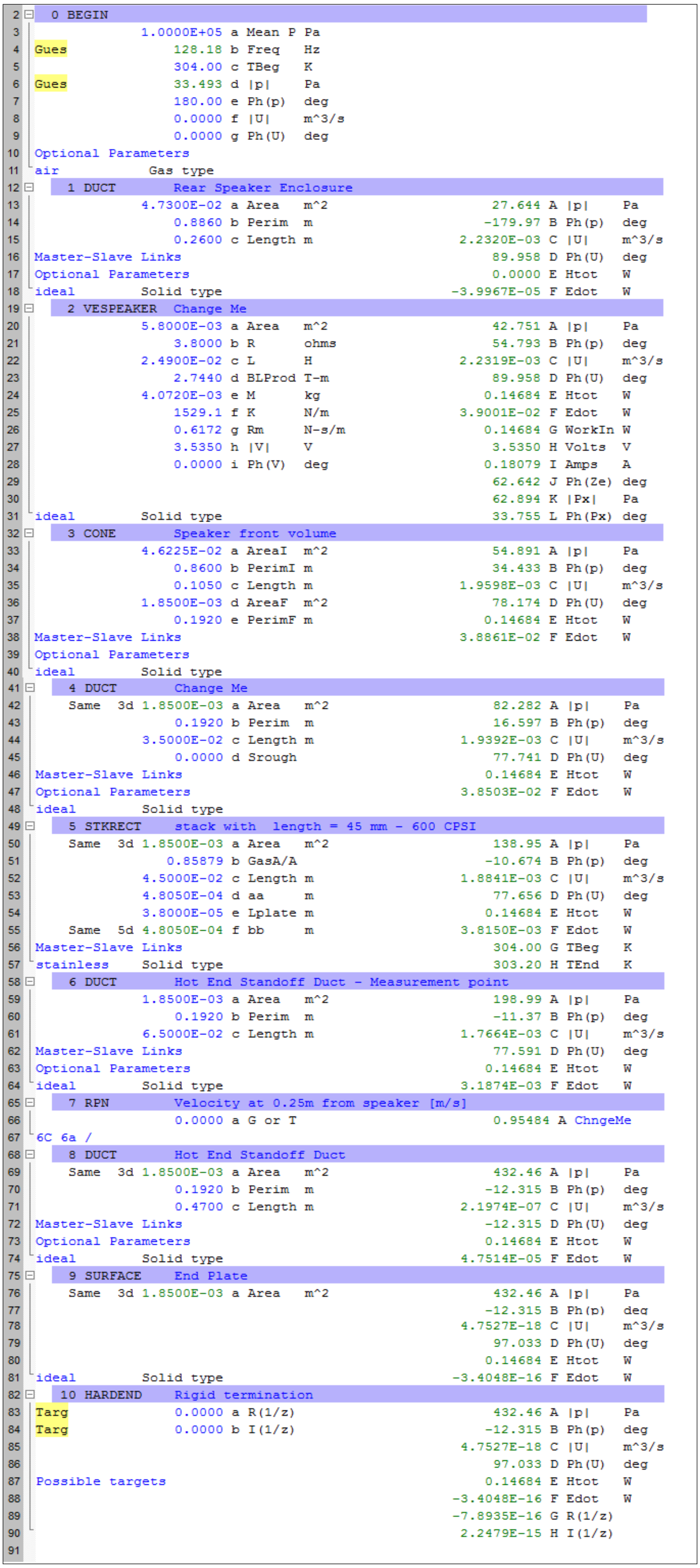

```
  0 BEGIN
                1.0000E+05 a Mean P  Pa
Gues                128.18 b Freq    Hz
                    304.00 c TBeg    K
Gues                33.493 d |p|     Pa
                    180.00 e Ph(p)   deg
                    0.0000 f |U|     m^3/s
                    0.0000 g Ph(U)   deg
Optional Parameters
air           Gas type
    1 DUCT          Rear Speaker Enclosure
                4.7300E-02 a Area    m^2          27.644 A |p|     Pa
                    0.8860 b Perim   m           -179.97 B Ph(p)   deg
                    0.2600 c Length  m        2.2320E-03 C |U|     m^3/s
Master-Slave Links                                89.958 D Ph(U)   deg
Optional Parameters                               0.0000 E Htot    W
ideal           Solid type                   -3.9967E-05 F Edot    W
    2 VESPEAKER     Change Me
                5.8000E-03 a Area    m^2          42.751 A |p|     Pa
                    3.8000 b R       ohms         54.793 B Ph(p)   deg
                2.4900E-02 c L       H        2.2319E-03 C |U|     m^3/s
                    2.7440 d BLProd  T-m          89.958 D Ph(U)   deg
                4.0720E-03 e M       kg          0.14684 E Htot    W
                    1529.1 f K       N/m      3.9001E-02 F Edot    W
                    0.6172 g Rm      N-s/m       0.14684 G WorkIn  W
                    3.5350 h |V|     V            3.5350 H Volts   V
                    0.0000 i Ph(V)   deg         0.18079 I Amps    A
                                                  62.642 J Ph(Ze)  deg
                                                  62.894 K |Px|    Pa
ideal           Solid type                        33.755 L Ph(Px)  deg
    3 CONE          Speaker front volume
                4.6225E-02 a AreaI   m^2          54.891 A |p|     Pa
                    0.8600 b PerimI  m            34.433 B Ph(p)   deg
                    0.1050 c Length  m        1.9598E-03 C |U|     m^3/s
                1.8500E-03 d AreaF   m^2          78.174 D Ph(U)   deg
                    0.1920 e PerimF  m           0.14684 E Htot    W
Master-Slave Links                            3.8861E-02 F Edot    W
Optional Parameters
ideal           Solid type
    4 DUCT          Change Me
      Same   3d 1.8500E-03 a Area    m^2          82.282 A |p|     Pa
                    0.1920 b Perim   m            16.597 B Ph(p)   deg
                3.5000E-02 c Length  m        1.9392E-03 C |U|     m^3/s
                    0.0000 d Srough               77.741 D Ph(U)   deg
Master-Slave Links                               0.14684 E Htot    W
Optional Parameters                           3.8503E-02 F Edot    W
ideal           Solid type
    5 STKRECT       stack with  length = 45 mm - 600 CPSI
      Same   3d 1.8500E-03 a Area    m^2          138.95 A |p|     Pa
                   0.85879 b GasA/A              -10.674 B Ph(p)   deg
                4.5000E-02 c Length  m        1.8841E-03 C |U|     m^3/s
                4.8050E-04 d aa      m            77.656 D Ph(U)   deg
                3.8000E-05 e Lplate  m           0.14684 E Htot    W
      Same   5d 4.8050E-04 f bb      m        3.8150E-03 F Edot    W
Master-Slave Links                                304.00 G TBeg    K
stainless       Solid type                        303.20 H TEnd    K
    6 DUCT          Hot End Standoff Duct - Measurement point
                1.8500E-03 a Area    m^2          198.99 A |p|     Pa
                    0.1920 b Perim   m            -11.37 B Ph(p)   deg
                6.5000E-02 c Length  m        1.7664E-03 C |U|     m^3/s
Master-Slave Links                                77.591 D Ph(U)   deg
Optional Parameters                              0.14684 E Htot    W
ideal           Solid type                    3.1874E-03 F Edot    W
    7 RPN           Velocity at 0.25m from speaker [m/s]
                    0.0000 a G or T              0.95484 A ChngeMe
6C 6a /
    8 DUCT          Hot End Standoff Duct
      Same   3d 1.8500E-03 a Area    m^2          432.46 A |p|     Pa
                    0.1920 b Perim   m           -12.315 B Ph(p)   deg
                    0.4700 c Length  m        2.1974E-07 C |U|     m^3/s
Master-Slave Links                               -12.315 D Ph(U)   deg
Optional Parameters                              0.14684 E Htot    W
ideal           Solid type                    4.7514E-05 F Edot    W
    9 SURFACE       End Plate
      Same   3d 1.8500E-03 a Area    m^2          432.46 A |p|     Pa
                                                 -12.315 B Ph(p)   deg
                                              4.7527E-18 C |U|     m^3/s
                                                  97.033 D Ph(U)   deg
                                                 0.14684 E Htot    W
ideal           Solid type                   -3.4048E-16 F Edot    W
   10 HARDEND       Rigid termination
Targ                0.0000 a R(1/z)               432.46 A |p|     Pa
Targ                0.0000 b I(1/z)              -12.315 B Ph(p)   deg
                                              4.7527E-18 C |U|     m^3/s
                                                  97.033 D Ph(U)   deg
Possible targets                                 0.14684 E Htot    W
                                             -3.4048E-16 F Edot    W
                                             -7.8935E-16 G R(1/z)
                                              2.2479E-15 H I(1/z)
```

❖ Numerical DeltaEC model of the 600 CPSI – 0.0225 mm length configuration

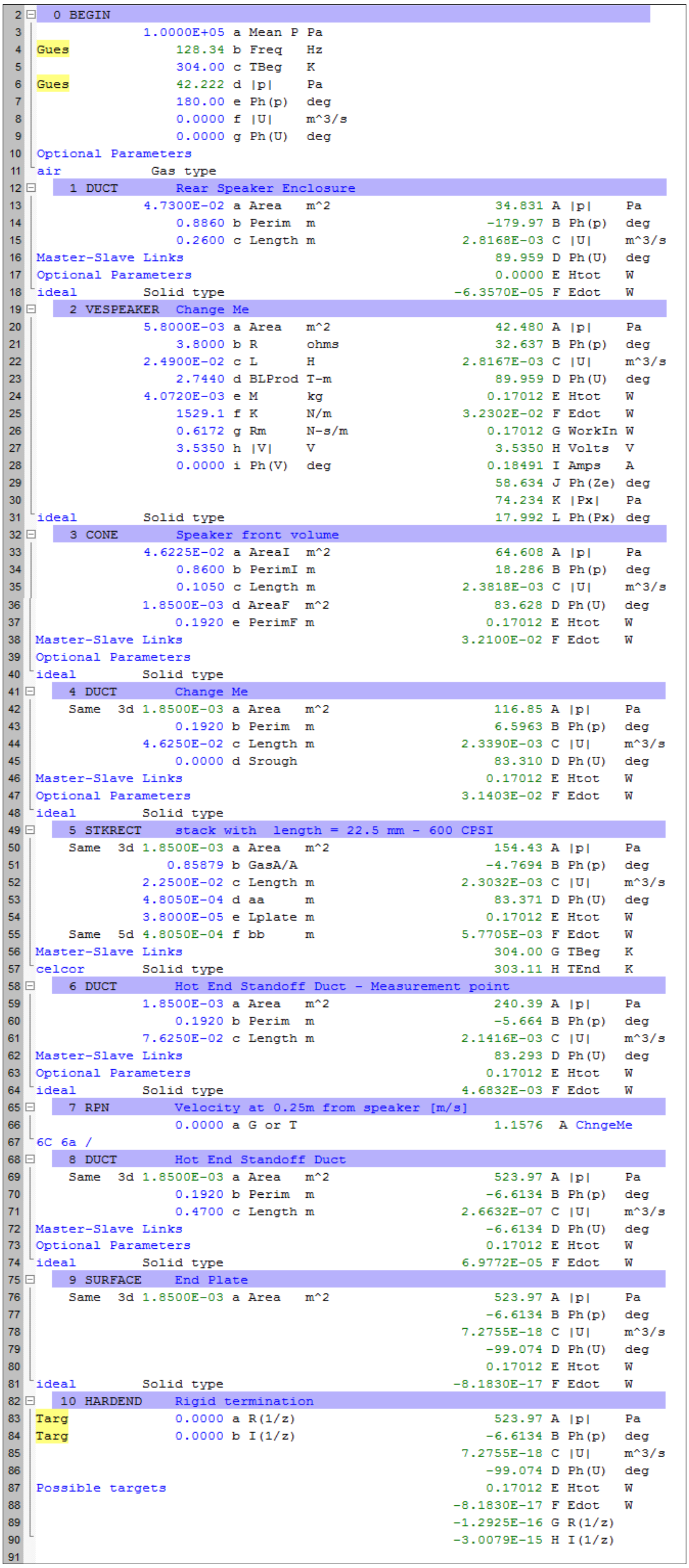

```
  0 BEGIN
             1.0000E+05 a Mean P Pa
Gues             128.34 b Freq   Hz
                 304.00 c TBeg   K
Gues             42.222 d |p|    Pa
                 180.00 e Ph(p)  deg
                 0.0000 f |U|    m^3/s
                 0.0000 g Ph(U)  deg
Optional Parameters
air           Gas type
    1 DUCT       Rear Speaker Enclosure
             4.7300E-02 a Area   m^2                    34.831 A |p|    Pa
                 0.8860 b Perim  m                     -179.97 B Ph(p)  deg
                 0.2600 c Length m                  2.8168E-03 C |U|    m^3/s
Master-Slave Links                                      89.959 D Ph(U)  deg
Optional Parameters                                     0.0000 E Htot   W
ideal        Solid type                            -6.3570E-05 F Edot   W
    2 VESPEAKER  Change Me
             5.8000E-03 a Area   m^2                    42.480 A |p|    Pa
                 3.8000 b R      ohms                   32.637 B Ph(p)  deg
             2.4900E-02 c L      H                  2.8167E-03 C |U|    m^3/s
                 2.7440 d BLProd T-m                    89.959 D Ph(U)  deg
             4.0720E-03 e M      kg                    0.17012 E Htot   W
                 1529.1 f K      N/m                3.2302E-02 F Edot   W
                 0.6172 g Rm     N-s/m                 0.17012 G WorkIn W
                 3.5350 h |V|    V                      3.5350 H Volts  V
                 0.0000 i Ph(V)  deg                   0.18491 I Amps   A
                                                        58.634 J Ph(Ze) deg
                                                        74.234 K |Px|   Pa
ideal        Solid type                                 17.992 L Ph(Px) deg
    3 CONE       Speaker front volume
             4.6225E-02 a AreaI  m^2                    64.608 A |p|    Pa
                 0.8600 b PerimI m                      18.286 B Ph(p)  deg
                 0.1050 c Length m                  2.3818E-03 C |U|    m^3/s
             1.8500E-03 d AreaF  m^2                    83.628 D Ph(U)  deg
                 0.1920 e PerimF m                     0.17012 E Htot   W
Master-Slave Links                                  3.2100E-02 F Edot   W
Optional Parameters
ideal        Solid type
    4 DUCT       Change Me
    Same  3d 1.8500E-03 a Area   m^2                    116.85 A |p|    Pa
                 0.1920 b Perim  m                      6.5963 B Ph(p)  deg
             4.6250E-02 c Length m                  2.3390E-03 C |U|    m^3/s
                 0.0000 d Srough                        83.310 D Ph(U)  deg
Master-Slave Links                                     0.17012 E Htot   W
Optional Parameters                                 3.1403E-02 F Edot   W
ideal        Solid type
    5 STKRECT    stack with  length = 22.5 mm - 600 CPSI
    Same  3d 1.8500E-03 a Area   m^2                    154.43 A |p|    Pa
                0.85879 b GasA/A                       -4.7694 B Ph(p)  deg
             2.2500E-02 c Length m                  2.3032E-03 C |U|    m^3/s
             4.8050E-04 d aa     m                      83.371 D Ph(U)  deg
             3.8000E-05 e Lplate m                     0.17012 E Htot   W
    Same  5d 4.8050E-04 f bb     m                  5.7705E-03 F Edot   W
Master-Slave Links                                      304.00 G TBeg   K
celcor       Solid type                                 303.11 H TEnd   K
    6 DUCT       Hot End Standoff Duct - Measurement point
             1.8500E-03 a Area   m^2                    240.39 A |p|    Pa
                 0.1920 b Perim  m                      -5.664 B Ph(p)  deg
             7.6250E-02 c Length m                  2.1416E-03 C |U|    m^3/s
Master-Slave Links                                      83.293 D Ph(U)  deg
Optional Parameters                                    0.17012 E Htot   W
ideal        Solid type                             4.6832E-03 F Edot   W
    7 RPN        Velocity at 0.25m from speaker [m/s]
                 0.0000 a G or T                        1.1576  A ChngeMe
6C 6a /
    8 DUCT       Hot End Standoff Duct
    Same  3d 1.8500E-03 a Area   m^2                    523.97 A |p|    Pa
                 0.1920 b Perim  m                     -6.6134 B Ph(p)  deg
                 0.4700 c Length m                  2.6632E-07 C |U|    m^3/s
Master-Slave Links                                     -6.6134 D Ph(U)  deg
Optional Parameters                                    0.17012 E Htot   W
ideal        Solid type                             6.9772E-05 F Edot   W
    9 SURFACE    End Plate
    Same  3d 1.8500E-03 a Area   m^2                    523.97 A |p|    Pa
                                                       -6.6134 B Ph(p)  deg
                                                    7.2755E-18 C |U|    m^3/s
                                                       -99.074 D Ph(U)  deg
                                                       0.17012 E Htot   W
ideal        Solid type                            -8.1830E-17 F Edot   W
   10 HARDEND    Rigid termination
Targ             0.0000 a R(1/z)                        523.97 A |p|    Pa
Targ             0.0000 b I(1/z)                       -6.6134 B Ph(p)  deg
                                                    7.2755E-18 C |U|    m^3/s
                                                       -99.074 D Ph(U)  deg
Possible targets                                       0.17012 E Htot   W
                                                   -8.1830E-17 F Edot   W
                                                   -1.2925E-16 G R(1/z)
                                                   -3.0079E-15 H I(1/z)
```